

University of Louisville

## ThinkIR: The University of Louisville's Institutional Repository

---

Electronic Theses and Dissertations

---

8-2014

### Nanoporous Bi<sub>2</sub>Te<sub>3</sub> thermoelectric based Knudsen gas pump.

Abderrazzak Faiz  
*University of Louisville*

Follow this and additional works at: <https://ir.library.louisville.edu/etd>



Part of the [Mechanical Engineering Commons](#)

---

#### Recommended Citation

Faiz, Abderrazzak, "Nanoporous Bi<sub>2</sub>Te<sub>3</sub> thermoelectric based Knudsen gas pump." (2014). *Electronic Theses and Dissertations*. Paper 419.  
<https://doi.org/10.18297/etd/419>

This Doctoral Dissertation is brought to you for free and open access by ThinkIR: The University of Louisville's Institutional Repository. It has been accepted for inclusion in Electronic Theses and Dissertations by an authorized administrator of ThinkIR: The University of Louisville's Institutional Repository. This title appears here courtesy of the author, who has retained all other copyrights. For more information, please contact [thinkir@louisville.edu](mailto:thinkir@louisville.edu).

NANOPOROUS  $\text{Bi}_2\text{Te}_3$  THERMOELECTRIC BASED KNUDSEN GAS PUMP

By

Abderrazzak Faiz

M.S. University of Louisville, 2008

A Dissertation

Submitted to the Faculty of the

J. B. Speed School of Engineering of the University of Louisville  
in Partial Fulfillment of the Requirements for the Degree of

Doctor of Philosophy

Department of Mechanical Engineering

University of Louisville

Louisville, KY 40292

August 2014



NANOPOROUS  $\text{Bi}_2\text{Te}_3$  THERMOELECTRIC BASED KNUDSEN GAS PUMP

By

Abderrazzak Faiz  
M.S. University of Louisville, 2008

A Dissertation Approved on

August 08, 2014

by the following Dissertation Committee:

---

Dr. Shamus P. McNamara (Dissertation Advisor)

---

Dr. Ellen G. Brehob (Co-advisor)

---

Dr. Stuart J. Williams

---

Dr. Gamini U. Sumanasekera

---

Dr. Yongsheng Lian



## DEDICATION

I dedicate this dissertation to my family:

My lovely wife, **Meryem Salim**, and my wonderful kids, **Aicha**, **Tasneem**, and **Yahya**.

**Meryem** always inspired me to do my very best and to stay strong through hard times.

My parents, **Faiz Said** and **Touhami Aicha**, my brothers and sisters, **Mohamed**, **El Houcine**, **Khadija**, **Fatima**, and **Mina** for their support, encouragement, love, and caring throughout my life.

## ACKNOWLEDGMENTS

I owe my gratitude to all those people who have participated to make this dissertation possible.

I would like to express my deepest gratitude to my advisor Dr. Shamus McNamara for his great help, unlimited patience, and excellent guidance. His office was always open, even before I started working in his lab.

I am also very grateful to my committee members, Dr. Stuart Williams and Dr. Lian Yongsheng for their time and awesome ideas. Dr. Gamini Sumanesakera for letting me using his lab and equipment for thermoelectric characterization and carbon nanotubes growth with the CVD system, and mentoring during my time in the Physics department. Dr. Ellen Brehob for her great ideas on the analysis of gas flow through nanoporous membranes.

Special thanks to Dr. Keynton who supported me during my first years in the PhD program, he is one of the best professors I have worked with.

Many thanks to my colleagues at the DREAM lab: Pranoy, Dr. Pharas, Alex, Stephanie, Li, and Devin.

I also thank Don Yeager, Mark Crain, Dr. Julia Aebersold, Ana, Curt McKenna, Joe Williams, Mike Martin, Dr. Resendo, Dr. Cindy, Dr. Yehya Senousy, Douglas Jackson, Dr. Tommy Roussel, and Scott Cambron for their help on the different projects I have worked on. Dr. Tereza was a great help with the Carbon Nanotubes growth.

I would like to thank Mr. Jamouli Mohamed, my best friend, for the great time working together late in the lab, excellent suggestion and fruitful discussions. Also thanks to all other friends (too many to list here), at the 4<sup>th</sup> ST and 6 miles masjid, for the great time we spent together and for their support whenever they could.

I cannot let this opportunity pass without thanking Dr. Abdelilah Safir for his help 8 years ago with the admission at the University of Louisville, his ideas were efficient, he was always supportive, smiling, and willing to help.

Lastly, a special thanks to the NSF and EPSCoR programs, the University of Louisville, department of Mechanical Engineering, and department of Physics and Astronomy for their financial support and quality education.

## ABSTRACT

### NANOPOROUS $\text{Bi}_2\text{Te}_3$ THERMOELECTRIC BASED KNUDSEN GAS PUMP

Abderrazzak Faiz

August 8, 2014

This dissertation reports on the fabrication of a bi-directional Knudsen gas pump using a multifunctional nanoporous thermoelectric material. The integration of the channels into the thermoelectric material has the advantages of reducing heat losses and power consumption, improving the pump efficiency, and reducing the overall pump size. The Knudsen pump operates on the thermal transpiration principle, the phenomenon that gas molecules drift from the cold end to the hot end of a narrow channel. The gas pumping is realized in the transition or free molecular regime. The Knudsen pump is needed in a great number of applications such as gas chromatography, spectroscopy, gas manipulation, and cooling in microelectronics.

Pressure and pressureless sintering techniques are used to fabricate the nanoporous thermoelectric material. The thermoelectric material was characterized by measuring the pore size distribution, electrical conductivity, and thermal conductivity, thermopower, and temperature distribution. Two Knudsen pumps are then fabricated. In the first pump, the circular thermoelectric sample is placed on a copper heat sink. When the power is turned on, one side of the thermoelectric sample gets hot, and the other side gets cold providing the necessary temperature gradient for thermal transpiration to take

place. Reversing the voltage polarity reverses the hot and cold sides and therefore reverses the pumping direction. The pump generated a pressure of 300 Pa for an input power of 0.96 W. In the second design, the fabricated square-shaped thermoelectric sample is placed in a machined plastic channel. 520 Pa pressure difference and 1  $\mu\text{l}/\text{min}$  flow rate are obtained for an input power of 1.33 W.

Using a combination of the Sharipov and thermoelectric equations, expression for the maximum pressure difference,  $\Delta P_{\text{max}}$ , and maximum mass flow rate,  $\dot{M}_{\text{max}}$ , are derived and analyzed. We conclude the following. As the thermoelectric figure of merit  $Z$  increases,  $\dot{M}_{\text{max}}$  and  $\Delta P_{\text{max}}$  increases. As the pore size increases, the  $\Delta P_{\text{max}}$  decreases, and  $\dot{M}_{\text{max}}$  increases. As the molecular mass of the working gas increases,  $\Delta P_{\text{max}}$  decreases, and  $\dot{M}_{\text{max}}$  increases. As the tangential momentum accommodation coefficient increases,  $\Delta P_{\text{max}}$  increases, and  $\dot{M}_{\text{max}}$  decreases.

The last section of this dissertation is concerned with gas flow through track-etch Whatman nanoporous membranes. We found that the tangential momentum accommodation coefficient fails to solve the discrepancy between experimental and theoretical flow rate. A simple measurement of pressure versus the flow rate through the membranes was conducted next. Among the analyzed models from the literature, the surface flow diffusion model provides the best fit to the experimental data.

## TABLE OF CONTENTS

ACKNOWLEDGMENTS .....	iv
ABSTRACT .....	vi
TABLE OF CONTENTS .....	viii
LIST OF TABLES .....	xiv
LIST OF FIGURES .....	xvi
<b>CHAPTER 1: INTRODUCTION.....</b>	<b>1</b>
1.1 Importance of gas micropumps.....	1
1.2 Features of the Knudsen pump.....	1
1.3 Knudsen pump conventional design.....	2
1.4 Thermoelectric module design.....	2
1.5 Thermoelectric based Knudsen pump .....	3
1.6 Gas flow through nanoporous membranes .....	4
1.7 Objectives .....	4
1.8 Dissertation outline .....	5
<b>CHAPTER 2: BACKGROUND AND LITERATURE REVIEW .....</b>	<b>6</b>
2.1 Mechanical micropumps.....	6
2.1.1 Piezoelectric.....	7
2.1.2 Electrostatic .....	8
2.1.3 Electromagnetic .....	8
2.1.4 Thermopneumatic.....	9
2.1.5 Shape memory alloy (SMA).....	10
2.1.6 Bimetallic.....	10
2.2 Non-mechanical micropumps .....	11
2.2.1 Electrowetting.....	11
2.2.2 Electrochemical .....	12

2.2.3	Electrohydrodynamic .....	12
2.2.4	Magnetohydrodynamic .....	13
2.2.5	Electroosmotic (DC and AC) .....	14
2.2.6	Accommodation pump .....	15
2.2.7	Knudsen compressor .....	17
2.2.8	Thermomolecular pump .....	17
2.3	Knudsen pump background .....	18
2.4	Working principle of the Knudsen pump .....	26
2.4.1	Knudsen number .....	26
2.5	Thermal transpiration models .....	32
2.5.1	The Maxwell model .....	32
2.5.2	The Knudsen model .....	33
2.5.3	The Kennard model .....	34
2.5.4	The Williams model .....	35
2.5.5	The Sharipov model .....	35
2.6	Thermoelectric effects .....	39
2.6.1	Seebeck effect .....	39
2.6.2	Peltier effect .....	40
2.6.3	Thomson effect .....	40
2.6.4	Kelvin effect .....	41
2.7	Thermoelectric figure of merit $ZT$ .....	42
2.8	Changes in the electron density when moving to low dimensional .....	44
2.9	$\text{Bi}_2\text{Te}_3$ thermoelectric material .....	45
2.10	Production of $\text{Bi}_2\text{Te}_3$ and its alloys .....	45
2.10.1	Growth from a melt .....	45
2.10.2	Powder metallurgy .....	46
2.11	Thermoelectric physical properties measurement .....	46
2.11.1	Electrical conductivity .....	46
2.11.2	Seebeck coefficient (Thermopower) .....	47
2.11.3	Thermal conductivity .....	48
2.11.4	Thermal diffusivity .....	50

2.12 Powder metallurgy .....	51
2.13 Powder preparation .....	53
2.13.1 Ball milling .....	55
2.14 Sintering .....	56
2.14.1 Definition .....	56
2.14.2 Densification and coarsening.....	57
2.14.3 Sintering stages.....	58
2.15 Effect of sintering variables .....	59
2.16 Sintering procedure .....	60
2.17 Tangential Momentum accommodation coefficient (TMAC) .....	61
2.18 Definition of the TMAC .....	62
2.19 Methods for measuring the TMAC.....	64
2.19.1 The Millikan Oil drop experiments .....	64
2.19.2 Rotating cylinder method.....	65
2.19.3 Spinning rotor gauge method .....	66
2.19.4 Molecular beam techniques .....	67
2.19.5 Flow through microchannels .....	68
2.20 Parameters affecting the TMAC .....	75
<b>CHAPTER 3: FABRICATION AND CHARACTERIZATION OF THE Bi<sub>2</sub>Te<sub>3</sub></b>	
<b>THERMOELECTRIC BASED KNUDSEN PUMP .....</b>	<b>78</b>
3.1 General fabrication process .....	78
3.2 Method for powder preparation .....	79
3.3 Method for sintered thermoelectric sample fabrication.....	81
3.3.1 Square and circular die sets .....	81
3.3.2 Pellet press .....	82
3.3.3 Sample compaction .....	82
3.3.4 Tube furnace for sintering compact samples .....	83
3.4 Method of sintered thermoelectric sample characterization.....	84
3.4.1 Temperature distribution along the sintered sample surface .....	84
3.5 Method for measuring the sintered sample thermoelectric properties.....	87
3.5.1 Seebeck coefficient and electrical resistivity.....	87



3.5.2	Thermal conductivity .....	89
3.6	Procedure to test if the sample is porous .....	92
3.7	Method for building the thermoelectric based Knudsen pump .....	93
3.8	Results of the powder and sintered thermoelectric sample characterization .....	95
3.8.1	Powder grain size versus milling time .....	95
3.8.2	Sintering experiments.....	96
3.8.3	Thermoelectric sample porosity testing .....	98
3.9	Sintered sample characterization .....	100
3.9.1	XRD and EDS results on the powder and thermoelectric sample.....	100
3.9.2	Physical properties of the thermoelectric sintered sample.....	102
3.9.3	Temperature measurement on the thermoelectric sintered sample .....	104
3.10	Results on the built thermoelectric based Knudsen pump .....	106
3.11	Pressure flow rate relationship.....	109
3.12	Pore size versus the sintering conditions.....	112
3.13	Electrical contacts .....	113
3.14	Conclusion.....	115

**CHAPTER 4: MODELING OF THE NANOPOROUS THERMEOELCTRIC  
BASED KNUDSEN PUMP .....117**

4.1	Mass flow rate of a Knudsen pump .....	117
4.2	Maximum pressure of a Knudsen pump.....	118
4.3	Maximum mass flow rate of a Knudsen pump .....	119
4.4	Mathematical modeling of the TE based Knudsen pump .....	119
4.4.1	Variation of $Q_C$ versus $I$ .....	122
4.5	Variation of $Q_C$ versus $V$ .....	124
4.6	Variation of $Q_C$ versus $X$ .....	126
4.7	Variation of $\Delta T$ versus $I$ .....	128
4.8	Variation of $\Delta T$ versus $V$ .....	129
4.9	Variation of $\Delta T$ versus $X$ .....	130
4.10	Shared interval between $Q_C$ and $\Delta T$ .....	131
4.11	Current giving a maximum $\Delta P _{\dot{M}=0}$ .....	133

4.12 Current giving a maximum $\dot{M}_{\max}$ .....	134
4.13 Current giving a maximum $\Delta T$ .....	136
4.14 Analysis of $\dot{M} _{\Delta P=0}$ and $\Delta P _{\dot{M}=0}$ for the TE Knudsen pump .....	137
4.14.1 General shape of $\Delta P _{\dot{M}=0}$ .....	137
4.14.2 Effect of the pore size and $Z$ value on $\Delta P_{\max}$ and $\dot{M}_{\max}$ .....	138
4.14.3 Effect of the working gas on $\dot{M}_{\max}$ and $\Delta P_{\max}$ .....	144
4.14.4 Effect of the TMAC value on $\Delta P_{\max}$ and $\dot{M}_{\max}$ .....	145
4.15 Conclusion .....	148
<b>CHAPTER 5: GAS FLOW THROUGH NANOPOROUS MEMBRANES.....</b>	<b>150</b>
5.1 Introduction .....	150
5.2 Theoretical equations for gas flow .....	151
5.3 Experimental procedure .....	151
5.4 Materials: .....	154
5.5 Experimental results .....	155
5.6 Discussion.....	159
5.6.1 End effect .....	159
5.6.2 Tangential Momentum Accommodation Coefficient measurement .....	159
5.6.3 Comparison of the experimental results with theoretical models .....	161
5.6.4 Surface flow through the nanoporous membranes .....	162
5.7 Conclusion .....	164
<b>CHAPTER 6: CONCLUSIONS AND FUTURE WORK .....</b>	<b>166</b>
6.1 Conclusions .....	166
6.2 Future work .....	169
REFERENCES .....	171
APPENDIX A: DETERMINATION OF THE PORE SIZE AND SURFACE AREA USING IMAGE $J$ .....	196
APPENDIX B: Machining the channel for the thermoelectric sintered sample using the CNC machine .....	201

CURRICULUM VITAE.....215

## LIST OF TABLES

Table 2.1: General properties of $\text{Bi}_2\text{Te}_3$ [124].	45
Table 2.2: Mechanical and chemical methods for powder preparation [150].	55
Table 2.3: Possible particle size for different milling techniques [151].	56
Table 2.4: Values of $A$ and $f$ obtained by Millikan using different gas-liquid drop or surface combinations.	65
Table 2.5: Obtained TMAC values from different research groups using the spinning rotor method.	67
Table 3.1: Dimensions and physical properties of the starting TE pellets.	80
Table 3.2: Fabricated samples with the corresponding sintering conditions. A nonporous sample was obtained for a pressure of 6 MPa, sintering temperature of 150 °C, and two hours sintering time using pressure sintering. PS and PSN correspond to pressure sintering and pressureless sintering respectively. C and S stand for circular and square respectively.	97
Table 3.3: Average, maximum, minimum, and standard deviation of the pore radius at different sintering conditions.	113
Table 4.1: Maximum and minimum permitted current $I$ for a given voltage $V$ . These intervals assure that $Q_C$ and $\Delta T$ will be positive, and therefore proper operation of the TE based pump. The gray values are used in figure 4.10.	139
Table 4.2: Physical properties and dimensions of the TE element used in the calculation of $I_{\max}$ , $I_{\min}$ , $\Delta P_{\max}$ , and $\dot{M}_{\max}$ .	141
Table 4.3: Pore sizes used in this study along with their transpirational flow coefficient $M_t$ , pressure return flow coefficient $M_p$ , and the Knudsen number calculated for air at room pressure and temperature.	142
Table 4.4: Molecular mass, mean free path [98] and the Knudsen number of the different gases investigated in figure 4.16. $M_t$ and $M_p$ calculated using equations in figure 4.15.	145
Table 5.1: Investigated membrane characteristics. The membrane size corresponds to the average pore diameter. The $Kn$ and $\delta$ are calculated for air at room conditions ( $\lambda=68$ nm). The number of pores is obtained by multiplying the membrane pore density by the area. The first three columns are data from the manufacturer and the rest are calculated.	152
Table 5.2: Comparison of the manufacturer and measured membrane pore size and pore density. Pore size is measured through analysis of SEM images of the membranes using ImageJ software. About 80 measurements were taken and averaged. Pore density is calculated by counting the number of pores on the image and dividing it by the image area (about 10 images used for pore density calculation).	155
Table 5.3: Experimental data for the different nanoporous membranes when both boxes (A and B) are kept at room temperature.	156
Table 5.4: Experimental data for the different nanoporous membranes when box A at room temperature and box B at 50 °C.	158

Table 5.5: $\alpha$ values calculated using the experimental $G$ values and fitting equations from the literature. ....	160
Table 5.6: Comparison between experimental and theoretical flow rate through the Whatman membranes. Numbers in the table correspond to the ratio of theoretical to experimental flow rate. Experimental box set up is kept at room temperature (25 °C)...	161
Table 5.7: Comparison between experimental and theoretical flow rate through the Whatman membranes. Numbers in the table correspond to the ratio of theoretical to experimental flow rate. Box A is at 25 °C and box B is at 50 °C. ....	162
Table 5.8: $K$ for the 15 nm membrane was calculated using the experimental data and equation (2.83). Equation (2.78) was then used to determine $d$ and calculate $K$ for the other membrane sizes.....	162
Table 5.9: Calculated flow rate using the using the calculated $K$ values (Table 5.8) and equation (2.82).....	163
Table B-1: Some Feeds and speeds values which can be used to machine plastic. ....	206

## LIST OF FIGURES

Figure 1.1: Knudsen pump conventional design. A heater heats the hot side, while the cold side is actively cooled using a heat sink. Long channels out of low thermal conductivity materials are used to improve the temperature gradient. ....	2
Figure 1.2: Schematic of the thermoelectric Knudsen pump. The thermoelectric module actively heats and cools the hot and cold sides of the membrane, respectively. The membrane is sandwiched between two Copper plates. A lot of heat is lost through the heat spreader plates. Temperature across the membrane is reduced due to the unavoidable gap between the membrane and the metal plate. ....	3
Figure 1.3: Schematic of the thermoelectric based Knudsen pump working principle. Once power is applied to the thermoelectric material, one side becomes cold, and the other side becomes hot. Gas flows from the cold side to the hot side through the pores. ...	4
Figure 2.1: Schematic of the working principal of a piezoelectric micropump. ....	7
Figure 2.2: Schematic of the electromagnetic micropump [44]. ....	9
Figure 2.3: Linear bimetallic strip. The differing thermal expansion caused stress in the actuator when heated, and therefore deformation. ....	11
Figure 2.4: Electrowetting effect. ....	12
Figure 2.5: Schematic of the formed double layer on the glass surface. ....	15
Figure 2.6: A schematic illustration of the accommodation pump, chamber A is connected to chamber B with a rough tube, while B is connected to C with a smooth tube. Pumping occurs from B to A [69]. $T_1 < T_2$ . ....	16
Figure 2.7: single stage schematic diagram of the thermomolecular pump [73]. Pumping occurs from B to A. ....	18
Figure 2.8: Schematic of the first pump made by Knudsen. ....	19
Figure 2.9: Schematic of the $i^{\text{th}}$ stage of a Knudsen compressor [71]. ....	20
Figure 2.10: (Right) Knudsen pump layout showing the different device components.(Left) Fabrication steps followed during the fabrication of the Knudsen pump [14]. ....	21
Figure 2.11: deflection of the pressure sensor membrane when power is turned on (a) Power is off, no deflection. (b) Power turned on, membrane deflection [14]. ....	22
Figure 2.12: (Right) Exploded view of a zeolite-based Knudsen pump. (Left) Sectional view of the Knudsen pump [85]. ....	23
Figure 2.13: A schematic layout of the ceramic based 9-stage [86]. ....	24
Figure 2.14: Exploded view of the lateral and radial designs. (Left) Lateral design. (Right) radial design [22]. ....	25
Figure 2.15: Fabrication steps for the multiple stages Knudsen pump. (Left) 48 stages [87]. (Right) 162 stages [89]. ....	26
Figure 2.16: Classification of the flow regimes based on Knudsen number $Kn$ . ....	27
Figure 2.17: Schematic of the competing flows for a tube in the transitional flow regime [94]. ....	29

Figure 2.18: Thermal transpiration through (a) an aperture, (b) a channel. The two chambers are maintained at different temperatures. A net flow occurs from the cold side to the hot side.....	30
Figure 2.19: $M_p$ values for a circular channel in the different flow regimes for different TMAC values [103]. .....	38
Figure 2.20: $M_t$ values for a circular channel in the different flow regimes for different TMAC values [103]. .....	38
Figure 2.21: Seebeck effect, temperature gradient along the bar caused a generation of an electromotive force.....	40
Figure 2.22: Schematic description of Thomson effect [106]. .....	41
Figure 2.23: Schematic dependence of thermal conductivity, electrical conductivity, and the Seebeck coefficient on the carrier concentration $n$ [121]. .....	43
Figure 2.24: $ZT$ value for different thermoelectric materials versus temperature [111]....	43
Figure 2.25: Density of state (DOS) as a function of energy for bulk material (3-D), quantum well (2-D), nanowire (1-D), and a quantum dot (0-D) [115]. .....	44
Figure 2.26: Electrical conductivity measurement [140]. .....	47
Figure 2.27: Schematic set-up for measuring the Seebeck coefficient. (a) Thermocouples are attached to the sample. (b) Thermocouples are attached to the heater and heat sink [140]. .....	48
Figure 2.28: A Schematic illustration of the experimental setup for measuring thermal diffusivity using the Angstrom method. ....	51
Figure 2.29: Powder metallurgy component production steps [149]. .....	53
Figure 2.30: Basic phenomena occurring during sintering [152]. .....	58
Figure 2.31: Rate of Densification in the three stages of sintering .....	59
Figure 2.32: A schematic diagram of the grain structure changes during sintering for spherical shape grain. ....	59
Figure 2.33: Effect of sintering conditions on the relative density ( $L$ : grain size, $T$ : temperature, $P$ : pressure) [152]. .....	60
Figure 2.34: General fabrication pattern of sintered parts. ....	60
Figure 2.35: Schematic showing the behavior of the gas molecules at the limit cases of the TMAC values. ....	63
Figure 2.36: Variation of the TMAC in the different flow regimes for a variety of gases as reported by different research groups [188]. .....	76
Figure 3.1: Schematic of the fabrication process to create the nanoporous $\text{Bi}_2\text{Te}_3$ TE material used in the bi-directional Knudsen pump. Commercial grade doped $\text{Bi}_2\text{Te}_3$ is ball milled to create a nanopowder, which is then sintered in a die press to obtain the final pellet. ....	79
Figure 3.2: High energy vibratory ball used in the experiment (Right). Stainless steel vacuum jar (Left). .....	80
Figure 3.3: 13mm die sets used of the fabrication of the nanoporous $\text{Bi}_2\text{Te}_3$ sample. (a) Circular heated die set. (b) Square die set. ....	82
Figure 3.4: 15-Ton manual hydraulic press used to compact the powder. ....	84
Figure 3.5: Thermal IR microscope used for testing the sintered sample. Source: QFI Corp. ....	85

Figure 3.6: A close up view showing the sintered sample sitting on the heated stage along with the connection wires. (a) Circular sample. (b) Square sample. Kapton Tape was used to electrically insulate the sample from the thermal stage. ....	86
Figure 3.7: Typical temperature distribution along the surface of the sintered circular sample generated with the InfraScope software. Stage is heated to 60°C. ....	86
Figure 3.8: (a) Setup used to measure the thermopower and electrical conductivity of the sintered sample. (b) Close up view of the TE sample sitting on the ceramic holder. Thermocouples and electrical wires are glued with silver paste. The ceramic heater induces a temperatures gradient across the sample. ....	88
Figure 3.9: Schematic of the thermopower and electrical resistivity measurement. Temperature gradient induced along the TE sample and measured by two thermocouples is converted to the thermopower. A current is run through the sample and used to measure the electrical resistivity. ....	89
Figure 3.10: Measuring principle of the thermal diffusivity. A laser heats the sample from one side and a detector, on the other side, detects the time-dependent temperature rise. ....	91
Figure 3.11: A schematic of the set-up used to check for the presence of pores, it consists of a syringe connected through a T-connector to the sample and the pressure sensor. ....	93
Figure 3.12: 13 mm wide channel machined on Acrylic plastic using 3-axis CNC machine as described in appendix B. ....	94
Figure 3.13: SEM images of the ball milled powder at different milling times. (Left) 5 hours. (Right) 10 hours. The starting material is a p-type Bi <sub>2</sub> Te <sub>3</sub> . Milling performed under vacuum. ....	95
Figure 3.14: Grain size versus the milling time. Dark circles are the measured data and the solid line corresponds to the power fit. G is the grain size and <i>t</i> is time. ImageJ software was used to analyze the SEM images and measure the grain size, the procedure is described in appendix A. Numbers above the data points are the standard deviations. ....	96
Figure 3.15: SEM image of a non-porous TE sample. (Right)Top face. (Left) Inside. ....	96
Figure 3.16: The pressure drops in a sealed cavity through the pores for sample#1 demonstrating that the sintered Bi <sub>2</sub> Te <sub>3</sub> is porous. ....	98
Figure 3.17: SEM image of nanoporous Bi <sub>2</sub> Te <sub>3</sub> showing sub-micron size pores. Inless detector was used with a 20 kV electron beam. (Left) Sample#1. (Right) Sample#12. ....	99
Figure 3.18: Sintered samples. Square and circular samples are fabricated using pressureless and pressure sintering respectively. ....	99
Figure 3.19: SEM images of a compact sample after sintering at different temperature. (a) No sintering.(b) 200°C.(c) 300°C.(d) 400°C. The analyzed sample was fabricated in conditions similar to sample#12. ....	100
Figure 3.20: Color change of the sintered sample after sintering at 400°C.(a) No sintering performed (used for comparison).(b) Sample sintered at 400°C. ....	100
Figure 3.21: EDS spectrum of the P-type Bi <sub>2</sub> Te <sub>3</sub> material. (A) Initial material. (B) Sintered sample [194]. ....	101
Figure 3.22: XRD patterns of the Bi <sub>2</sub> Te <sub>3</sub> powder and sintered sample. (A) sintered sample, (B) 5 hours milled powder. Space group R-3m, System Rhombohedral, PDF 01-072-1836 [194]. ....	102



Figure 3.23: (Left) Specific heat of sample#1 measured with differential scanning calorimeter (DSC). (Right) Thermal diffusivity of sample#1 measured using laser flash analyzer.....	102
Figure 3.24: Physical properties of the sintered sample. (A) Thermal conductivity, (B) Electrical conductivity, (C) Thermopower, and (D) $ZT$ value. Measurement performed on sample#1.....	103
Figure 3.25: Thermopower of the sintered nanoporous sample#12 plotted against temperature. The two plots were obtained from two different runs under the same experimental conditions.....	104
Figure 3.26: Testing of the TE circular sample under forward and reverse currents verifies that a temperature gradient can be obtained. The ambient temperature is 60°C. (Left) Temperature distribution from an IR camera. (Right) Plot of the temperature versus the distance along the white line in the left images. Cooling below the ambient temperature can be observed. $\Delta T \approx 15^\circ\text{C}$ .....	105
Figure 3.27: Testing of the TE square sample#12 under forward and reverse current verifies that a temperature gradient can be obtained. The ambient temperature is 60°C. (Left) Temperature distribution from an IR camera. (Right) Plot of the temperature versus the distance along the white line in the left images. Cooling below the ambient temperature can be observed. $\Delta T \approx 15^\circ\text{C}$ .....	105
Figure 3.28: Temperature difference versus the applied power for sample#12 using the QFI microscopy.....	106
Figure 3.29: Image of the built $\text{Bi}_2\text{Te}_3$ TE Knudsen pump using small portion of a sintered sample fabricated using conditions of sample#1.....	106
Figure 3.30: Experimental pressure differential obtained with the fabricated Knudsen pump. The pressure is permitted to come to room pressure before switching the voltage polarity and reversing the pump direction.....	107
Figure 3.31: Fabricated nanoporous $\text{Bi}_2\text{Te}_3$ TE Knudsen pump using sample#13. The nanoporous TE sample is placed in a rectangular channel. Wires are soldered on the sides. The pump is sealed using vacuum epoxy glue [194].....	108
Figure 3.32: Experimental pressure differential obtained with the fabricated Knudsen pump in figure 3.31. Pressure is permitted to come to room pressure before switching the voltage polarity [194].....	109
Figure 3.33: Measured pressure across the TE based Knudsen pump when the syringe pump is set up for different flow rates. This curve permits to generate a plot that relates pressure and flow rate.....	110
Figure 3.34: Graph of the pressure versus flow rate that is obtained for three different levels of power in the nanoporous TE. The marks are the experimentally obtained data, and the lines represent a linear fit to the measurements [194].....	111
Figure 3.35: Maximum pressure and maximum flow rate versus the input power for device in figure 3.31. The linear fit equations in figure 3.34 were used to calculate the maximum pressure and flow rate. $M$ , $\Delta P$ , and $P_{\text{power}}$ are flow rate, pressure difference, and input power.....	111
Figure 3.36: Examples of electrical contacts. Rosin paste flux was used to improve the solder flow and therefore enhance the contact quality.....	114
Figure 3.37: Temperature difference across the different square sample faces. Electrical wires were soldered on the (A) faces.....	115

Figure 4.1: Schematic of the nanoporous TE element showing some terms used in the mathematical equations.  $W$ ,  $L$ , and  $H$  are the TE width, length and thickness.  $Q_H$  and  $Q_C$  are the rejected heat on the hot side and absorbed heat from the cold side respectively. ....120

Figure 4.2:  $Q_C$  versus the current  $I$ . Grey region represent the interval where the TE sample is extracting heat from the cold side. ....123

Figure 4.3:  $Q_C$  variation versus the voltage  $V$ .  $Q_C(0)$  must be positive. ....125

Figure 4.4:  $Q_C$  variation versus the  $X$ . ....126

Figure 4.5: Variation of  $\Delta T$  versus  $I$ , the grey region presents the values of  $I$  giving a positive  $\Delta T$ . ....128

Figure 4.6: Variation of  $\Delta T$  versus  $V$ , the grey region presents the values of  $V$  giving a positive  $\Delta T$ . ....129

Figure 4.7: Variation of  $\Delta T$  versus  $X$ , the grey region presents the values of  $X$  giving a positive  $\Delta T$ . ....130

Figure 4.8: ranges of  $\frac{I}{X}$  leading to a positive  $Q_C$  and  $\Delta T$ .  $Q_C$  Will be positive when  $\frac{I_1}{X} < \frac{I}{X} < \frac{I_2}{X}$ , and  $\Delta T$  will be positive when  $\frac{I}{X} < \frac{V}{\rho}$ . The region between  $\frac{I_1}{X}$  and  $\frac{V}{\rho}$  represents the interval of  $\frac{I}{X}$  where both  $Q_C$  and  $\Delta T$  are positive. ....132

Figure 4.9: General shape of the  $\Delta P|_{\dot{M}=0}$  plot. The thick dashed line corresponds to the  $\Delta P|_{\dot{M}=0}$  versus current  $I$  for a constant voltage  $V$ . The solid line is the response when  $Q_C$  is zero and that is the maximum pressure for a given voltage and current.  $I_{opt}$  is the current for which  $\Delta P|_{\dot{M}=0}$ . ....137

Figure 4.10:  $\Delta P|_{\dot{M}=0}$  versus  $I$  for a given voltage  $V$ .  $\Delta P|_{\dot{M}=0}$  values follow the parabola trend discussed in figure 4.9 . The corresponding max and min currents for the shown voltages are highlighted in table 4.1. ....140

Figure 4.11:  $\Delta P_{max}$  versus the TE figure of merit  $Z$  at the optimum current  $I_{opt}$  for 22 nm, 50 nm and 102.7 nm pore sizes. ....141

Figure 4.12:  $\dot{M}_{max}$  versus the TE figure of merit  $Z$  at the optimum current  $I_{opt}$  22nm, 50 nm and 102.7 nm pore sizes. Increasing the pore radius will increase the mass flow rate. The working gas is air. ....142

Figure 4.13:  $\dot{M}_{max}$  in the different flow regimes. The maximum mass flow is obtained at the slip flow regime, where the pore size is largest. Higher  $Z$  values yield higher mass flow rate.  $Z= 0.00144 \text{ K}^{-1}$  is the value we have measured for the sintered sample fabricated in the lab,  $Z=0.00297 \text{ K}^{-1}$  is the current value in TE coolers and generators. In practice, a non-zero pressure difference causes a pressure driven backflow that causes  $\dot{M}$  to have a maximum in the transitional flow regime.  $Kn$  values along the x-axis are calculated for air at room temperature and pressure. ....143

Figure 4.14:  $\Delta P_{max}$  in the different flow regimes. The maximum pressure is obtained in the free molecular flow regime where the pore size is much smaller.  $Kn$  is calculated for air at room temperature and pressure.  $Z= 0.00144 \text{ K}^{-1}$  is the value we have measured for

the sintered sample fabricated in the lab, $Z=0.00297 \text{ K}^{-1}$ is the current value in TE coolers and generators.....	144
Figure 4.15: Plot of $M_t$ and $M_p$ reported by sharipov [103]. The fitting equations were used to calculate $M_t$ and $M_p$ for different gases. Circles are Sharipov's data and the square ones are the calculated values using the fitting equations. ....	145
Figure 4.16: $\dot{M}_{\max}$ versus the figure of merit $Z$ for different working gases. As the molecular mass increases the mass flow rate increases. $M_p$ and $M_t$ for the different gases are shown in table 4.4. The pore size is 50 nm for all gases. ....	146
Figure 4.17: $\Delta P_{\max}$ versus the figure of merit $Z$ for different working gases and a pore radius of 50 nm. As the molecular mass decreases the pressure increases. $M_p$ and $M_t$ for the different gases are shown in table 4.4. ....	146
Figure 4.18: $\Delta P_{\max}$ for different TMAC values. As $\alpha$ increases the $\Delta P_{\max}$ increases. The working gas is air at room temperature and pressure. The pore radius is 50 nm. ....	147
Figure 4.19: $\dot{M}_{\max}$ for different TMAC values. As $\alpha$ decreases the $\dot{M}_{\max}$ increases. The working gas is air at room temperature and pressure and the pore radius is 50 nm. ....	147
Figure 5.1: A Scanning Electron Microscopy image of a 80nm pore diameter track-etched polycarbonate membrane. ....	152
Figure 5.2: Schematic of the setup used to measure the pressure versus the flow rate for the track-etched Whatman membranes. Box A is kept at room temperature all the time. Box B is either left at room temperature or heated to 50 °C depending on the experiment. ....	153
Figure 5.3: Image of the nanoporous Whatman membrane glued on an Aluminum substrate. A hole for gas flow is drilled on the plate underneath the membrane. ....	154
Figure 5.4: Pressure difference across the 15 nm Whatman membrane versus time for different flow rate values set on the syringe pump. ....	155
Figure 5.5: Flow rate versus the pressure difference when no membrane is connected to the set up. The circular data corresponds to the situation when the experimental box was heated to 50 °C. ....	156
Figure A-1: ImageJ main window containing the menu bar and the different tools for image analysis. ....	197
Figure A-2: A line (Yellow color) is drawn on top of the SEM scale bar line to define the ..... 198	198
Figure A-3: set scale window allows the definition of the true spatial scale of the image. A line with a known distance is used to perform the calibration. ....	198
Figure A-4: ROI manager showing all the drawn lines. Once Measure button is selected, measurements are displayed in a result window. Checking 'Show All' shows all drawn geometries in the image being analyzed. ....	199
Figure A-5: SEM image of a nanoporous membranes, the blue lines are used to measure the pore size. The 100 nm scale bar is used to define the measurement scale. ....	200
Figure A-6: Results window is open once 'm' or 'measure' is selected. Parameters shown on the table are defined through analyze → set measurements. ....	200
Figure B-1: Opening the part to be machined in Visual Mill 6.0. ....	201
Figure B-2: igs file imported to Visual Mill 6.0 showing the channel to be machined. ...	201
Figure B-3: Setup tab. ....	202

Figure B-4: Machine tab in which the machining type is specified. The channels for the thermoelectric samples were machined using 3-axis machine type. ....	202
Figure B-5: Post-Processor tab in which Mach 3-MM is used in this case. ....	202
Figure B-6: Box Stock window, clicking “Copy Model Bounding Box” transfers the channel dimensions. The overall size of the plastic channel is 31 mm long and 23 mm wide. The machined plastic is 6.35 mm thick. ....	203
Figure B-7: Setting the Stock Box coordinates. ....	204
Figure B-8: Align Part and Stock tab. ....	205
Figure B-9: Create/select tool tab. ....	206
Figure B-10: Visual Mill Create tab. ....	207
Figure B-11: Machining Features/Regions tab. ....	207
Figure B-12: Clearance tab. ....	208
Figure B-13: Cut Parameters tab. ....	209
Figure B-14: Cut Levels tab. ....	210
Figure B-15: Posting the G-code after setting the Horizontal and Finishing Machining. ....	211
Figure B-16: Opening the G-code in the Mach3 CNC. ....	212
Figure B-17: Jog tab in the Mach 3. X, Y, and Z are used to change the stock holder position. ....	212
Figure B-18: Tools/Fixtures tab where the zero position is set. ....	213
Figure B-19: Running G-code in the Mach 3. The line being executed is highlighted. The machining path is shown in blue color. ....	214

## CHAPTER 1: INTRODUCTION

### **1.1 Importance of gas micropumps**

Thermally driven gas pumps are pumps with no moving parts. They are needed in a variety of nanotechnology and micro electro mechanical systems (MEMS) applications. Some of these applications are gas chromatography [1-4], spectroscopy [5-7], microplasma manufacturing [8-10], energy harvesting, gas manipulation, micropropulsion, chemical sensing devices[11], cooling in microelectronics, drug delivery, bypass medical devices [12], protein immunoassays, and pneumatic actuation of Lab-on-chip devices (LOC) [13-16]. The type of thermal pump investigated in this work is called the Knudsen pump.

The Knudsen pump relies on the principle of thermal transpiration [17, 18]. If two chambers, connected with narrow tubes, are subjected to different temperatures, a net gas flow occurs from the cold chamber to the hot chamber because of the difference in the molecular fluxes from each chamber.

### **1.2 Features of the Knudsen pump**

The Knudsen pump has a lot of attractive features. It is devoid of moving parts which constitute the main reason of failure for many pumps. It has a very low leakage rate. Any liquid can be pumped pneumatically, regardless of its characteristics such as PH or conductivity. The pump can be readily miniaturized, operate at low voltages, and generate a continuous flow rate.

### 1.3 Knudsen pump conventional design

The majority of the reported work on the Knudsen pump used a conventional design [19-21] (Figure 1.1). The heater is placed adjacent to the hot end of the nanoporous material, and the cold end is passively cooled with a heat sink. Longer channels are used in order to maintain a sufficient temperature gradient between the two ends, but at the same time, these long channels have the drawback of reducing the flow rate through increased flow resistance. Nanoporous membranes made out of low thermal conductivity materials such as glass, plastic, and polymer are preferred since their heat transfer are less which helps maintain the temperature gradient.

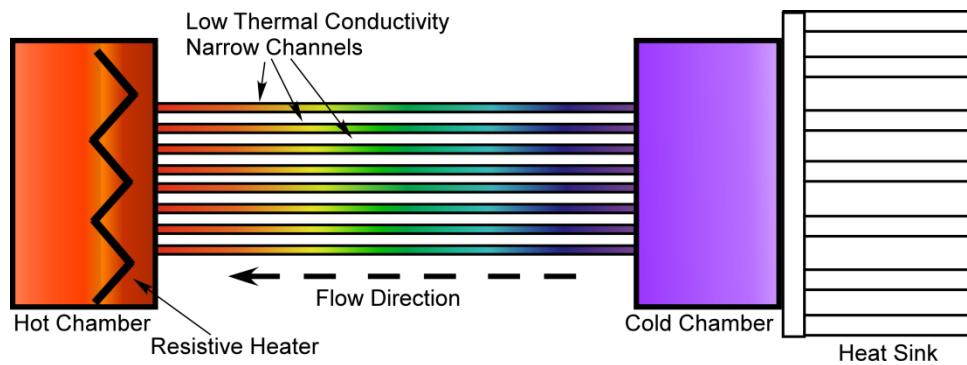


Figure 1.1: Knudsen pump conventional design. A heater heats the hot side, while the cold side is actively cooled using a heat sink. Long channels out of low thermal conductivity materials are used to improve the temperature gradient.

### 1.4 Thermoelectric module design

A thermoelectric module replaces the heater/heat sink, resulting in an improved temperature difference by actively cooling the cold end [22] (Figure 1.2). Heat is transferred through the Copper heat spreaders between the membrane ends. The pump in this case is bi-directional. When the applied voltage to the thermoelectric module is reversed, the hot and cold sides are reversed and therefore the pump direction. The drawbacks with this design are the significant amount of heat losses through the metallic

heat plates, and the air gaps between the membrane and the heat spreaders, limiting the pump performance.

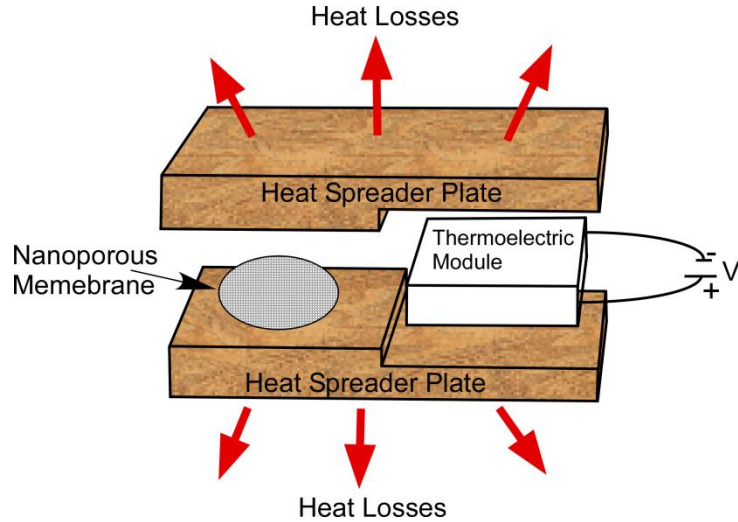


Figure 1.2: Schematic of the thermoelectric Knudsen pump. The thermoelectric module actively heats and cools the hot and cold sides of the membrane, respectively. The membrane is sandwiched between two Copper plates. A lot of heat is lost through the heat spreader plates. Temperature across the membrane is reduced due to the unavoidable gap between the membrane and the metal plate.

### 1.5 Thermoelectric based Knudsen pump

To overcome these challenges we propose to use a multifunctional, nanoporous sintered  $\text{Bi}_2\text{Te}_3$  thermoelectric. The thermoelectric properties are used to generate the temperature difference needed for thermal transpiration. The sub-micron pores which extend through the thermoelectric material function as channels for gas flow (Figure 1.3). This multifunctional material eliminates the air gap between the heater and nanoporous material that exists in a traditional pump, and thus potentially improving the temperature difference and pump performance, making the pump bi-directional, and reducing the overall size of the pump.

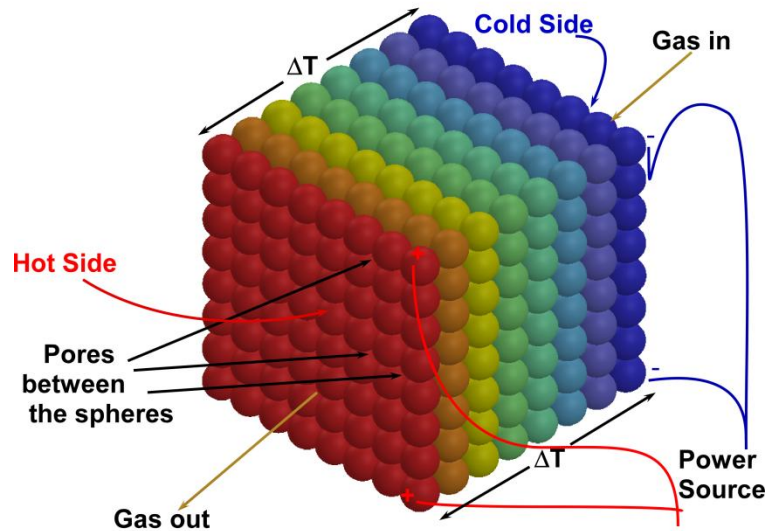


Figure 1.3: Schematic of the thermoelectric based Knudsen pump working principle. Once power is applied to the thermoelectric material, one side becomes cold, and the other side becomes hot. Gas flows from the cold side to the hot side through the pores.

### 1.6 Gas flow through nanoporous membranes

Nanoporous membranes are widely used in many application such gas mixtures separation and filtration. They can also be used in gas micropumps such the Knudsen pump. A good understanding and prediction of the gas flow through these membranes is needed to better understand and predict the performances of the membranes based devices.

### 1.7 Objectives

**Objective#1:** Make and characterize nanoporous thermoelectric materials suitable for a Knudsen pump.

**Objective#2:** Build, model, and test Knudsen pumps based on nanoporous thermoelectric materials.

**Objective#3:** Accurately understand and predict the gas flow through nanoporous membranes.



## 1.8 Dissertation outline

The introduction chapter gives a broad overview of the research, describes the research problems and the suggested solutions using powder metallurgy and thermoelectric material. The background and literature review chapter (Chapter 2) provides a complete background about the gas pumps and the Knudsen pump, defines the thermal transpiration phenomenon, discusses the different processes and effects involved in the research (Powder metallurgy, sintering, thermoelectricity), talks about the Tangential Momentum Accommodation Coefficient (TMAC), and finally covers the different models used in this research to calculate flow rate through nanoporous membranes.

Fabrication and characterization of the  $\text{Bi}_2\text{Te}_3$  thermoelectric based Knudsen pump chapter (Chapter 3) discusses the different fabrication steps, characterization techniques, and obtained results. A mathematical model of the fabricated pump is discussed in chapter 4. Effect of different parameters such as pore size, figure of merit  $Z$ , molecular mass of the working, and the TMAC value on the pump outputs is also covered.

Gas flow through nanoporous membranes is discussed in chapter 5. Gas flow through track-etch Whatman membranes is measured, analyzed, and compared to different theoretical models.

Finally, the conclusions and future work chapter summarizes the achieved results and discusses future work to clarify further points encountered in this research.

## CHAPTER 2: BACKGROUND AND LITERATURE REVIEW

Micropumps are pivotal components in many types of microfabricated devices including Micro Electro Mechanical Systems (MEMS), Lab on a Chip (LOC), and micro Total Analysis Systems ( $\mu$ TAS). They are also needed in many microfluidic devices.

When comparing micropumps, the Knudsen pump appears to possess two unique characteristics, absence of moving parts and possibility to be driven by an exterior source of energy, such as waste heat or solar radiation.

In general micropumps can be classified into two categories mechanical and non-mechanical micropumps. The first category has moving parts such as valves, membranes, and flaps. The driving forces for these moving parts can be piezoelectric, electrostatic, pneumatic, thermo-pneumatic effects. On the other hand, non-mechanical micropumps don't have moving parts, the momentum, which drive the fluid, is generated from a non-mechanical energy source. The actuation mechanisms for such pumps can be electrowetting, electrochemical, electro-osmosis, electrohydrodynamic. This second category is more diverse than the first one and uses a wide range of scientific phenomenon to actuate the pump.

### **2.1 Mechanical micropumps**

Mechanical micropumps can also be subdivided into different groups based on the actuation type, whether the actuator is integrated or external, and the type of the moving

part (valve, flap, and membrane). In this short review we sub-categorize mechanical and non-mechanical micropumps based on the actuation type.

### 2.1.1 Piezoelectric

This type of actuation has the advantage of being fast response time and simple structure, the piezoelectric element is attached to a membrane, an electric field, when applied to the membrane, causes it to deflect up or down, in other words, become convex or concave depending on the electric voltage. A schematic of the micropump is shown in figure 2.1. First work on this type of pump was started by Lintel [23], actuation was provided with thin glass membrane actuated with a piezoelectric disc. A peristaltic pump published by Smits [24-26] has three active valves, containing piezoelectric material, that are opened/closed by electrical means. The pump is made on silicon using etching technique and can generate a flow rate up to 3  $\mu\text{l}/\text{min}$ . More work on the piezoelectric based micropumps can be found in the following references [27-33].

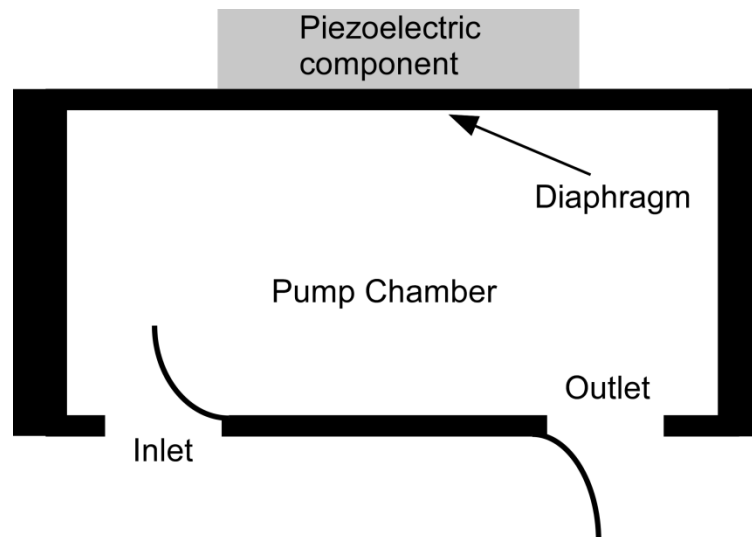


Figure 2.1: Schematic of the working principal of a piezoelectric micropump.

### 2.1.2 Electrostatic

The electrostatic force between parallel-plate is generated due to the electrostatic conservative force field between the plates, the expression of the generated force,  $F$ , is:

$$F = \frac{dW}{dx} = \frac{1}{2} \frac{\varepsilon_0 \varepsilon_r A V^2}{x^2} \quad (2.1)$$

where  $W$  is the energy stored,  $\varepsilon = \varepsilon_0 \varepsilon_r$  is the dielectric constant,  $A$  plate area,  $V$  is the voltage, and  $x$  is distance between the plates.

In electrostatically actuated micropumps [34-38], the diaphragm is forced to deflect toward the counterelectrode causing a change of volume inside the chamber and therefore fluid motion. The advantage of this type of pumps is the low power consumption and the fast response time.

### 2.1.3 Electromagnetic

A magnet or a set of coils are attached to the membrane, when a current is run through the coils, a magnetic field is generated force between the magnet and the coils causing the membrane to deflect (Figure 2.2). The direction of movement depends on the current direction. The main disadvantage of this type of actuation is the difficulty to miniaturize the coil. The generated force,  $F$ , is based on Lorentz equation:

$$F = (I \times B)L \quad (2.2)$$

where  $I$  is the current,  $B$  is the magnetic field, and  $L$  is the length of the wire. From the equation it can be concluded that the amount of force will depend on the current,  $I$ , and length,  $L$ , of wire around the coil. Examples of pumps based on the electromagnetic actuation are reported in these references [39-43].

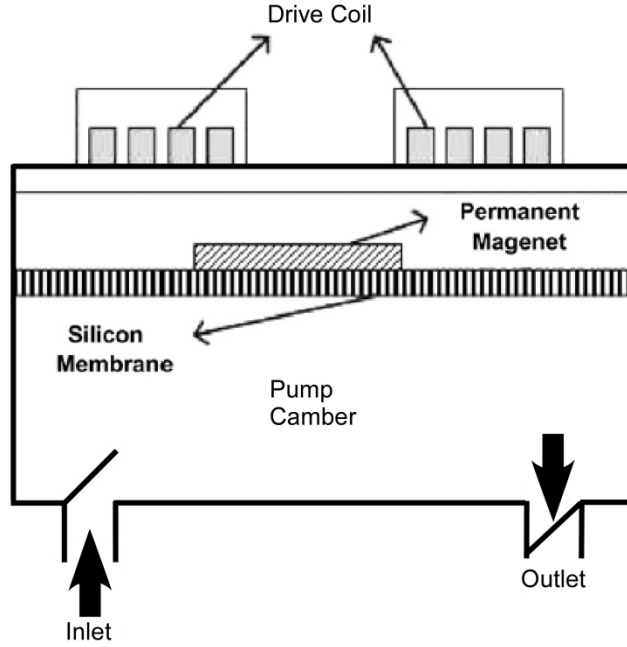


Figure 2.2: Schematic of the electromagnetic micropump [44].

#### 2.1.4 Thermopneumatic

The pump membrane is deflected due to contraction and expansion of fluid inside a sealed cavity caused by heating and cooling. The membrane deflection causes a change in the chamber volume and therefore fluid movement. For liquids the increase in pressure,  $\Delta P$ , is given by [44]:

$$\Delta P = E \left( \beta \Delta T - \frac{\Delta V}{V} \right) \quad (2.3)$$

where  $E$  is the bulk modulus of elasticity,  $\beta$  is the thermal expansion coefficient,  $\Delta T$  is the temperature increase, and  $\Delta V/V$  is the ratio of volume change. Pumps based on the thermopneumatic actuation can generate high pressure and displacement of the diaphragm. The first thermopneumatic pump was reported by Zdeblick [45]. Air trapped inside a cavity is caused to expand and contract with the help of an aluminum resistive heater etched on the face of a Pyrex wafer on the top part of the cavity; reported maximum flow rate and pressure are 34  $\mu\text{l}/\text{min}$  and 5 kPa respectively. Two types of

diaphragms (flat and corrugated) have been compared in [46]. The corrugated diaphragm pump showed a 3.3 times larger flow rate. Other designs and implementations of the thermopneumatic-actuated micropumps can be found in these articles [47-49].

### **2.1.5 Shape memory alloy (SMA)**

Shape memory alloys (SMA) are unique type of materials with the ability to recover their shape when the temperature is increased [50]. They have attractive properties such as high force to volume ratio, high damping capacity, and biocompatibility. TiNi has been used for the fabrication of SMA actuated micropumps [51-56]. It undergoes two solid phase transformations. At high temperature the phase is called austenite and at low temperatures the phase is called martensite. Larger deformations are possible with martensite due to its higher ductility. Actuation force is generated when the TiNi is heated to high temperature above the phase transformation and constrained from changing its shape. SMA can operate only at low frequencies, below 100 Hz, due to their low cooling rate [57]. The higher operating temperatures can also alter the properties of the fluid inside the micropump chamber.

### **2.1.6 Bimetallic**

A bimetallic actuator consists of two thin layers, in direct contact, with different coefficients of thermal expansion (CTE), as the temperature of the actuator changes, one layer expands more than the other causing a bending out of the plane (Figure 2.3). Heating of the layers can be introduced through current (Joule heating). For a maximum bending, materials with larger CTEs are used. The two materials are deposited on the top of the pump membrane; the bending causes a change in the chamber pressure and therefore results in fluid flow. Thermal alternating is needed to get a continuous flow

rate. This type of actuator is simple to implement and uses low voltage. The main disadvantage is the limited operation frequency (only low frequencies). A good number of papers about micropumps and MEMS devices using bimetallic actuation have been reported in the literature [58]. The same actuation is sometime combined with other actuation type to realize microfluidic devices [59, 60].



Figure 2.3: Linear bimetallic strip. The differing thermal expansion caused stress in the actuator when heated, and therefore deformation.

## 2.2 Non-mechanical micropumps

Non-mechanical micropumps don't have moving parts; they rather transform non-mechanical energy into kinetic energy of the fluid. Different types of micropumps based on electrokinetic, electrowetting, and surface tension gradient have been reported.

### 2.2.1 Electrowetting

It is based on the modification of the surface wetting properties with an applied electric field. Fluid is transported by surface tension which is dominant at the microscale engineering processes. As shown in figure 2.4, when a voltage is applied to the fluid-dielectric substrate, the surface tension decrease and movement is generated. Mercury drop motion inside a microchannel was shown by Yun [61]. The channel was filled with an electrolyte; the movement of the mercury caused a drag of the electrolyte which caused deflection of the membrane. 500 picoliter pumping of water with 1400 V applied

voltage was obtained by Hoshino using a pulled glass tube [62]. Modeling of the electrowetting effect has been also reported [63].

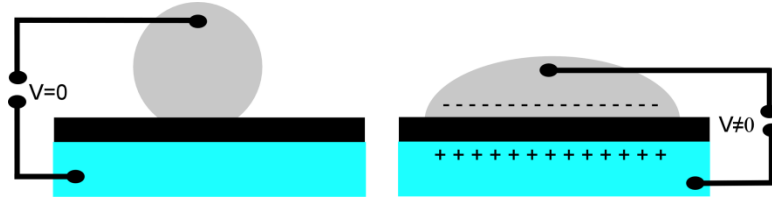


Figure 2.4: Electrowetting effect.

### 2.2.2 Electrochemical

The main components of this type of micropump are electrodes for applying voltage, channels, electrolysis chamber, inlet, and outlet [64]. The driving force for the electrochemical pump is the generated bubbles by electrolysis. This later is defined as the decomposition of liquids by means of electric currents, the liquid needs to be a conductor of electricity. Electrolysis of water is expressed by the following two reactions at anode and electrode respectively.  $O_2$  and  $H_2$  gases are produced during these two reactions.



The reservoir containing the water is connected to a channel filled with fluid to be pumped. The gases from the water decomposition cause the fluid flow through the channel. The electrochemical pump is simple to fabricate, readily integrable with microfluidic devices, and can pump up to the millimeter range with less amount of power.

### 2.2.3 Electrohydrodynamic

The unique advantage of the electrodynamic micropump is the absence of moving parts and that the applied force from the electric field act directly on the fluid. Electrical



to mechanical energy transduction is realized by electric field acting on induced charges by the electrodes in the fluid. Thus, the electrodes must be in direct contact with the fluid to be pumped. Also, another condition to be satisfied is that the fluid must have a low conductivity ( $10^{-12}$  to  $10^{-6}$  S/m) [65] and dielectric in nature. The induced charges are introduced to the fluid using different methods, induction, injection, polarization, and ion drag [66].

The amount,  $F$ , of force exerted on the charges is given by [66]:

$$\vec{F} = q\vec{E} + \vec{P}\nabla\cdot\vec{E} - \frac{1}{2}E^2\nabla\left[E^2\left(\frac{\partial\varepsilon}{\partial\rho}\right)_T\rho\right] \quad (2.6)$$

where  $\vec{P}\nabla\cdot\vec{E}$  is the dielectrophoretic force,  $q$  is the charge density,  $\varepsilon$  is the fluid permittivity,  $E$  is the electric field,  $\rho$  is the fluid density,  $\vec{P}$  is the polarization vector, and  $T$  is temperature.

Ritcher fabricated the first electrohydrodynamically driven micropump [66], it consisted of two opposite grids with an area of 3 mm by 3 mm. Pumping was observed with both DC and AC driving voltage. A maximum pressure of 2480 Pa is obtained with a 700 V input voltage.

#### 2.2.4 Magnetohydrodynamic

The Lorentz force is used to pump liquid metals and ionized gases [67]. Magnetohydrodynamic deals with the flow of electrically conducting liquids in electric and magnetic fields. The force on the fluid is perpendicular to both electric and magnetic fields. The pressure head difference,  $\Delta P$ , and flow rate,  $Q$ , have the following expressions [65]:

$$\Delta P = J_y B_x L \quad (2.7)$$

$$Q = |J_y B_x| \frac{\pi r^4}{8\mu} \quad (2.8)$$

where  $J_y$  is the current density,  $B_x$  is the magnetic flux density,  $L$  distance between electrodes,  $r$  is half the hydraulic diameter of the microchannel, and  $\mu$  is the density.

The micropump reported in [65] achieved a pressure head of 18 mm and flow rate of 63  $\mu\text{l}/\text{min}$  for an input current of 38 mA and 1.8 mA respectively, the tube diameter and magnetic field are 2 mm and 0.44 T.

Magnetohydrodynamic micropumps can pump fluids with higher conductivities (1 S/m or higher), making a suitable for medical/biological applications.

### **2.2.5 Electroosmotic (DC and AC)**

Electroosmotic flow is the motion of liquid caused by a potential across a capillary tube or a microchannel. The glass surface contains negatively-charged functional groups that attract negatively-charged ones which forms a double layer at the glass wall. When an electric field is applied to the fluid, the charges on the double layer are induced to move by Coulomb force carrying the fluid in the same direction (Figure 2.5). The double layer can be manipulated by a DC and AC electric field. The disadvantages of micropumps based on electroosmotic flow are the large amount of bubbles formed by the large current in the open channel and next to the electrodes; these bubbles tend to block the flow. Ions, contaminating the fluid, are sometime introduced through electrolysis and reactions at the electrodes [68].

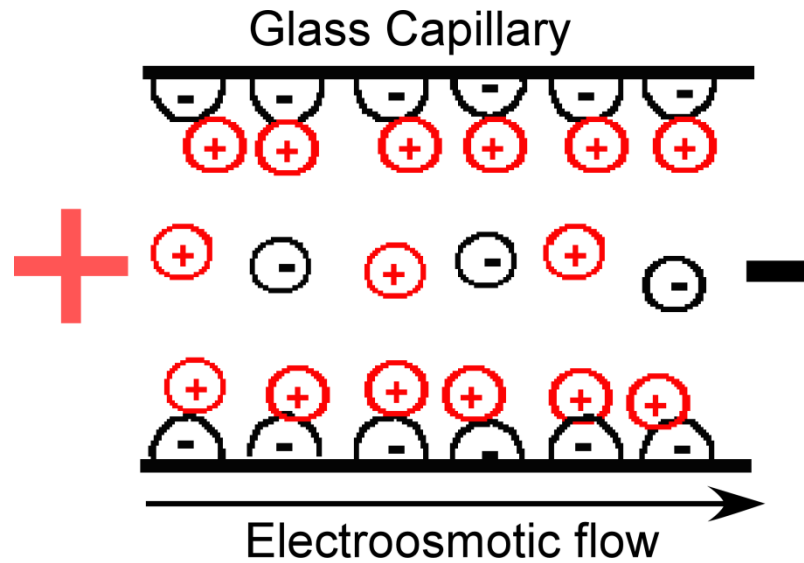


Figure 2.5: Schematic of the formed double layer on the glass surface.

Another category of non-mechanical pumps are the thermal molecular pumps, the pumping energy in this case is supplied by temperature changes. Next, we will review different variations of these types of pumps, mainly accommodation pump, Knudsen compressor, and thermomolecular pump.

### 2.2.6 Accommodation pump

The first accommodation pump was fabricated by Hobson. Three chambers, A, B, and C, are connected by two tubes forming a V shape. A and B at room temperature and C is cooled with liquid  $N_2$ , the tube connecting A and C is atomically rough while the one between B and C is atomically smooth (Figure 2.6) [69]. When equilibrium is reached, the ratio of pressure between the different chambers is given by:

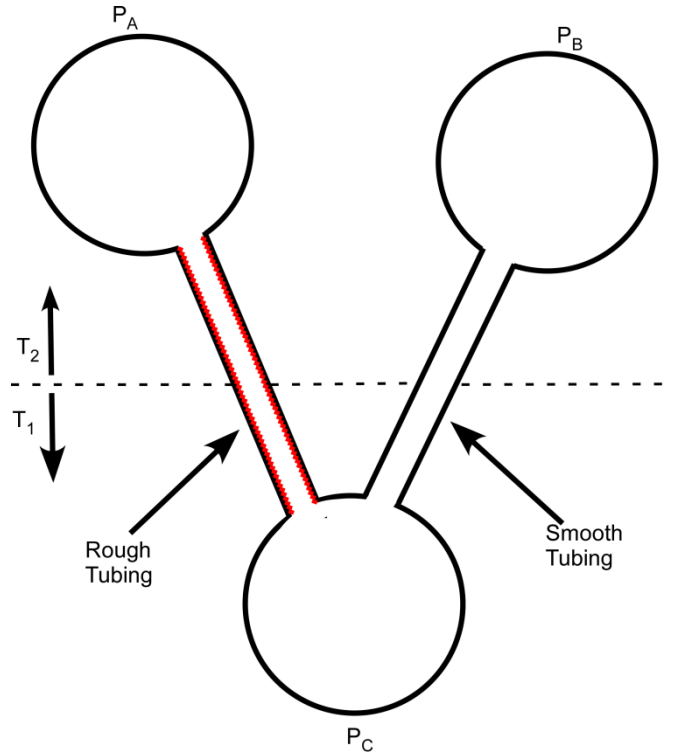


Figure 2.6: A schematic illustration of the accommodation pump, chamber A is connected to chamber B with a rough tube, while B is connected to C with a smooth tube. Pumping occurs from B to A [69].  $T_1 < T_2$ .

$$\frac{P_A}{P_C} = \sqrt{\frac{T_2}{T_1}} \quad (2.9)$$

$$\frac{P_B}{P_C} = \frac{1}{\gamma} \sqrt{\frac{T_2}{T_1}} \quad (2.10)$$

Combining the two previous equations yields the compression ratio:

$$\frac{P_A}{P_B} = \gamma \quad (2.11)$$

$P$  is the pressure, and subscripts  $A$ ,  $B$ , and  $C$  refer to chambers  $A$ ,  $B$  and  $C$ , respectively. Equations (2.9) and (2.10) were obtained from separate analysis in which two chambers were connected by an aperture and a long tube. Hobson found that the equilibrium equation# (2.9), obtained with the aperture, is reproduced in the case of roughened tube. For a smooth Pyrex glass tube, the compression ratio,  $\gamma$ , found

experimentally to be in the range  $1.1 < \gamma < 1.3$ , was introduced as correction factor. Multiple stages, 3 and 28, using alternating rough-smooth tubes have been fabricated by the same author [69, 70].

### **2.2.7 Knudsen compressor**

A Knudsen compressor is somewhat similar to the accommodation pump, both tubes are rough. The rough tube in the accommodation pump is much smaller, about three orders of magnitudes smaller, while the smooth one is much larger. The flow regimes in the small and large tube are free molecular and transitional, respectively. Pumping will stop when the gas mean free path is larger than the radius for both tubes. The first compressor was fabricated by Muntz group at the University of Southern California [71, 72]. The details on this type of pump are described in section 2.3: the Knudsen pump background.

### **2.2.8 Thermomolecular pump**

Hemmerich [73] adopted the Hobson's design and explanation for the accommodation pump and built the thermomolecular pump. He has used separate heat sources and heat sinks for each stage (Figure 2.7). The main parts for pumping are the heater and the ducts, the heater accelerates the particles by thermal accommodation and the cool duct walls (cooled with water) permit some degree of specular reflection of hot particles [73]. The working principle was explained by Hobson [74], and also confirmed by the modeling and calculation of Logan and Stickney [75]. For a rough surface, hot and cold molecules are scattered according to the cosine law independent of the angle of incidence, whereas for a smooth surface, hot molecules striking the cold surface are

scattered away from the normal, while the cold molecules impinging on the hot surface are scattered toward the normal.

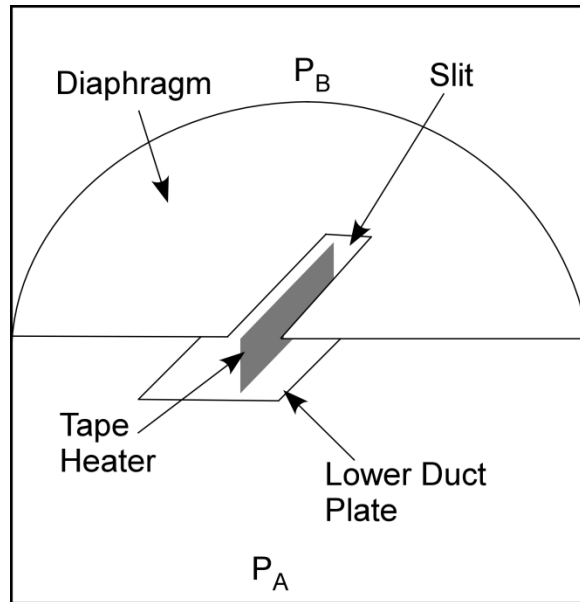


Figure 2.7: single stage schematic diagram of the thermomolecular pump [73]. Pumping occurs from B to A.

In a different design, Stacy replaced the slit with an aperture which separates two chambers whose volumes are independent on the final generated pressure. The active surfaces were made out of carbonized Nickel. The gas inside the chamber is at a pressure such that the flow regime is free molecular. The overall pressure ratio depended mainly on the angular distributions of molecular scattering at the surfaces, and on the geometrical arrangement of these surfaces [76].

### 2.3 Knudsen pump background

Reynolds was the first to notice that a temperature gradient on either side of a porous plate at equal pressure will cause the gas to transpire through the plate from the cold side to the hot side. Reynolds termed the phenomenon as thermal transpiration [17]. In 1910, Martin Knudsen made the first multiple stages pump based on thermal transpiration phenomenon [77, 78]. He cascaded (connected in series) ten capillary

segments formed in glass tube. The temperature gradient necessary for thermal transpiration was obtained by heater placed at every other junction (Figure 2.8). The operating pressure was below atmospheric pressure to ensure that the gas flow is the transitional regime. A pressure increase by a factor of ten was obtained with the ten capillary segments set-up. The efficiency of the pump was limited due to high thermal conductivity of the glass tube used for gas flow.

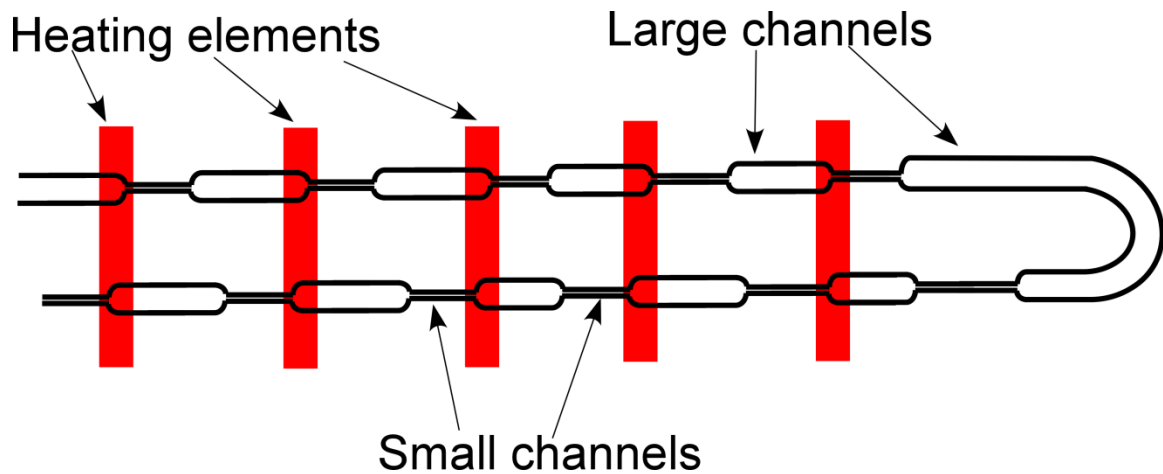


Figure 2.8: Schematic of the first pump made by Knudsen.

The amazing progress in the nanotechnology and microfabrication techniques has made it possible to operate the Knudsen pump at atmospheric pressure [14]. Also it became possible to fabricate membranes with small, precise pore sizes, and extremely low thermal conductivities which help in improving the efficiency of the Knudsen pump.

A modern version of Knudsen experiment was suggested by Pham-Van-Diep et al [79] in 1994. The same design was demonstrated by Vargo et al [80, 81] and given the name Knudsen compressor.

The new version of the Knudsen compressor was built by cascading multiple stages. Each stage has a capillary and a connector section [71, 82]. Figure 2.9 shows a schematic of a single stage along with temperature  $T$  and pressure  $P$  variation along the

two sections. One side was heated using resistive heater and the other side was thermally grounded. The temperature increases linearly along the capillary section, and flow occurs from the cold side to the hot side by thermal transpiration. The connector section has a larger diameter and permits a cooling of the working gas before entering the new stage. A pressure drop of 11.5 Torr was obtained using Helium [80]. The same group has used radiant heating from xenon and halogen lamps for low and high fluxes respectively [83]. Nanoporous silicon aerogel doped with 8% carbon, to improve absorption of the radiant energy and decrease the thermal conductivity, were used as the membrane for thermal transpiration flow. One, two, five, and fifteen stages have been investigated.

Young et al [84] showed the possibility of constructing a Knudsen compressor that can attain gas compression from 1 atm up to 10 atm.

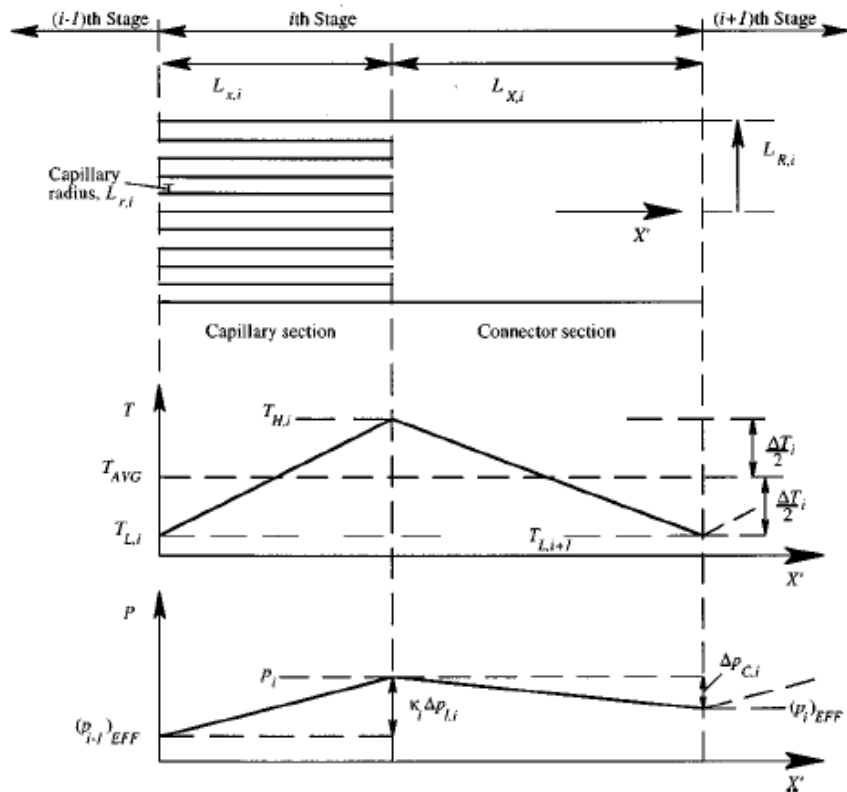


Figure 2.9: Schematic of the  $i^{\text{th}}$  stage of a Knudsen compressor [71].



McNamara and Gianchandani [14] reported the first fully micromachined Knudsen pump using a six-mask process (Figure 2.10). A polysilicon heater heats one side, while the other side was passively maintained at room temperature. The heater is suspended on a thin dielectric membrane in order to minimize heat flow from the heater to the substrate. Micromachined capacitive pressure sensors near the cold chamber were used to measure the pressure. A glass substrate is used to provide thermal insulation and, thereby, improve the energy efficiency. A long channel length is used to improve thermal isolation between the hot and cold chambers. The high pressure drop can be observed from the deflection of the vacuum cavity pressure sensor (Figure 2.11). The pressure sensor membrane is flat when no power is applied to the Knudsen pump (Figure 2.11a). The mass flow rate is estimated to be  $10^{-6}$  cm<sup>3</sup>/min. The fabricated device has a footprint of 1.5 mm × 2 mm and the generated pressure difference is 54.7 kPa for an input power of 80 mW.

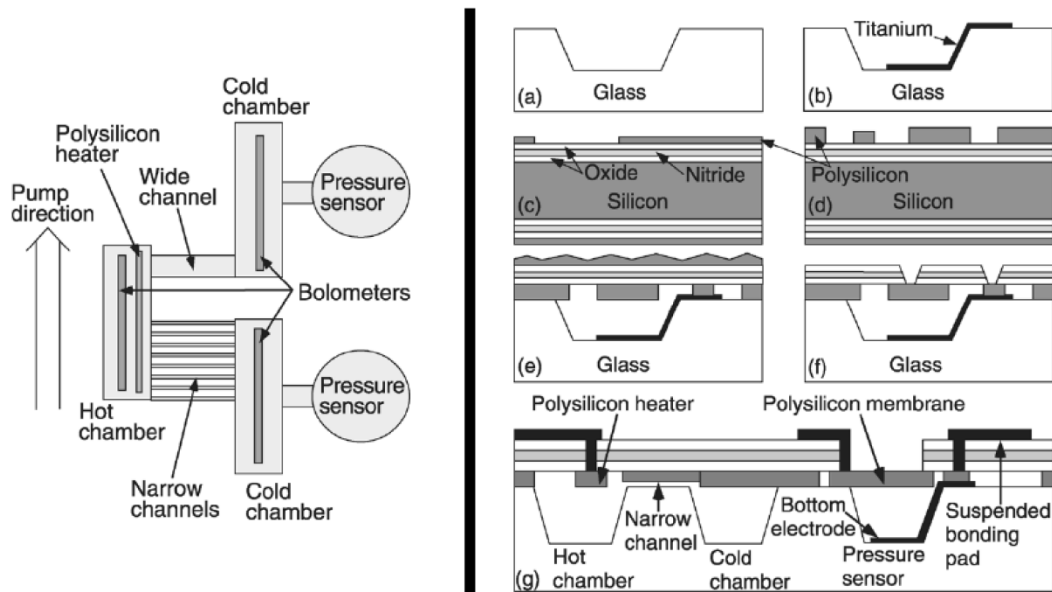


Figure 2.10: (Right) Knudsen pump layout showing the different device components.(Left) Fabrication steps followed during the fabrication of the Knudsen pump [14].

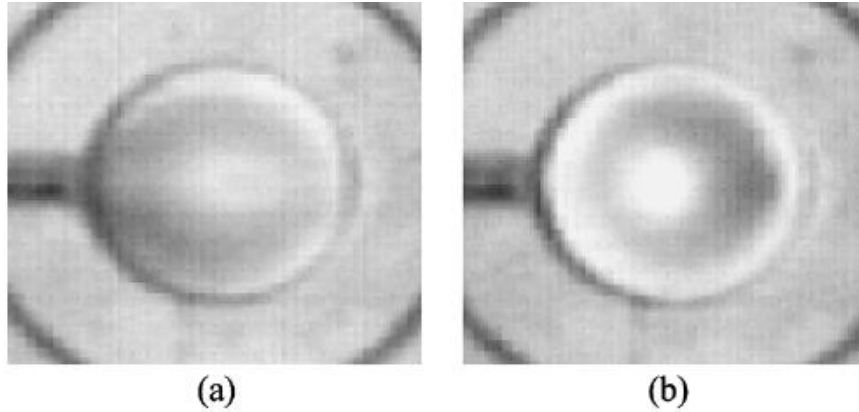


Figure 2.11: deflection of the pressure sensor membrane when power is turned on (a) Power is off, no deflection. (b) Power turned on, membrane deflection [14].

Gupta [19, 85] has constructed a Knudsen pump that operates at atmospheric pressure using naturally occurring zeolite, Clinoptilolite, as the membrane for thermal transpiration flow. The zeolite has a pore density less than  $10^{14}$  pores/cm<sup>2</sup>. Figure 2.12 shows an exploded and a sectional view of the fabricated pump. Two circular zeolite discs are sandwiched with the heater and thin perforated aluminum discs which serve to distribute the temperature uniformly along the membrane surface without blocking the gas flow.

The temperature gradient was generated using thin etched-foil resistive elements placed next to the zeolite disc shape membranes while the cold side was sitting on a heat sink. A typical gas flow rate of  $6.6 \cdot 10^{-3}$  cc/min-cm<sup>2</sup> was obtained with a single 2.3 mm thick zeolite membrane and a power input of less than 300 mW/cm<sup>2</sup>.

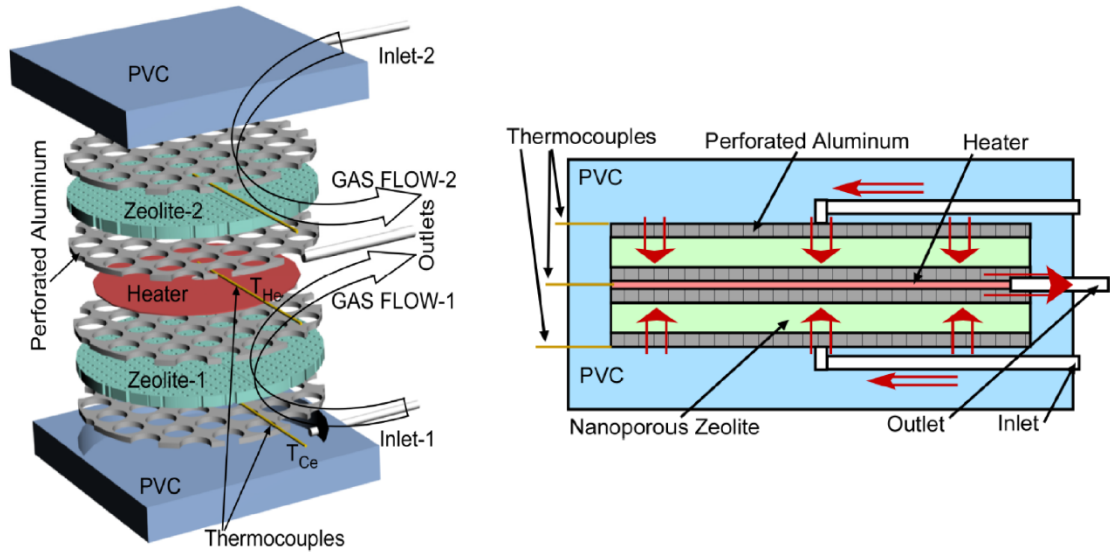


Figure 2.12: (Right) Exploded view of a zeolite-based Knudsen pump. (Left) Sectional view of the Knudsen pump [85].

Gupta et al also made a multistage cascaded Knudsen pump using porous ceramic discs [86]. Figure 2.13 shows a schematic layout of the 9-cascaded pumps. The nanoporous ceramic discs used in the device have a diameter of 5 mm and a thickness of 2.85 mm.

The substrate holding the membranes, heater and heat sink is made of a thermally insulating material, polyetherimide, in order to minimize the heat losses. Each stage has two brass caps with microgrooved channels to direct the flow. Heating is achieved with thin, etched foil resistive heater elements of  $29.5 \Omega$  laminated between insulating layers.

Device testing was performed in two modes, pressure mode permits to measure the maximum head pressure that the device can generate, and the flow mode permits a measure of the maximum flow rate. The pump has a planar architecture and can generate a maximum pressure of 12 kPa and a gas flow rate of  $3.8 \mu\text{L}/\text{min}$ .

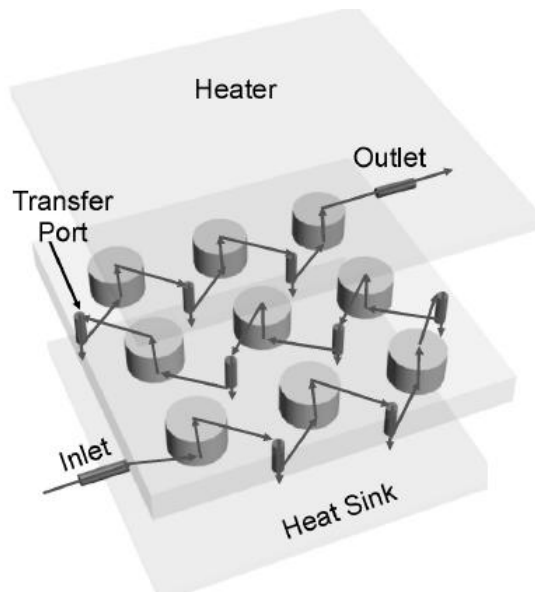


Figure 2.13: A schematic layout of the ceramic based 9-stage [86].

Kunal and McNamara [22] from our group have fabricated the first bi-directional pump working on the principle of thermal transpiration. A thermoelectric module was used to generate the temperature gradient necessary for the pump operation, efficiency was improved since cold and hot sides were actively heated and cooled by the thermoelectric Peltier module. Two designs were investigated, lateral and radial. Figure 2.14 shows a schematic of the two designs. The thermoelectric is thermally coupled to the nanoporous membrane using copper plates on both sides. The copper material was chosen because it has a very high thermal conductivity (398 W/Km) which helps spread the heat uniformly across the membrane. Switching the voltage applied to the thermoelectric module reverses the hot and cold sides, and thus reverses pumping direction. Commercial Mixed Cellulose Ester membrane with 50 nm pore size was used for the lateral design, ten membranes, 105  $\mu\text{m}$  thick, were stacked to achieve a 1 mm total thickness. The same type of membranes was also used for the radial design with 100 nm pore size. The thermoelectric modules have a  $ZT$  of 0.804 and 0.795 for the lateral design and the radial design respectively.

Better performances are obtained with the radial design. When both devices are operated at a power of 3.4 W, the radial pump design produced a normalized flow rate that is 50 times greater than the lateral pump design. The radial design achieved a maximum flow of  $0.74 \text{ cm}^3/\text{min}$  and a maximum pressure of 1.69 kPa.

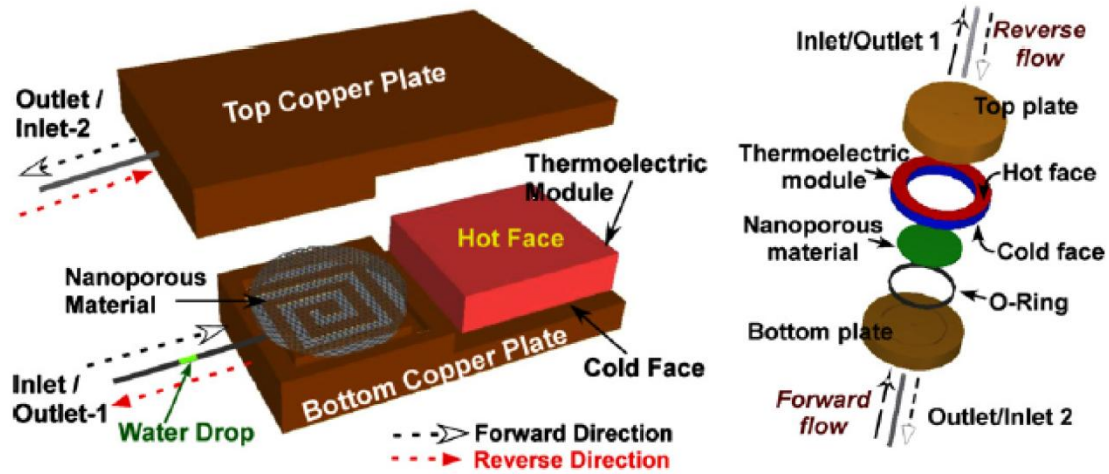


Figure 2.14: Exploded view of the lateral and radial designs. (Left) Lateral design. (Right) radial design [22].

Recently, Gupta et al, at the university of Michigan reported a 48 cascaded stage pump [87, 88] and a 162 cascaded stage pump [89, 90]. They have a foot print of 10.35 mm by 11.45 mm, and 12 mm by 15 mm respectively. The devices are fabricated on a single silicon wafer using a 5-mask fabrication process. Figure 2.15 shows the fabrication steps for both devices.

The 162 stages device can reduce the pressure from ambient pressure (760 Torr) to about 7 Torr (0.933 kPa) with a power input of about 0.44 W. The 48 stages device was tested at two different pressures and resulted in a pressure reduction from 760 Torr to < 50 Torr, and from 250 Torr to about 5 Torr using a power of about 1350 mW.

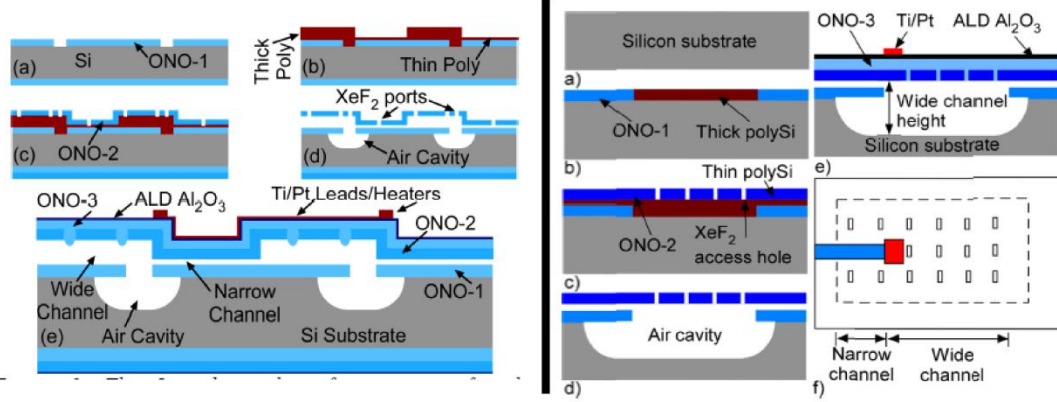


Figure 2.15: Fabrication steps for the multiple stages Knudsen pump. (Left) 48 stages [87]. (Right) 162 stages [89].

In all of the reported Knudsen pumps, a heater from a different material than the membrane is placed adjacent to one side of the pump; the other side is either left open to room temperature or cooled with some other means. The air gaps which exist between the heater/cooling systems and the transpiration membrane lower the temperature gradient across the membrane and thus the efficiency of the pump. In this work we propose to make the membrane and the heating/cooling components as one element which will eliminate the air gaps and improve the device performance.

## 2.4 Working principle of the Knudsen pump

### 2.4.1 Knudsen number

One of the parameters used to characterize the gas flow regimes is the Knudsen number ( $Kn$ ). It is defined as the ratio of mean free path ( $\lambda$ ) of the gas molecule, i.e., the average distance traveled by a molecule between collisions, to the hydraulic diameter  $H$  of the channel.  $H$  is equal to the radius in the case of a circular channel.

$$Kn = \frac{\lambda}{H} \quad (2.12)$$

For a rectangular channel,  $H$  has the following expression:

$$H = \frac{4A}{P} \quad (2.13)$$

where  $A$  is the sectional area, and  $P$  is the channel perimeter.

The mean free path can be calculated using the following equation [91]:

$$\lambda = \frac{1}{\sqrt{2}\pi d^2 \left(\frac{\rho}{m}\right)} \quad (2.14)$$

where  $\rho$  is the density,  $m$  is the molecular mass,  $d$  is the radius of influence range of intermolecular force. Assuming the working gas to be ideal ( $p = \rho \frac{R}{m} T$ ), it can be inferred that  $\lambda$  can be increased by decreasing the density  $\rho$  which can be achieved either by decreasing the pressure  $p$ , or by increasing the absolute temperature  $T$ .  $m$  is the molecular mass and  $R$  is the gas constant.

Another way to calculate  $\lambda$  is through viscosity coefficient,  $\mu$  [92]:

$$\lambda = \frac{\sqrt{\pi} \mu}{2p} \left[ \frac{2k_B T}{m} \right]^{1/2} \quad (2.15)$$

where  $k_B$  is the Boltzmann constant ( $1.380658 \times 10^{-23} \text{J/K}$ ).

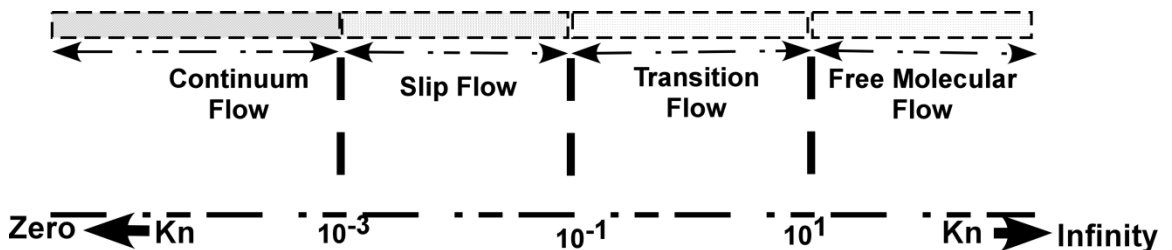


Figure 2.16: Classification of the flow regimes based on Knudsen number  $Kn$ .

The mean free path of air at standard atmospheric conditions is about 60 nm [93].

The value of the Knudsen number determines the degree of rarefaction; flow regimes are separated based on the Knudsen number as shown in figure 2.16, continuum, slip, transitional and free molecular flow regimes.

Continuum regime: Also called hydrodynamic regime. The Knudsen number is small,  $Kn \leq 0.001$ , interaction between molecules is happening continuously. This regime can be achieved by increasing the channel diameter or increasing the pressure. The influence of the wall is limited to a thin layer along the wall equal to the gas mean free path.

Slip flow:  $10^{-3} \leq Kn \leq 10^{-1}$ , as the Knudsen number increases, the boundary layer starts to become dominant between the bulk of the fluid and the wall surface.

Free molecular flow:  $Kn \geq 10$ , the Knudsen number reaches the point where the mean free path of gas molecules is greater than the channel diameter. The amount of interaction of gas molecules with the channel wall is greater than the intermolecular impacts which dictate more attention to the channel wall properties; this can be studied through accommodation coefficients. The region between the free molecular and slip flow regime is called transition flow ( $10^{-1} \leq Kn \leq 10$ ).

Another parameter,  $\delta$ , that is widely used to characterize gas rarefaction is called the rarefaction parameter; its expression is given by:

$$\delta = \frac{\sqrt{\pi}}{2} \frac{H}{\lambda} = \frac{\sqrt{\pi}}{2} \frac{1}{Kn} \quad (2.16)$$

Smaller values of  $\delta$  correspond to the free molecular regime, while larger values correspond to the continuum regime.

Figure 2.17 shows the two competing flows in the transitional flow regime as explained by Loeb [94]. He stated that when a temperature gradient is established along a



tube whose flow regime is transitional, two types of flow are competing with each other, the thermal creep along the tube wall and a pressure driven flow along the interior section. Thermal creep occurs along a very thin layer,  $\lambda$ , from the cold side to the hot side.

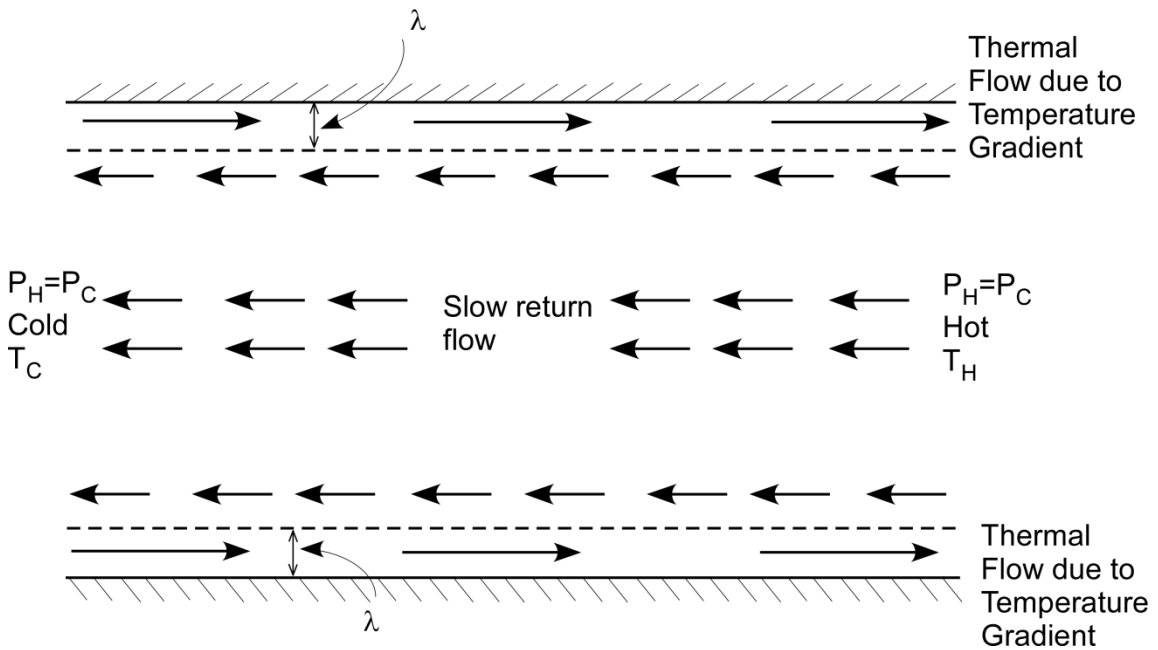


Figure 2.17: Schematic of the competing flows for a tube in the transitional flow regime [94].

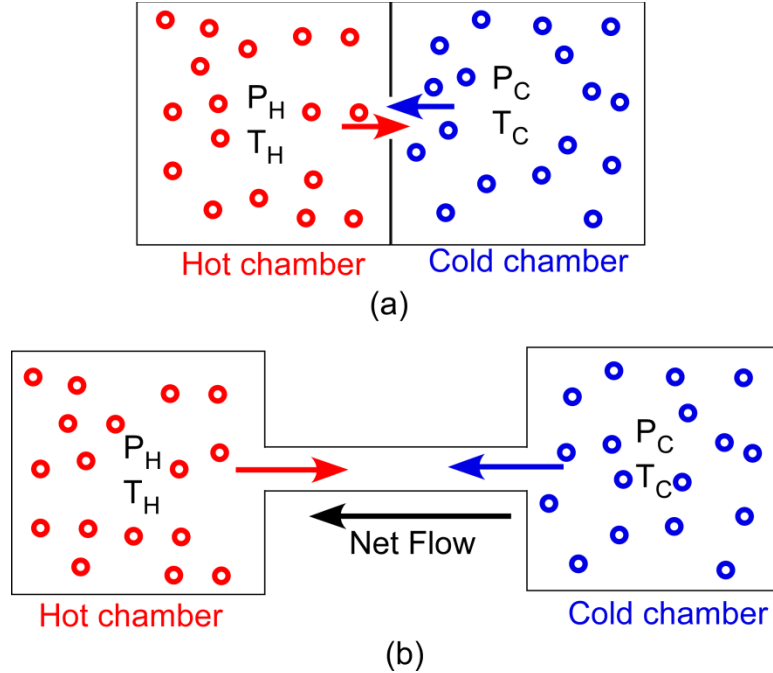


Figure 2.18: Thermal transpiration through (a) an aperture, (b) a channel. The two chambers are maintained at different temperatures. A net flow occurs from the cold side to the hot side.

Consider two vessels, filled with an ideal gas and maintained at different temperatures ( $T_H$  and  $T_C$ ) (Figure 2.18a). The aperture size is small compared to the gas mean free path and no collisions occur in the aperture. The following equations are valid for an ideal gas inside a chamber:

$$PV = nRT \quad (2.17)$$

$$n \propto \frac{P}{T} \quad (2.18)$$

$$KE_{av} = \frac{3}{2}k_B T = \frac{1}{2}M_{molecule}\bar{c}^2 \quad (2.19)$$

$$\bar{c} \propto \sqrt{T} \quad (2.20)$$

where  $P$  is the pressure,  $T$  is the temperature,  $R$  is the gas constant,  $n$  is the amount of substance of gas,  $KE_{av}$  is the average kinetic energy,  $M_{molecule}$  is the mass of one gas

molecule,  $k_B$  is the Boltzmann constant ( $1.38066 \times 10^{-23}$  J/K), and  $\bar{c}$  is the average velocity of the gas molecules.

It can be deduced from the previous equations that the flux,  $\dot{N}$ , through the aperture is proportional to  $P$  and inversely proportional to the square root of  $T$ .

$$\dot{N} \propto n\bar{c} \propto \frac{P}{\sqrt{T}} \quad (2.21)$$

The net flux,  $\dot{N}_{net}$ , through the aperture is equal to the difference between the fluxes from both vessels.

$$\dot{N}_{net} \propto \left[ \frac{P_H}{\sqrt{T_H}} - \frac{P_C}{\sqrt{T_C}} \right] \quad (2.22)$$

Setting the  $\dot{N}_{net}$  to zero, we obtain the equilibrium equation found by Reynolds [17].

$$\frac{P_H}{P_C} = \frac{\sqrt{T_H}}{\sqrt{T_C}} \quad (2.23)$$

Reynolds called the effect thermal transpiration. If we start with the same pressure in both chambers ( $P_H=P_C$ ), gas will flow from the cold side to the hot side. Siu [95] studied the effect of geometry and reflectivity from the channel wall and has predicted that equation (2.23) is valid for short tubes in the case of specular reflection and in long tubes for diffuse reflection.

A continuous flow will be generated if both vessels are kept at the same pressure all the time, this can be realized by opening both vessels to the atmosphere. When the two vessels are connected with a long narrow channel such that the flow regime is free molecular (Figure 2.18b), gas/wall interactions occur a lot along the channel. At the

steady state, the net flow is zero and the same equilibrium equation as in the case of an aperture is obtained.

A different explanation of the thermal transpiration phenomenon based on the momentum transfer between the wall and gas molecules was given by Sone [91]. When gas rests over a plane wall which is subjected to a temperature gradient, Sone stated that the amount of momentum transferred to a small area of the wall,  $dS$ , is higher for molecules from the hotter side due their higher average speed. The overall momentum transferred to the wall has a component in the direction opposite to the temperature gradient. As a counteraction, a force is exerted on the gas molecules in the temperature gradient direction, in other words, gas will flow from the cold side to the hot side.

## 2.5 Thermal transpiration models

Different models, which relate pressure and temperature along a cylindrical tube, have been derived and studied experimentally and theoretically. The following models will be discussed: Maxwell, Knudsen, Kennard, Williams, and Sharipov.

### 2.5.1 The Maxwell model

Maxwell derived one of the earliest equations that relate the amount of gas passing through a tube section per unit time,  $Q$  [18]. He assumed the temperature to vary gradually along the tube such that the temperature is uniform throughout any section and that the gas motion is slow. Maxwell derived the following equation, which relates the quantity of gas passing through any section of the tube,  $Q$ , the rate of variation of pressure,  $p$ , and temperature,  $T$ .

$$\frac{Q}{\pi r a^2} + \frac{1}{8\mu} (a^2 + 4Va) \frac{dp}{dx} - \frac{3}{4} \frac{\mu}{\rho T} \frac{dT}{dx} = 0 \quad (2.24)$$

where  $\rho$  is the density,  $\mu$  is the coefficient of viscosity,  $p$  is the pressure,  $x$  is the tube axis,  $a$  is the tube radius, and  $V$  is the coefficient of slipping which depends on the gas mean free path,  $\lambda$ , and amount of gas molecules reflected diffusively from the tube wall,  $f$ .

For a uniform temperature,  $Q$  has the following expression:

$$Q = \frac{\pi\rho a^4}{8\mu} \frac{dp}{dx} \left[ 1 + 4 \frac{V}{a} \right] \quad (2.25)$$

$$V = \frac{2}{3} \left( \frac{2}{f} - 1 \right) \lambda \quad (2.26)$$

Experimental measurement on glass capillary tubes gave  $V=8/p$  and  $15/p$  for air and hydrogen, respectively. The unit of  $p$  is dynes/cm<sup>2</sup>.

For a tube subjected to a temperature gradient, Maxwell showed that a large pressure is obtained in the hot side when the flow stops,  $Q=0$ . The pressure gradient in this case is given by:

$$\frac{dp}{dx} = \frac{6\mu^2}{\rho T} \frac{1}{a^2 + 4Va} \frac{dT}{dx} \quad (2.27)$$

### 2.5.2 The Knudsen model

First, Knudsen derived an expression which relates the pressure and temperature gradient along a cylindrical tube [96]. The relation was valid for hydrodynamic and free molecular regimes.

$$\frac{dp}{dT} = \frac{1}{\frac{a^2}{\lambda^2} \frac{1}{k_1} \left( \frac{0.81}{0.49} \right) \frac{\pi}{16} + \frac{8}{3} \frac{1}{k_1} \frac{a}{\lambda}} \frac{p}{2T} \quad (2.28)$$

The value of  $k_1$  is equal to 1 and between 2 and 3 for large and small Knudsen numbers, respectively. Further work was performed by Knudsen to improve the

applicability of equation (2.28) in the intermediate Knudsen number values through taking into account the collisions of molecules which have had their last collision with the walls. For values of  $a/\lambda \sim 1$ , he obtained the following approximate expression:

$$\frac{dp}{dT} = \frac{1}{1 + \frac{2a}{\lambda}} \frac{p}{2T} \quad (2.29)$$

Knudsen has observed and concluded that the transport of gas through porous medium is occurring due to the colliding and bouncing of molecules from the wall of the porous membrane [77, 97]. Knudsen derived the following equation for the mass flow rate,  $\dot{M}$  :

$$\dot{M}_{Knudsen} = \frac{2}{3} \frac{\Delta P \pi a^3 N}{L} \sqrt{\frac{8}{RT\pi}} \quad (2.30)$$

$N$  is the number of channels (number of pores). This equation is used in chapter 5 to calculate the flow rate across the Whatman membranes.

### 2.5.3 The Kennard model

Kennard derived the mass flow rate along a round tube of radius  $a$  for high density gases, in this case the mean free path is small compared  $a$  which is in turn small compared to the tube length [98]. The mass flow rate  $Q$  expression is:

$$Q = -\frac{\pi}{8} \frac{a^4 p}{\mu RT} \left( 1 + 4 \frac{\zeta}{a} \right) \frac{dp}{dx} + \frac{3\pi}{4} \frac{\mu a^2}{T} \frac{dT}{dx} \quad (2.31)$$

$\zeta$  is the slip distance at the wall of the tube. Other parameters are defined later. In the case of no flow along the tube, the relationship between  $p$  and  $T$  is:

$$\frac{dp}{dx} = \frac{6\mu^2 R}{a^2 p \left( 1 + \frac{4\zeta}{a} \right)} \frac{dT}{dx} \quad (2.32)$$

#### 2.5.4 The Williams model

James Williams derived a mathematical model that predicts the overall flow along a tube under the influence of a pressure gradient down the center and a counter flow, due to thermal creep, along the wall [99]. He has assumed the temperature uniform on each side and that the slender channel equations are valid. The model was successful in predicting the flow for very high pressures, i.e. in the near continuum flow regime. Pressure and temperature are related by the following equation:

$$\frac{dp}{dT} = \frac{\frac{6\mu^2 R}{a^2}}{p + \frac{4\mu}{a} \left( \frac{2-\sigma}{\sigma} \right) \sqrt{\frac{\pi R T_w}{2}}} \quad (2.33)$$

where  $\mu$  is the viscosity coefficient,  $\sigma$  is the molecular reflection coefficient,  $a$  is the tube radius,  $T_w$  is the absolute temperature of the wall, and  $R$  is the gas constant. Equation (2.33) is similar to the one derived by Kennard when  $4\mu \left( \frac{2-\sigma}{\sigma} \right) \sqrt{\frac{\pi R T_w}{2}}$  is replaced by  $\zeta$ .

#### 2.5.5 The Sharipov model

The Sharipov model is applicable in all flow regimes [100]. It is derived under the assumption that the temperature and pressure gradients,  $\tau$  and  $\nu$ , are small. Their expressions are given by:

$$\nu \approx \frac{a}{L} \frac{\Delta P}{P_{av}} \quad (2.34)$$

$$\tau \approx \frac{a}{L} \frac{\Delta T}{T_{av}} \quad (2.35)$$

this assumption is verified under the condition  $L \gg a$  for circular channel or  $L \gg h$  for rectangular channel at any given pressure or temperature ratio.  $L$  and  $h$  are the channel

length and height, respectively. The same condition neglects the influence of the channel ends.

Therefore, the kinetic equation can be linearized and the reduced flow rate  $Q$  can be written as the combination of two opposing flows, thermal creep and pressure driven flow:

$$Q = -\nu \cdot M_p + \tau \cdot M_t \quad (2.36)$$

$Q$  is related to the mass flow rate  $\dot{M}$  by the following equation:

$$Q = \frac{1}{\pi a^2 P} \left( \frac{2kT}{m} \right)^{\frac{1}{2}} \dot{M} \quad (2.37)$$

In the case of a rectangular channel, the mass flow rate is given by [101]:

$$\dot{M} = \frac{h^2 w P_{av}}{L} \sqrt{\frac{m}{2k_B T_{av}}} \left[ \frac{\Delta T}{T_{av}} M_t - \frac{\Delta P}{P_{av}} M_p \right] \quad (2.38)$$

For a circular channel [100]:

$$\dot{M} = \frac{\pi a^3 P_{av}}{L} \sqrt{\frac{m}{2k_B T_{av}}} \left[ \frac{\Delta T}{T_{av}} M_t - \frac{\Delta P}{P_{av}} M_p \right] \quad (2.39)$$

where  $a$ ,  $L$ ,  $h$ , and  $w$  are the channel radius, length, height, and width, respectively.  $P_{av}$  and  $T_{av}$  are the average pressure and temperature,  $\Delta P$  and  $\Delta T$  are the pressure and temperature differences across the channel,  $m$  is the molecular mass of the gas,  $k_B$  is Boltzmann's constant.  $\pi a^2$  in the  $Q$  expression is replaced by  $hw$  in the case of a rectangular channel.

$M_p$  and  $M_t$  are positive values which depend on the inverse Knudsen number. The S-model [102] was used to solve the linearized Boltzmann equation assuming non-isothermal flow.



The derivation starts with the S-model in the case of stationary flow expressed as follow:

$$\mathbf{V} \frac{\partial f}{\partial \mathbf{r}'} = \frac{p}{\mu} \left\{ f^M \left[ 1 + \frac{2m\mathbf{q}' \cdot \mathbf{V}}{15pk_B T} \left( \frac{mV^2}{2k_B T} - \frac{5}{2} \right) \right] - f \right\} \quad (2.40)$$

$$f^M = n \left( \frac{m}{2\pi k_B T} \right)^{3/2} \exp \left( -\frac{mV^2}{2k_B T} \right) \quad (2.41)$$

where  $V=v-u'$ ,  $f(\mathbf{r}',\mathbf{v})$  is the velocity distribution function,  $f^M$  is the local Maxwellian distribution function,  $v$  is the molecular velocity,  $u'$  is the bulk velocity,  $\mathbf{r}'$  is the position vector,  $\mathbf{q}'$  is the heat flow vector,  $n$  is the numerical density of the gas. The local values of the number density  $n$ , temperature,  $T$ , bulk velocity  $\mathbf{u}'$ , and heat flux,  $\mathbf{q}'$ , can be calculated using  $f(\mathbf{r}',\mathbf{v})$ .

The following distribution function  $f$  is used to linearize the S-model in equation (2.40).

$$f(\mathbf{r},\mathbf{c}) = f^0 \left[ 1 + g(y,z,c) + vx + \alpha \left( c^2 - \frac{5}{2} \right) \right] \quad (2.42)$$

Solving the new equation,  $M_p$  and  $M_t$  can be calculated using the following equations:

$$M_p = -2 \frac{h}{w} \int_{\frac{-w}{2h}}^{\frac{w}{2h}} \int_{\frac{-1}{2}}^{\frac{1}{2}} u_p(y,z) dy dz \quad (2.43)$$

$$M_t = 2 \frac{h}{w} \int_{\frac{-w}{2h}}^{\frac{w}{2h}} \int_{\frac{-1}{2}}^{\frac{1}{2}} u_t(y,z) dy dz \quad (2.44)$$

It should be noted that the aforementioned derivation is for a rectangular channel [101]. The one for a circular channel can be found in the following reference [103].

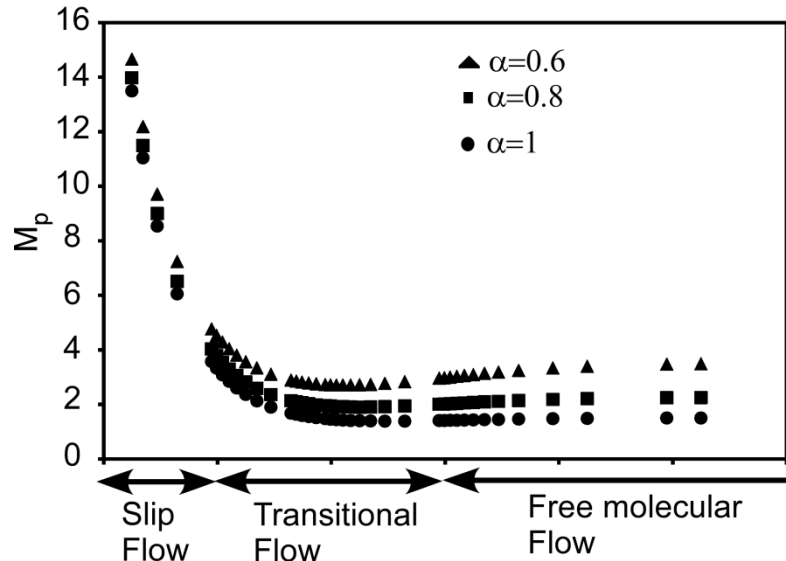


Figure 2.19:  $M_p$  values for a circular channel in the different flow regimes for different TMAC values [103].

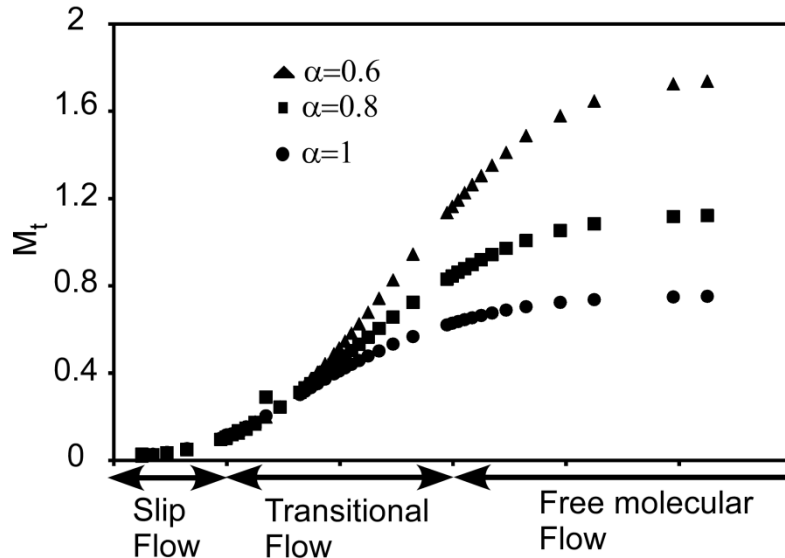


Figure 2.20:  $M_t$  values for a circular channel in the different flow regimes for different TMAC values [103].

Figures 2.19 and 2.20 show the computed values of  $M_p$  and  $M_t$  in the different flow regimes for a circular channel. One can notice that as the Knudsen number increases,  $M_t$  increases and  $M_p$  decreases.  $M_p$  and  $M_t$  can have different values based on

the value of  $\alpha$  (TMAC). The higher the TMAC value, the higher the  $M_t$  and the lower the  $M_p$ . Therefore, an accurate measurement of the TMAC value of the channel is needed in order to accurately compute the mass flow rate and the pressure difference generated with a device operating on the thermal transpiration principal. The values of  $M_p$  and  $M_t$  shown in the previous figures will be used in the TE modeling chapter to study the effect of different parameters (TMAC, pore size, gas type) on the TE based Knudsen pump performance.

## **2.6 Thermoelectric effects**

### **2.6.1 Seebeck effect**

The first thermoelectric effect was discovered in 1821 by German-Estonian physicist Thomas Johann Seebeck [104]. He showed that an electromotive force and hence a current can be produced when heat is applied at the junction of two dissimilar metals or semiconductors, A and B, connected in a closed loop [105]. Figure 2.21 illustrates the Seebeck effect in the case of a one material. Nowadays, the Seebeck effect is used to measure temperature (using thermocouple) with a great accuracy and sensitivity. The relation between temperature and voltage is governed by the following equation:  $V = \alpha_{AB}(T_h - T_c)$ . Where  $V$  is the voltage,  $\alpha_{AB}$  is the differential Seebeck coefficient or differential thermopwer (V/K) for the two conductors A and B, and  $T_h$  and  $T_c$  are the hot and cold temperatures respectively.

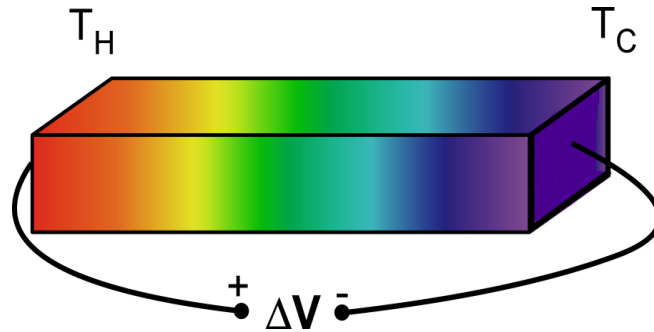


Figure 2.21: Seebeck effect, temperature gradient along the bar caused a generation of an electromotive force.

### 2.6.2 Peltier effect

Thirteen years after Seebeck discovery, the French physicist Jean Charles Athanase Peltier discovered the second thermoelectric effect [105]. Peltier found that the passage of an electrical current causes a generation of heat at the junction of two different metals. Heat is either absorbed or rejected depending on the current direction. Heat ( $H$ ) absorbed or liberated at the junction is directly proportional to the current ( $I$ ) passing through the junction, the magnitude of this heat is given by:  $H = I \cdot \pi_{AB}$ , where  $\pi_{AB}$  is the differential Peltier coefficient for conductors A and B (J/A). The Seebeck coefficient is much simpler to measure than the Peltier coefficient due to Joule heating occurring during the Peltier coefficient measurements that causes an erroneous measurement of the amount of heat rejected or absorbed.

Most metals have very small absolute values of the Seebeck coefficient compared to semiconductors.

### 2.6.3 Thomson effect

Thomson effect is the generation of heat along a current-carrying wire whose ends are maintained at different temperature (Figure 2.22). This effect was observed by Lord Kelvin in 1851. The amount of heat energy generated or given out is given by the following equation [106]:

$$\Delta Q = \tau \cdot I \cdot t \cdot \Delta T \quad (2.45)$$

where  $\tau$  is the Thomson coefficient,  $\Delta T$  is the temperature difference,  $I$  is the current, and  $t$  is time. Thomson effect is different that joule heating.

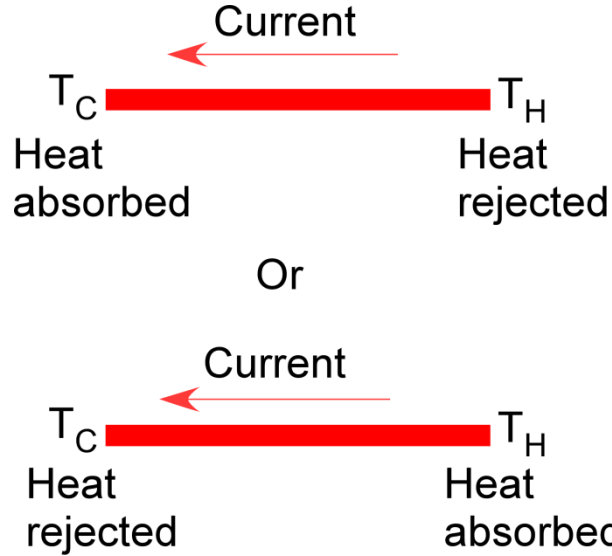


Figure 2.22: Schematic description of Thomson effect [106].

#### 2.6.4 Kelvin effect

Lord Kelvin (William Thomson) showed that the three thermoelectric effects, previously discussed, are thermodynamically related by the following equations [107]:

$$\pi_{AB} = T \cdot \alpha_{AB} \quad (2.46)$$

$$\tau_A - \tau_B = T \cdot \frac{d\alpha_{AB}}{dT} \quad (2.47)$$

The previous equations are known as Kelvin relations. Knowing the temperature dependence of one of the three parameters permits the determination of the other two. For a single conductor, the previous equations can be written as [107]:

$$\pi = T \cdot \alpha \quad (2.48)$$

$$\tau = T \cdot \frac{d\alpha}{dT} \quad (2.49)$$

## 2.7 Thermoelectric figure of merit $ZT$

The effectiveness of a thermoelectric material can be measured by a figure of merit  $Z$  [108, 109].

$$Z = \frac{\alpha^2 \sigma}{K} \quad (2.50)$$

where:  $\alpha$  is the Seebeck coefficient or thermopower;  $\sigma$  the electrical conductivity;  $K$  the total thermal conductivity with contribution from the lattice  $K_L$  and the electron  $K_e$ .

The three parameters appearing in the figure of merit expression are affected by the carrier concentration. Figure 2.23 shows a plot of the thermopower, electrical conductivity, and thermal conductivity against the carrier concentration. With increasing carrier concentration, the electrical conductivity increases and thermopower decrease. The power factor,  $\alpha^2 \sigma$ , maximizes at an intermediate value. The electron electrical conductivity portion also increases with increasing carrier concentration while the lattice part remains constant. The optimal doping concentration is around  $10^{19}/\text{cm}^3$  [110].

Almost all materials exhibit thermoelectric effect, but only those with value of  $ZT$  larger than 0.5 are regarded as thermoelectric materials. Bismuth Telluride and its alloys, Antimony, Selenium, are the best thermoelectric materials at room temperature [111-113] they have a  $ZT$  value  $\sim 1$  (Figure 2.24). For medium and high temperature applications, materials such as PbTe [114] and silicon-germanium [111] can be used.

Increasing the thermopower in thermoelectric bulk materials cause an increase in the thermal conductivity resulting in limited improvement in the  $ZT$ . The three parameters,  $\alpha$ ,  $K$ , and  $\sigma$ , are interconnected in a way makes it difficult to control independently. In the last two decades, research for higher  $ZT$  value thermoelectric materials followed two different paths[115]; one is searching for new bulk material [116,

117] such as phonon-glass/electron –crystals (PGEC) materials [118], skutterudites [117, 119], and clathrates [120] in which phonon scattering is high without any impact on the transport of electrons. The other one is using low dimensional material systems.

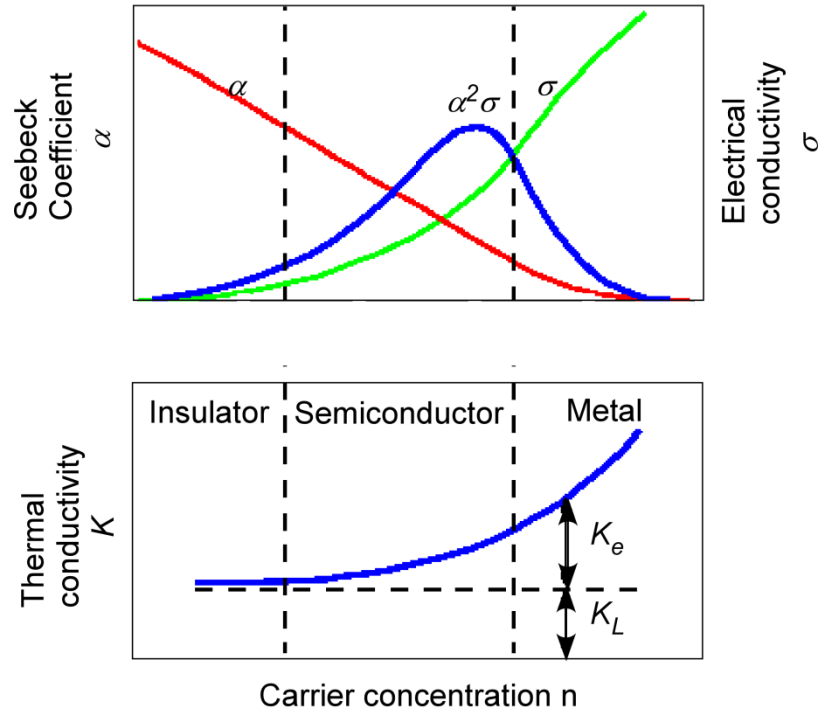


Figure 2.23: Schematic dependence of thermal conductivity, electrical conductivity, and the Seebeck coefficient on the carrier concentration  $n$  [121].

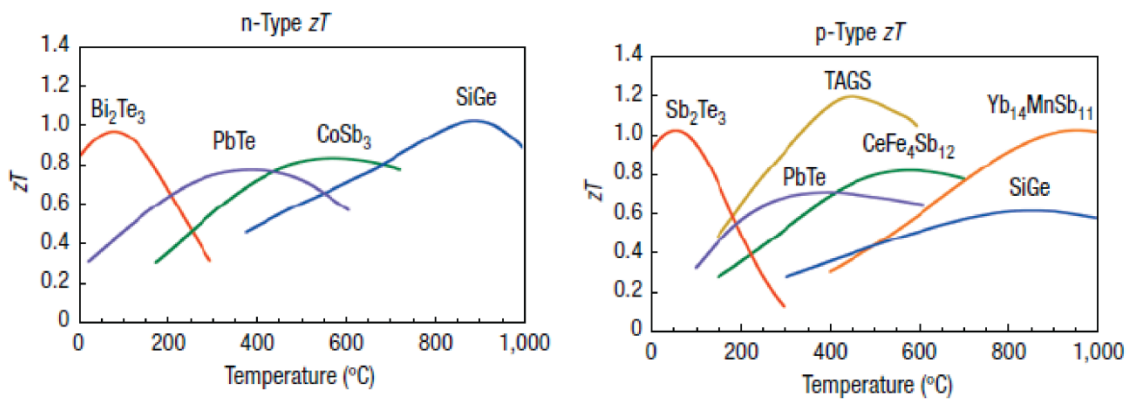


Figure 2.24:  $ZT$  value for different thermoelectric materials versus temperature [111].

## 2.8 Changes in the electron density when moving to low dimensional

The first work on the feasibility of low-dimensional thermoelectric material was started by Slack and Dresselhaus [122, 123]. Theoretical analysis was performed on a one and 2-dimensional material, Slack and al. have derived the  $Z$  expression in terms of the Fermi level and a parameter  $\beta$ . They have found that  $Z$  increases with increasing  $\beta$  and that moving from two to one-dimension yields higher figure of merit  $Z$ . An application to the bismuth telluride quantum wire showed an improvement in all three directions, binary, bisectrix, and trigonal directions, when the width is less than 10 nm. Another comparison of the  $Z$  value was conducted on a quantum wire, 1 nm wide, and a 2-dimension film, 1 nm thick, showed an increase from 2.5 to 6 in the case of quantum wire. In the general, as the dimensions of the thermoelectric material approach the nanoscale, there a possibility of controlling  $\alpha$ ,  $K$ , and  $\sigma$  quasi-independently through quantum confinement effects [115], in other words, the motion is restricted in one direction (2-D), or two directions (1-D), or three directions (0-D) which is referred to as quantum dot. The power factor,  $\alpha^2\sigma$ , is proportional to the density of state (Figure 2.25) which becomes narrower as the dimension is moved from bulk material to quantum dot. If the density of state is tuned and placed close to the Fermi level, the  $Z$  value can be increased.

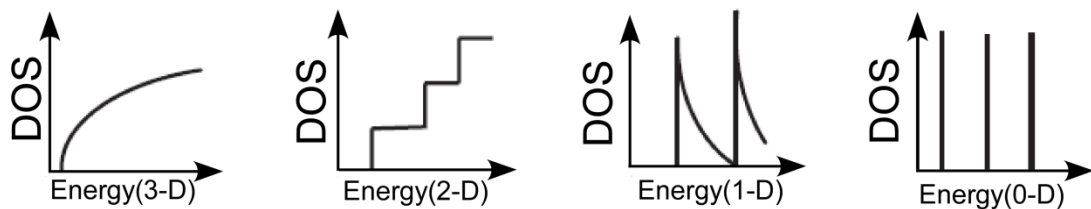


Figure 2.25: Density of state (DOS) as a function of energy for bulk material (3-D), quantum well (2-D), nanowire (1-D), and a quantum dot (0-D) [115].



## 2.9 Bi<sub>2</sub>Te<sub>3</sub> thermoelectric material

Bi<sub>2</sub>Te<sub>3</sub> is the best semiconductor element for thermoelectric refrigeration [124]. It can easily be cleaved in planes perpendicular to the c axis due to the weak van der Waals binding between layers [125]. Table 2.1 shows the general properties of Bi<sub>2</sub>Te<sub>3</sub> [124].

Table 2.1: General properties of Bi<sub>2</sub>Te<sub>3</sub> [124].

Property	Symbol	Value	Temperature
Hexagonal unit	a	4.3835 Å	20 °C
Cell dimensions	c	30.487 Å	20 °C
Density	$\rho$	7858.7 Kg.m <sup>-3</sup>	20 °C
Specific heat		15070+54.4T-0.13T <sup>2</sup> (J K <sup>-1</sup> Kg-mole <sup>-1</sup> )	Up to 550 °C
Debye temperature	$\Theta_D$	155.5 K	0 K
Melting point	$T_m$	585 °C	
Thermal conductivity	$K_L$	1.5 W m <sup>-1</sup> K <sup>-1</sup> $\perp$ to c axis 0.7 W m <sup>-1</sup> K <sup>-1</sup> // to c axis	300 K 300 K

## 2.10 Production of Bi<sub>2</sub>Te<sub>3</sub> and its alloys

### 2.10.1 Growth from a melt

Crystal growth from a melt is the most popular method for growing single crystals at large scale. It is based on melting the different constituents to form a homogeneous mixture and then freeze the melt. Distribution of impurities is very low in this type of production. Better quality thermoelectric can be produced if a sort of directional-freezing is implemented. The Bridgman technique, used to grow Bi<sub>2</sub>Te<sub>3</sub> based thermoelements [126, 127], can produce large boules or ingots of a single crystal, it consists of heating a polycrystalline material above its melting temperature and slowly cooling it down from one end where a highly oriented crystal material is placed. The zone melting techniques [128], developed by Pfann in 1951, is widely used to grow high quality single crystals including Bi<sub>2</sub>Te<sub>3</sub> alloys [129-131]. During the growth, a polycrystalline crystal is slowly passed through heater, only a narrow region of the crystal is molten. Impurities diffuse to

the liquid-solid interface and accumulate at the end of the ingot. For single crystals growth, a seed crystal is needed at the starting of the growth. Many other techniques are also available for growing crystals from melt and these are Kyropoulos Method [132, 133], Verneuil Method [134], and Czochralski technique [135].

### **2.10.2 Powder metallurgy**

Thermoelectric elements grown from the melt have the highest figure of merit compared to the one produced with powder metallurgy technique [124]. The latter has few advantages such as robustness, homogeneity, and possibility to reduce the phonon part of the thermal conductivity which can result in increase of the figure of merit  $ZT$ .

Different varieties of the powder metallurgy technique such as hot-pressing [136-138], and hot extrusion [136], have been used to produce  $\text{Bi}_2\text{Te}_3$  alloys. The powder metallurgy procedure for producing  $\text{Bi}_2\text{Te}_3$  thermoelectric pellets is explained in detail in the chapter entitled “fabrication of the  $\text{Bi}_2\text{Te}_3$  thermoelectric based Knudsen pump”.

## **2.11 Thermoelectric physical properties measurement**

### **2.11.1 Electrical conductivity**

Electrical conductivity translates the ability of a material to conduct electrical current, during measurement, one needs to take into account the extra resistance introduced by the electrical contacts. One way to avoid this is through using extra probes, other than the one used for the current flow, for measuring the voltage (Figure 2.26). Sample cross section area and probe distance need to be known accurately. Isothermal conditions must be maintained for accurate measurement, if a temperature difference between the thermoelement ends arises from some asymmetrical arrangement, this will generate a voltage based on the Seebeck effect which will lead to erroneous voltage

measurement and therefore inaccurate electrical conductivity values. One way to surpass this issue was suggested by Goldsmid [139], he has used an alternating current with high frequency, to avoid the temperature gradient that may be generated by the Peltier effect, two balancing resistances, and a slide wire. Once the set-up is balance, the thermoelement resistance can be calculated from the values of the balancing resistances.

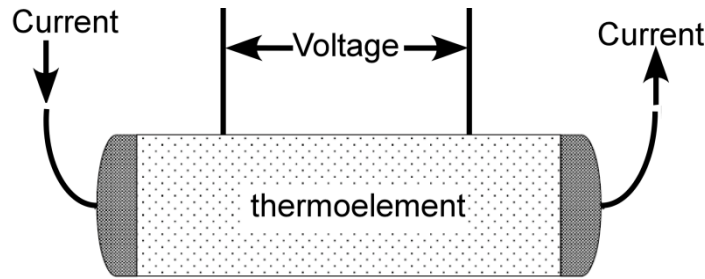


Figure 2.26: Electrical conductivity measurement [140].

### 2.11.2 Seebeck coefficient (Thermopower)

Thermopower remains one of the easiest quantities to measure, a temperature gradient is applied and the generated electromotive force (voltage) across the thermoelement is measured. Two possible arrangements (Figure 2.27) were suggested by Goldsmid [140], the thermoelectric sample is placed between a heater and a heat sink. In the first arrangement (Figure 2.27(a)), the thermocouples can cause measurement errors at the point of contact with the thermoelement, this issue can be avoided by using long leads and thin diameter thermocouple wires (less than  $60 \mu\text{m } \varnothing$ ) along with sufficient thermal anchoring. In the second arrangement (Figure 2.27(b)), the thermocouples are attached to the heater and heat sink. There will be a difference if the sample is soldered to or pressed against the heater/heat sink made of copper. When the sample properties are non-uniform, most of the measured thermopower comes from the regions close to the ends where the temperature gradient is high, leading to measurement errors.

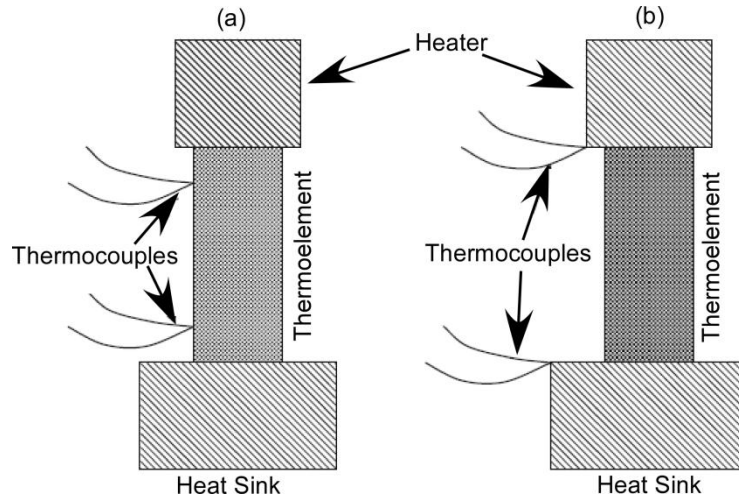


Figure 2.27: Schematic set-up for measuring the Seebeck coefficient. (a) Thermocouples are attached to the sample. (b) Thermocouples are attached to the heater and heat sink [140].

### 2.11.3 Thermal conductivity

#### (A) *Steady state method*

Thermal conductivity is one of the difficult parameters to measure due to the unavoidable heat losses and its smallness, especially with thermoelectric materials, which can be affected with minimal change in the temperature. The same set-up described in figure 2.27 can also be used to measure the thermal conductivity providing that the whole set-up is placed in a vacuum chamber which helps minimize heat losses through convection and radiation [140]. One technique that is widely used to measure the thermal conductivity is the steady state-method [141]. The thermal conductivity is given by:

$$K = \frac{Q_T L_0}{A \Delta T} \quad (2.51)$$

where  $Q_T$  is the heating power through the thermoelement,  $L_0$  is the distance between the thermocouple leads,  $\Delta T$  is the temperature difference, and  $A$  is the sample cross section area; the sample is sandwiched between a resistive heater (strain gauge) and T-shaped heat sink. Small Cn-Cr thermocouples, for measuring the temperature, are attached to

small copper flags previously attached to the sample. Measurement under vacuum along with appropriate thermal shielding are needed for accurate measurement. Measurement is done when the material temperature is not changing with time.

**(B) Comparative method**

In this method, the sample is placed in series with a standard material and the heater. Better results are obtained when the thermal conductivity of the standard material is in the same range as the sample. The heat flow is assumed to be the same through the sample and the standard material, the thermal conductivity is given by:

$$K_s = K_{ref} \left( \frac{A_{ref} \Delta T_{ref} L_s}{A_s \Delta T_s L_{ref}} \right) \quad (2.52)$$

where  $A$  is the cross section area,  $L$  is the thickness. Subscripts  $s$  and  $ref$  refer to the sample and standard material.

**(C)  $3\omega$  method**

This method has been used to measure the thermal conductivity of thin film samples [142]. A thin film (Au or Pt), deposited onto the sample, serves to generate heat pulse and a temperature monitor through temperature-resistivity relationship. When a current AC (frequency  $\omega$ ) is applied, the measured voltage will have three frequency components ( $\omega$ ,  $2\omega$ ,  $3\omega$ ) mainly due to the joule heating. The voltage expression is given by:

$$V = RI = I_0 e^{i\omega t} \left( R_0 + \frac{\delta R}{\delta T} \Delta T \right) = I_0 e^{i\omega t} \left( R_0 + C_0 e^{i2\omega t} \right) \quad (2.53)$$

The thermal conductivity is calculated from the slope of  $\Delta T$  versus  $\log(\omega)$ .

#### 2.11.4 Thermal diffusivity

Another technique that is widely used to measure the thermal conductivity is through measurement of thermal diffusivity,  $d_{th}$ . Thermal conductivity can be determined using the following equation:

$$K = d_{th}DC_V \quad (2.54)$$

where  $D$  is the sample density and  $C_V$  is the specific heat of the sample. The first one is determined from the sample dimensions and material density, and the other term  $C_V$  is measured using differential scanning calorimeter.

##### (A) *Laser flash method*

This method is used in this work to measure the thermal diffusivity of the thermoelectric sintered sample. Full explanation of the method is placed in the fabrication of the thermoelectric based Knudsen pump chapter.

##### (B) *Angstrom method*

Figure 2.28 shows a schematic of the experimental set-up used to measure the thermal diffusivity based on the Angstrom method. A heat sine wave is applied to one side of the sample. The temperature variation at two different positions, separated by a distance  $L$ , is recorded. Phase amplitude difference of the two temperature signals are extracted and used in the following equation [143], derived by Angstrom, to calculate the thermal diffusivity.

$$d_{th} = \frac{\omega L^2}{2Ln^2\left(\frac{A}{B}\right)} = \frac{\omega L^2}{2\beta^2} \quad (2.55)$$

where:  $\omega$  is the angular frequency of the heat wave,  $L$  is thermocouple separation,  $\beta$  is the phase difference between the two signals,  $A$  and  $B$  are the two temperature signals amplitude.

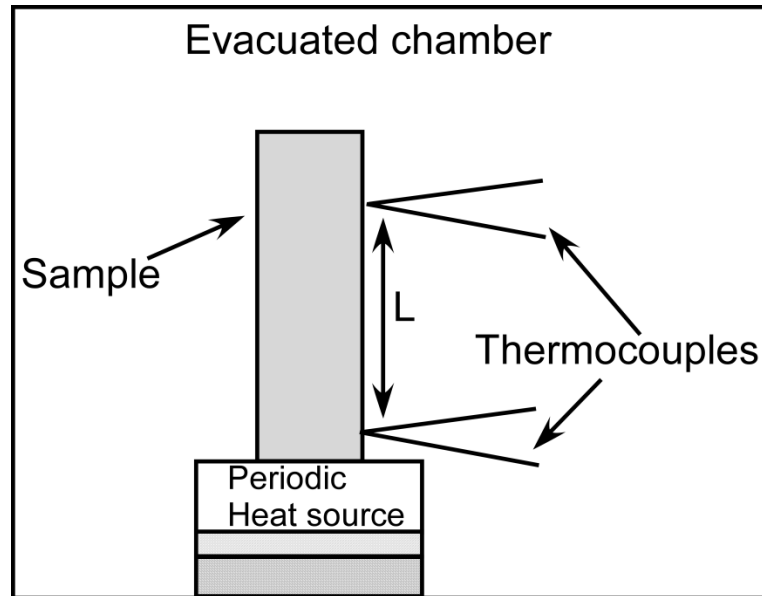


Figure 2.28: A Schematic illustration of the experimental setup for measuring thermal diffusivity using the Angstrom method.

## 2.12 Powder metallurgy

Powder metallurgy is the process of pressing blended fine powder and then sinter the compressed material in a controlled atmosphere to form a solid sample. Figure 2.29 shows the different steps involved during the fabrication of a component using powder metallurgy.

Advantages of powder metallurgy

- **Processing of materials with very high melting point:** Materials with high melting temperature such as tungsten, molybdenum and tantalum are hard to melt or cast. Powder metallurgy offers a practical way for processing these types of materials [144].

- **Controlled levels of porosity:** Various degrees of porosity can be obtained by controlling the particle [145].
- **Cost effective:** Powder metallurgy can be a cost effective alternative to casting, forging, and stamping [146].
- **Mixing and processing of materials that are hard to mix:** Materials with totally different characteristics can be mixed, compacted and processed. Metallurgically immiscible materials may be combined to produce different structures which are hard to make using the melt method [147].
- **Availability of powder material:** It is possible to have a wide range of mechanical and physical properties of a product due to the availability of powder with very wide range of properties [148].
- **Production rate:** The rate of production is very high compared to other techniques [148].
- **Tolerance:** Products with tolerance as small as  $\pm 0.02$  mm are possible with powder metallurgy [148].



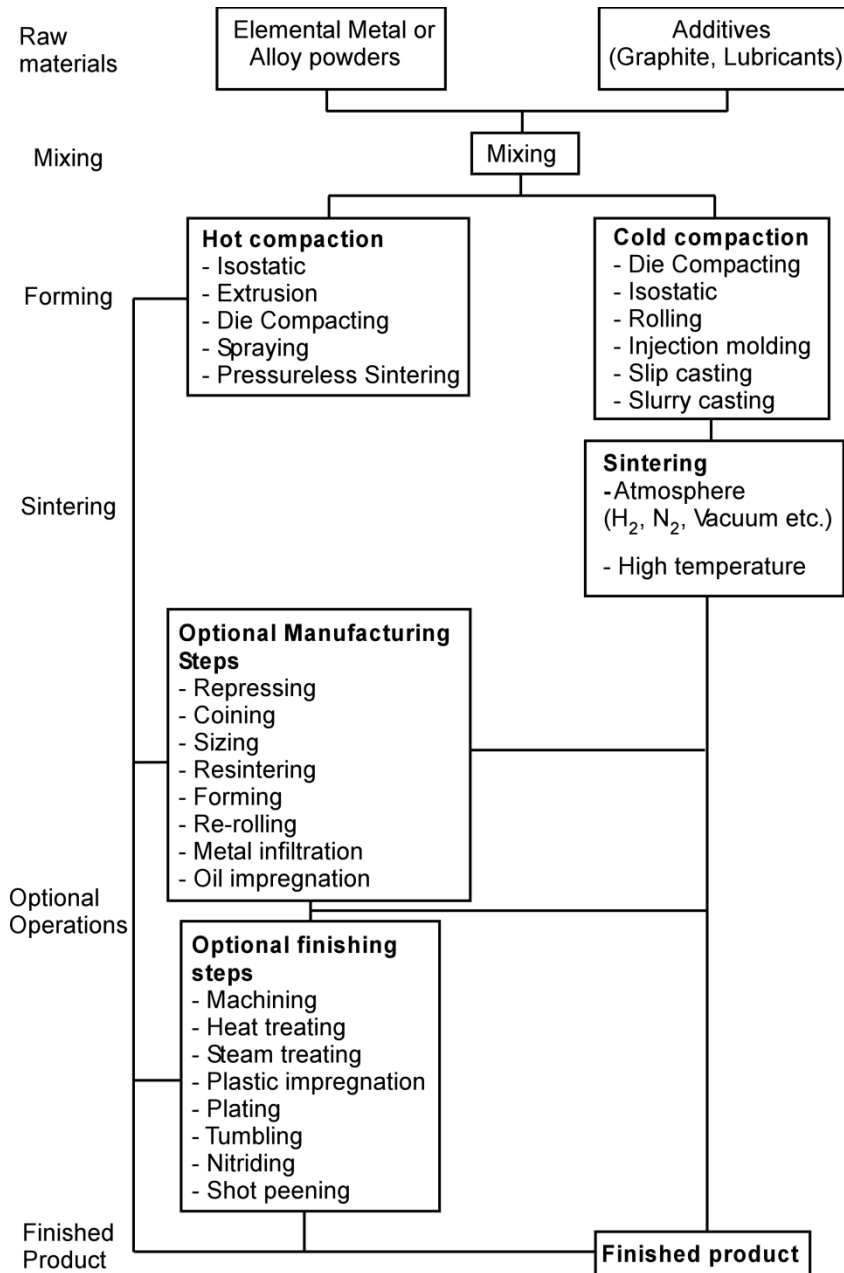


Figure 2.29: Powder metallurgy component production steps [149].

### 2.13 Powder preparation

Powder preparation can be divided into two categories: mechanical methods and chemical methods. Mechanical methods are used to prepare powders from naturally occurring raw materials while chemical methods use powders from synthetic or modified

natural materials as the starting materials. Table 2.2 shows the common powder preparation methods [150].

Desired characteristics of a powder [150]:

- Fine particle size ( $< 1 \mu\text{m}$ )
- Narrower or monodisperse particle size distribution.
- Spherical or equiaxial particle shape.
- No or soft particle agglomeration.
- High purity and single phase.

Table 2.2: Mechanical and chemical methods for powder preparation [150].

Powder preparation method	Advantages	Disadvantages
<b>Mechanical:</b> comminution	Inexpensive, wide applicability	Limited purity, limited homogeneity, large particles
Mechanochemical synthesis	Fine particle size, good for monoxides, low temperature route	Limited purity, limited homogeneity
<b>Chemical:</b>  Solid-state reaction	Simple apparatus, inexpensive	Agglomerated powder, limited homogeneity for multicomponent powders
Liquid solutions Precipitation or coprecipitation: solvent vaporization (spray drying, spray pyrolysis, freeze drying, sol-gel processing); combustion (Pechini method, glycine nitrate process) Nonaqueous liquid reaction	High purity, small particles, composition control, chemical homogeneity High purity, small particles	Expensive, poor for monoxides, powder agglomeration usually a problem Limited to monoxides
Vapor-phase reaction Gas-solid reaction	Inexpensive	Low purity, limited to monoxides
Gas-liquid reaction; reaction between gases	High purity, small particles	Expensive, limited to monoxides

### 2.13.1 Ball milling

Ball milling is one of the simplest and inexpensive mechanical techniques for making the powder. The grain size depends on the amount of powder to be milled, milling speed and time, temperature and atmosphere of milling, the size of mill and

milling media. The smallest particle size is  $\sim 0.1 \mu\text{m}$ . The disadvantages of this technique are the limited grain size, and possibility of introducing impurities from the ball media and/or the inside of the mill. Table 2.3 gives the possible particle size for different milling techniques [151].

Table 2.3: Possible particle size for different milling techniques [151].

<b>Milling technique</b>	<b>Possible particle size</b>
Jaw crushers	To 5 mm
Cone crushers	To 5 mm
Crushing rolls	To $\sim 1$ mm
Hammer mill	To $\sim 0.5$ mm
Jet mill	1 to $\sim 50 \mu\text{m}$
Vibratory mill	1 to $\sim 50 \mu\text{m}$
Ball mill	$0.5 - 10 \mu\text{m}$
Attrition mill	$0.1 - 5 \mu\text{m}$
Roller mill	$0.1 - 5 \mu\text{m}$

## 2.14 Sintering

### 2.14.1 Definition

Sintering is a processing technique used to produce density-controlled materials and components from metal and/or ceramic powders by applying thermal energy [152]. Also defined by the International Standards Organization (ISO) as “the thermal treatment of a powder or compact at temperature below the melting point of the main constituent, for the purpose of increasing its strength by bonding together the particles” [149]. The basic phenomena occurring during this process are: densification and grain growth. Nowadays, sintering is used to fabricate parts of all kinds.

The sintering temperature  $T$  is usually in the range  $\frac{T_M}{2} < T < \frac{19}{20}T_M$  [153], where  $T_M$  is the melting temperature of the sintered material.

The variables affecting the final sintered product can be classified into two types:

Variables related to the material (powder): this type can also be divided to two groups:

1. Geometrical: includes shape, size and size distribution, state of agglomeration, melting temperature, and mixedness in the case of more than one type of powder, etc.
2. Chemistry: Homogeneity, composition, purity, etc.

The material variables are more difficult to control, but have a significant effect on the final product.

Variables related to sintering condition: include temperature, pressure, pressing and sintering times, sintering atmosphere, rate of heating and cooling, etc. These parameters must be controlled with sufficient accuracy.

#### **2.14.2 Densification and coarsening**

Figure 2.30 shows the two basic phenomena that occur during sintering, densification and coarsening.

Densification: act of reducing porosity in a sample thereby making it more dense.

Coarsening: is inherent in all systems consisting of grain of varying size; during heating the grains coalesce and coarsen by diffusion, such that the smaller grains are consumed by the larger grains as the system moves toward a lower interfacial energy [153].

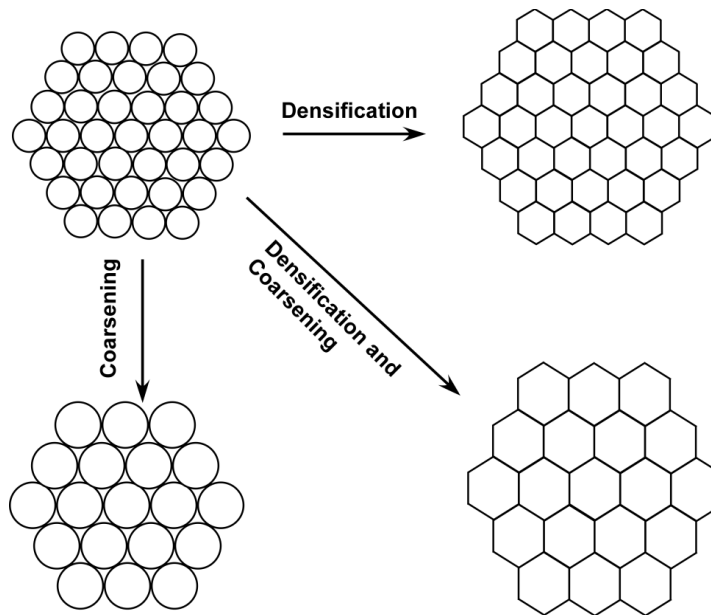


Figure 2.30: Basic phenomena occurring during sintering [152].

### 2.14.3 Sintering stages

The evolution of a densifying compact can be separated into an initial stage, intermediate stage, and a final stage [154]. Figure 2.31 shows the evolution of the sintered sample relative density at the different sintering stages.

Initial stage: comprises neck growth along the grain boundary between adjacent particles.

Intermediate stage: occurs when the necks between the adjacent particles are no longer small compared to the particle radii. The porosity is mainly from the through-pores (interconnected pores) extending through the whole compact thickness (relative density up to 93%).

Final stage: occurs when porosity is isolated and placed at multiple particle junctions (relative density > 93 %).

Figure 2.32 show the different changes occurring at each sintering stage in the case of a two spherical grains.

To obtain a porous product, sintering needs to be terminated somewhere in the intermediate stage.

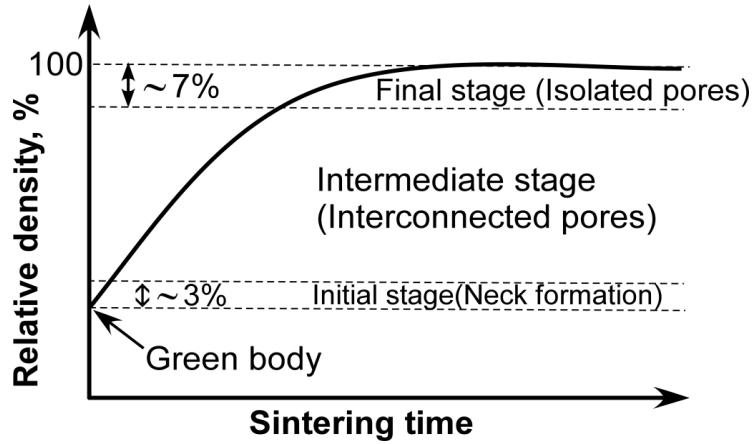


Figure 2.31: Rate of Densification in the three stages of sintering.

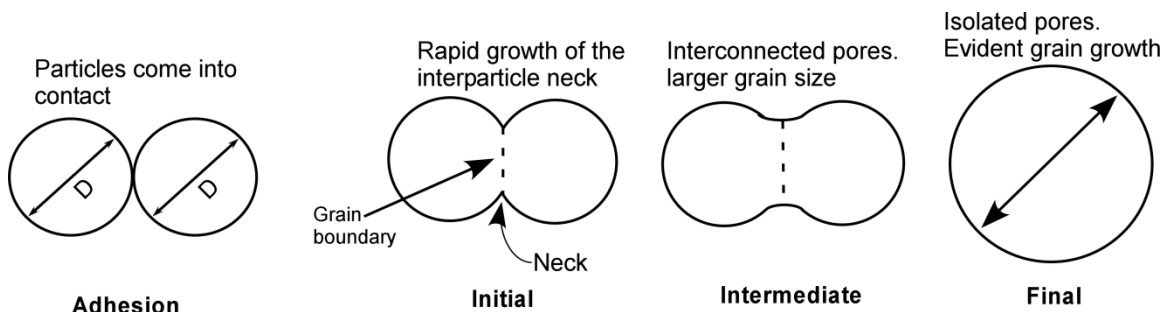


Figure 2.32: A schematic diagram of the grain structure changes during sintering for spherical shape grain.

### 2.15 Effect of sintering variables

In general, the densification or sintering rate is increased by increasing the sintering pressure and/or temperature or by decreasing the powder size [152]. Figure 2.33 shows a schematic of the effect of the sintering process parameters on the powder densification.

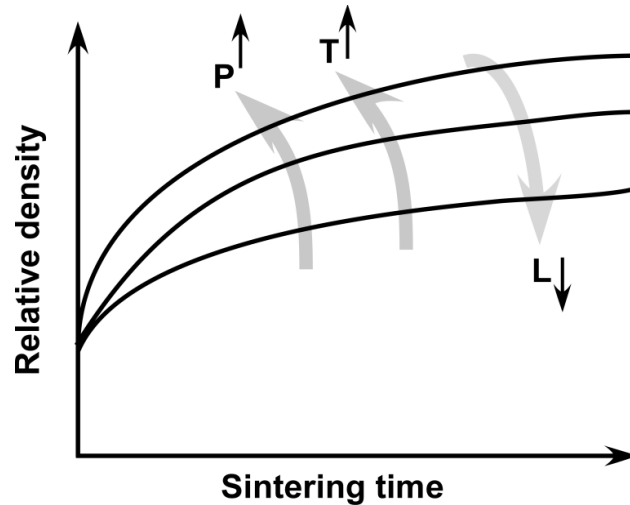


Figure 2.33: Effect of sintering conditions on the relative density ( $L$ : grain size,  $T$ : temperature,  $P$ : pressure) [152].

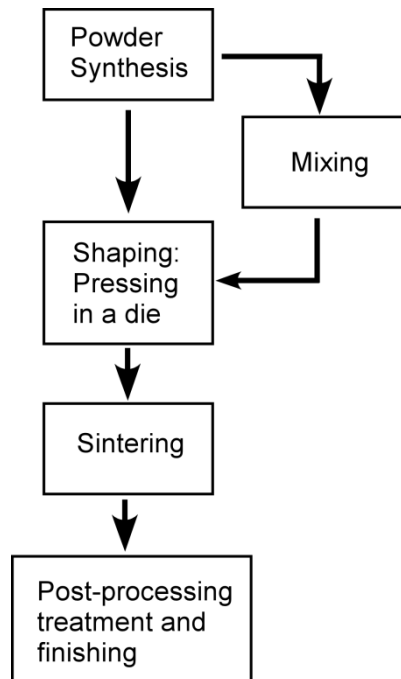


Figure 2.34: General fabrication pattern of sintered parts.

### 2.16 Sintering procedure

The next step after preparing the powder is pressing; the powder is poured in a die and pressed to form the green body (unsintered product). If sintering (thermal treatment) is performed while the powder is being pressed, the process is called pressure sintering, otherwise the compact sample is sintered in a furnace and the process is called



pressureless sintering. Figure 2.34 shows a diagram of the main steps followed during the fabrication of a sintered part.

Extra steps can be added depending on the final product, examples of these steps are:

Mixing: comes after powder preparation in the case of more than one kind of powder. It involves mixing of the different powders to form a homogeneous mixture.

Post-processing and finishing: includes cutting and polishing of the sintered part.

Hot re-pressing: Used to improve the mechanical properties of the sintered part.

Plating, coating, mechanical treatment, etc.

### **2.17 Tangential Momentum accommodation coefficient (TMAC)**

The Knudsen pump will generate a sufficient flow rate when the flow regime is either transitional or free molecular. At these flow regimes the mean free path,  $\lambda$ , of the gas molecules is comparable or larger than the channel characteristic length,  $H$ . Furthermore, because of the small size of the channel, the ratio of surface area to volume increases significantly. Therefore effect of the channel wall properties such as the wall temperature, gas/wall interactions and roughness needs to be taken into account when computing flow rate and pressure. One of the parameters used in studying and understanding the gas-wall interactions in gas microflows is the Tangential Momentum Accommodation Coefficients (TMAC), which has a tangential and a normal components. It was first introduced by Maxwell, and it is defined as the fraction of gas molecules reflected diffusively from a solid surface.

## 2.18 Definition of the TMAC

The concept of interaction of gas molecules with a solid surface was started by Maxwell [18]. At first Maxwell assumed the surface to be fixed, smooth, and perfectly elastic. In this case any molecule striking the surface will have its normal component reversed while the other components are not altered. In other words, every molecule will be reflected specularly. A lot experimental evidences showed that this simple model is unrealistic; most of engineering surfaces are not smooth. Therefore the specular reflection model can only be used for the aim of comparison and not to extract useful information about the system. The second type of reflection that Maxwell assumed is the diffusive reflection. He stated that some molecules impinging on the surface are first captured then can be re-emitted in any direction with equal probability.

The mathematical expression of the TMAC in terms of the tangential momentum is:

$$\sigma = \frac{\tau_i - \tau_r}{\tau_i - \tau_w} \quad (2.56)$$

where ( $\tau_i$ ) is the tangential momentum of the incoming molecules, and ( $\tau_r$ ) is the tangential momentum of reflected molecules.  $\tau_w$  is the channel wall momentum, and is equal to zero for stationary walls.

The two limit values of the TMAC are shown in figure 2.35:

- Specular reflection  $\sigma = 0$ , the tangential velocity of the molecules reflected from the walls is unchanged  $\tau_i = \tau_r$ . The normal component of the velocity is reversed due to the normal momentum transfer. The impinging molecules are reflected from the surface like a light beam from a mirror.
- Diffuse reflection  $\sigma = 1$ , in this case the incoming molecules stays on the wall for a sufficient time, then reflected from the wall with zero average tangential velocity

$\tau_r=0$  and a temperature equal to that of the wall. Molecules are assumed to be completely accommodated to the wall.

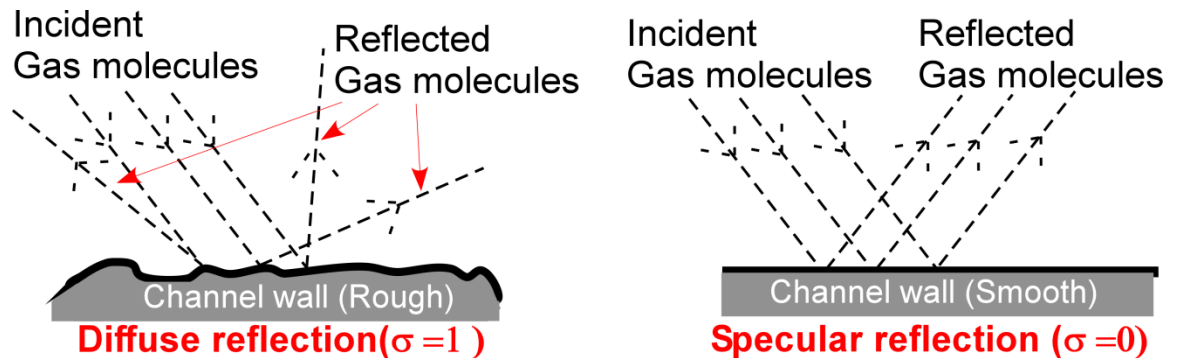


Figure 2.35: Schematic showing the behavior of the gas molecules at the limit cases of the TMAC values.

The model suggested by Knudsen is somewhat similar to Maxwell model; the only difference is in the temperature of the re-emitted molecules which is not necessarily equal to the channel wall temperature.

Another model describing the gas/wall interaction was introduced by Hulbert-Sherman-Nocilla [155, 156]. The model assumes the reflected molecules as if coming from a virtual gas at a given temperature and a velocity. The temperature magnitude is adjustable and the velocity is symmetrical to the normal to the wall. Diffusive reflection occurs when the reflected molecules have a zero temperature and a velocity equal in magnitude to the incoming ones. The other limit case (specular reflection with full accommodation) occurs when the reflected molecules have zero velocity and the molecules are reflected with a temperature equal to the wall temperature. The model also permits the expression of the temperature and velocity in terms of the angle of incidence.

Thermal accommodation coefficient [157] is another parameters widely used to quantify the accommodation extent of molecules to the wall temperature. Its expression is

similar to the previously mentioned TMAC except that energy per unit surface area per unit time is used instead of the momentum.

## 2.19 Methods for measuring the TMAC

In this section, different approaches available in the literature for measuring the TMAC are reviewed.

### 2.19.1 The Millikan Oil drop experiments

Millikan determined the size of the charge on a single electron; he put a charge on a tiny drop of oil and measured the magnitude of the electrical field to stop the oil drop from falling. When a drop is suspended, its  $m.g$  is exactly equal to the electrostatic force  $q.E$  where  $m$  is the oil mass,  $g$  is the acceleration due to gravity,  $q$  is the charge on the drop, and  $E$  is the electrical field. Millikan noticed during his experiments that the smaller drops fell more rapidly than expected by Stokes' law, due to the unavailability of theoretical work on the motion of spherical droplets in gaseous mediums to correct the Stokes' law equation and suggested to add an empirical correction term which will take into account the gas medium inhomogeneities. The new expressions of Stokes' law,  $X$ , and the oil drop velocity,  $v$ , are given by [158]:

$$v = \frac{2}{9} \frac{a^2 (\rho_{drop} - \rho_{gas}) g}{\mu} \left( 1 + A \frac{\lambda}{a_{drop}} \right) \quad (2.57)$$

$$X = 6\pi\mu a v \left( 1 + A \frac{\lambda}{a} \right)^{-1} \quad (2.58)$$

where  $\rho$  is the density,  $\mu$  is the viscosity of the surrounding gas,  $\lambda$  is the gas mean free path,  $a_{drop}$  is the drop radius, and  $A$  is a constant which can be determined experimentally. Millikan derived an expression which relates  $A$  and  $f$ , the amount of molecules reflected diffusively as defined by Maxwell [18]. The expression is given by:

$$f = \frac{1.4008}{A + 0.7004} \quad (2.59)$$

$A$  and  $f$  values reported by Millikan for different gas-drop combinations are shown in table 2.4. Next, we will discuss the rotating cylinder method that Millikan employed to compare the measured  $f$  values.

Table 2.4: Values of  $A$  and  $f$  obtained by Millikan using different gas-liquid drop or surface combinations.

Gas- liquid drop combination	$A$	$f$
Air-machined brass surface or old shellac surface	0.70	1.00
CO <sub>2</sub> -machined brass surface or old shellac surface	0.70	1.00
Air-Mercury	0.70	1.00
Air-Oil	0.864	0.895
CO <sub>2</sub> -Oil	0.823	0.9195
Hydrogen-Oil	0.813	0.9256
Air-Glass (Warburg-Knudsen)	0.872	0.8908
Helium- Oil	0.901	0.8747
Air-Fresh shellac	1.07	0.7912

Some of the  $A$  values shown in table 2.4 are obtained by averaging the values obtained by different researchers who used the same set-up as Millikan at different times and conditions or some other techniques [158].

### 2.19.2 Rotating cylinder method

In order to compare the obtained values of  $A$ , and  $f$ , Millikan decided to use the constant deflection method which he believed to be the most accurate technique at that time.

The experimental set-up, used by Millikan [158], Stacy [159], and Van Dyke [160], consisted of a two concentric cylinders with radii of  $a$  and  $b$  ( $a=5.3412$  cm,

$b=6.0632$  cm) and length  $L$  (24.88 cm), the outer cylinder is rotating at an angular velocity,  $\omega$ , while the inner one is fix. A more detailed description of the experimental set-up is given at [160]. Millikan calculated the torsional moment due to the viscous drag acting on the cylindrical surface of gas, for the case of slip, and determined the gas viscosity,  $\eta$ . In order to calculate the coefficient of slip,  $\zeta$ , it is sufficient to measure the deflection angles  $\theta$  and  $\theta'$  using the following equation [158]:

$$\zeta = \left( \frac{\eta}{\eta_a} - 1 \right) \frac{1}{K} = \left( \frac{\theta}{\theta'} - 1 \right) \frac{1}{K} \quad (2.60)$$

where

$$\eta = \frac{\pi I (b^2 - a^2) \theta}{4t^2 L a^2 b^2 \omega_1 \left[ 1 + 2\zeta \frac{a^3 + b^3}{ab(b^2 - a^2)} \right]} \quad (2.61)$$

$$K = 2 \frac{a^3 + b^3}{ab(b^2 - a^2)} \quad (2.62)$$

$I$  and  $t$  and are the moment of inertia and its half period of vacuum.  $\theta'$  is measured at a pressure where the second term of equation (2.61) is neglected.  $\zeta$  is related to  $A$  by:

$$\zeta = A\lambda \quad (2.63)$$

where  $\lambda$  is the gas mean free path. When the cylindrical surfaces were coated with the same oil used by Millikan in the oil drop experiment, the  $A$  values were in good agreement for both air and CO<sub>2</sub>.

### 2.19.3 Spinning rotor gauge method

The spinning rotor gauge can be used to measure the viscosity, velocity slip, and the TMAC [161]. It consists of a steel sphere (the rotor) which is magnetically levitated within a closed tube and is accelerated to a given rotational frequency. Once the driving force for the rotational movement is removed, the sphere starts to decelerate due to the

drag force from the surrounding gas [161-163]. The sphere deceleration rate as a function of the pressure is measured and the TMAC value,  $\alpha$ , is calculated using the following equation [161]:

$$c_m = \frac{2 - \alpha}{\alpha} \left[ (1 - \alpha) \frac{\sqrt{\pi}}{2} + (0.9875)\alpha \right] \quad (2.64)$$

where  $c_m$  is the velocity slip coefficient determined from the slope of the linear plot of the torque on the rotor (sphere) versus the inverse pressure ( $1/p$ ). Table 2.5 shows some of the obtained TMAC values from different research groups using the spinning rotor method. The TMAC values in the last row were calculated by Agrawal [163] using tabulated data in the following articles [164, 165].

Table 2.5: Obtained TMAC values from different research groups using the spinning rotor method.

Gas type	TMAC value	References
Ar	0.9105	[161]
He	0.9542	
Kr	0.933	
He	1.033	[166]
Ne	1.008	
Ar	1.029	
Kr	1.035	
Xe	1.039	
He	0.941	
Ar	0.8968	
Kr	0.8706	
N <sub>2</sub>	0.86	
Methane	1.04	

#### 2.19.4 Molecular beam techniques

Molecular beam techniques can be used to simulate satellite flights through subjecting a specific surface to a beam of gas having the velocity of the satellite in the free molecular flow regime. In this technique, supersonic beams of gases is directed at

the surface of a flat plate at different angles of incidence, the forces are then measured by means of beam microbalance and used to determine the normal and tangential momentum accommodation coefficient. Early work with this method was conducted by Omelik [167] who tested five types of surfaces under ultrahigh vacuum for better control of the beam angles of approach. The working fluid was nitrogen and the flow regime was free molecular ( $Kn=1000$ ). The surface size was 5 by 5 cm<sup>2</sup>. Low TMAC values were reported in the case of glass for low angle of incidence, values of TMAC larger than 1, which correspond to an inverse reflection of molecules, were obtained with glass cloth surfaces.

Rettner [168] used the same technique with beams of N<sub>2</sub> to measure the TMAC value of lubricated Pt surface, sputtered carbon films, and glass. The reported accommodation coefficient is close to unity indicating a full accommodation at the surface.

Several other research groups have used the molecular beam techniques to measure the TMAC for different surfaces at different angles of incidence; their results can be found in the following references [169-171].

### **2.19.5 Flow through microchannels**

This technique involves the measurement of flow, through microchannels, to determine the main quantities such as pressure, temperature, and flow rate. These quantities are then fit or compared to models derived either theoretically using the Navier-Stokes equation or numerically from molecular dynamic, Direct Simulation Monte Carlo (DSMC), or a simplified form of the Boltzmann equation.



Arkilic used the slip flow solution to the Navier-Stokes equation to extract the TMAC for argon and nitrogen experimental flows through micro-machined channels. The Navier-Stokes equation is solved using the first order boundary condition suggested by Maxwell [172]. The experimental mass flow rate,  $\dot{M}$ , is normalized by the difference in the square of the inlet and outlet pressure,  $P_{in}^2 - P_{out}^2$  (Equation (2.65)).

$$\frac{\dot{M}}{P_{in}^2 - P_{out}^2} = \frac{H^3W}{24\mu LRT} + \frac{H^3W}{4\mu LRT} \frac{2-\alpha}{\alpha} Kn_o P_{out} \frac{1}{P_{av}} \quad (2.65)$$

where  $H$ ,  $W$ , and  $L$  are the microchannel height, width, and length, respectively.  $T$  is the absolute temperature,  $P_{av}$  is the inlet and outlet average pressure,  $\mu$  is the gas viscosity,  $R$  is the specific gas constant,  $\alpha$  is the TMAC value, and  $Kn_o$  is the Knudsen number defined at the channel outlet.

A different version of equation (2.65) in the case of circular channel is used in chapter 5 to compute the theoretical mass flow rate through Whatman track-etch membranes [173].

$$\dot{M} = \frac{\pi Na^4}{24\mu LRT} \left( \left( \frac{P_{out}}{P_{in}} \right)^2 - 1 + 12Kn\sigma \left( \frac{P_{out}}{P_{in}} - 1 \right) \right) \quad (2.66)$$

As shown from equation (2.65), The TMAC value ( $\alpha$ ) is determined from the slope of the linear fit of  $\frac{\dot{M}}{P_{in}^2 - P_{out}^2}$  versus  $\frac{1}{P_{av}}$ . Arkilic reported values of  $\alpha$  equal to 0.8 and 0.88 for argon and nitrogen respectively using a micromachined channel 1.33  $\mu\text{m}$  high, 52.25  $\mu\text{m}$  wide, and 7500  $\mu\text{m}$  long [174, 175].

A series of other slip models have been investigated by different research groups [174, 176-178]. Colin [179] used a second order model for slip flow in rectangular microchannels giving a higher precision for Knudsen numbers up to 0.25. Colin reported

an  $\alpha$  value of 0.93 for nitrogen and helium. The channels were machined with a Deep Reactive Ion etching with depth from 0.5  $\mu\text{m}$  to 4.5  $\mu\text{m}$ .

Hsieh [180] studied gas flow through microchannel (200  $\mu\text{m}$  by 50  $\mu\text{m}$ ) with  $\text{N}_2$  as the working gas. The TMAC was calculated from the slope of  $\frac{\dot{M}}{P_{in} - P_{out}}$  versus  $P_{out}$ , the values were between 0.3 and 0.7 for a Knudsen number between 0.001 and 0.02. Air flow through microchannels have also been investigated, the reported TMAC value 0.85 with a Knudsen number of 0.0017 [181]. Gas flow (Argon, Nitrogen, and Oxygen) measurements through carbon nanotube with 200 nm diameter showed small values of TMAC,  $0.52 \pm 0.1$  has been reported for the three gases [182].

For  $Kn \ll 1$  the gas flow through nanoporous membranes can be calculated with the Hagen-Poiseuille equation assuming the flow to be laminar [97].

$$\dot{M}_{Viscous} = \frac{\Delta P \pi \alpha^4 N P_{av}}{8 \mu R T L} \quad (2.67)$$

The previous equation is used in chapter 5 to calculate the mass flow rate through Whatman membranes.

When the mean free path of the gas is comparable to the pore size of the membrane, momentum transfers between different gas molecules and between gas molecules and the channel wall are comparable. In this case, gas flow occurs by the combined effects of viscous and Knudsen mechanisms. The following equation is used to determine the flow rate in the transitional flow regime [97]:

$$\dot{M}_{Transitional} = \frac{\Delta P \pi \alpha^4 N P_{av}}{8 \mu R T L} + \frac{2}{3} \frac{\Delta P \pi \alpha^3 N}{L} \sqrt{\frac{8}{R T \pi}} \quad (2.68)$$

The aforementioned literature review of flow through microchannels is concerned with hydrodynamic and slip flow regimes, it may be extended a little to the transitional flow regime provided that the right boundary conditions are used. The transitional and near free molecular flow regimes are complicated to model because the Boltzmann equation (BE) must be solved. A huge amount of work and effort has been done to simplify and solve the BE and extract information about the flow [92].

Graur *et al.*[183, 184] determined the TMAC value for rectangular and circular microchannels using the flow rate data. Experimental pressure and mass flow rate data were used in the following expression to obtain the dimensionless flow rate  $G$ :

$$G_{circular} = \frac{L\sqrt{2RT}}{\pi a^3 (P_{in} - P_{out})} \dot{M} \quad (2.69)$$

$$G_{rectangular} = \frac{L\sqrt{2RT}}{WH^2 (P_{in} - P_{out})} \dot{M} \quad (2.70)$$

$$\delta = \frac{\sqrt{\pi}}{2} \frac{1}{Kn} \quad (2.71)$$

where  $a$  is the channel radius in the case of circular channel,  $W$ , and  $H$  are the width and height of the rectangular channel case,  $L$  is the channel length,  $\dot{M}$  is the mass flow rate,  $T$  is the absolute temperature,  $R$  is the specific gas constant,  $P_{in}$  and  $P_{out}$  are the pressure at the inlet and outlet of the channel respectively. The  $G$  values were then plotted against the rarefaction parameter,  $\delta$ , along with the numerical solution  $G$  of the Bhatnagar-Gross-Krook (BGK) equation for different TMAC values. The reported TMAC values based on visual graphic comparison are about 1 for helium, 0.96 for nitrogen, and 0.94 for argon in the case of rectangular channel. The results are obtained for a circular microchannel for helium and argon.

Thermal transpiration flow through microchannel can also be used to determine the TMAC value, once the mass flow rate,  $\dot{M}$ , and absolute temperature at both sides of the channel,  $T_{in}$  and  $T_{out}$ , are measured. The following expression, which takes into account the thermal transpiration phenomenon, can be used to calculate the  $G$  values [103]:

$$G = \frac{LT_{av}\sqrt{2RT_{av}}}{\pi a^3 P_1(T_{out} - T_{in})} \dot{M} \quad (2.72)$$

where  $P_1$  is the cold side pressure.  $T_{av}$  is the average temperature. These  $G$  values can then be plotted versus  $\delta$  and graphically compared to numerically obtained ones to extract the TMAC values. In the case of rectangular channel, the quantity  $\pi a^3$  in equation (2.72) is replaced by  $WH^2$ . The following equations are obtained from fitting  $G$  values, obtained by solving the Boltzmann Equation numerically, versus the rarefaction parameter,  $\delta$ , and the TMAC value,  $\alpha$  [92, 185].

$$\alpha = \frac{4.01433 + 0.204556\delta - G}{2.67281} \quad (2.73)$$

$$\alpha = \frac{4.06709 + 0.121024\delta + 0.009663\delta^2 - G}{2.67281} \quad (2.74)$$

It is also possible to evaluate the TMAC value when the channel is subject to both pressure and temperature gradients, the mass flow rate expression derived by Sharipov, previously discussed in the thermal transpiration models section, can be used.

$$\dot{M} = \frac{\pi a^3 P_{av}}{L} \sqrt{\frac{m}{2k_B T_{av}}} \left[ \frac{\Delta T}{T_{av}} M_t - \frac{\Delta P}{P_{av}} M_p \right] \quad (2.75)$$

Once the equilibrium between the thermal transpiration and pressure driven flow is established, the mass flow rate  $\dot{M}$  is zero, setting equation (2.75) equal to zero, we obtain:

$$\frac{M_t}{M_p} = \frac{\Delta P}{P_{av}} \frac{T_{av}}{\Delta T} \quad (2.76)$$

Once the temperatures and pressures at the inlet and outlet of the channel are measured,  $P$ ,  $T$ ,  $P_{av}$ ,  $T_{av}$ , and  $M_t/M_p$  can be calculated. Determination of the TMAC values is again from the graphical comparison of  $M_t/M_p$  versus with the numerically available one at different TMAC values [101, 103].

**(A) Combination of gas flow and surface flow**

As the membrane pore radii become smaller, specifically, the tube dimension is comparable to the mean free path of gas molecules, the surface transport becomes about equal to the gas transport [186, 187]. For this reason, we will use a flow rate expression which has a surface term and a gas flow term.

In general, the steady state transport equation reported by Sears [187] is given by:

$$\dot{n} = -\Theta D_s \frac{d\sigma}{dx} - \frac{16}{3} \frac{A^2}{\Theta (2\pi mk)^{\frac{1}{2}}} \frac{d \left( \frac{p}{T^{\frac{1}{2}}} \right)}{dx} \quad (2.77)$$

where  $\Theta$  is the perimeter of the tube ( $=2\pi a$ ) and  $A$  is its cross-sectional area ( $=\pi a^2$ ),  $D_s$  is the surface diffusion coefficient,  $\dot{n}$  is the net steady state, number of molecules passing through plane at  $x$  position, per unit time,  $m$  is the mass of a molecule,  $k$  is the Boltzmann constant,  $p$  is the pressure,  $T$  is the absolute temperature, and  $\sigma$  is the surface concentration of the adsorbed atoms. The thermal transpiration equilibrium equation (

$\frac{p}{T^2} = \text{constant}$ ) can be obtained from equation (2.77) when the surface flow ( $\Theta D_s \frac{d\sigma}{dx}$ )

and net flow ( $\dot{n}$ ) are zero.

We will be using equation (2.77) and the constant temperature analysis as described in [186] to calculate the mass flow rate for the polycarbonate membranes.

Since surface diffusion is more likely to occur for smaller pores, we will use the experimental data obtained for the smallest membrane (15 nm) in order to calculate the  $K$  value which will be then used to determine the molecular diameter,  $d$ , based on the following equation from the same paper:

$$K = \frac{3\pi^2 \lambda d}{16a^2} \quad (2.78)$$

Once  $d$  is determined for the 15 nm membrane, it will be then used to calculate the  $K$  values for the rest of the membrane sizes. Here we assumed  $d$  to be the same for all membranes because the experimental conditions, membrane material and working gas are kept the same.

Using the following expressions for  $D_s$  and  $\sigma$  respectively [186]:

$$D_s = \frac{1}{4d\sigma} \sqrt{\frac{\pi kT}{2m}} \quad (2.79)$$

$$\sigma = q_z e^{\varepsilon/kT} \left( \frac{h^2}{2\pi m kT} \right) \frac{p}{kT} \quad (2.80)$$

and integrating equation (2.77) between  $x=0, p=p_1$ , and  $x=L, p=p_2$  ( $p_2 > p_1$ ), we get:

$$\dot{n} = -\frac{\Theta}{4d} \left( \frac{\pi kT}{2m} \right)^{1/2} \frac{d \ln p}{dx} - \frac{16}{3} \frac{A^2}{\Theta (2\pi m kT)^{1/2}} \frac{dp}{dx} \quad (2.81)$$

$$\dot{n} = \frac{8}{3} \frac{Aa}{\sqrt{2m\pi kT}} \frac{p_1}{L} \left( K \ln\left(\frac{p_1}{p_2}\right) + \frac{p_1}{p_2} - 1 \right) \quad (2.82)$$

The following mathematical relationship  $\frac{1}{\sigma} \frac{d\sigma}{dx} = \frac{d \ln p}{dx}$  was used to derive equation (2.81).

To calculate the  $K$  value for the 15 nm membrane, the following equation is derived from equation (2.82):

$$K = \frac{\frac{\dot{M}}{8 \frac{NAaM_1}{3 \sqrt{2m\pi kT}} \frac{p_1}{L}} - \frac{p_2}{p_1} + 1}{\ln\left(\frac{p_2}{p_1}\right)} \quad (2.83)$$

where  $\dot{M}$  is the experimental mass flow rate  $M_1$  ( $4.81 \cdot 10^{-26}$  Kg) is the mass of a one gas molecule, and  $N$  is the number of pores.

## 2.20 Parameters affecting the TMAC

From the above discussion on the different methods used to measure the TMAC, it can be inferred that this value changes with surface material and roughness, gas type, Knudsen number, and boundary conditions (slip coefficients) used to fit the experimental data. Shazin *et al.*[188] measured the TMAC on atomically clean silver, clean titanium, and titanium coated by oxygen. It was found that for cleaned surfaces, the TMAC depended on the type of gas being used (0.71 for helium and 0.92 for krypton) while this value was around one for the coated surface (0.96 for helium and 1 for krypton).

Figure 2.36 shows the TMAC variation in the different flow regimes as reported by different research groups [188]. Horizontal lines because the TMAC values were reported for an interval of the Knudsen number. For monoatomic gases, most of the

TMAC values lie between 0.8 and 1.02, in the other hand, Agrawal et al. inferred from data on diatomic gases that the TMAC value decreases with increasing Knudsen number. The following equation, which relates the TMAC value and the Knudsen number, has been inferred by Agrawal.

$$\alpha = 1 - \log(1 + Kn^{0.7}) \quad (2.84)$$

The equation predicts the TMAC values in accordance with the reported measurements in the literature for small Knudsen numbers. For high Knudsen number, the equation predicts a rapid decrease in the TMAC value. Agrawal believes that extra experimental verification is needed in this range of Knudsen numbers [163].

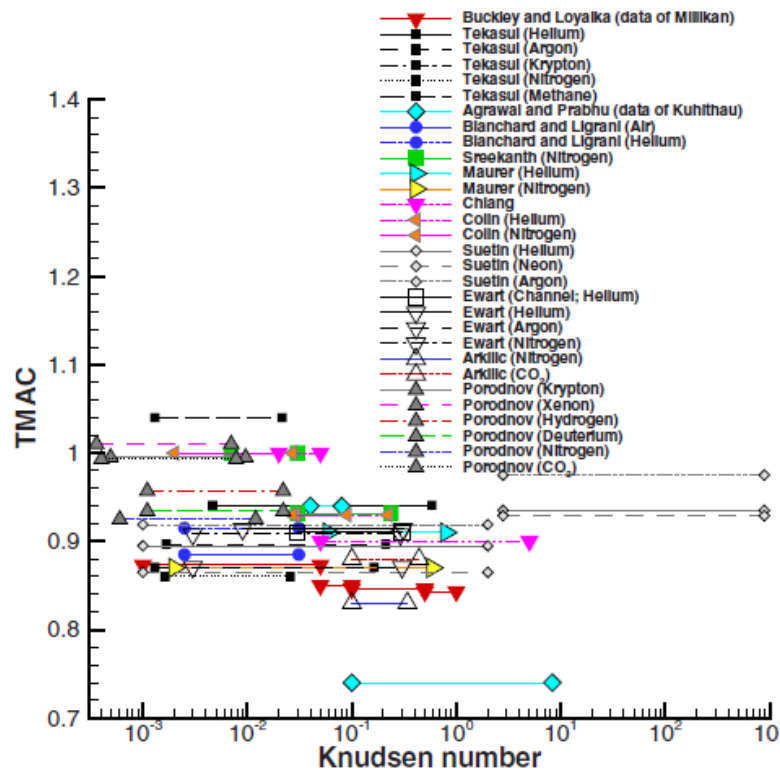


Figure 2.36: Variation of the TMAC in the different flow regimes for a variety of gases as reported by different research groups [188].

In summary, the TMAC value is not always equal to unity; it is the result of interaction among the experiment parameters such as type of gas, pressure, temperature,



and surface type and roughness. A good determination of the TMAC value will help to accurately predict the micro-flow outputs mainly the flow rate and pressure gradient.

## CHAPTER 3: FABRICATION AND CHARACTERIZATION OF THE $\text{Bi}_2\text{Te}_3$ THERMOELECTRIC BASED KNUDSEN PUMP

This chapter describes the methodology, fabrication, characterization, and testing results of the thermoelectric (TE) based Knudsen pump. First, the fabrication and characterization of the p-type  $\text{Bi}_2\text{Te}_3$  powder is discussed. Next a talk about the procedure followed for the fabrication, characterization of the nanoporous TE pellet is explored followed with the corresponding results. The final part deals with the fabrication and testing of the TE based Knudsen pump.

### **3.1 General fabrication process**

Two sintering techniques were investigated for making the nanoporous TE material. Pressure sintering or pressure-assisted sintering [150] (Figure 3.1(left)) in which a pressure is applied while the sample is being sintered. The second technique is pressureless sintering which uses no pressure when the sample is being sintered in a tube furnace [150] (Figure 3.1 (right)). In both procedures, TE pellets are placed in a jar and ball milled to form a powder which is pressed to form the compact sample. If heat is applied to the powder while it is being pressed, the process is called pressure sintering. Otherwise the process is said pressureless sintering and the thermal treatment step is performed in a tube furnace to complete the fabrication.

### 3.2 Method for powder preparation

Commercial high quality p-type  $\text{Bi}_2\text{Te}_3$  pellets (Crystal Ltd Russia), grown from a liquid melt and used in TE modules for both cooling and power generation, were used as the starting material for the fabrication of the nanoporous TE samples. Table 3.1 shows the physical properties and dimensions of the starting TE pellets. A VQ-N desktop high energy vibratory ball mill (Figure 3.2) manufactured by Across International (Berkeley heights, NJ) was used in the grinding experiments. It has higher impact energy created by three dimensional movements, e.g. rotation, vibration and oscillation with a frequency of 1200 RPM. The ball mill can be used in either dry or wet method to mill materials, mix all kinds of solids, and suspended liquids. It has an external programmable timer that can be programmed for any value ranging from 1 sec to 999 sec. The ball mill is equipped with a Lid interlock which prevents the mill from running if the lid is not closed.

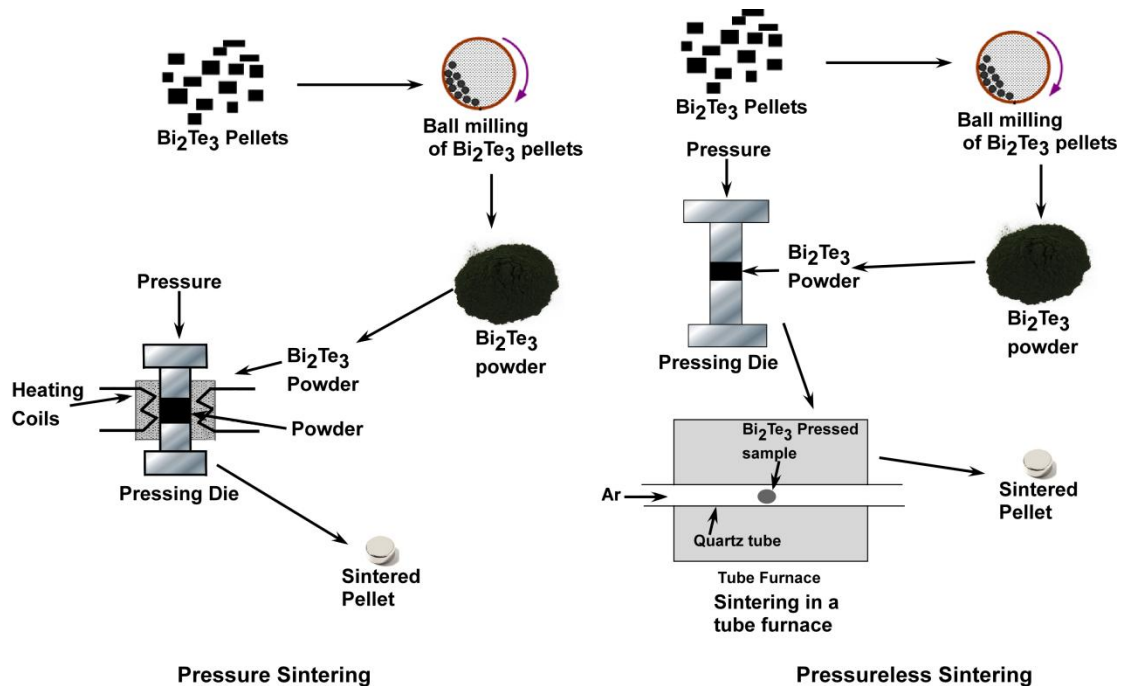


Figure 3.1: Schematic of the fabrication process to create the nanoporous  $\text{Bi}_2\text{Te}_3$  TE material used in the bi-directional Knudsen pump. Commercial grade doped  $\text{Bi}_2\text{Te}_3$  is ball milled to create a nanopowder, which is then sintered in a die press to obtain the final pellet.

The jar (Figure 3.2), containing the material to grind, is made out of stainless steel material, has a volume of 80 ml, has a barbed fitting for pumping, and is filled with 111 stainless steel spherical balls. 13 balls have a 10 mm diameter and 98 balls have a 6 mm diameter. The three-dimensional rotation is transmitted through a pulley and a belt from a 0.5 HP motor.

Table 3.1: Dimensions and physical properties of the starting TE pellets.

Width (mm)	Height (mm)	Length (mm)	Figure of merit ( $K^{-1}$ )	Electrical conductivity at 300K ( $\Omega.cm$ ) <sup>-1</sup>
1.4	1.4	2.52	$2.97 \cdot 10^{-3}$	890

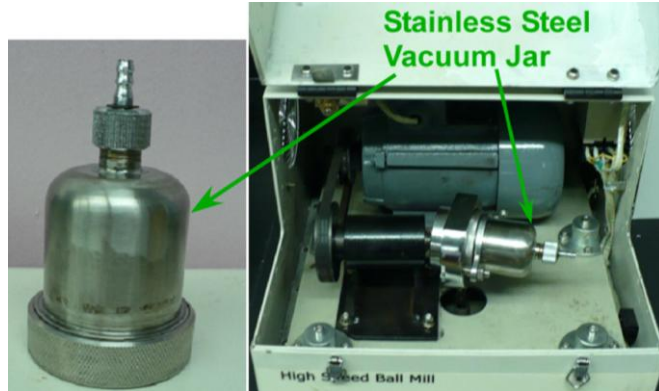


Figure 3.2: High energy vibratory ball used in the experiment (Right). Stainless steel vacuum jar (Left).

The jar was filled with 15 grams of the  $Bi_2Te_3$  TE pellets and pumped, through the barbed fitting, for 10 minutes with a mechanical pump and then mounted in the ball mill machine. The grinding was performed in 15 minutes periods separated by 30 minutes cool-down periods. Milling time was varied from 15 min to 10 hrs. Scanning electron microscopy (SEM) images were taken for each milling time and image processing was conducted to obtain measurement of the grain size using ImageJ analysis software developed by the National Institutes of Health. Similar analysis was conducted on sintered samples in order to measure the pore size.

A SUPRA 35 VP (Carl Zeiss) field-emission scanning electron microscope (FESEM) was used; it has a resolution of 1.3 nm at 15 kV. Real-time images were displayed on a 19" monitor. Stage control and image acquisition was achieved by SmartSEM™ (SEM control graphical user interface) with Windows® XP. The SEM is also coupled to an energy-dispersive X-ray spectroscopy (SEM-EDAX) detector for elemental composition. The accelerating voltage was set to 20 kV. The working distance is 1.5 mm and the detector is Inlens. A small amount of the prepared powder is placed on a double face carbon tape which has been previously mounted onto an SEM specimen holder.

X-ray diffraction (XRD) was also performed on the milled powders as well as the sintered sample using a Bruker X-ray diffractometer, type D8 Discovery which uses Cu  $K\alpha$  radiation.

### **3.3 Method for sintered thermoelectric sample fabrication**

#### **3.3.1 Square and circular die sets**

A 13×13 mm hardened stainless steel square die (Figure 3.3b), with a hardness Rc 62, was used to make square pellets. Its sleeves height and diameter (OD) are 34 mm and 45 mm respectively. It is not equipped with a heater and therefore it can only be used in pressureless sintering. In the other hand, the 13 mm diameter (ID) die (Figure 3.3a), made out of a highly polished stainless steel with a hardness Rc 62, can be used in both pressure and pressureless sintering. The sleeves height and diameter (OD) are 40 mm and 92 mm respectively. The temperature controller allows heating up to 250 °C with a 1 °C step, and an accuracy of +/-1 °C. Temperature is measured with a Pt 100 thermocouple. Both die sets are manufactured by Across International LLC.

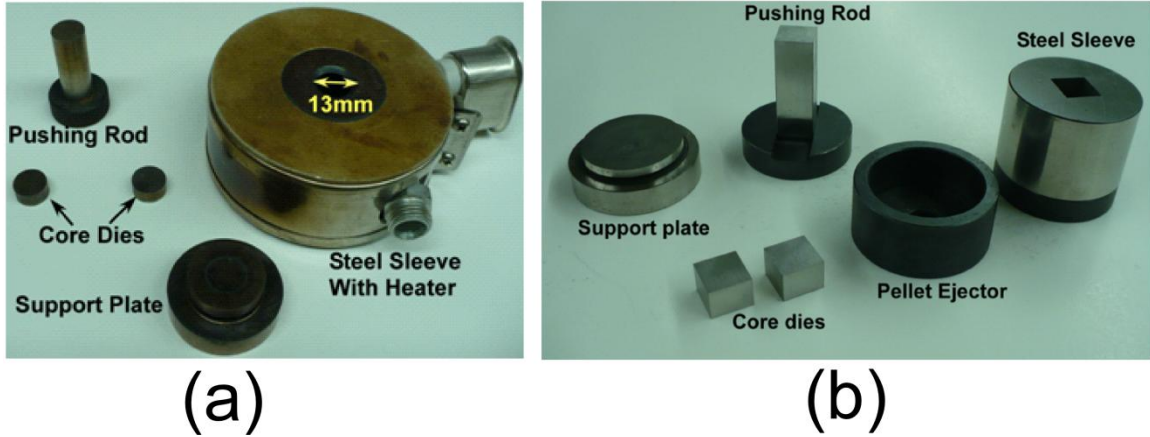


Figure 3.3: 13mm die sets used of the fabrication of the nanoporous  $\text{Bi}_2\text{Te}_3$  sample. (a) Circular heated die set. (b) Square die set.

### 3.3.2 Pellet press

Figure 3.4 shows the hydraulic press, by Across International LLC, used to form the compact samples. It has a built-in hydraulic pump with auto return function. It is designed to work with a variety of die sizes and can sustain up to 15 metric tons of pressure.

### 3.3.3 Sample compaction

To compact the powder, one core die is inserted from the bottom of the steel sleeve which and then placed on the support plate. Next, about 2 grams of powder is poured in the die cavity, the die is gently tapped to level the powder in the die, the second core die is then inserted followed by the pushing rod. The loaded die is taken to the pressing machine and placed and the spinning screw. Once the alignment between the pushing rod and the spinning screw is established, pressure is gradually applied to the die. To dislodge the pellet, first, the pressure is released by slowly turning the bottom knob counter-clockwise. The set-up is left for couple of hours to cool down before the die is removed from the press, the support plate is replaced with the pellet ejector and the whole set is returned back to the pressing machine. Pressure is slowly applied until the pushing

rod pushes the sample and the core die out of the die. Weight and thickness are measured in order to calculate the sample porosity. After each use, all the die parts are cleaned and stored in a desiccator.

### **3.3.4 Tube furnace for sintering compact samples**

After compacting the powder in the square die or in the circular die with heater turned off, the resulting samples are sintered in a tube furnace under running ultra-high purity argon gas. The compact sample was placed on a quartz glass holder and pushed to the center of a one inch diameter quartz tube which was placed in the tube furnace. A maximum of three samples could be loaded into the tube at one time. The set-up is flushed with argon for 10 minutes before ramping the temperature. The furnace temperature was programmed to rise at a rate of 1 °C /min up to 200 °C and held at this temperature for 2 hrs. After that time, the furnace is cooled down to room temperature by the same rate of heating. Sintering time and temperature were varied in order to check the effect of these two parameters on the sintered sample. The argon flow rate was kept at 50 sccm during the whole sintering cycle.

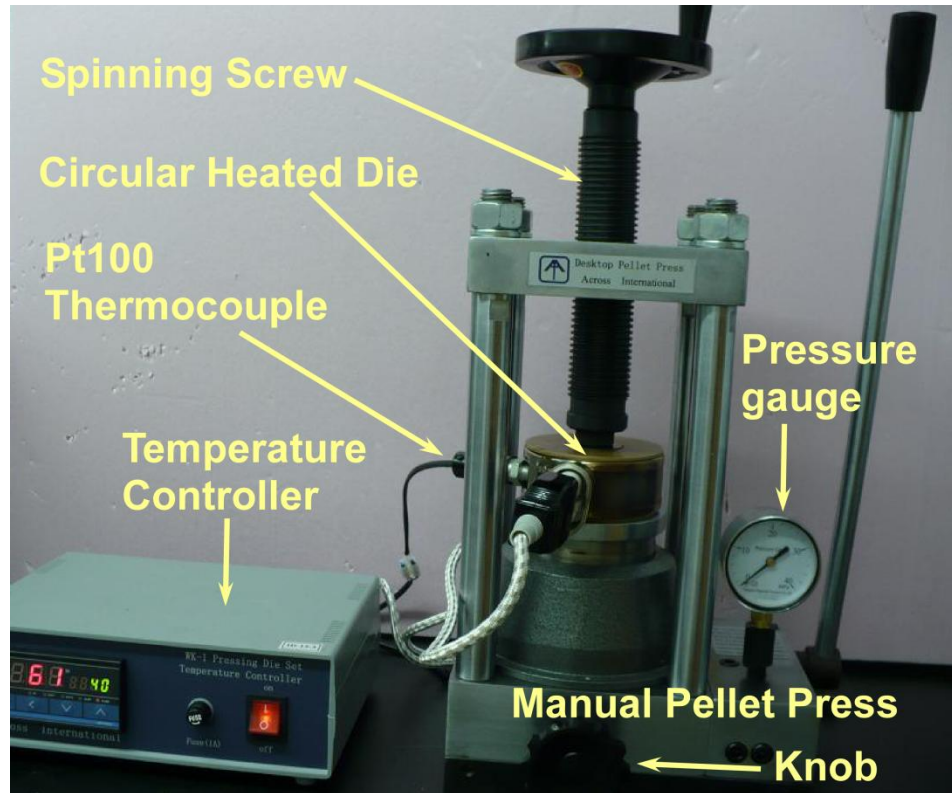


Figure 3.4: 15-Ton manual hydraulic press used to compact the powder.

### 3.4 Method of sintered thermoelectric sample characterization

#### 3.4.1 Temperature distribution along the sintered sample surface

Testing of the heating/cooling properties of the sintered TE sample was performed using InfraScope thermal mapper system (Quantum Focus Instruments Corp, Vista, CA USA). It is an advanced InfraRed (IR) microscope which measures the radiance, in units of  $\text{mW}/\text{cm}^2$ , from target objects. The instrument uses this information to calculate the actual temperature of a target. The system has three main parts: a computer which controls the whole system, liquid nitrogen (LN<sub>2</sub>)-cooled detector with 6 objectives (three Mid Wave IR objective lens (12 $\times$ , 4 $\times$ , 1 $\times$ ) and three optical lenses (2.5 $\times$ , 5 $\times$ , and 25 $\times$ )) and a power unit for heating the sample holder and powering all the different elements of the system (Figure 3.5). The InfraScope is mounted on a vibration isolation table to avoid any measurement degradation due to



vibration. The optical head contains the liquid nitrogen-cooled 215 x 215 element Indium-Antimonide (InSb) infrared focal plane array (IRFPA) detector.

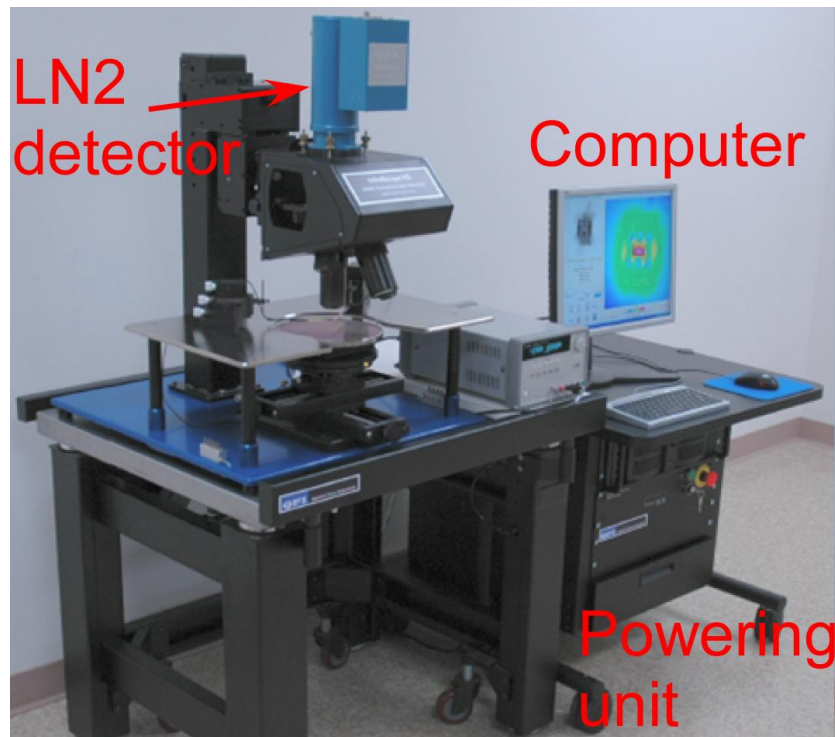


Figure 3.5: Thermal IR microscope used for testing the sintered sample. Source: QFI Corp.

The IR detector requires operation at cryogenic temperature; its Dewar can take up 300 ml of Liquid N<sub>2</sub> and can last for more than 8 hours. The Dewar should be partly filled, perhaps a third or half, then allowed to boil and vent for a few minutes before completely filling it. The sample is carefully fixed to the heated stage using Kapton tape; it should not move or creep, any slight movement can spoil the measurement. The same tape is also used to electrically insulate the sample from the thermal stage (Figure 3.6). For an accurate measurement of the emissivity and use of this value in subsequent measurements, stage and hence sample need to be heated. The best stage temperature is about 60 °C.

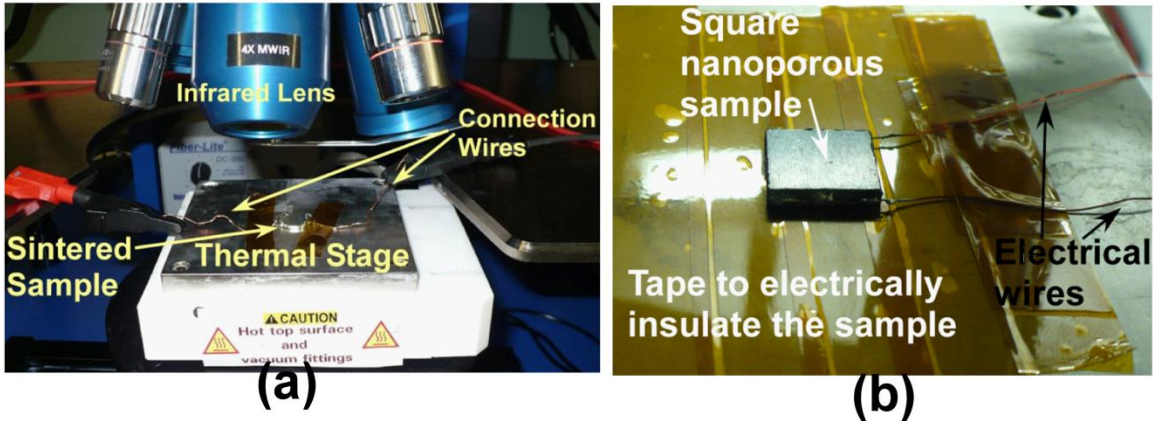


Figure 3.6: A close up view showing the sintered sample sitting on the heated stage along with the connection wires. (a) Circular sample. (b) Square sample. Kapton Tape was used to electrically insulate the sample from the thermal stage.

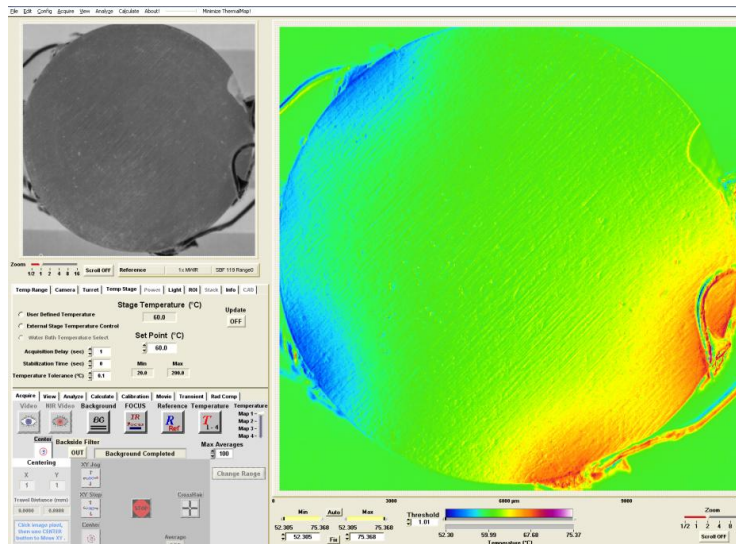


Figure 3.7: Typical temperature distribution along the surface of the sintered circular sample generated with the InfraScope software. Stage is heated to 60°C.

Electrical wires are soldered, along the sintered sample thickness, using a standard lead-based solder made of lead and tin. Voltage is applied to the sample from a Keithley 2400 sourcemeter placed on the isolation table. After launching The InfraScope system software, the system performs a series of initializations and diagnostics with each being tracked and reported within an initialization panel. Objectives are rotated manually. Three steps need to be performed for a true temperature thermal mapping. First, an unpowered Radiance Reference image is acquired. Second, an unpowered temperature

image to check the set-up. Third, a powered temperature image to record the powered device true temperature.

2 methods are possible for exporting screen images from the InfraScope, direct TIF, BMP and PNG image exports from InfraScope using Print Screen technique, and exports to any file format via Paint Shop Pro. Specific regions on the acquired images can be analyzed deeply with the rectangular Region-Of-Interest (ROI) tab, and user defined line trace are also possible. Temperature or emissivity in these regions can be extracted or exported as text files for further analysis. Movies can be captured, and up to 100 sequential frames of temperature images can captured. Figure 3.7 shows the main window of the InfraScope software.

### **3.5 Method for measuring the sintered sample thermoelectric properties**

#### **3.5.1 Seebeck coefficient and electrical resistivity**

The sintered sample was cut to small squares of about 5 mm by 5 mm. A set-up (Figure 3.8) in Dr. Gamini's lab was used to measure the Seebeck coefficient ( $\alpha = -dV/dT$ ) and the electrical resistivity simultaneously. The set-up is capable of measuring thermopower and electrical resistivity at ultra-high vacuum (about  $2 \times 10^{-7}$  Torr). Its main components are the reactor, tube furnace, ceramic heater, turbo pump, and LabVIEW software for data processing. The reactor consists of a 25 cm long quartz tube (20 mm ID) with a  $2^{3/4}$  inch conflate flange (knife-edge flange with a copper gasket for sealing).

Figure 3.9 shows a schematic of the thermopower and electrical resistivity measurement. A Keithley 2410 source meter is used to generate a time dependent heat pulse across the TE sample. Two Keithley 2182 nanovoltmeters were used to measure

the voltage across the two thermocouples for thermopower calculation. Keithley 4200 sourcemeter is used to apply a constant current through the sample for electrical resistivity measurement. The measurement is performed in two parts. A heat pulse is generated across the TE sample and the voltage at two different positions is measured to determine the thermopower using simple analog subtraction [189, 190]. In the second part, a current is run through the sample and voltage is measured permitting calculation of the electrical resistivity. The cycle is repeated several times and the average value for each temperature is recorded.

The square-shaped sample was set on a ceramic holder with one face in contact with a ceramic resistive heater (1.5 x 8 mm Omega). Highly conductive silver paint was used to improve the heat transfer between the sample and the ceramic heater. The same conductive silver paint was also used at the tip of the thermocouples and electrical wires to improve the thermal/electrical contact.

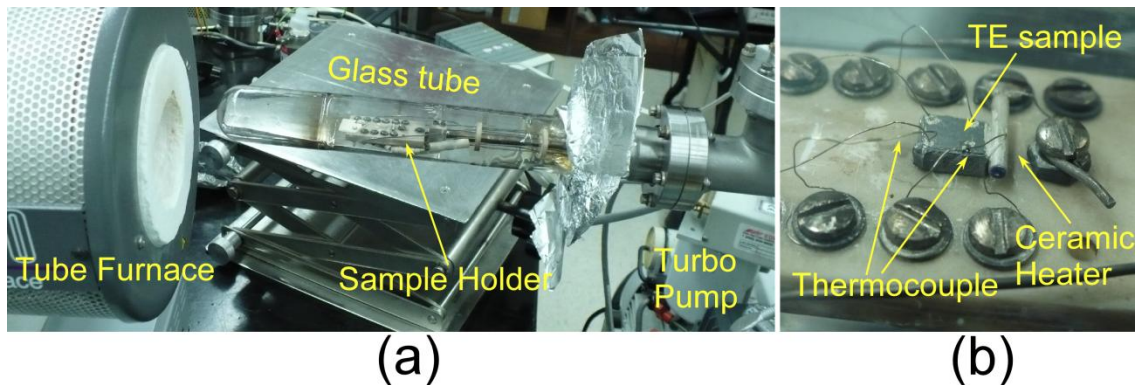
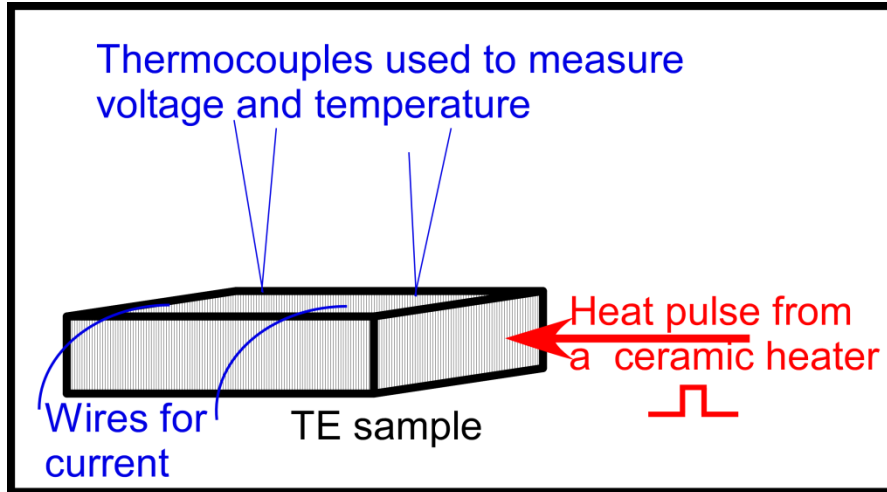


Figure 3.8: (a) Setup used to measure the thermopower and electrical conductivity of the sintered sample. (b) Close up view of the TE sample sitting on the ceramic holder. Thermocouples and electrical wires are glued with silver paste. The ceramic heater induces a temperatures gradient across the sample.



Vacuum chamber  $10^{-7}$ Torr

Figure 3.9: Schematic of the thermopower and electrical resistivity measurement. Temperature gradient induced along the TE sample and measured by two thermocouples is converted to the thermopower. A current is run through the sample and used to measure the electrical resistivity.

### 3.5.2 Thermal conductivity

Laser flash diffusivity was used to measure the sintered sample thermal diffusivity,  $D$ . The latter is related to the thermal conductivity,  $k$ , through the specific heat,  $C_p$ , and the sample density,  $\rho$ , (Equation (3.1)).

$$k = DC_p\rho \quad (3.1)$$

The sintered sample was taken out from the die carefully. In order to calculate the sample density; thickness  $H$ , mass  $m$  were measured and used in the following formula:

$$Density = \frac{4m}{H\pi d^2} \quad (3.2)$$

Diameter  $d$  is 13 mm. in the case of square sample, the following expression is used:

$$Density = \frac{m}{Hw^2} \quad (3.3)$$

$w$  is the width of the square sample (13 mm).

(A) *Specific heat measurement*

Specific heat was measured using a differential Scanning Calorimeter (DSC Q20 TA Instruments) [191]. The sample is subjected to a linear temperature and the heat flow rate as a function of temperature is recorded. Similar procedure is performed on a reference material, Sapphire, under the same conditions. The specific heat as a function of temperature of the sample is determined through comparison of the heat flow rates.

The apparatus was purged with N<sub>2</sub>, and two aluminum pans are placed in the DSC. The temperature of the chamber was increased to 400 °C, at rate of 10 °C /min, and held for 4 min. After that the chamber is cooled down. The same cycle was repeated for the TE sample and the reference sample (Sapphire) and the heat curve (heat flow versus temperature) was recorded. The weight of the TE and reference sample was between 60 and 70 mg.

To minimize the measurement error, the same pans were used in all cycles. The Sapphire data were calibrated using the specific heat capacity data reported by Archer [192]. The following equation was then used to calculate the specific capacity of the TE sample:

$$C_p(s) = C_{p,ref} \frac{H_s W_{ref}}{H_{ref} W_s} \quad (3.4)$$

where  $C_p$ ,  $H$  and  $W$  are the specific heat capacity, vertical displacement between sample holder and sample/ reference thermal curve, and the sample/ reference weight. Ref and s subscripts refer to the reference and TE samples. Collected heat flow data were opened in TA universal analysis software and saved in .xls format for further analysis.

**(B) Thermal diffusivity measurement**

13 mm diameter sample (thickness between 2 and 3 mm) was sent to the Center of Applied Energy Research (CAER) at the University of Kentucky, thermal diffusivity is measured using Netzsch laser flash analyzer (LFA 427 Netzsch Instruments, Inc.). Measurement at different temperatures was carried out to investigate the effect of temperature on thermal diffusivity. Figure 3.10 shows a schematic of the measurement procedure. A short pulse laser beam irradiates the upper surface of the specimen (nanoporous sintered sample), the beam travels through the sample thickness, and a very sensitive temperature sensor records the change of temperature against time. To determine the sample diffusivity, the following equation is used:

$$d_{th} = 0.1388 \frac{h^2}{t_{1/2}} \quad (3.5)$$

$d_{th}$  is the thermal diffusivity,  $h$  is the sample thickness, and  $t_{1/2}$  is half the time before the heat pulse reaches the back surface.

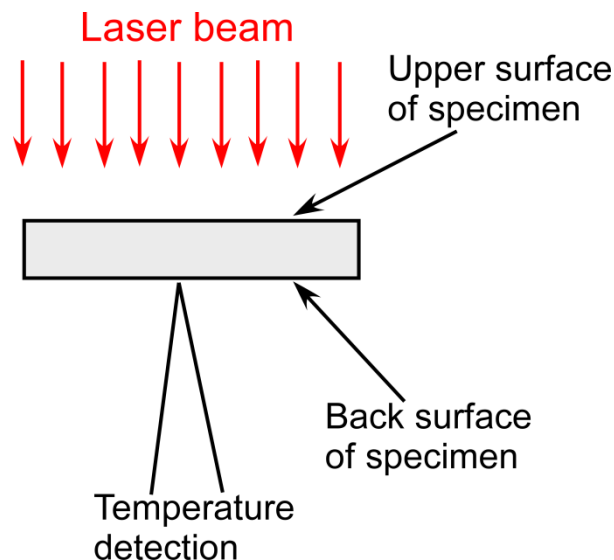


Figure 3.10: Measuring principle of the thermal diffusivity. A laser heats the sample from one side and a detector, on the other side, detects the time-dependent temperature rise.

### 3.6 Procedure to test if the sample is porous

Looking at the SEM image, it was hard to confirm that the pores (dark regions) extend through the whole sample thickness. For this reason, a second testing method was realized; it consisted of mounting the sintered sample through a T-connector to a pressure sensor (Accuracy: 0.02% Full scale, precision: 0.06% Full scale) and syringe (Figure 3.11). The syringe serves as the pressure source for the set-up.

The sample was placed on a plastic holder with a hole in the center connected to the plastic tube; vacuum epoxy glue was applied around the sample perimeter to make sure no leakage occurs. A T-valve (not shown in the figure) was used to isolate the sintered sample from the rest of set-up. This T-valve serves for leak-checking the set-up before starting the experiment.

3 ml Luer Lock Tip plastic syringe with 27G×1/2" (0.21 mm inner diameter) needle was used to apply pressure. Plastic tubes, (0.04 " I.D, 0.07 " O.D) from McMaster-Carr, were used to connect the different elements in the experimental set-up. A digital pressure transducer, Series 6000 by Mensor Corporation, was used to measure pressure at a rate of one measurement per second. Once a pressure is applied, a custom LabVIEW program plots the pressure drop versus time of the set-up.



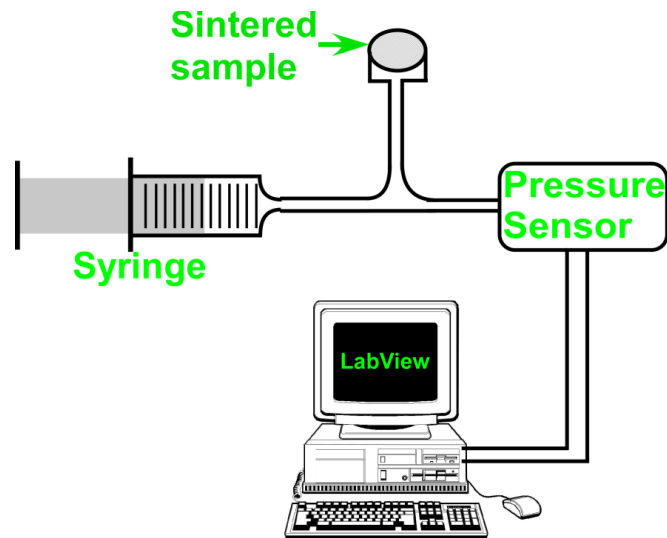


Figure 3.11: A schematic of the set-up used to check for the presence of pores, it consists of a syringe connected through a T-connector to the sample and the pressure sensor.

### 3.7 Method for building the thermoelectric based Knudsen pump

Two geometries, circular and square, of the thermoelectric samples have been fabricated. A small portion of the circular sintered sample was used to build a Knudsen pump, 36 AWG magnet wires were stripped with a sand paper to remove the insulation layer and soldered on the sides of the nanoporous sample. A small amount of non-spill paste rosin soldering flux was added to improve the adhesion. The sample with soldered wires was placed on copper base with a glued plastic tube (0.01 " I.D). Vacuum epoxy glue (*Loctite E 20HP*) was applied all around the sample to avoid any leakage. A plastic tube was connected to the pressure sensor for pressure head measurement.

A different design was adopted for the square shape sintered samples. After soldering the connection 22 AWG wires as explained above, the sample was placed inside a channel machined on a plastic substrate. The channel was drawn using SolidWorks CAD software, the dimensions were 3 cm long, 13 mm wide, and the depth depended on the sample thickness which is related to the amount of pressed powder. The drawing was saved as .igs file and transferred, using a USB, to the computer connected to

the CNC milling machine with VisualMill 6.0 machining program. The machine was set to 3-axis milling and the milling speed was 14000 RPM. The machining was performed in two parts, horizontal rough machining and parallel finishing machining. An End mill (3.175 mm diameter, 38.1 mm long, and 2 flutes) made out of carbide was used for the machining. Complete machining steps are described in appendix B. Epoxy glue was applied on the sides of the channel touching the sample. Figure 3.12 shows an example of a channel machined on  $\frac{1}{4}$  Acrylic plastic. A thin plastic cover, with glued inlet and outlet tubes (0.01 " I.D), was used as a top cover.

To measure the pressure difference that may be obtained with the pump, a digital pressure sensor from Mensor, Inc. (Accuracy: 0.02% Full scale, precision: 0.06% Full scale), with a dead volume of 0.8 cc, is connected to one side of the pump, the other side was open to the atmosphere. A similar pressure sensor was used to monitor the atmospheric pressure .A custom LabVIEW program was written to plot the room pressure, the Knudsen pump pressure, and their difference.

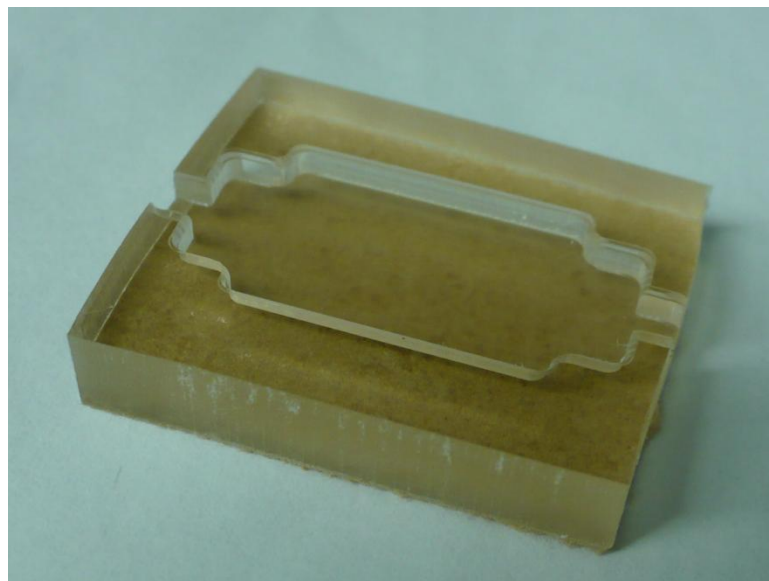


Figure 3.12: 13 mm wide channel machined on Acrylic plastic using 3-axis CNC machine as described in appendix B.

### 3.8 Results of the powder and sintered thermoelectric sample characterization

#### 3.8.1 Powder grain size versus milling time

Figure 3.13 shows SEM images of ball milled powders for 5 and 10 hours under vacuum. Milling is performed under vacuum. Powder agglomeration, which is clearly seen in the SEM images, is due to increased surface energy of the particles. Fine powders possess high surface to volume ratio and thus high surface energy. They tend to agglomerate into particle cluster entities in order to achieve some reduction in surface energy. The grain size was measured using ImageJ software as described in appendix A.

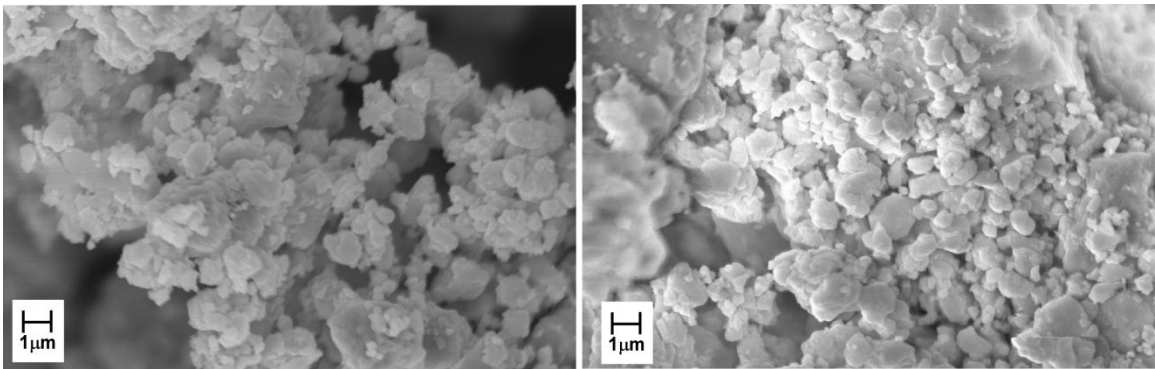


Figure 3.13: SEM images of the ball milled powder at different milling times. (Left) 5 hours. (Right) 10 hours. The starting material is a p-type  $\text{Bi}_2\text{Te}_3$ . Milling performed under vacuum.

Figure 3.14 shows a plot of the  $\text{Bi}_2\text{Te}_3$  grain size against the ball milling time. It can be concluded that as the milling time increases the grain size decreases.

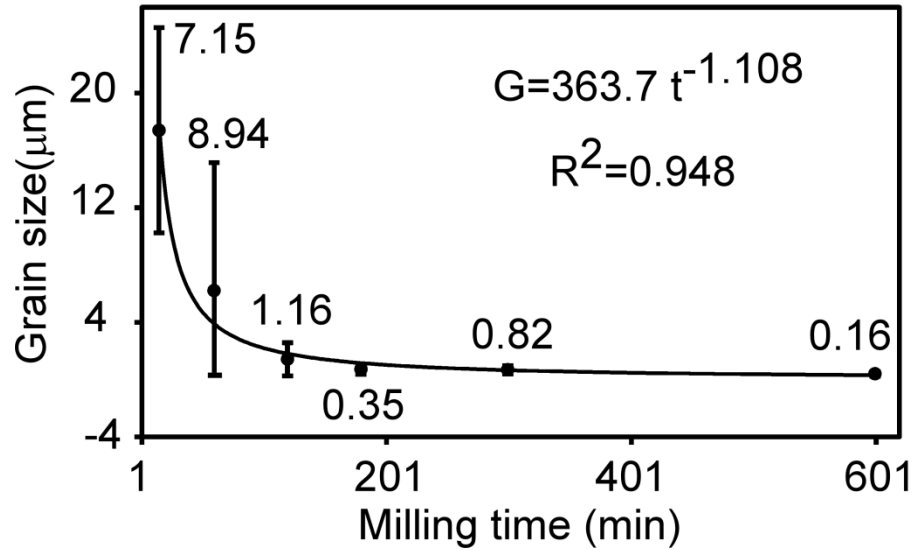


Figure 3.14: Grain size versus the milling time. Dark circles are the measured data and the solid line corresponds to the power fit.  $G$  is the grain size and  $t$  is time. ImageJ software was used to analyze the SEM images and measure the grain size, the procedure is described in appendix A. Numbers above the data points are the standard deviations.

### 3.8.2 Sintering experiments

A series of sintering experiments were conducted on in order to obtain a porous sample. The produced sample was tested for porosity before proceeding to new experimental conditions. Example of a non-porous sample is shown in figure 3.15 .The SEM image clearly shows that the outer surface and inside are not porous.

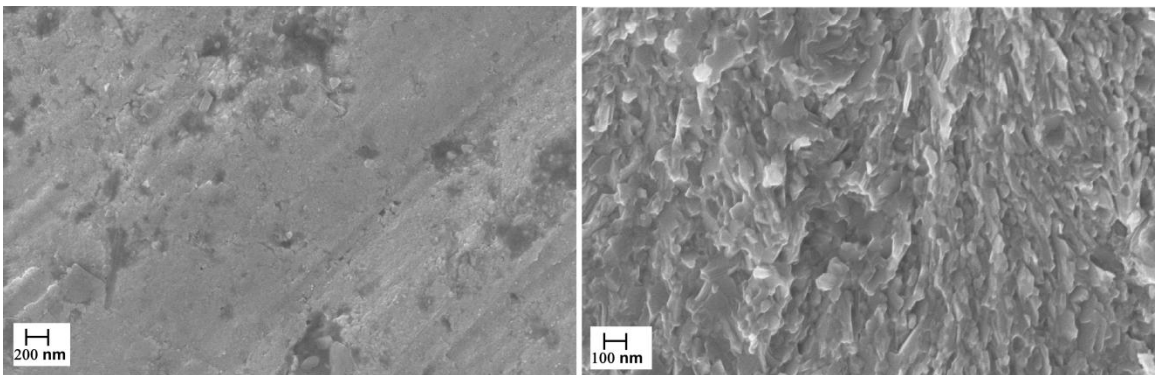


Figure 3.15: SEM image of a non-porous TE sample. (Right)Top face. (Left) Inside.

Table 3.2 summarizes all performed experiemnts. Regardless of the powder milling time, a nanoporous pellet was obtained for a pressure of 6 MPa, sintering

temperature of 150 °C, and two hours sintering time using pressure sintering in the circular die. With the square die, only pressureless sintering is possible, a non-porous sample is obtained for pressures above 12 MPa. 2 grams of powder was used for each experiment.

Table 3.2: Fabricated samples with the corresponding sintering conditions. A nanoporous sample was obtained for a pressure of 6 MPa, sintering temperature of 150 °C, and two hours sintering time using pressure sintering. PS and PSN correspond to pressure sintering and pressureless sintering, respectively.

Sample number	Powder milling time(hrs)	Pressure (MPa)	Pressing time (hrs)	Temperature (°C)	Sintering type	Geometry
#1	3,5, 8	6	2	150	PS	○
#2	3,5,8	10	2	150	PS	○
#3	3,5,8	6	2	175	PS	○
#4	5	6	2	200	PS	○
#5	5	6	2	250	PS	○
#6	5	8	2	250	PS	○
#7	5	10	2	250	PS	○
#8	5	14	2	250	PS	○
#9	5	6	2	300	NPS	○
#10	5	6	2	350	NPS	○
#11	5	6	2	400	NPS	○
#12	3,8	6	1	150	NPS	□
#13	5,10	6	1	200	NPS	□
#14	5,10	6	1	250	NPS	□
#15	5,10	8	1	150	NPS	□
#16	5,10	8	1	200	NPS	□
#17	5,10	8	1	250	NPS	□
#18	5,10	10	1	150	NPS	□
#19	5,10	10	1	200	NPS	□
#20	5,10	10	1	250	NPS	□
#21	5,10	12	1	150	NPS	□
#22	5,10	12	1	200	NPS	□
#23	5,10	12	1	250	NPS	□
#24	5,10	14	1	150	NPS	□
#25	5,10	14	1	200	NPS	□
#26	5,10	14	1	250	NPS	□

### 3.8.3 Thermoelectric sample porosity testing

Figure 3.16 shows an example of the pressure drop of the whole set-up, used to test the sample porosity, for a porous sintered sample. The pressure went down from about 250 kPa to 100 kPa proving that the sample is porous.

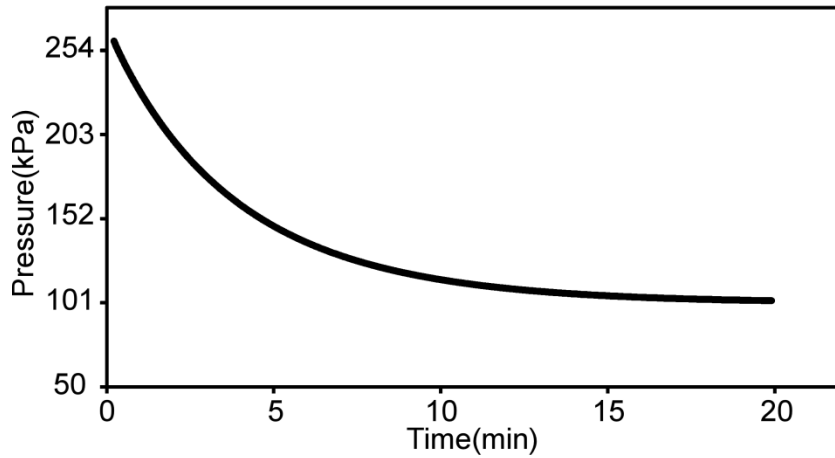


Figure 3.16: The pressure drops in a sealed cavity through the pores for sample#1 demonstrating that the sintered  $\text{Bi}_2\text{Te}_3$  is porous.

Figure 3.17 shows an SEM image for both the circular and square sintered samples. The dark regions are the sub-micron pores through which gas flow. Figure 3.18 shows image of the sintered samples.

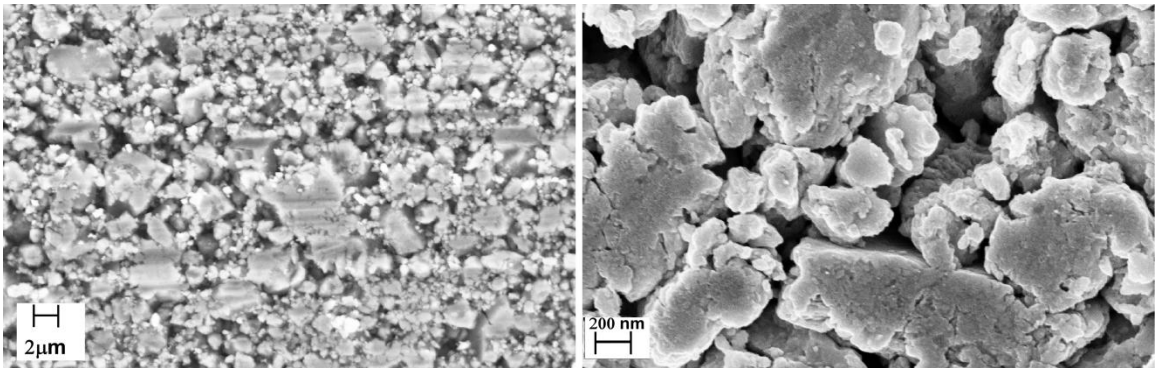


Figure 3.17: SEM image of nanoporous  $\text{Bi}_2\text{Te}_3$  showing sub-micron size pores. Inless detector was used with a 20 kV electron beam. (Left) Sample#1. (Right) Sample#12.

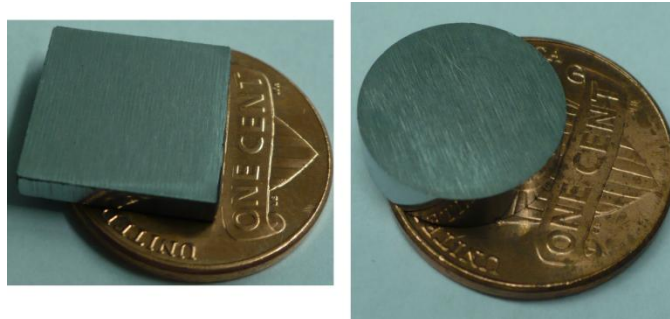


Figure 3.18: Sintered samples. Square and circular samples are fabricated using pressureless and pressure sintering respectively.

More focus was placed on the square sample due to the difficulty of getting a sufficient temperature along the section area with the circular sample. This point will be discussed in more detail later in the chapter. Effect of the sintering temperature on the sintered sample was investigated carefully. Temperature was varied from 150°C to 400°C with a 50°C step. After each sintering temperature, the sample was imaged with the SEM (Figure 3.19).

The sample starts to decompose at around 350°C; a dark color was seen on the tube wall and on the sample surface (Figure 3.20). No clear modification is observed on the sample porosity. The sample surface after sintering at 400°C shows that the pressed powder starts to crystallize (Figure 3.19d). This may be due to the sintering atmosphere, argon, since the melting temperature (585°C) for  $\text{Bi}_2\text{Te}_3$  is not reached yet.



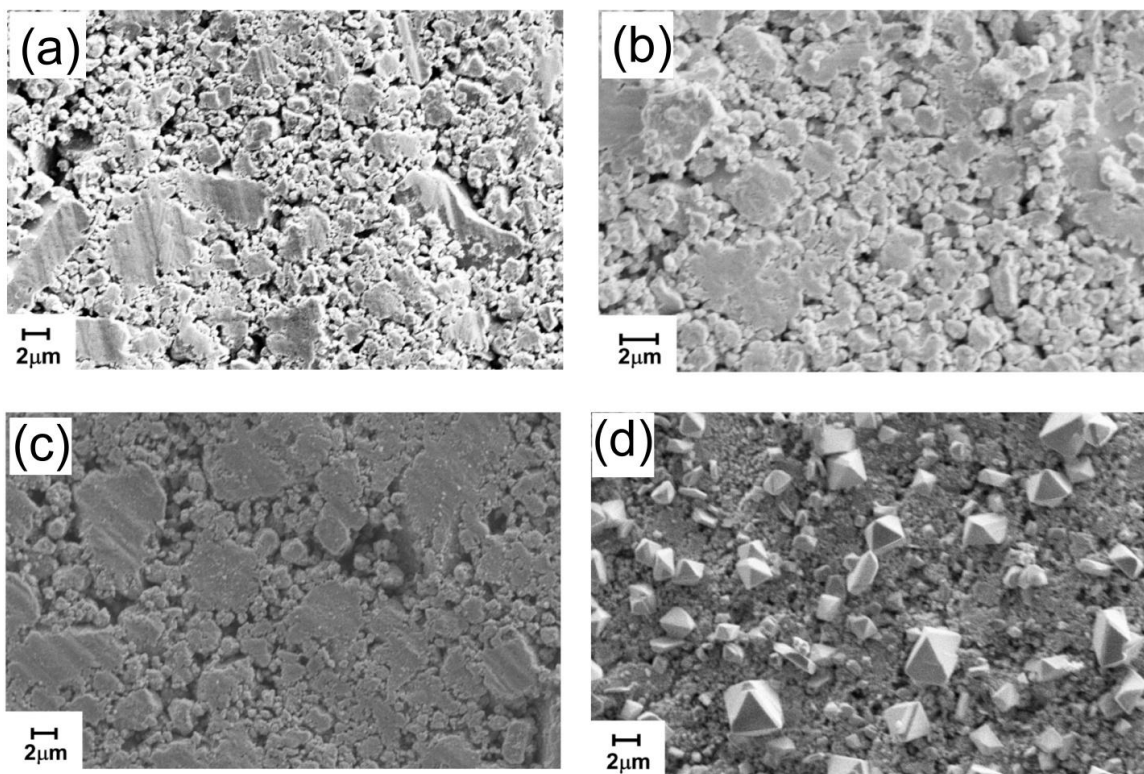


Figure 3.19: SEM images of a compact sample after sintering at different temperature. (a) No sintering.(b) 200°C.(c) 300°C.(d) 400°C. The analyzed sample was fabricated in conditions similar to sample#12.

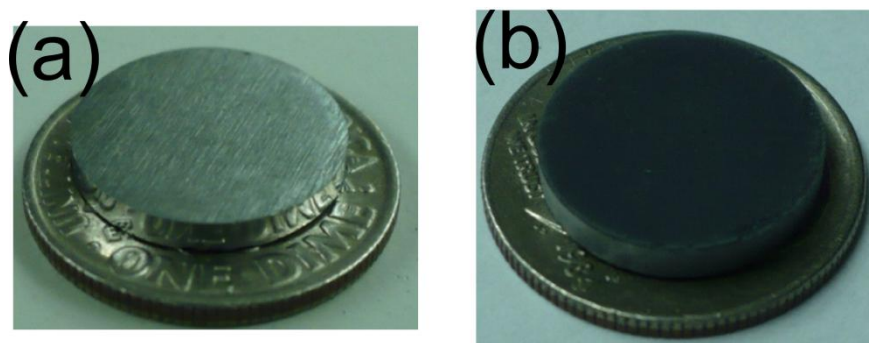


Figure 3.20: Color change of the sintered sample after sintering at 400°C.(a) No sintering performed (used for comparison).(b) Sample sintered at 400°C.

### 3.9 Sintered sample characterization

#### 3.9.1 XRD and EDS results on the powder and thermoelectric sample

Figure 3.21 shows an energy-dispersive X-ray spectroscopy (EDS) spectrum of the starting material and the sintered sample. The powder is made up of Bi, Sb, and Te.



Sb is the doping material for p-type  $\text{Bi}_2\text{Te}_3$ . No additional peaks are present, indicating that no impurities were introduced during milling and sintering steps.

X-ray diffraction (XRD) patterns of the powder and sintered sample are shown in figure 3.22. The two patterns have similar peaks indicating that there were no changes in the crystal phases during the pressing and sintering steps. The average crystallite size for the powder and the sintered sample was calculated from XRD peak broadening based on the Scherrer equation [193]. The average crystallite sizes were 226.95 Å and 370.9 Å for the powder and the sintered sample, respectively. These results indicate that the crystal size increased during sintering and that the particles, forming the powder, are made up of large amount of crystallites.

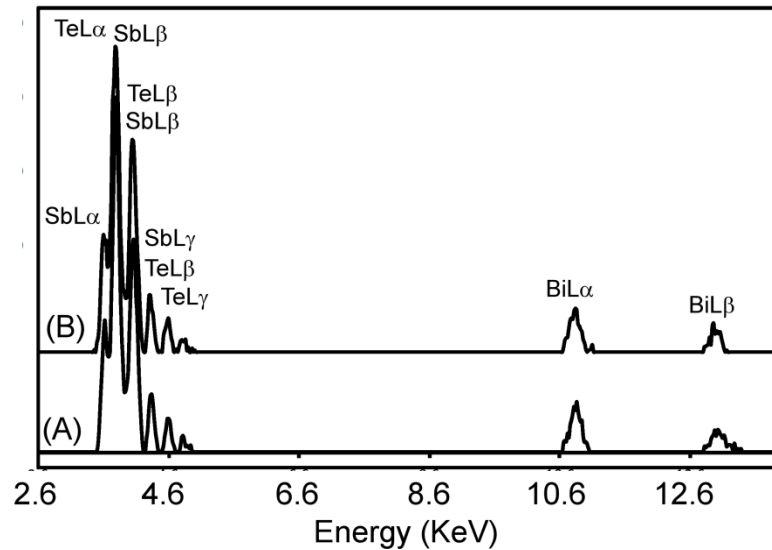


Figure 3.21: EDS spectrum of the P-type  $\text{Bi}_2\text{Te}_3$  material. (A) Initial material. (B) Sintered sample [194].

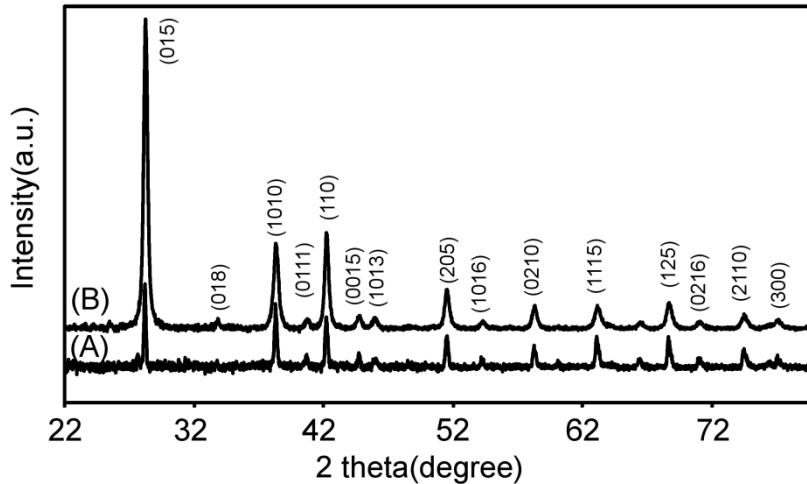


Figure 3.22: XRD patterns of the  $\text{Bi}_2\text{Te}_3$  powder and sintered sample. (A) sintered sample, (B) 5 hours milled powder. Space group R-3m, System Rhombohedral, PDF 01-072-1836 [194].

### 3.9.2 Physical properties of the thermoelectric sintered sample

Thermal diffusivity and specific heat of the sintered sample were measured at different temperature (Figure 3.23). These measured values along with the sample density were used in equation (3.1) in order to determine the thermal conductivity. Figure 3.24 shows the four physical properties, thermal conductivity, thermopower, electrical conductivity, and figure of merit  $ZT$ , of the sintered sample. The sample has a density of (2.79 mm thickness and 2 g mass). A small piece of the sintered sample (70 mg) was used in the differential scanning calorimeter (DSC) for specific heat measurement.

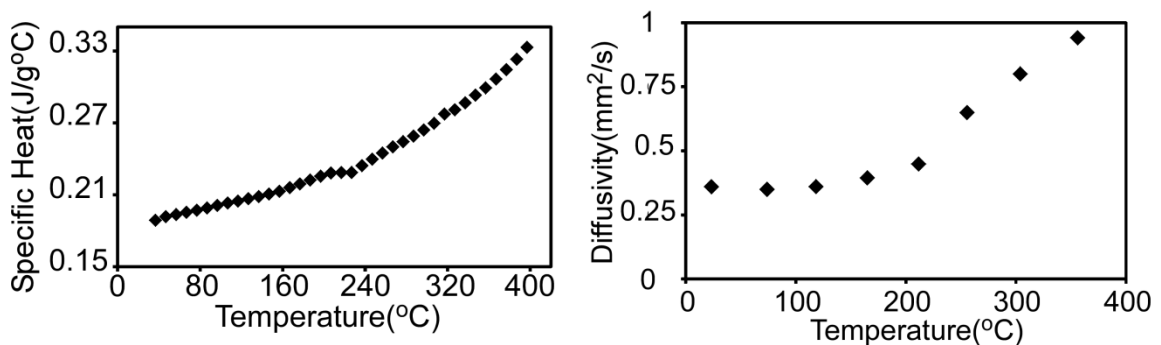


Figure 3.23: (Left) Specific heat of sample#1 measured with differential scanning calorimeter (DSC). (Right) Thermal diffusivity of sample#1 measured using laser flash analyzer.

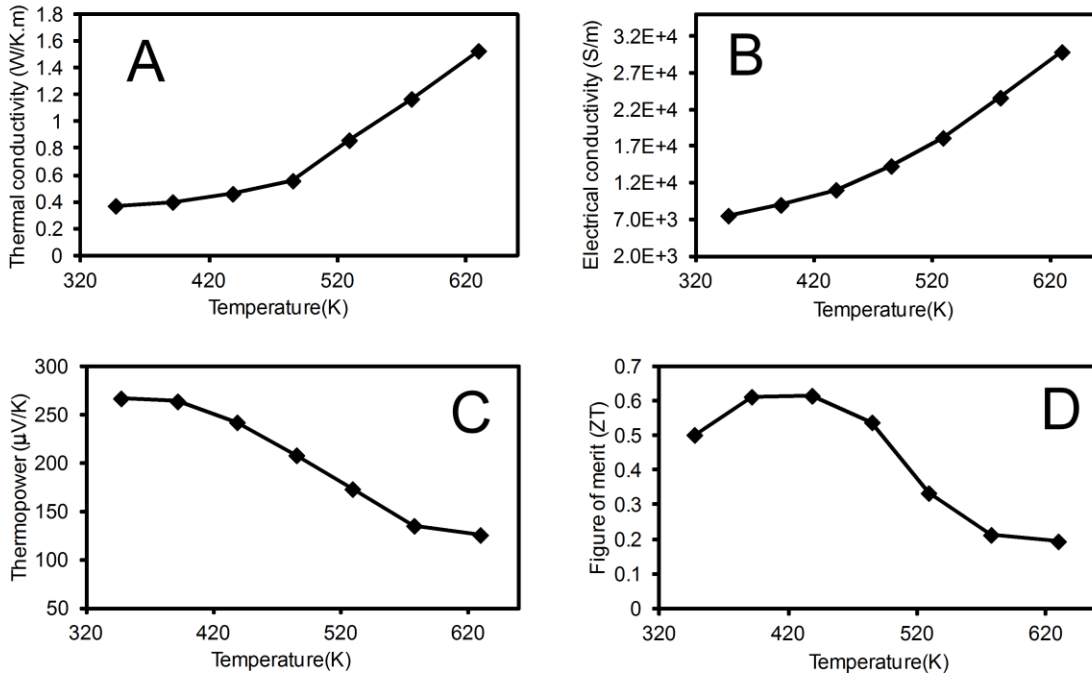


Figure 3.24: Physical properties of the sintered sample. (A) Thermal conductivity, (B) Electrical conductivity, (C) Thermopower, and (D)  $ZT$  value. Measurement performed on sample#1.

Figure 3.25 shows more thermopower data for square sample#12. The two curves are the measured thermopower under the same conditions. The difference in the 2 runs is possibly due to some material properties changing at the high temperature.

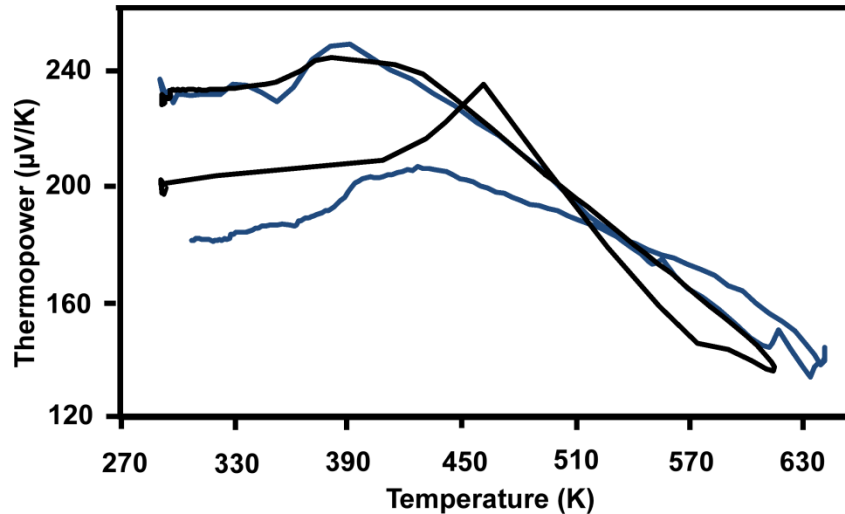


Figure 3.25: Thermopower of the sintered nanoporous sample#12 plotted against temperature. The two plots were obtained from two different runs under the same experimental conditions.

### 3.9.3 Temperature measurement on the thermoelectric sintered sample

Quantum focus instrument (QFI) setup was used to obtain the temperature distribution along the sintered sample surface. The stage temperature was set to 60°C, immediately after equilibrium was reached; a 0.23 V from a sourcemeter was applied to the sintered sample via wires soldered on its sides. InfraScope system software was used to collect and analyze the heated sample images.

A line was drawn along the surface of the sintered sample using the ROI option. The purpose of plotting the line is to compare the temperature distribution under forward and reverse currents. Figure 3.26 shows the temperature distribution along the drawn line for a sample fabricated similarly to #1, cooling under the ambient temperature is observed.

Similar analysis was done on the square sample (Figure 3.27). Applied voltage was 0.36 V.

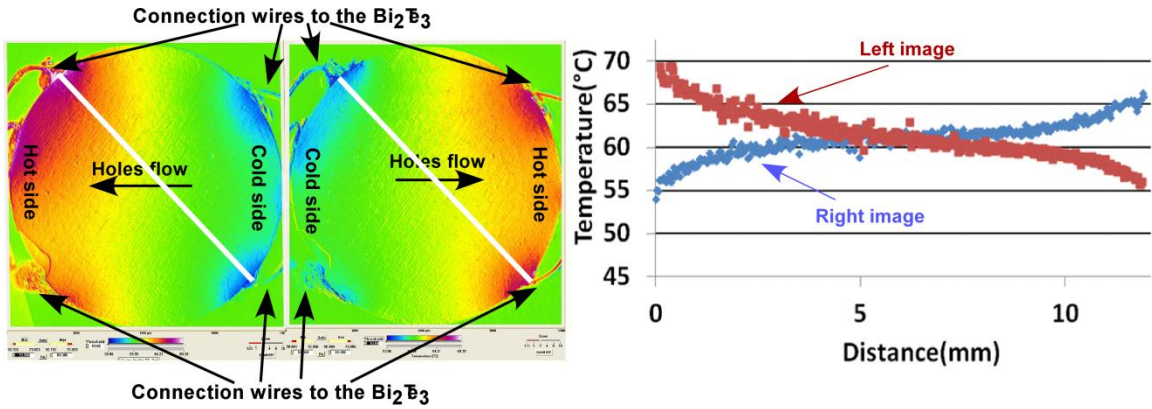


Figure 3.26: Testing of the TE circular sample under forward and reverse currents verifies that a temperature gradient can be obtained. The ambient temperature is 60°C. (Left) Temperature distribution from an IR camera. (Right) Plot of the temperature versus the distance along the white line in the left images. Cooling below the ambient temperature can be observed.  $\Delta T \approx 15^\circ\text{C}$ .

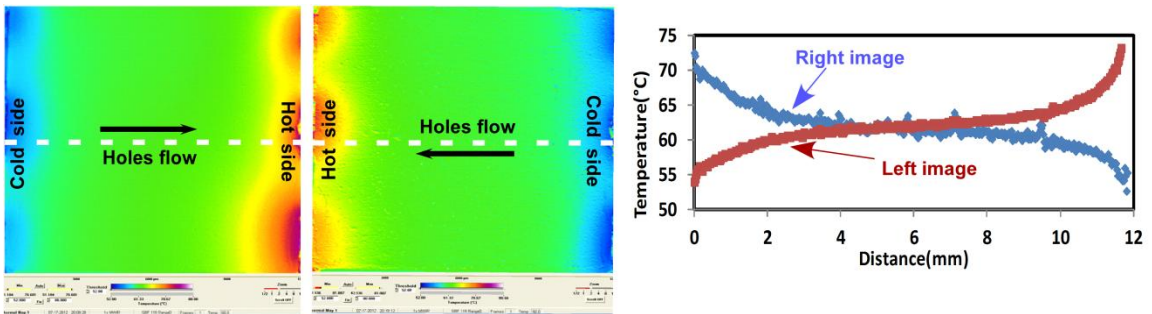


Figure 3.27: Testing of the TE square sample#12 under forward and reverse current verifies that a temperature gradient can be obtained. The ambient temperature is 60°C. (Left) Temperature distribution from an IR camera. (Right) Plot of the temperature versus the distance along the white line in the left images. Cooling below the ambient temperature can be observed.  $\Delta T \approx 15^\circ\text{C}$ .

The QFI microscope also was used to measure the possible temperature difference for different input powers (Figure 3.28). The sample was set flat on the heated stage, for each applied power, the line scan feature was used to plot the temperature distribution and therefore obtain the temperature difference.

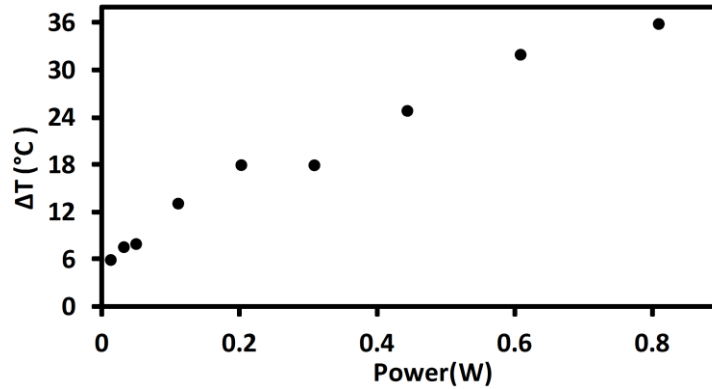


Figure 3.28: Temperature difference versus the applied power for sample#12 using the QFI microscopy.

### 3.10 Results on the built thermoelectric based Knudsen pump

#### (A) *Circular sample*

Figure 3.29 shows an image of the built Knudsen pump using a small piece of the circular sample#1, the main components of the pump are: the nanoporous TE material, connection wires, and the tubing.

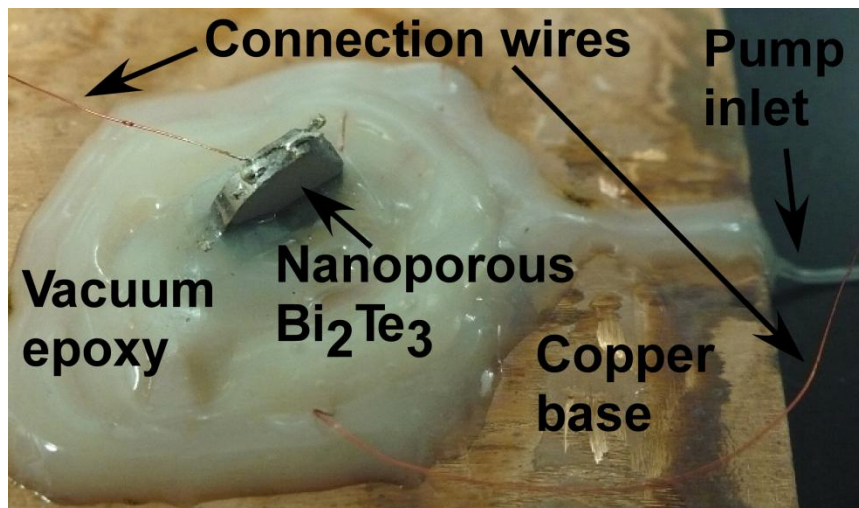


Figure 3.29: Image of the built  $\text{Bi}_2\text{Te}_3$  TE Knudsen pump using small portion of a sintered sample fabricated using conditions of sample#1.

Different voltages were applied to the pump and pressure was recorded. Figure 3.30 shows the pressure generated by the pump when operated in both the forward and

reverse directions; the applied voltage was 0.8 V. Once a voltage is supplied to the pump (bottom wire connected to the positive polarity of the power supply), the top side becomes hot and the bottom side becomes cold, which creates the temperature gradient for thermal transpiration flow. A differential pressure of 300 Pa is obtained for an input power of 0.96 W.

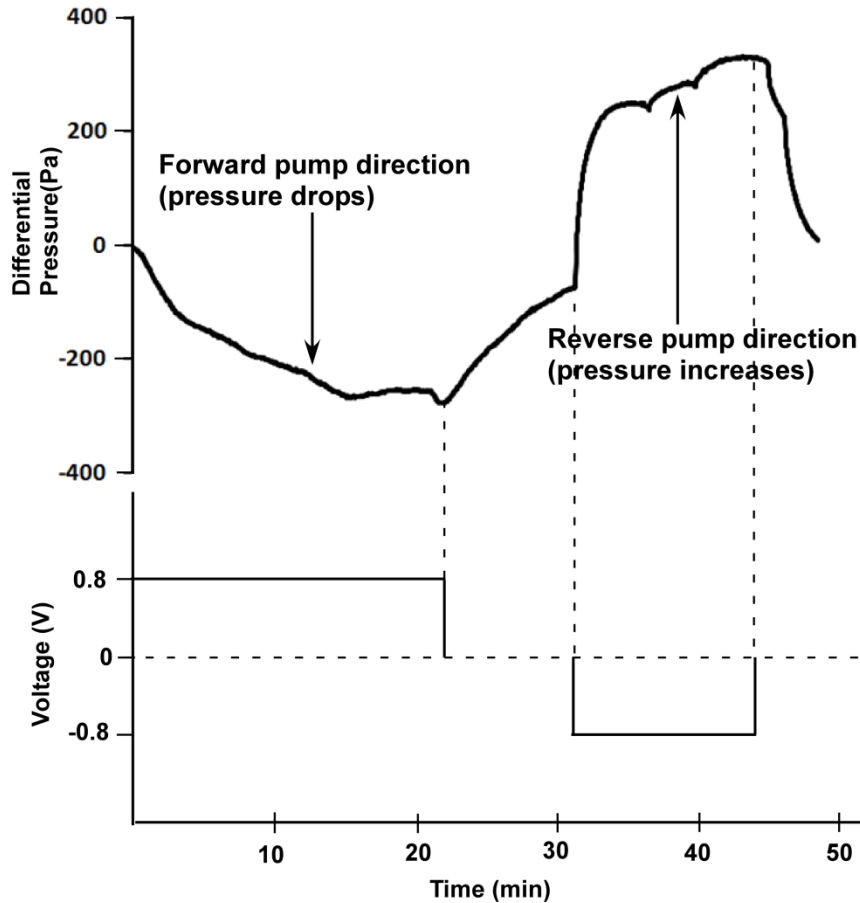


Figure 3.30: Experimental pressure differential obtained with the fabricated Knudsen pump. The pressure is permitted to come to room pressure before switching the voltage polarity and reversing the pump direction.

**(B) Square sample**

Figure 3.31 shows an image of the built Knudsen pump using a square sample. It has a footprint of  $3 \times 2 \text{ cm}^2$ . A voltage (1 V, 1.33 W) was applied to the device and the

pressure was recorded with a pressure sensor (Accuracy: 0.02% Full scale, precision: 0.06% Full scale) and plotted with a custom LabVIEW program (Figure 3.32).

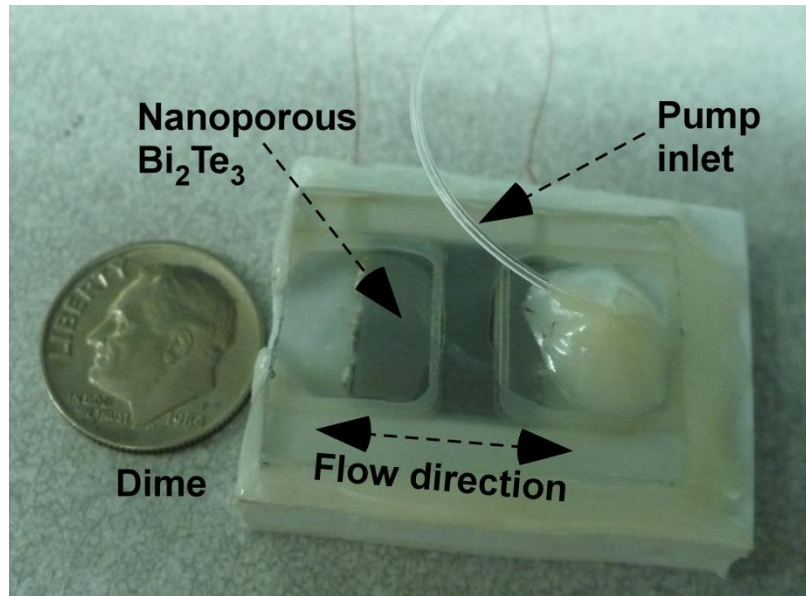


Figure 3.31: Fabricated nanoporous Bi<sub>2</sub>Te<sub>3</sub> TE Knudsen pump using sample#13. The nanoporous TE sample is placed in a rectangular channel. Wires are soldered on the sides. The pump is sealed using vacuum epoxy glue [194].



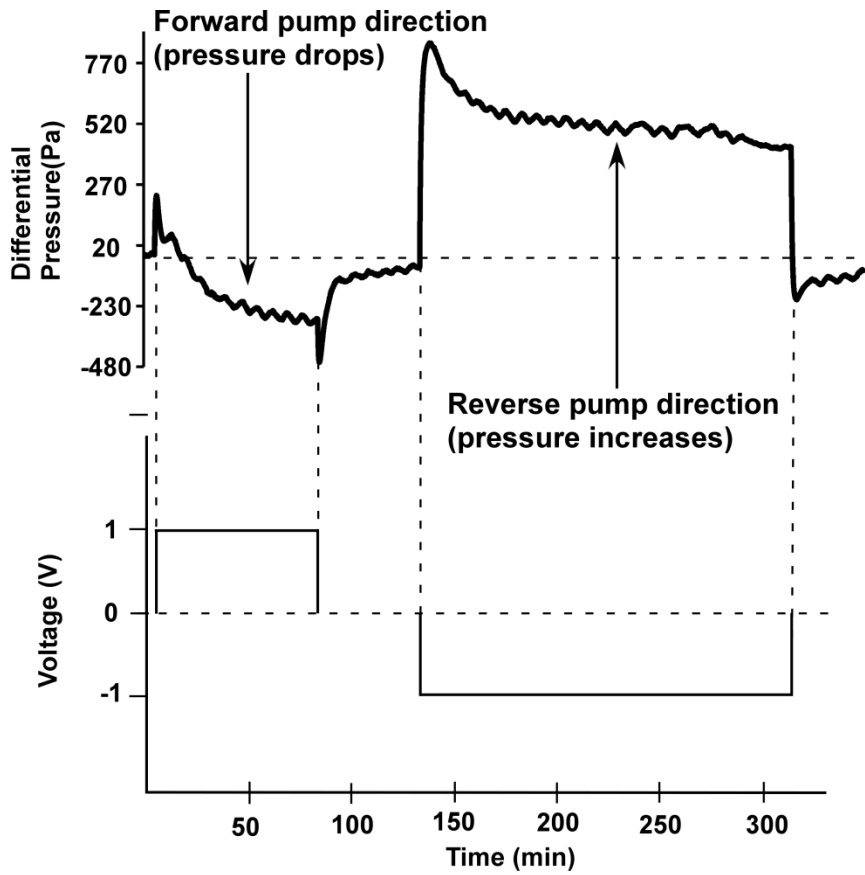


Figure 3.32: Experimental pressure differential obtained with the fabricated Knudsen pump in figure 3.31. Pressure is permitted to come to room pressure before switching the voltage polarity [194].

The vertical spikes occur when the pump is turned on or off. The addition or removal of heat causes a temporary increase or decrease in pressure due to the gas expansion or contraction. Operation at negative pressure proves that the Knudsen pump does not work due to gas heating. The measured flow rate for this device is 1  $\mu\text{l}/\text{min}$ . The procedure followed for measuring the flow rate is described in the next section.

### 3.11 Pressure flow rate relationship

In order to determine a relationship between the generated pressure and the flow rate, a syringe pump and pressure sensor are attached to one side of the channel using a T-connector. The other side of the channel is open to atmosphere. The syringe pump sets the gas flow rate while a temperature gradient is generated by the TE material, and the

resulting pressure difference across the TE material is measured. Figure 3.33 shows the generated pressure, for a given input power, when the syringe pump is set for different flow rate values. The pressure is allowed to stabilize before moving to the next flow rate value. Figure 3.34 shows the measured pressure versus the flow rate of the Knudsen pump shown in figure 3.31. The linear relationship between the gas flow rate and pressure is typical for a pump based on the principle of thermal transpiration. The negative values of pressure on this graph indicate that the syringe pump supplies a gas flow rate that exceeds the pumping ability of the nanoporous thermoelectric. The maximum pressure difference is 300 Pa, and the maximum flow rate is 1.8  $\mu\text{l}/\text{min}$  at a power of 3.32 W.

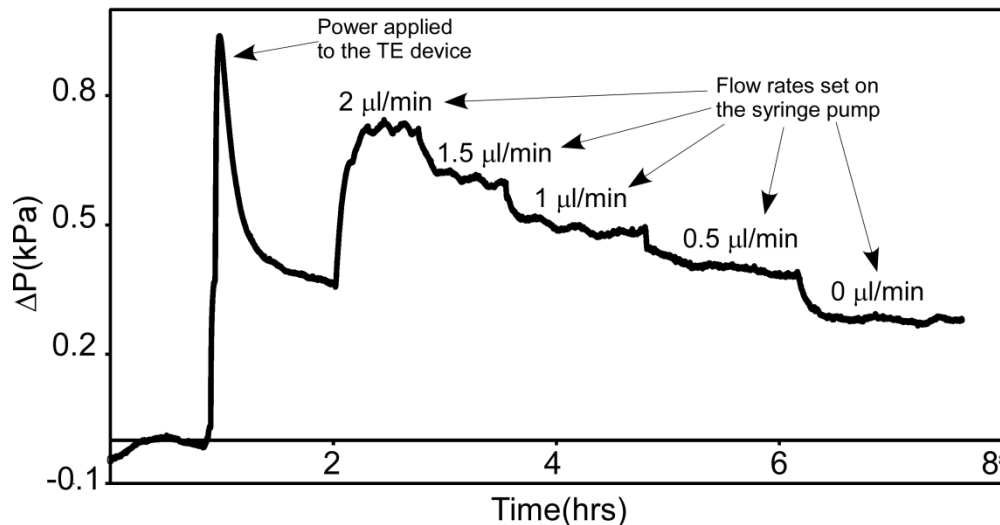


Figure 3.33: Measured pressure across the TE based Knudsen pump when the syringe pump is set up for different flow rates. This curve permits to generate a plot that relates pressure and flow rate.

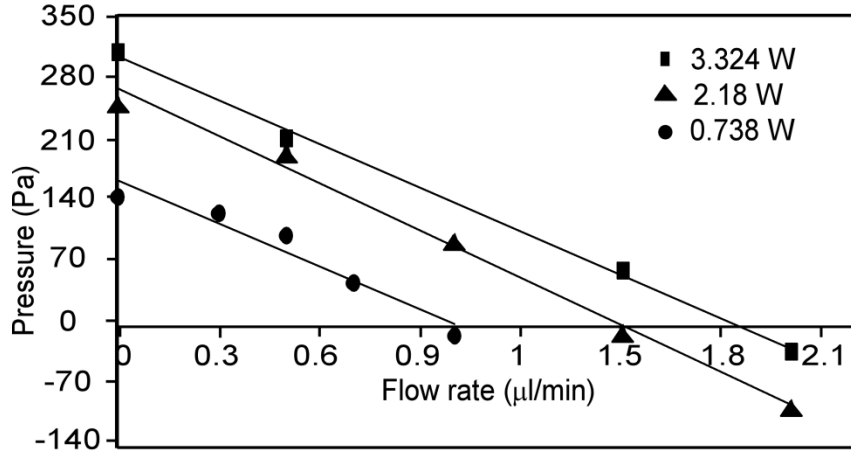


Figure 3.34: Graph of the pressure versus flow rate that is obtained for three different levels of power in the nanoporous TE. The marks are the experimentally obtained data, and the lines represent a linear fit to the measurements [194].

The linear fit equations in figure 3.34 were used to extract relationships between the input power, maximum pressure and maximum flow rate. Figure 3.35 shows the obtained results. The pressure is maximum when the flow rate is zero. The flow rate is maximum when the pressure is zero.

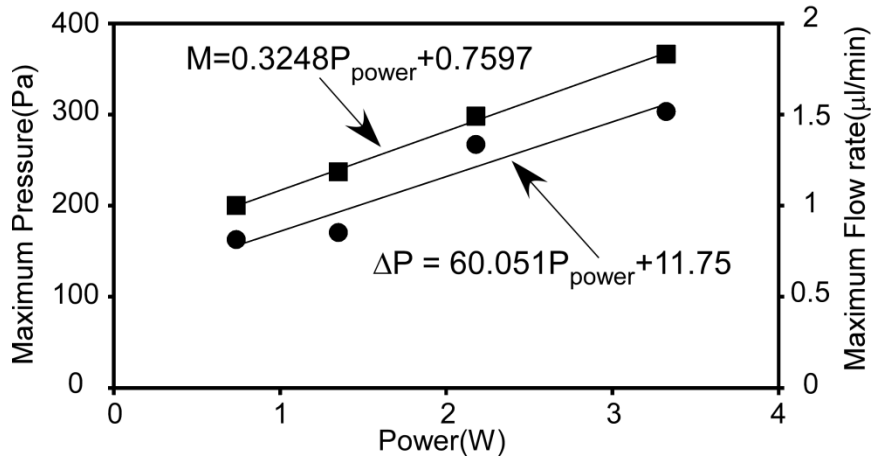


Figure 3.35: Maximum pressure and maximum flow rate versus the input power for device in figure 3.31. The linear fit equations in figure 3.34 were used to calculate the maximum pressure and flow rate.  $M$ ,  $\Delta P$ , and  $P_{power}$  are flow rate, pressure difference, and input power.

### **3.12 Pore size versus the sintering conditions**

Effect of the sintering conditions on the pore size was investigated through analysis of SEM images, a series of images were collected for each experimental condition. ImageJ, as described in appendix A, was used to calculate the pore area. The collected data were further analyzed, using Microsoft Excel, where descriptive statistics, particularly mean, maximum and minimum pore radius and the standard deviation were computed. The radius was calculated for a circle with an area equal to the one calculated using ImageJ. Table 3.3 summarizes the obtained results.

The fabricated pump in figure 3.31 is pressed at 6 MPa and sintered at 200 °C. The corresponding pore radius and Knudsen number are 434 nm of 0.15 respectively assuming air as the working gas. The flow in this case is transitional. Further decrease in the pore radius so that the flow is in the free molecular regime will improve the generated pressure.

Table 3.3: Average, maximum, minimum, and standard deviation of the pore radius at different sintering conditions.

<b>Pressure (MPa)</b>	<b>Sintering temperature (°C)</b>	<b>Average pore radius (nm)</b>	<b>Maximum pore radius (nm)</b>	<b>Minimum pore radius (nm)</b>	<b>Standard deviation (nm)</b>
<b>6</b>	<b>Before sintering</b>	701.8	2080.5	243.2	346.6
	<b>200 °C</b>	434	755.8	205	130.5
	<b>250 °C</b>	646.4	1223	343.4	176.8
<b>8</b>	<b>Before sintering</b>	217.1	515.3	100	81.3
	<b>200 °C</b>	309	698.7	88.2	146.8
	<b>250 °C</b>	288	456.1	157.4	82.9
<b>10</b>	<b>Before sintering</b>	248.4	392.4	136.4	49.5
	<b>200 °C</b>	245.5	446.5	138.5	75.4
	<b>250 °C</b>	234.6	383.6	143.1	64
<b>12</b>	<b>Before sintering</b>	288.07	581.1	115.2	98.3
	<b>200 °C</b>	205.44	539.5	72.35	79.6
	<b>250 °C</b>	206.25	479.6	66.12	76.7
<b>14</b>	<b>Before sintering</b>	170.2	383.1	60.5	61.5
	<b>200 °C</b>	254.7	480.6	94.77	87.5

### 3.13 Electrical contacts

Contact resistance is a major issue in the performance of TE devices. Even with high figure of merit Z material, if the contact resistance is high, the overall performance of the TE device is degraded [195]. A great portion of the consumed power is due to the poor electrical contacts. In this work regular tin-lead solder along with rosin paste flux to improve solder flow was used. Example of electrical contacts to the TE material is shown in figure 3.36.

Nickel and Cobalt materials have been investigated as intermediate layers to the regular tin-lead solder. Nickel is widely used as diffusion barrier for copper in TE coolers and generators [196]. About 100 nm thick layer of Ni or Co was sputtered along the TE

thickness, the sides of the TE element were covered with aluminum foil, after the deposition, a dark color was observed on the exposed area. No improvements were noticed when trying to solder electrical wires to these samples.

Electroless plating [197, 198], widely used to make contacts to TE elements, was not explored because the solution constituents will clog the TE element pores.

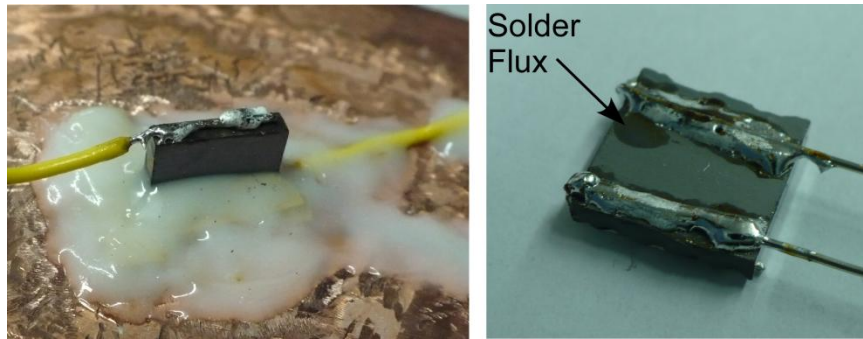


Figure 3.36: Examples of electrical contacts. Rosin paste flux was used to improve the solder flow and therefore enhance the contact quality.

The pumping from the cold side to the hot side based on thermal transpiration occurs perpendicular the TE sample cross-sectional area. It will be preferable to use the top surface and go through the sample thickness since this will have a higher pore density, but the issue was in the amount of temperature gradient along each direction. The first one, along the cross section, have shown higher temperature gradient for the same input power. The measured temperature difference across the six faces of the square sample is shown in figure 3.37.

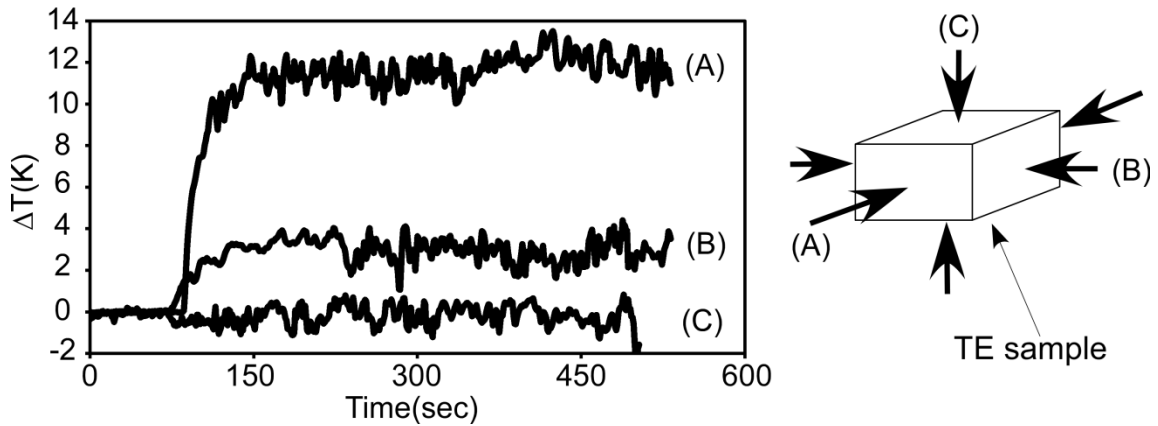


Figure 3.37: Temperature difference across the different square sample faces. Electrical wires were soldered on the (A) faces.

### 3.14 Conclusion

A bi-directional Knudsen pump has been fabricated using a multifunctional  $\text{Bi}_2\text{Te}_3$  thermoelectric material. The fabrication starts by ball milling of p-type  $\text{Bi}_2\text{Te}_3$  pellets in a high energy ball mill under vacuum, 10-hour milling time showed an average grain size of  $0.4 \mu\text{m}$ . Pressure and pressureless sintering techniques were used to compact the powder and form a nonporous sample. When using the pressureless technique, the sintering was performed inside a tube furnace under running argon gas. A nanoporous sample was obtained for a pressure of 6 MPa and  $150^\circ\text{C}$  sintering temperature using the circular die.

Two different pumps are fabricated, in the first one; the square nanoporous sample is placed in a machined plastic channel, once the power is turned on, one side of the thermoelectric sample gets hot, and the other side gets cold providing the necessary temperature gradient for thermal transpiration to take place. Reversing the voltage polarity causes a reverse in the hot and cold sides and therefore reversing the pumping direction. The maximum pressure and flow rate are 300 Pa and  $1.8 \mu\text{l}/\text{min}$  for an input power of 3.32 W. In the second circular design, the thermoelectric sample is placed on a

copper block to help get rid of the excess heat. For an input voltage of 0.8 V, the generated pressure is about 300 Pa.

XRD and EDS analysis on the powder and sintered samples were similar indicating no phase change and no impurities were introduced during the fabrication. Physical properties (electrical conductivity, thermal conductivity, the Seebeck coefficient, and the figure of merit  $Z$ ) of the sintered sample were measured against temperature. The electrical conductivity and figure of merit  $Z$  of the sintered sample decreased after sintering mainly due to the thermoelectric oxidation.

Characterization of the sintered samples pore area showed an average pore radius of 434 nm. The corresponding Knudsen number is 0.15 assuming air as the working gas. Further decrease of pore size such that the Knudsen number is larger than 10, and a reduction of the electrical contact resistance will improve the overall pump performance.



## CHAPTER 4: MODELING OF THE NANOPOROUS THERMOELECTRIC BASED KNUDSEN PUMP

This chapter describes a mathematical model of the thermoelectric (TE) based Knudsen pump [194]. The model is derived using well-established TE equations, which relate the different parameters of a TE element, and the Sharipov's equation connecting the mass flow rate and pressure data for a Knudsen pump. Effects of pore size, TE figure of merit  $Z$ , and working gas are investigated and their impacts on the generated pressure and mass flow rate are discussed.

### 4.1 Mass flow rate of a Knudsen pump

Starting with the Sharipov's equation [100] which relates the mass flow rate and pressure for the Knudsen pump:

$$\dot{M} = P_{av} \sqrt{\frac{m}{2K_B T_{av}}} \frac{a\pi a^2}{L} \left[ \frac{\Delta T}{T_{av}} M_t - \frac{\Delta P}{P_{av}} M_p \right] \quad (4.1)$$

where  $a$  is the channel radius,  $L$  is the channel length,  $P_{av}$  and  $T_{av}$  are the average pressure and temperature,  $\Delta P$  and  $\Delta T$  are the pressure and temperature differences across the channel,  $m$  is the molecular mass of the gas,  $k_B$  is Boltzmann's constant ( $1.3806 \cdot 10^{-23} \text{ m}^2 \text{ Kg s}^{-2} \text{ K}^{-1}$ ), and  $M_t$  and  $M_p$  are temperature driven and pressure driven flow coefficients that depend upon the Knudsen number [103].

For a membrane or a TE sample with an average pore radius,  $a$ , and a total section area  $A$ , the total number of pores,  $N_{pores}$ , is given by:

$$A_{void} = \varepsilon.A \quad (4.2)$$

$$N_{pores} = \frac{\varepsilon.A}{\pi a^2} \quad (4.3)$$

where  $A_{void}$  is the total area covered by all pores.  $\pi a^2$  is section area of one pore (assumed to be circular), and  $\varepsilon$  is the TE/membrane porosity.

Using expression (4.3), equation (4.1) can be written as:

$$\dot{M} = \frac{aA\varepsilon P_{av}}{L} \sqrt{\frac{m}{2k_B T_{av}}} \left[ \frac{\Delta T}{T_{av}} M_t - \frac{\Delta P}{P_{av}} M_p \right] \quad (4.4)$$

#### 4.2 Maximum pressure of a Knudsen pump

The largest pressure difference that can be obtained is found by setting the mass flow rate to zero. Equation (4.4) becomes:

$$\Delta P|_{\dot{M}=0} = \frac{\Delta T}{T_{av}} \frac{M_t}{M_p} P_{av} \quad (4.5)$$

We assume that the hot side of the Knudsen pump is open to the atmosphere,  $P_H = P_{atm}$ , and the  $T_C$  is known.

Now, we will try to derive an expression for  $P_{av}$ , and  $T_{av}$ .

$$\Delta P|_{\dot{M}=0} = P_H - P_C \quad (4.6)$$

We try to express  $P_{av}$  in terms of  $P_{atm}$  and  $\Delta P|_{\dot{M}=0}$ .

$$P_{av} = \frac{P_H + P_C}{2} = P_{atm} - \frac{\Delta P|_{\dot{M}=0}}{2} \quad (4.7)$$

We assume that the cold side  $T_C$  temperature is known,

$$T_{av} = \frac{T_H + T_C}{2} \quad (4.8)$$

$$T_{av} = \frac{\Delta T}{2} + T_C \quad (4.9)$$

Using equations (4.5), (4.7) and (4.9),  $\Delta P|_{\dot{M}=0}$  for a given  $\Delta T$  can be written as:

$$\Delta P|_{\dot{M}=0} = \frac{\Delta T}{T_{av}} \frac{M_t}{M_p} \left[ P_{atm} - \frac{\Delta P|_{\dot{M}=0}}{2} \right] \quad (4.10)$$

$$\Delta P|_{\dot{M}=0} = \frac{P_{atm} \frac{M_t}{M_p} \frac{\Delta T}{T_{av}}}{1 + \frac{1}{2} \frac{M_t}{M_p} \frac{\Delta T}{T_{av}}} \quad (4.11)$$

### 4.3 Maximum mass flow rate of a Knudsen pump

The largest mass flow rate that can be obtained is found by setting the pressure difference to zero. Using equation (4.4), and setting  $\Delta P$  equal to zero, we get the following equation:

$$\dot{M}|_{\Delta P=0} = \frac{A \varepsilon a P_{av}}{L} \sqrt{\frac{m}{2k_B T_{av}}} \left[ \frac{\Delta T}{T_{av}} M_t \right] \quad (4.12)$$

Using expressions of  $P_{av}$ , and  $T_{av}$  from equations (6) and (8), equation (11) can be written as:

$$\dot{M}|_{\Delta P=0} = \frac{M_t A \varepsilon a P_{atm}}{L} \sqrt{\frac{m}{2k_B}} \frac{\Delta T}{[T_{av}]^{\frac{3}{2}}} \quad (4.13)$$

### 4.4 Mathematical modeling of the TE based Knudsen pump

Figure 4.1 shows a schematic of the square-shaped nanoporous TE element, along with different terms used in the mathematical analysis.

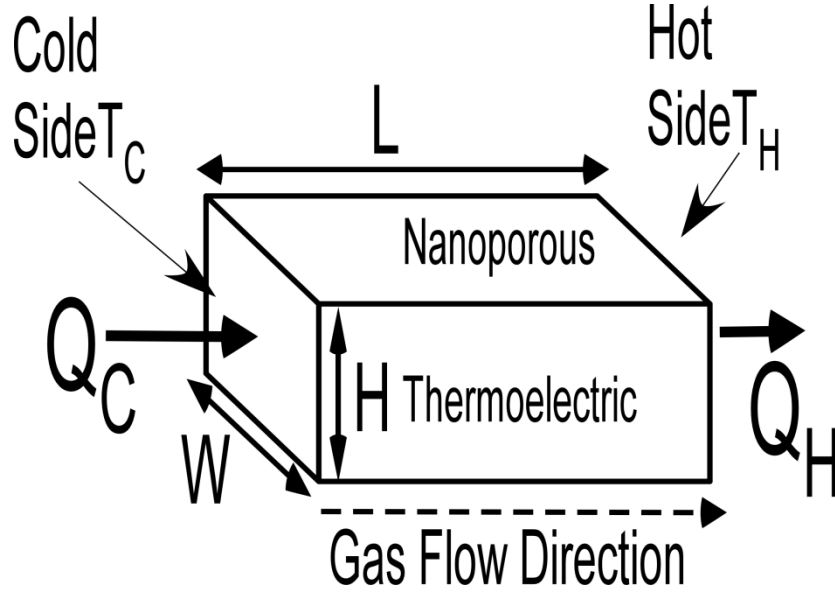


Figure 4.1: Schematic of the nanoporous TE element showing some terms used in the mathematical equations.  $W$ ,  $L$ , and  $H$  are the TE width, length and thickness.  $Q_H$  and  $Q_C$  are the rejected heat on the hot side and absorbed heat from the cold side respectively.

The heat fluxes through the cold and hot sides of a rectangular TE are expressed by the following equations [199, 200]:

$$Q_H = \bar{\alpha}IT_H - \bar{K} \frac{A}{L} \Delta T + \frac{1}{2} \bar{\rho} \frac{L}{A} I^2 \quad (4.14)$$

$$Q_C = \bar{\alpha}IT_C - \bar{K} \frac{A}{L} \Delta T - \frac{1}{2} \bar{\rho} \frac{L}{A} I^2 \quad (4.15)$$

where  $\bar{\alpha}$ ,  $\bar{\rho}$  and  $\bar{K}$  are the Seebeck coefficient or thermopower, electrical resistivity, and thermal conductivity, respectively, at the average temperature  $T_{av} = \frac{T_C + T_H}{2}$ .  $I$  is the applied current to the TE material, and  $Q_H$  and  $Q_C$  are the rejected heat on the hot side and absorbed heat from the cold side, respectively. The first  $Q_C$  term,  $\bar{\alpha}IT_C$ , is the Peltier cooling effect. The second term,  $\frac{1}{2} \bar{\rho} \frac{L}{A} I^2$ , represents the Joule heating effect. The Joule heat is distributed throughout the element, so  $\frac{1}{2}$  the heat goes towards the cold side,

and  $\frac{1}{2}$  the heat goes towards the hot side. The last term,  $\bar{K} \frac{A}{L} \Delta T$ , represents the Fourier effect in which heat conducts from a higher temperature to a lower temperature. The Peltier cooling is reduced by the losses associated with electrical resistance and thermal conductance.

$\Delta T$  and  $Q_C$  values affect significantly the pressure difference and mass flow rate generated by the Knudsen pump. Mathematically speaking,  $\Delta T$  and  $Q_C$  can have positive and negative values. A negative  $\Delta T$  is not practical since the hot side temperature is always higher than the cold side. A negative  $Q_C$  signifies that heat is being absorbed from the cold side by some other means other than the TE material.

Next, we are going to determine the intervals of current  $I$ , voltage  $V$ , and  $X = \frac{A}{L}$ , ratio of cross section area to length, for which  $\Delta T$  and  $Q_C$  are positive.  $\bar{\alpha}$ ,  $\bar{\rho}$  and  $\bar{K}$ , fundamental physical properties of the TE material, can also affect the values of  $\Delta T$  and  $Q_C$ , but they are not considered in this analysis because the sintering conditions are kept unchanged which will always yield a TE nanoporous sample with the same physical properties. The only parameter that can change during the fabrication is the sample thickness, and that depends on the amount of powder being pressed.

The input power and temperature gradient across the TE material are given by:

$$P_{power} = Q_H - Q_C = \bar{\alpha} I \Delta T + \bar{\rho} \frac{1}{X} I^2 = VI \quad (4.16)$$

$$\Delta T = \frac{V - \bar{\rho} \frac{1}{X} I}{\bar{\alpha}} \quad (4.17)$$

Inserting  $\Delta T$  expression in the  $Q_C$  equation (4.15), we obtain the following expression:

$$Q_C = \bar{\alpha}IT_C + \frac{\bar{K}I\bar{\rho}}{\bar{\alpha}} - \frac{XV\bar{K}}{\bar{\alpha}} - \frac{\bar{\rho}I^2}{2X} \quad (4.18)$$

First, we will use equation (4.18) to determine the intervals of  $I$ ,  $V$ , and  $X = \frac{A}{L}$  for which  $Q_C$  is positive. Next, we analyze  $\Delta T$  using equation (4.17) and determine the corresponding intervals of  $I$ ,  $V$ , and  $X = \frac{A}{L}$ . Finally, we will try to analyze both sets of intervals, and try to deduce the shared interval regions in order to operate the TE material in them.

#### 4.4.1 Variation of $Q_C$ versus $I$

Differentiating equation (4.18) with respect  $I$  leads to the following equation:

$$\frac{dQ_C}{dI} = \bar{\alpha}T_C + \frac{\bar{K}\bar{\rho}}{\bar{\alpha}} - \frac{\bar{\rho}I}{X} \quad (4.19)$$

Setting equation (4.19) equal to zero and solving for  $I$ .  $Q_C$  is maximal for an input current  $I = \frac{X}{\bar{\rho}} \left( \bar{\alpha}T_C + \frac{\bar{K}\bar{\rho}}{\bar{\alpha}} \right) = I_1$ , and for  $Q_C$  to be positive,  $Q_C(I = I_1) > 0$ . Figure 4.2 shows the general shape of  $Q_C$  when the input current is varied.

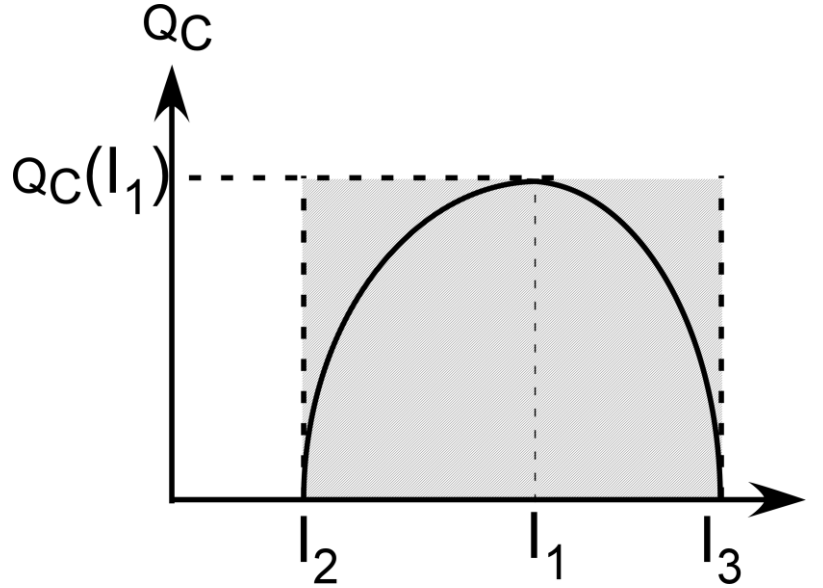


Figure 4.2:  $Q_C$  versus the current  $I$ . Grey region represent the interval where the TE sample is extracting heat from the cold side.

Now, inserting  $I_1$  into equation (4.18) results in the following equation:

$$Q_C(I = I_1) = \frac{X}{\bar{\rho}} \left( \bar{\alpha} T_C + \frac{\bar{K}\bar{\rho}}{\bar{\alpha}} \right)^2 - \frac{XV\bar{K}}{\bar{\alpha}} - \left( \frac{\bar{\rho}}{2X} \right) \left( \frac{X}{\bar{\rho}} \right)^2 \left( \bar{\alpha} T_C + \frac{\bar{K}\bar{\rho}}{\bar{\alpha}} \right)^2 \quad (4.20)$$

$$Q_C(I = I_1) = X \left[ \frac{1}{2\bar{\rho}} \left( \bar{\alpha} T_C + \frac{\bar{K}\bar{\rho}}{\bar{\alpha}} \right)^2 - \frac{V\bar{K}}{\bar{\alpha}} \right] \quad (4.21)$$

From equation (4.21), it appears that  $Q_C(I = I_1)$  will be positive when:

$$\frac{1}{2\bar{\rho}} \left( \bar{\alpha} T_C + \frac{\bar{K}\bar{\rho}}{\bar{\alpha}} \right)^2 - \frac{V\bar{K}}{\bar{\alpha}} > 0 \quad (4.22)$$

Rearranging the terms in equation (4.22), we obtain the voltage interval for which  $Q_C(I = I_1) > 0$ .

$$V < \frac{\alpha}{2\bar{\rho}\bar{K}} \left( \bar{\alpha} T_C + \frac{\bar{K}\bar{\rho}}{\bar{\alpha}} \right)^2 \quad (4.23)$$

The current interval  $[I_2, I_3]$  for which  $Q_C$  is positive is obtained by setting  $Q_C = 0$ :

$$I^2 - \frac{2X}{\bar{\rho}} \left( \bar{\alpha} T_C + \frac{\bar{K}\bar{\rho}}{\bar{\alpha}} \right) I + \frac{2V\bar{K}X^2}{\bar{\rho}\bar{\alpha}} = 0 \quad (4.24)$$

For equation (4.24) to have real solution, the discriminant  $\Delta$  needs to be positive.

$$\Delta = \frac{4X^2}{\bar{\rho}^2} \left( \bar{\alpha} T_C + \frac{\bar{K}\bar{\rho}}{\bar{\alpha}} \right)^2 - \frac{8V\bar{K}X^2}{\bar{\rho}\bar{\alpha}} > 0 \quad (4.25)$$

$$\Delta = \frac{4X^2}{\bar{\rho}^2} \left[ \left( \bar{\alpha} T_C + \frac{\bar{K}\bar{\rho}}{\bar{\alpha}} \right)^2 - \frac{2V\bar{K}\bar{\rho}}{\bar{\alpha}} \right] > 0 \quad (4.26)$$

$\frac{4X^2}{\bar{\rho}^2}$  is always positive, the 2<sup>nd</sup> term of equation (4.26) is similar to the one obtained in

(4.22) for  $Q_C(I = I_1) > 0$ . Thus the current interval for which is positive is given by the following equation:

$$\frac{I_{1,2}}{X} = \frac{1}{\bar{\rho}} \left\{ \left( \bar{\alpha} T_C + \frac{\bar{K}\bar{\rho}}{\bar{\alpha}} \right) \pm \left[ \left( \bar{\alpha} T_C + \frac{\bar{K}\bar{\rho}}{\bar{\alpha}} \right)^2 - \frac{2V\bar{K}\bar{\rho}}{\bar{\alpha}} \right]^{\frac{1}{2}} \right\} \quad (4.27)$$

#### 4.5 Variation of $Q_C$ versus $V$

Differentiating equation (4.18) with respect to  $V$ , we get:

$$\frac{dQ_C}{dV} = -\frac{\bar{K}X}{\bar{\alpha}} \quad (4.28)$$



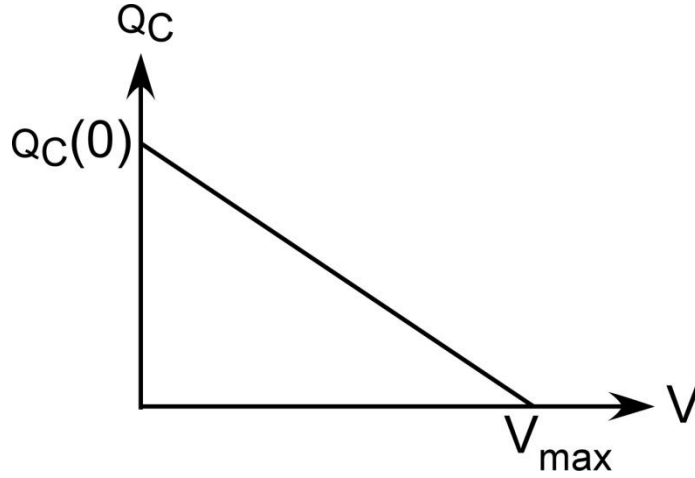


Figure 4.3:  $Q_C$  variation versus the voltage  $V$ .  $Q_C(0)$  must be positive.

Figure 4.3 shows the general shape of  $Q_C$  versus  $V$ ,  $Q_C$  starts with a maximum at  $V = 0$ , then starts decreasing with increasing  $V$ .  $Q_C(0)$  must be positive.

$$Q_C(0) = I \left( \bar{\alpha} T_C + \frac{\bar{K}\bar{\rho}}{\bar{\alpha}} - \frac{I\bar{\rho}}{2X} \right) > 0 \quad (4.29)$$

$$\bar{\alpha} T_C + \frac{\bar{K}\bar{\rho}}{\bar{\alpha}} - \frac{I\bar{\rho}}{2X} > 0 \quad (4.30)$$

$$\frac{I}{X} < \frac{2}{\bar{\rho}} \left( \bar{\alpha} T_C + \frac{\bar{K}\bar{\rho}}{\bar{\alpha}} \right) \quad (4.31)$$

$Q_C$  will cross the  $V$  axis at  $V = V_{\max}$ .  $Q_C(V = V_{\max}) = 0$ .

$$\frac{dQ_C}{dV} = -\frac{\bar{K}X}{\bar{\alpha}} \quad (4.32)$$

$$V_{\max} = \frac{\bar{\alpha}I}{\bar{K}X} \left( \bar{\alpha} T_C + \frac{\bar{K}\bar{\rho}}{\bar{\alpha}} - \frac{I\bar{\rho}}{2X} \right) \quad (4.33)$$

Equations (4.31) and (4.33) are the conditions on  $I$ ,  $V$ , and  $X$  for  $Q_C$  to be positive.

#### 4.6 Variation of $Q_C$ versus $X$

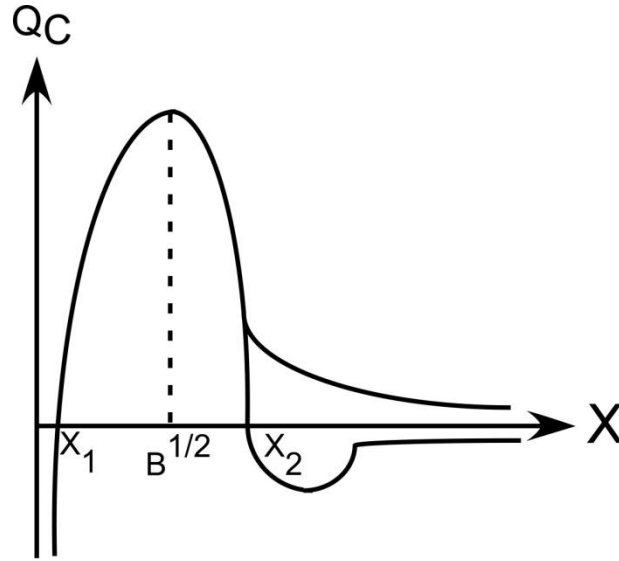


Figure 4.4:  $Q_C$  variation versus the  $X$ .

Differentiating equation (4.18) with respect to  $X$ , we get:

$$\frac{dQ_C}{dX} = -\frac{\bar{K}V}{\bar{\alpha}} + \frac{\bar{\rho}I^2}{2X^2} \quad (4.34)$$

$$\frac{dQ_C}{dX} = \frac{1}{X^2} \left[ -\frac{\bar{K}V}{\bar{\alpha}} X^2 + \frac{\bar{\rho}I^2}{2} \right] \quad (4.35)$$

$$\frac{dQ_C}{dX} = \frac{\bar{K}V}{\bar{\alpha}X^2} (\sqrt{B} - X)(\sqrt{B} + X) \quad (4.36)$$

where

$$\sqrt{B} = \sqrt{\frac{\bar{\alpha}\bar{\rho}I^2}{2\bar{K}V}} \quad (4.37)$$

Figure 4.4 shows a general shape of  $Q_C$  versus  $X$ ,  $Q_C$  will cross the  $X$ -axis at a one or two points depending on values of the different parameters.

In both cases,  $Q_C(\sqrt{B})$  needs to be positive for the TE sample to pump heat away from the cold side.

$$Q_C(\sqrt{B}) = \bar{\alpha}IT_C + \frac{\bar{K}I\bar{\rho}}{\bar{\alpha}} - \frac{\bar{K}V}{\bar{\alpha}} \sqrt{\frac{\bar{\alpha}\bar{\rho}I^2}{2\bar{K}V}} - \frac{\bar{\rho}I^2}{2} \sqrt{\frac{2\bar{K}V}{\bar{\alpha}\bar{\rho}I^2}} \quad (4.38)$$

$$Q_C(\sqrt{B}) = \bar{\alpha}IT_C + \frac{\bar{K}I\bar{\rho}}{\bar{\alpha}} - \sqrt{\frac{2\bar{K}V\bar{\rho}I^2}{\bar{\alpha}}} \quad (4.39)$$

$$Q_C(\sqrt{B}) = I \left[ \bar{\alpha}T_C + \frac{\bar{K}\bar{\rho}}{\bar{\alpha}} - \sqrt{\frac{2\bar{K}V\bar{\rho}}{\bar{\alpha}}} \right] \quad (4.40)$$

Multiplying  $Q_C(\sqrt{B})$  in equation (4.40) by the positive quantity

$\bar{\alpha}T_C + \frac{\bar{K}\bar{\rho}}{\bar{\alpha}} + \sqrt{\frac{2\bar{K}V\bar{\rho}}{\bar{\alpha}}}$  we get:

$$\left( \bar{\alpha}T_C + \frac{\bar{K}\bar{\rho}}{\bar{\alpha}} \right)^2 - \frac{2\bar{\rho}V\bar{K}}{\bar{\alpha}} > 0 \quad (4.41)$$

which is the same condition obtained during the analysis of  $Q_C$  versus  $I$  (equation (4.22)).

Now, we will determine the interval of  $X$  for which  $Q_C$  is positive. We will solve the quadratic equation  $Q_C(X) = 0$ .

$$Q_C = \bar{\alpha}IT_C + \frac{\bar{K}I\bar{\rho}}{\bar{\alpha}} - \frac{XV\bar{K}}{\bar{\alpha}} - \frac{\bar{\rho}I^2}{2X} = 0 \quad (4.42)$$

$$\left( \bar{\alpha}IT_C + \frac{\bar{K}I\bar{\rho}}{\bar{\alpha}} \right) X - \frac{X^2V\bar{K}}{\bar{\alpha}} - \frac{\bar{\rho}I^2}{2} = 0 \quad (4.43)$$

$$X^2 - \frac{\bar{\alpha}}{\sqrt{K}} \left( \bar{\alpha} T_C + \frac{\bar{K} \bar{\rho}}{\bar{\alpha}} \right) X - \frac{\bar{\rho} I^2}{2} \frac{\bar{\alpha}}{\sqrt{K}} = 0 \quad (4.44)$$

For equation (4.44) to have solution, its discriminant  $\Delta$  must be positive.

$$\Delta = \left[ \frac{\bar{\alpha} I}{\sqrt{K}} \right]^2 \left[ \left( \bar{\alpha} T_C + \frac{\bar{K} \bar{\rho}}{\bar{\alpha}} \right)^2 - \frac{2 \sqrt{K} \bar{\rho}}{\bar{\alpha}} \right] > 0 \quad (4.45)$$

Equation (4.45) is similar to the one in (4.22) derived during analysis of  $Q_C$  versus  $I$ .

The interval  $[X_1, X_2]$  for which  $Q_C$  will be positive is given by:

$$\frac{X_{1,2}}{I} = \frac{\bar{\alpha}}{2 \sqrt{K}} \left\{ \left( \bar{\alpha} T_C + \frac{\bar{K} \bar{\rho}}{\bar{\alpha}} \right) \pm \left[ \left( \bar{\alpha} T_C + \frac{\bar{K} \bar{\rho}}{\bar{\alpha}} \right)^2 - \frac{2 \sqrt{K} \bar{\rho}}{\bar{\alpha}} \right]^{\frac{1}{2}} \right\} \quad (4.46)$$

#### 4.7 Variation of $\Delta T$ versus $I$

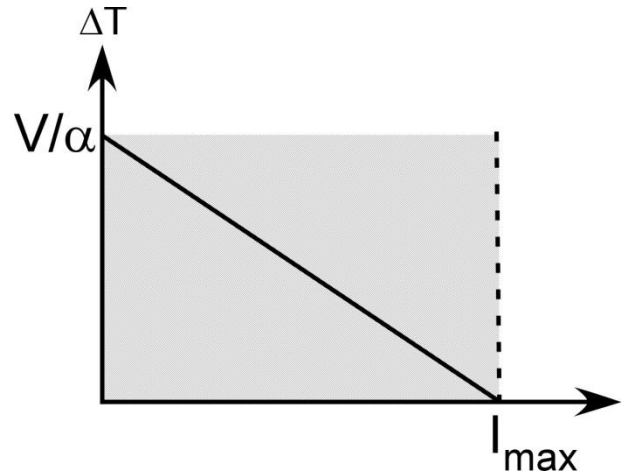


Figure 4.5: Variation of  $\Delta T$  versus  $I$ , the grey region presents the values of  $I$  giving a positive  $\Delta T$ .

Differentiating equation (4.17) with respect to  $I$ , we get:

$$\Delta T = \frac{V - \bar{\rho} \frac{1}{X} I}{\bar{\alpha}} \quad (4.47)$$

$$\frac{d\Delta T}{dI} = -\frac{\bar{\rho}}{\alpha X} \quad (4.48)$$

Figure 4.5 shows the variation of  $\Delta T$  versus the input current  $I$ , it appears that  $I$  needs to be less than  $I_{\max}$  for  $\Delta T$  to be positive.

$$I_{\max} = \frac{XV}{\bar{\rho}} \quad (4.49)$$

$$I < \frac{XV}{\bar{\rho}} \quad (4.50)$$

#### 4.8 Variation of $\Delta T$ versus $V$

Differentiating equation (4.17) with respect to  $V$ , we get:

$$\frac{d\Delta T}{dV} = \frac{1}{\alpha} \quad (4.51)$$

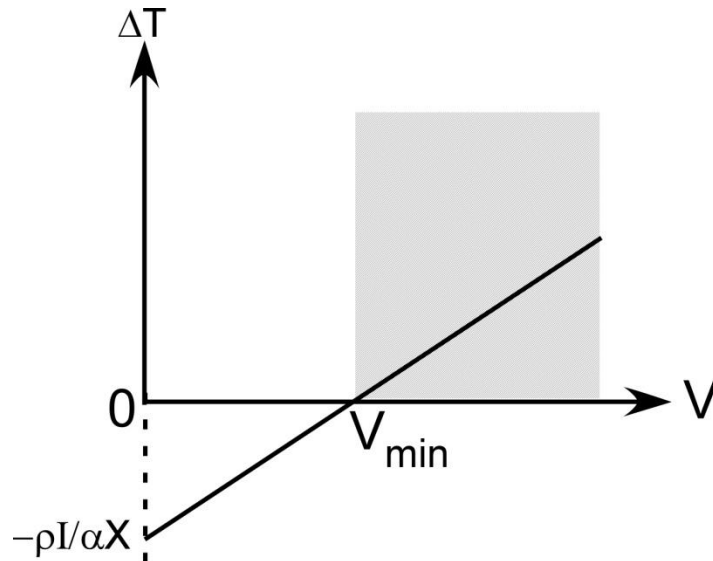


Figure 4.6: Variation of  $\Delta T$  versus  $V$ , the grey region presents the values of  $V$  giving a positive  $\Delta T$ .

Figure 4.6 shows a schematic plot of  $\Delta T$  versus  $V$ .  $V$  needs to be larger than  $V_{\min}$  for  $\Delta T$  to be positive.

$$V_{\min} = \frac{\bar{\rho}l}{X} \quad (4.52)$$

$$V > \frac{\bar{\rho}l}{X} \quad (4.53)$$

#### 4.9 Variation of $\Delta T$ versus $X$

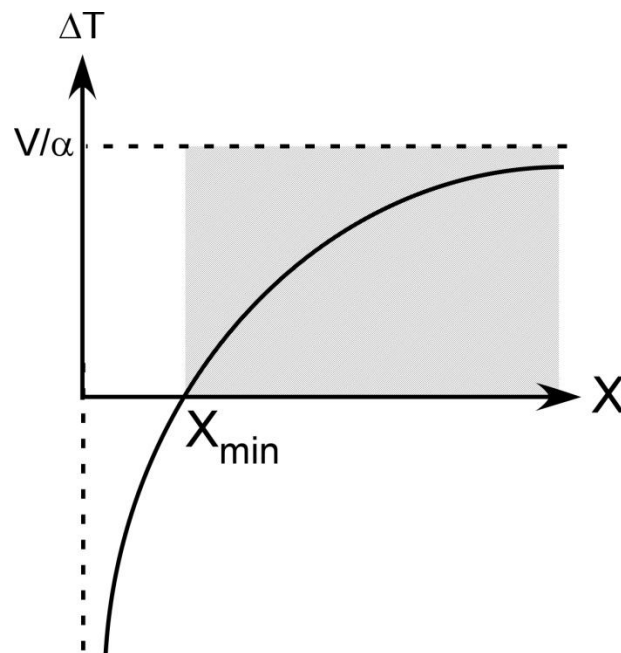


Figure 4.7: Variation of  $\Delta T$  versus  $X$ , the grey region presents the values of  $X$  giving a positive  $\Delta T$ .

From equation (4) we get:

$$\frac{d\Delta T}{dX} = \frac{\bar{\rho}l}{\alpha X^2} \quad (4.54)$$

Figure 4.7 shows the general shape of versus  $X$ .  $X$  needs to be larger than  $X_{\min}$  for  $\Delta T$  to be positive.

$$X_{\min} = \frac{\bar{\rho}I}{V} \quad (4.55)$$

$$X > \frac{\bar{\rho}I}{V} \quad (4.56)$$

Equations (4.50), (4.53), and (4.56) are all similar. The requirement for  $\Delta T$  to be positive is:

$$\frac{I}{X} < \frac{V}{\bar{\rho}} \quad (4.57)$$

So far, we have found the intervals of voltage  $V$ , current  $I$ , and area to length ratio  $X$  which yield a positive  $Q_C$  and  $\Delta T$ .

#### 4.10 Shared interval between $Q_C$ and $\Delta T$

In the following analysis, we will try to find the intervals of voltage  $V$ , current  $I$ , and area to length ratio  $X$  for which both  $Q_C$  and  $\Delta T$  will be positive.

For a given voltage  $V$  that satisfies equation (4.23).

$$V < \frac{\alpha}{2\bar{\rho}\bar{K}} \left( \bar{\alpha}T_C + \frac{\bar{K}\bar{\rho}}{\bar{\alpha}} \right)^2 \quad (4.58)$$

We can calculate  $\frac{I_1}{X}$  and  $\frac{I_2}{X}$  using equation (4.27).

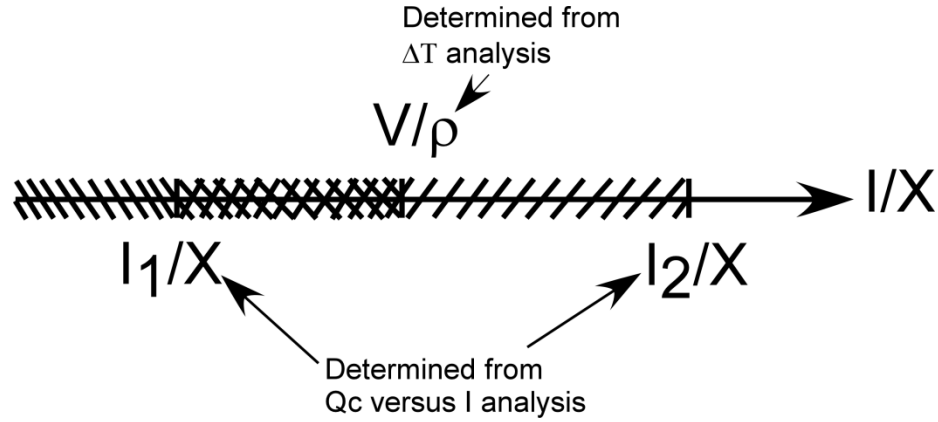


Figure 4.8: ranges of  $\frac{I}{X}$  leading to a positive  $Q_C$  and  $\Delta T$ .  $Q_C$  Will be positive when

$\frac{I_1}{X} < \frac{I}{X} < \frac{I_2}{X}$ , and  $\Delta T$  will be positive when  $\frac{I}{X} < \frac{V}{\rho}$ . The region between  $\frac{I_1}{X}$  and  $\frac{V}{\rho}$  represents the interval of  $\frac{I}{X}$  where both  $Q_C$  and  $\Delta T$  are positive.

It can be deduced from figure 4.8 that in order for  $Q_C$  and  $\Delta T$  to be positive at the same time, voltage  $V$  needs to be chosen so that  $\frac{V}{\rho}$  is larger than  $\frac{I_1}{X}$ , and smaller than  $\frac{I_2}{X}$ .

In conclusion, for the TE sample to pump heat from the cold side ( $Q_C > 0$ ), the voltage  $V$  needs to be in the following interval:  $\frac{\bar{\rho}I_1}{X} < V < \frac{\bar{\rho}I_2}{X}$ .

Using equation (4.15)  $\Delta T$  can be expressed as follows:

$$\Delta T = \frac{\bar{\alpha}IT_C - \frac{1}{2}\bar{\rho}\frac{L}{A}I^2 - Q_C}{\bar{K}\frac{A}{L}} \quad (4.59)$$



Inserting  $\Delta T$  expression in equations (4.11) and (4.13),  $\Delta P|_{\dot{M}=0}$  and  $\dot{M}|_{\Delta P=0}$  can be written as follow:

$$\Delta P|_{\dot{M}=0} = \frac{2P_{atm} \frac{M_t}{M_p} \left[ \bar{\alpha}IT_C - \frac{1}{2}\bar{\rho} \frac{L}{A} I^2 - Q_C \right]}{\left[ \bar{\alpha}IT_C - \frac{1}{2}\bar{\rho} \frac{L}{A} I^2 - Q_C \right] \left[ 1 + \frac{M_t}{M_p} \right] + 2\bar{K} \frac{A}{L} T_C} \quad (4.60)$$

$$\dot{M}|_{\Delta P=0} = 2M_t \varepsilon.a.P_{atm} \left( \frac{A}{L} \right)^{\frac{3}{2}} \sqrt{\frac{\bar{K} m}{K_B}} \frac{\bar{\alpha}IT_C - \frac{1}{2}\bar{\rho} \frac{L}{A} I^2 - Q_C}{\left[ \bar{\alpha}IT_C - \frac{1}{2}\bar{\rho} \frac{L}{A} I^2 - Q_C + 2\bar{K} \frac{A}{L} T_C \right]^{\frac{3}{2}}} \quad (4.61)$$

#### 4.11 Current giving a maximum $\Delta P|_{\dot{M}=0}$

Differentiating equation (4.60) with respect to  $I$  give the following expression (assuming  $Q_C = 0$ ):

$$\frac{d\Delta P|_{\dot{M}=0}}{dI} = 2P_{atm} \frac{M_t}{M_p} \frac{2\bar{K} \frac{A}{L} T_C \left[ \bar{\alpha}T_C - \bar{\rho} \frac{L}{A} I \right]}{\left\{ \left[ \bar{\alpha}IT_C - \frac{1}{2}\bar{\rho} \frac{L}{A} I^2 \right] \left[ 1 + \frac{M_t}{M_p} \right] + 2\bar{K} \frac{A}{L} T_C \right\}^2} \quad (4.62)$$

Equation (4.62) has a maximum at  $I = I_{opt} = \frac{\bar{\alpha}T_C}{\bar{\rho}} \frac{A}{L}$ .

$$\Delta P|_{\dot{M}=0} (I = I_{opt}) = \frac{2P_{atm} \frac{M_t}{M_p} \left( \frac{(\bar{\alpha}T_C)^2}{2\bar{\rho}} \frac{A}{L} \right)}{\left( \frac{(\bar{\alpha}T_C)^2}{2\bar{\rho}} \frac{A}{L} \right) \left( 1 + \frac{M_t}{M_p} \right) + 2\bar{K} \frac{A}{L} T_C} = \Delta P_{max} \quad (4.63)$$

$\Delta P_{max}$  Corresponds to the  $\Delta P|_{\dot{M}=0}$  for an input current  $I = I_{opt}$ . For any current  $I$ , the maximum pressure and mass flow rate are obtained when  $Q_C$  is zero, which justifies

our assumption for  $Q_C$ . Dividing both the numerator and the denominator of equation (4.63) by  $\bar{K}$ , we obtain:

$$\Delta P_{\max} = \frac{P_{\text{atm}} \frac{M_t}{M_p} \left( \frac{(\bar{\alpha} T_C)^2}{\bar{K} \bar{\rho}} \right)}{\left( \frac{(\bar{\alpha} T_C)^2}{2 \bar{K} \bar{\rho}} \right) \left( 1 + \frac{M_t}{M_p} \right) + 2 T_C} \quad (4.64)$$

The figure of merit  $Z$  of a TE material is given by [108, 109].

$$Z = \frac{\bar{\alpha}^2}{\bar{K} \bar{\rho}} \quad (4.65)$$

$Z$  has units of reciprocal of temperature.

$$\Delta P_{\max} = \frac{P_{\text{atm}} \frac{M_t}{M_p} Z T_C}{\frac{Z T_C}{2} \left( 1 + \frac{M_t}{M_p} \right) + 2} \quad (4.66)$$

$\Delta P_{\max}$  is independent of the dimensions of a rectangular-shaped TE. This result suggests that a pump can be optimized for mass flow rate without affecting the maximum pressure.

#### 4.12 Current giving a maximum $\dot{M}_{\max}$

For the mass flow rate  $\dot{M}|_{\Delta P=0}$  expression (4.61) to have real values, current  $I$  needs to be in the interval  $[0, I_{\max}]$ , where  $I_{\max}$  represents the largest root of the following quadratic equation:

$$\bar{\alpha} I T_C - \frac{1}{2} \bar{\rho} \frac{L}{A} I^2 + 2 \bar{K} \frac{A}{L} T_C \quad (4.67)$$

$$I_{\max} = \frac{A}{L} \left( \frac{\bar{\alpha}T_C}{\bar{\rho}} + \sqrt{\left( \frac{\bar{\alpha}T_C}{\bar{\rho}} \right)^2 + 4 \frac{\bar{K}T_C}{\bar{\rho}}} \right) \quad (4.68)$$

If  $Q_C$  is not zero, the new current interval will be smaller and can be calculated by solving the quadratic equation inside the cubic square root in equation (4.61).

Using equation (4.61) and assuming  $Q_C = 0$ , we are going to determine the optimal current that gives the maximum mass flow rate. To simplify the derived expressions we use the following expressions:

$$B = \bar{\alpha}IT_C - \frac{1}{2} \bar{\rho} \frac{L}{A} I^2 \quad (4.69)$$

$$C = 2\bar{K} \frac{A}{L} T_C \quad (4.70)$$

$$\frac{d\dot{M}}{dI} \Big|_{\Delta P=0} = D \frac{\left( B + C - \frac{3}{2} \right) \left( \bar{\alpha}T_C - \bar{\rho} \frac{L}{A} I \right) \sqrt{B+C}}{(B+C)^3} \quad (4.71)$$

$$\frac{d\dot{M}}{dI} \Big|_{\Delta P=0} = D \frac{\left( B + C - \frac{3}{2} \right) \left( \bar{\alpha}T_C - \bar{\rho} \frac{L}{A} I \right)}{\sqrt{B+C} (B+C)^2} \quad (4.72)$$

Analyzing equation (4.72), and operating with current  $I$  in the interval  $[0, I_{\max}]$ ,

we found that  $\dot{M} \Big|_{\Delta P=0}$  has a maximum at  $I = I_{opt} = \frac{\bar{\alpha}T_C}{\bar{\rho}} \frac{A}{L}$ .  $\dot{M} \Big|_{\Delta P=0}$  and  $\Delta P \Big|_{\dot{M}=0}$  will be maximal at the same current  $I = I_{opt}$ .

$$\dot{M} \Big|_{\Delta P=0} (I = I_{opt}) = M_t \varepsilon . a . P_{atm} \frac{A}{L} \sqrt{\frac{m}{K_B}} \frac{Z \sqrt{T_C}}{\left[ \frac{ZT_C}{2} + 2 \right]^{\frac{3}{2}}} = \dot{M}_{\max} \quad (4.73)$$

#### 4.13 Current giving a maximum $\Delta T$

Differentiating  $\Delta T$  (equation (4.59)) with respect to  $I$  ( $Q_C$  is zero), we obtain the following equation:

$$\frac{d\Delta T}{dI} = \frac{\bar{\alpha}T_C - \bar{\rho} \frac{L}{A} I}{\bar{K} \frac{A}{L}} \quad (4.74)$$

$$\Delta T, \dot{M}|_{\Delta P=0}, \text{ and } \Delta P|_{\dot{M}=0} \text{ are maximum for an input current } I = I_{opt} = \frac{\bar{\alpha}T_C}{\bar{\rho}} \frac{A}{L}.$$

These results agree with each other since a maximum temperature difference across a membrane will give a maximum mass flow rate and maximum pressure difference.

$$\Delta T(I = I_{opt}) = \frac{1}{2} Z T_C^2 = \Delta T_{max} \quad (4.75)$$

$\Delta T_{max}$  is independent of the TE dimensions [201, 202]. Next, we will use equations (4.66) and (4.73) to analyze the effects of the pore radius, figure of merit  $Z$ , type of working gas, and the tangential momentum accommodation coefficient (TMAC) on the maximum generated pressure and mass flow rate.

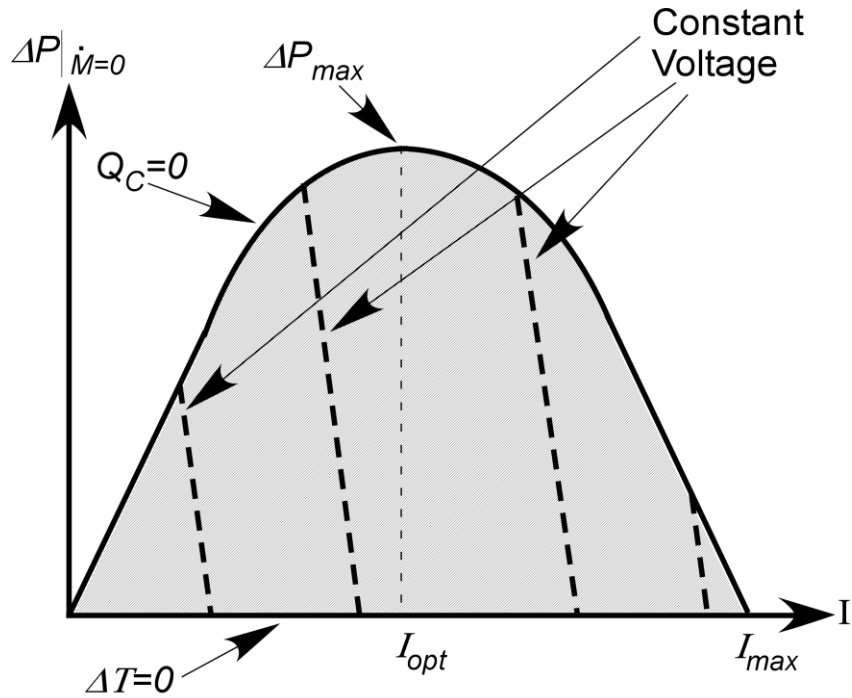


Figure 4.9: General shape of the  $\Delta P|_{\dot{M}=0}$  plot. The thick dashed line corresponds to the  $\Delta P|_{\dot{M}=0}$  versus current  $I$  for a constant voltage  $V$ . The solid line is the response when  $Q_C$  is zero and that is the maximum pressure for a given voltage and current.  $I_{opt}$  is the current for which  $\Delta P|_{\dot{M}=0}$ .

#### 4.14 Analysis of $\dot{M}|_{\Delta P=0}$ and $\Delta P|_{\dot{M}=0}$ for the TE Knudsen pump

##### 4.14.1 General shape of $\Delta P|_{\dot{M}=0}$

Figure 4.9 shows the general behavior of  $\Delta P|_{\dot{M}=0}$  versus the input current  $I$ . The solid parabolic line corresponds to  $Q_C = 0$ , along the line  $\Delta T$  and  $\Delta P|_{\dot{M}=0}$  are maximum for a given input current  $I$ . Values above the parabola line are not practical because the  $Q_C$  values are negative, which requires that heat is being pumped from the cold side by some external means other than the TE element. The gray region, under the parabola, corresponds to possible values of  $Q_C$  larger than zero. The value of  $Q_C$  is dependent on the TE material properties and the pump design.  $\Delta T$  is zero along the x-axis (current,  $I$ ) and that corresponds to the case where the rate of heat pumped by the TE reaches its

maximum,  $\Delta P|_{\dot{M}=0}$  is zero and the Knudsen pump can no longer pump. The thick dashed lines illustrate different values of current required to pump varying values of heat ( $Q_C$ ) from the cold side for a constant TE voltage  $V$ . The short interval of current is due to the conditions, discussed previously, on  $I$ ,  $V$ , and  $X$  to maintain positive values for  $\Delta T$  and  $Q_C$ . Table 4.1 gives the maximum and minimum currents for a given voltage  $V$ . The physical properties and dimensions of the TE element used in the calculation are collected in table 4.2. Figure 4.10 shows a plot of  $\Delta P|_{\dot{M}=0}$ , similar to the one in figure 4.9, which was generated for some  $V$  values (highlighted in table 4.1).

#### 4.14.2 Effect of the pore size and $Z$ value on $\Delta P_{\max}$ and $\dot{M}_{\max}$

Plots of  $\Delta P_{\max}$  and  $\dot{M}_{\max}$  (equations (4.66) and (4.73) ) against the TE  $Z$  value for of 22 nm, 50 nm and 102.7 nm pore radii are shown in figures 4.11 and 4.12, respectively. Table 4.3 gives the  $M_t$  and  $M_p$  [103] along with the corresponding Knudsen number for the studied pore sizes.  $P_{atm} = 101.325$  kPa, and  $T_C = 273.15$  K. Higher figure of merit  $Z$  material are desired because they can generate higher  $\Delta P_{\max}$  and  $\dot{M}_{\max}$ . A decrease in the channel radius,  $a$ , from 102.7 nm to 22 nm, leads to an increase in  $\Delta P_{\max}$  and a decrease in  $\dot{M}_{\max}$ . Using air as the working gas, the Knudsen number for studied pores (Table 4.3) lies in the interval [ 0.1, 10] corresponding to a transitional flow regime. The pressure driven backflow, corresponding to the second term with the negative sign in equation (4.1), decreases with decreasing pore sizes explaining the larger generated pressure  $\Delta P_{\max}$  for smaller pores.

Table 4.1: Maximum and minimum permitted current  $I$  for a given voltage  $V$ . These intervals assure that  $Q_C$  and  $\Delta T$  will be positive, and therefore proper operation of the TE based pump. The gray values are used in figure 4.10.

<b>Voltage (V)</b>	<b><math>I_{\max}</math> (A)</b>	<b><math>I_{\min}</math> (A)</b>
0.005	0.019	0.014
0.01	0.038	0.027
0.015	0.056	0.041
0.02	0.075	0.055
0.025	0.094	0.07
0.03	0.113	0.085
0.035	0.132	0.099
0.04	0.150	0.115
0.045	0.169	0.13
0.05	0.188	0.146
0.055	0.207	0.162
0.06	0.226	0.178
0.065	0.2444	0.195
0.07	0.263	0.212
0.075	0.282	0.229
0.08	0.30	0.247
0.085	0.3195	0.266
0.09	0.338	0.284
0.095	0.357	0.304
0.1	0.376	0.324
0.105	0.395	0.344
0.11	0.414	0.366
0.115	0.432	0.388
0.12	0.451	0.411
0.125	0.47	0.434
0.13	0.489	0.46
0.135	0.508	0.486
0.14	0.526	0.514
0.001	0.0038	0.0027
0.003	0.0113	0.0081
0.002	0.0075	0.0054
0.007	0.0263	0.019
0.009	0.034	0.0246
0.004	0.015	0.011
0.145	0.545	0.5435
0.1456	0.547	0.5472

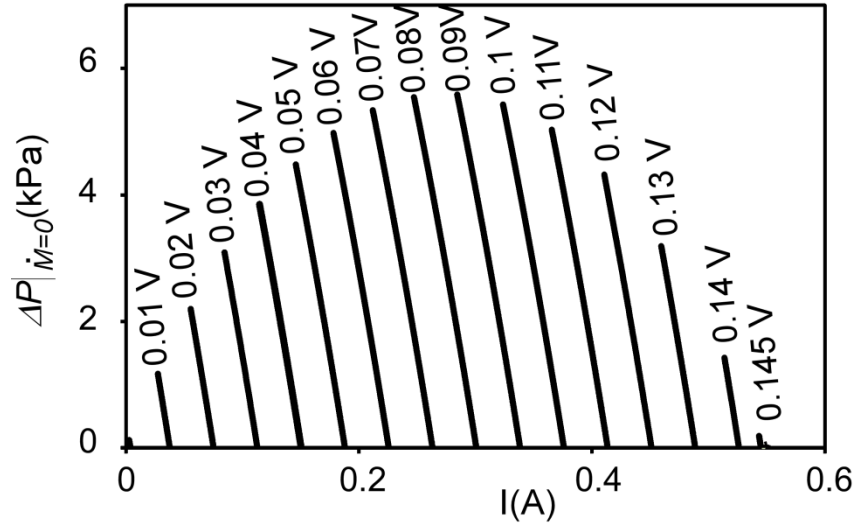


Figure 4.10:  $\Delta P|_{\dot{M}=0}$  versus  $I$  for a given voltage  $V$ .  $\Delta P|_{\dot{M}=0}$  values follow the parabola trend discussed in figure 4.9 . The corresponding max and min currents for the shown voltages are highlighted in table 4.1.

Similar results are seen in figures 4.13 and 4.14. The  $\Delta P_{\max}$  is largest in the free molecular flow regime, where the opposing flow is minimized. Ideally  $\dot{M}_{\max}$  is maximum in the slip flow regime where the pore size is larger and therefore the amount of gas flowing through the porous element per unit time is larger. In reality, a pressure driven backflow is always present and acts in the opposite direction of the thermal transpiration flow. The pressure driven backflow increases as the pore size increases causing a reduction in the overall mass flow rate. For the case of  $\Delta P=100$  Pa, the  $\dot{M}$  (Figure 4.13) peaks in the transitional flow regime [72]. As the pore size keeps increasing, the mass flow rate due to the backflow overcomes the thermal transpiration flow and yield a negative flow.



Table 4.2: Physical properties and dimensions of the TE element used in the calculation of  $I_{\max}$ ,  $I_{\min}$ ,  $\Delta P_{\max}$ , and  $\dot{M}_{\max}$ .

TE properties			
Thermal conductivity (W/m·K)	Electrical resistivity ( $\mu\Omega\cdot m$ )	Seebeck coefficient ( $\mu V/K$ )	$Z$ ( $K^{-1}$ )
0.37	133	266.8	0.0014
TE dimensions			
Width (mm)	Thickness (mm)	Length (mm)	Porosity $\varepsilon$
13	0.5	13	0.297

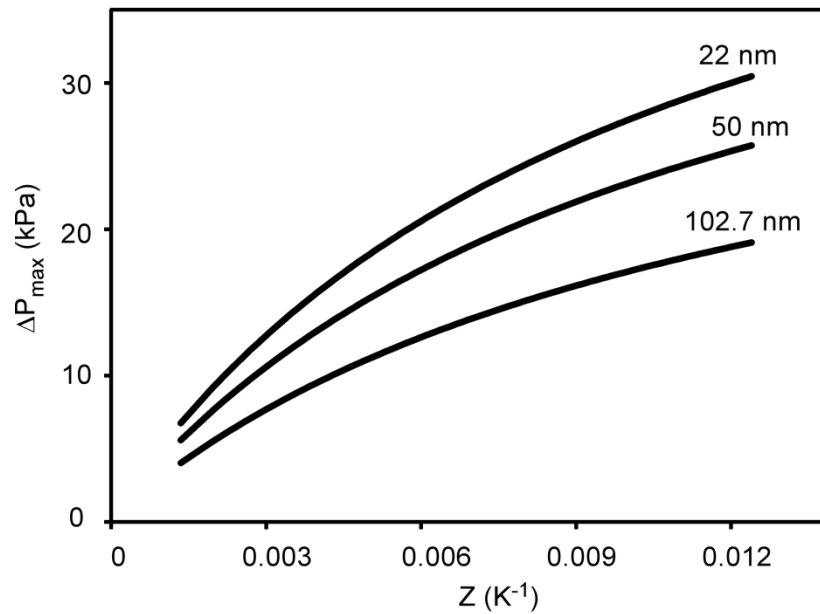


Figure 4.11:  $\Delta P_{\max}$  versus the TE figure of merit  $Z$  at the optimum current  $I_{opt}$  for 22 nm, 50 nm and 102.7 nm pore sizes.

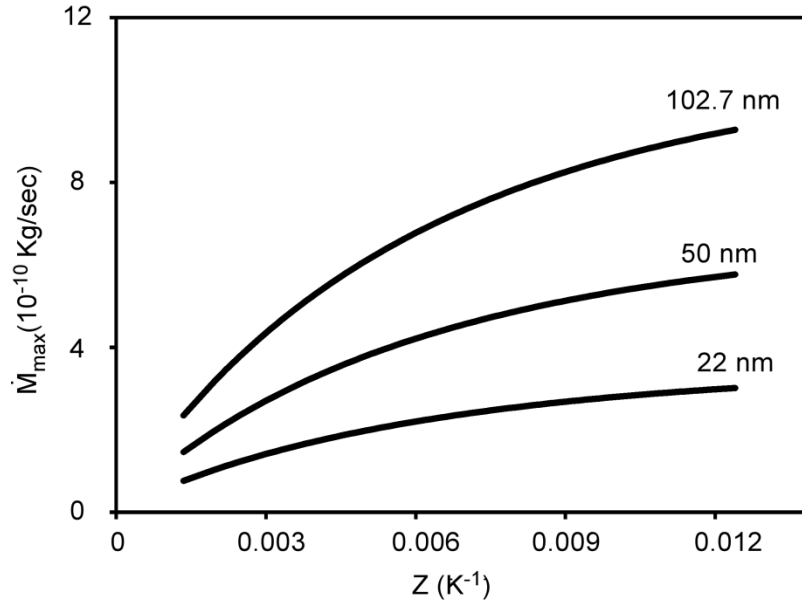


Figure 4.12:  $\dot{M}_{\max}$  versus the TE figure of merit  $Z$  at the optimum current  $I_{opt}$  22nm, 50 nm and 102.7 nm pore sizes. Increasing the pore radius will increase the mass flow rate. The working gas is air.

Table 4.3: Pore sizes used in this study along with their transpirational flow coefficient  $M_t$ , pressure return flow coefficient  $M_p$ , and the Knudsen number calculated for air at room pressure and temperature.

	$M_t$	$M_p$	$Kn$
22 nm	0.53	1.388	2.96
50 nm	0.449	1.42	1.3
102.7 nm	0.351	1.56	0.63

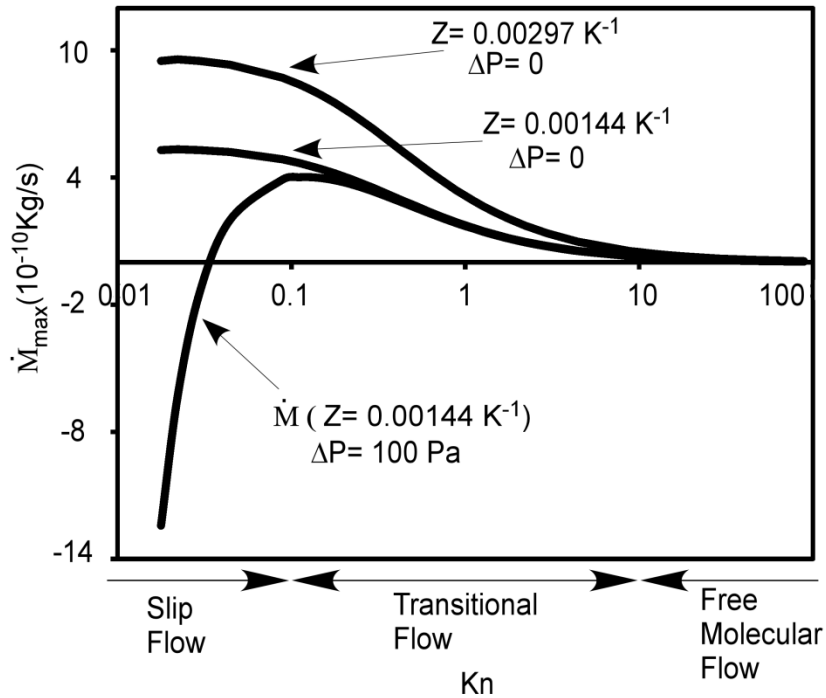


Figure 4.13:  $\dot{M}_{max}$  in the different flow regimes. The maximum mass flow is obtained at the slip flow regime, where the pore size is largest. Higher  $Z$  values yield higher mass flow rate.  $Z=0.00144 \text{ K}^{-1}$  is the value we have measured for the sintered sample fabricated in the lab,  $Z=0.00297 \text{ K}^{-1}$  is the current value in TE coolers and generators. In practice, a non-zero pressure difference causes a pressure driven backflow that causes  $\dot{M}$  to have a maximum in the transitional flow regime.  $Kn$  values along the x-axis are calculated for air at room temperature and pressure.

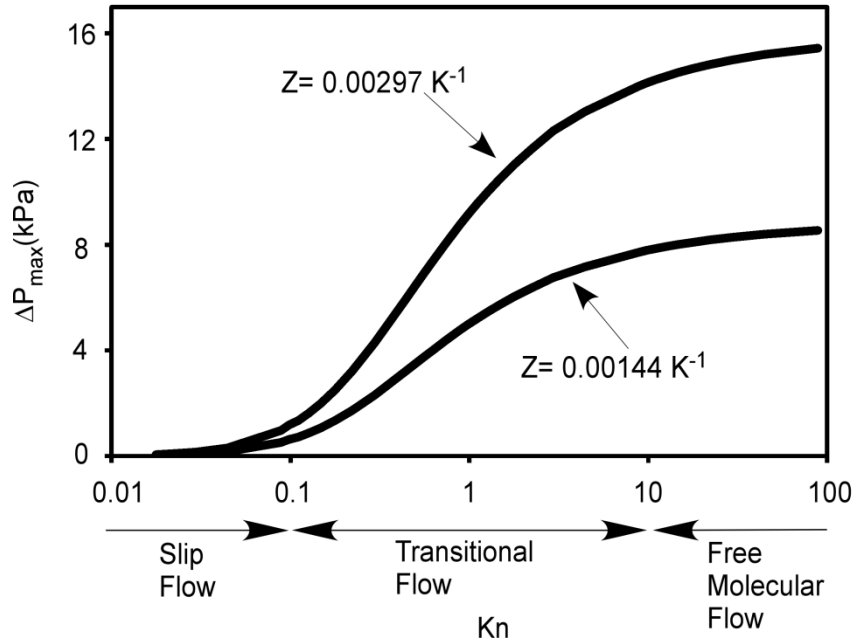


Figure 4.14:  $\Delta P_{\max}$  in the different flow regimes. The maximum pressure is obtained in the free molecular flow regime where the pore size is much smaller.  $Kn$  is calculated for air at room temperature and pressure.  $Z = 0.00144 \text{ K}^{-1}$  is the value we have measured for the sintered sample fabricated in the lab,  $Z = 0.00297 \text{ K}^{-1}$  is the current value in TE coolers and generators.

#### 4.14.3 Effect of the working gas on $\dot{M}_{\max}$ and $\Delta P_{\max}$

Effect of the molecular mass of the working gas has been also investigated. Table 4.4 shows the different gases that we have considered.  $M_t$  and  $M_p$  values for the different gases were obtained by fitting the data from Sharipov's paper [103]. Figure 4.15 shows the fitted data along with the equations used to calculate  $M_t$  and  $M_p$  for each gas. Figure 4.16 shows the resulting mass flow rate plotted against the TE  $Z$  value. The pore radius is 50 nm. Higher  $Z$  values result in a higher mass flow rate. As the molecular mass of gas increases the mass flow rate increases. The opposite trend is seen for the maximum generated pressure. As the molecular mass increases, the maximum pressure decreases.

Table 4.4: Molecular mass, mean free path [98] and the Knudsen number of the different gases investigated in figure 4.16.  $M_t$  and  $M_p$  calculated using equations in figure 4.15.

	Working gas					
	Xe	Ar	O <sub>2</sub>	Air	He	H <sub>2</sub>
Molecular mass (10 <sup>-26</sup> kg)	21.8	6.63	5.31	4.81	0.66	0.34
Mean free path (nm)	37.6	66.6	67.9	64	186.2	117.7
Knudsen number	0.75	1.28	1.36	1.28	3.72	2.35
$M_t$	0.368	0.434	0.437	0.4298	0.554	0.50
$M_p$	1.502	1.424	1.422	1.429	1.405	1.39

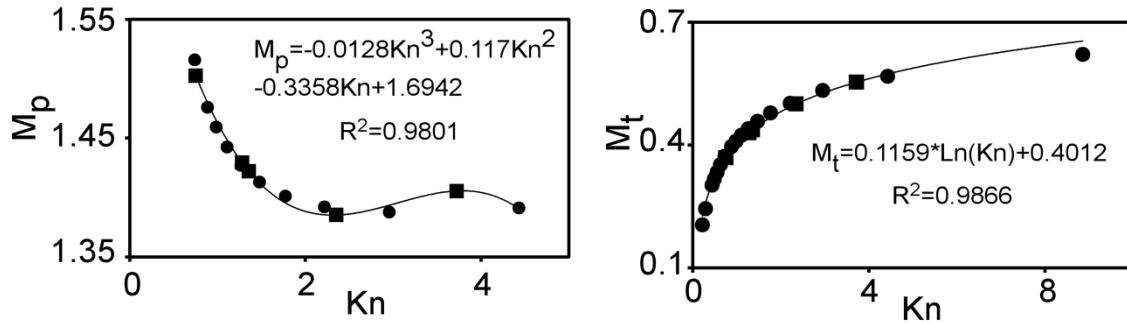


Figure 4.15: Plot of  $M_t$  and  $M_p$  reported by sharipov [103]. The fitting equations were used to calculate  $M_t$  and  $M_p$  for different gases. Circles are Sharipov's data and the square ones are the calculated values using the fitting equations.

#### 4.14.4 Effect of the TMAC value on $\Delta P_{\max}$ and $\dot{M}_{\max}$

Another parameter that can affect the overall pressure and mass flow rate of a knudsen pump is the tangential momentum accommodation coefficient (TMAC),  $\alpha$ , which has to do with the interaction of the gas molecules with the channel wall. This coefficient depends on many parameters such as wall and gas molecule temperatures, mean free path of the gas molecules and wall roughness [183, 203]. All previous generated plots in this chapter assumed  $\alpha$  to be unity, implying a complete diffusive reflection at the wall surface.

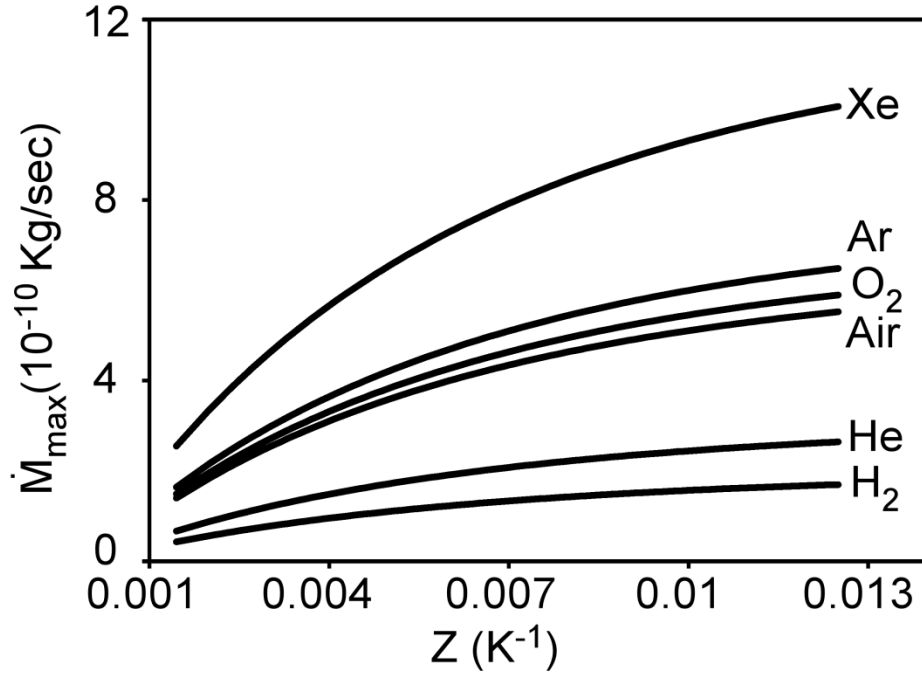


Figure 4.16:  $\dot{M}_{\max}$  versus the figure of merit  $Z$  for different working gases. As the molecular mass increases the mass flow rate increases.  $M_p$  and  $M_t$  for the different gases are shown in table 4.4. The pore size is 50 nm for all gases.

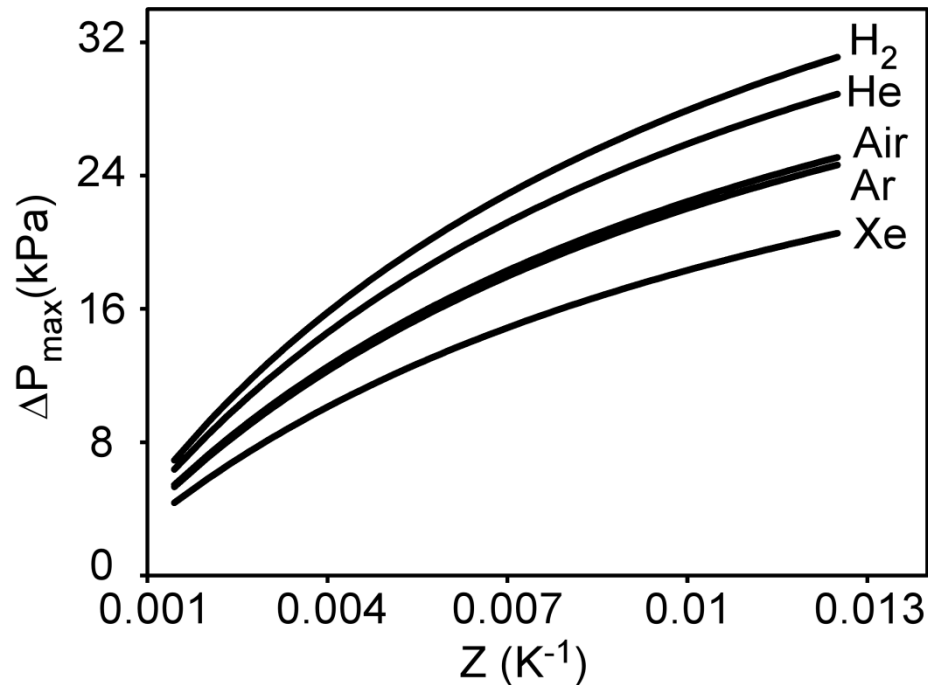


Figure 4.17:  $\Delta P_{\max}$  versus the figure of merit  $Z$  for different working gases and a pore radius of 50 nm. As the molecular mass decreases the pressure increases.  $M_p$  and  $M_t$  for the different gases are shown in table 4.4.

We have studied three different  $\alpha$  values, 0.6, 0.8, and 1. The corresponding  $M_i$  values are shown in table 4.4 for a 50 nm pore radius. Figures 4.18 and 4.19 show the pressure and mass flow rate for each  $\alpha$  value. It can be concluded that as  $\alpha$  increases the generated pressure increases and the mass flow rate decreases.

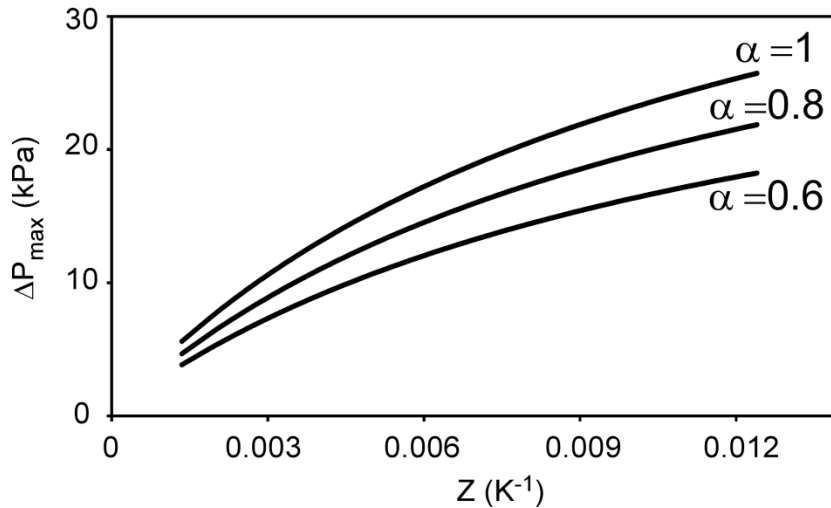


Figure 4.18:  $\Delta P_{\max}$  for different TMAC values. As  $\alpha$  increases the  $\Delta P_{\max}$  increases. The working gas is air at room temperature and pressure. The pore radius is 50 nm.

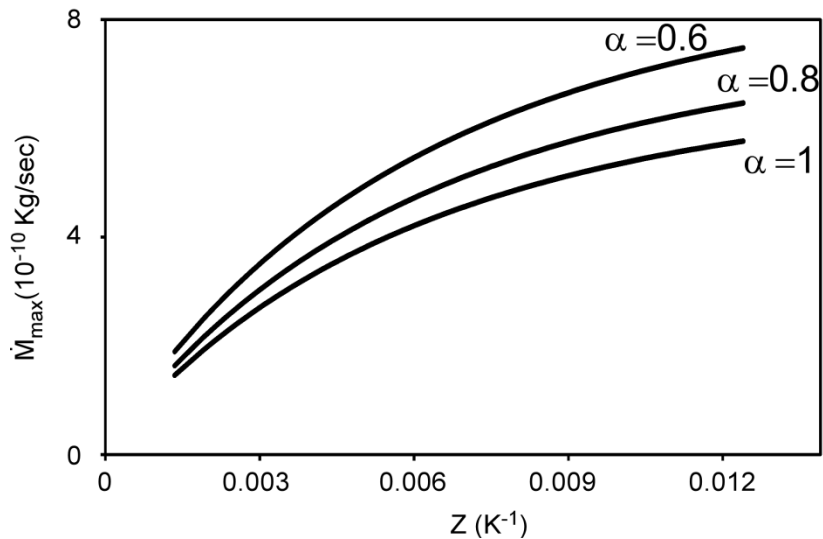


Figure 4.19:  $\dot{M}_{\max}$  for different TMAC values. As  $\alpha$  decreases the  $\dot{M}_{\max}$  increases. The working gas is air at room temperature and pressure and the pore radius is 50 nm.

#### 4.15 Conclusion

A mathematical model for the nanoporous TE based Knudsen pump was derived. The starting point is the Sharipov's equation, which relates the pressure and the mass flow rate for a thermal transpiration device, and the TE equations relating current, voltage, temperature, and heat flow. We found an optimal current,  $I_{opt}$ , that results in the maximum pressure difference,  $\Delta P|_{\dot{M}=0}$ , mass flow rate,  $\dot{M}|_{\Delta P=0}$ , and temperature difference,  $\Delta T$ .

The effect of pore size, TE material figure of merit  $Z$ , working gas, and the TMAC value on the  $\Delta P_{max}$  and  $\dot{M}_{max}$  were studied and discussed. Three pore radii were used as an example: 25 nm, 50 nm, and 102.7 nm. We found that as the pore size becomes smaller within the free molecular regime, the generated pressure increases and the mass flow rate decreases. We also found that the mass flow rate has a peak in the transitional flow regime.

Similarly to TE coolers and generators, higher  $Z$  value TE materials yield a higher pressure and a higher mass flow rate. Different gases, due to the difference in their molecular mass and mean free path, will have a different mass flow rate and pressure. The higher the molecular mass, the higher the mass flow rate and the lower the pressure difference.

The TMAC value, assumed in many applications to be equal to unity, has an effect on the  $\Delta P_{max}$  and  $\dot{M}_{max}$ . Three values were studied: 0.6, 0.8, and 1. We found that as the TMAC value increases, the pressure difference increases and the mass flow rate



decreases. The TMAC depends on parameters such as the channel wall temperature and roughness. The next chapter will describe a set-up for measuring the TMAC.

## CHAPTER 5: GAS FLOW THROUGH NANOPOROUS MEMBRANES

This chapter describes pressure/flow rate analysis conducted on commercial track-etched Whatman membranes. These membranes can be used in devices based on thermal transpiration to generate flow rate and pressure difference. The goal behind the analysis is to be able to determine the pressure difference and/or flow rate using the experimental conditions, working gas characteristics, and membrane physical properties. Methods are first described, followed by theoretical calculation using different models. Finally, a comparison between theoretical and experimental results is established and conclusions are extracted.

### 5.1 Introduction

Commercial nanoporous membrane with pore sizes 200 nm or less can be used to generate pressure and flow rate using the thermal transpiration effect. Bell [204] from our group used polypropylene nanoporous membrane to fabricate an infusion pump driven with the body heat. Gupta et al.[19] used nanoporous ceramic (zeolite) to fabricate multiple stages Knudsen pump. With the development in nanotechnology and microfabrication, much more applications of the nanoporous membranes are expected in the future. Therefore a good understanding of the relationship between the flow rate and pressure data will help accurately predict these membranes' performance.

## 5.2 Theoretical equations for gas flow

The following equations, which have been described in the background chapter, will be used to calculate the mass flow rate through the membranes using the membrane and working gas properties, working temperature, and in some cases one of the experimental pressure across the membrane.

- Sharipov's equation (2.69).
- Arkilic's equation (2.66).
- Poiseuille's equation (2.67).
- Knudsen flow equation (2.30).
- Knudsen and Poiseuille flows combined (2.68).
- Sears' equation (2.77), combination of gas flow and surface flow.

## 5.3 Experimental procedure

All experiments were performed in a plastic box in order to reduce pressure and temperature fluctuations around the membrane which may alter the experimental readings. The studied membranes (25 mm diameter) are track-etch type nuclepore polycarbonate membrane (Figure 5.1) from Whatman<sup>TM</sup> GE Healthcare. They have straight pore channels made through particle bombardment followed by chemical etching of the irradiated regions. Table 5.1 summarizes the investigated membrane characteristics.

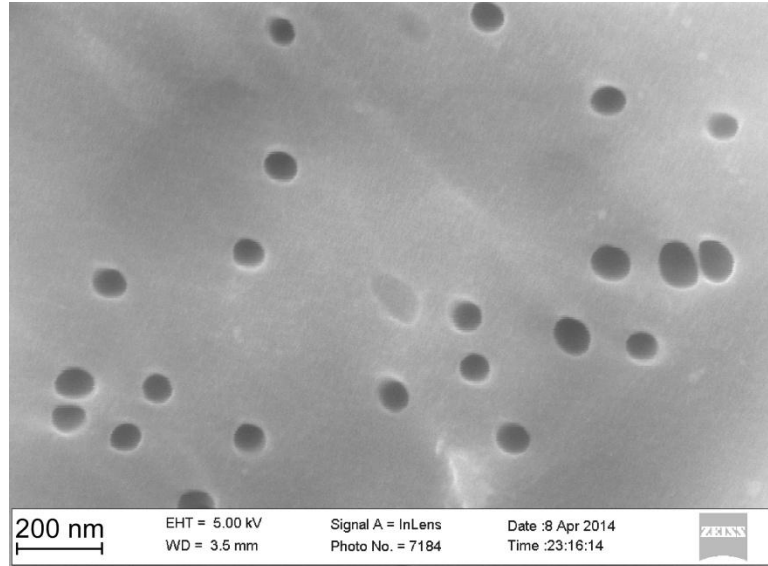


Figure 5.1: A Scanning Electron Microscopy image of a 80nm pore diameter track-etched polycarbonate membrane.

Table 5.1: Investigated membrane characteristics. The membrane size corresponds to the average pore diameter. The  $Kn$  and  $\delta$  are calculated for air at room conditions ( $\lambda=68$  nm). The number of pores is obtained by multiplying the membrane pore density by the area. The first three columns are data from the manufacturer and the rest are calculated.

Membrane pore size (nm)	Thickness ( $\mu\text{m}$ )	Pore density $10^8$ (pores/cm <sup>2</sup> )	Length/radius ratio	Knudsen number $Kn$	Number of pores $N \times 10^8$	Rarefaction parameter $\delta$
15	6	6	800	9.07	29.45	0.098
30	6	6	400	4.53	29.45	0.195
50	6	6	240	2.72	29.45	0.326
80	6	6	150	1.7	29.45	0.52
400	10	1	50	0.34	4.9	2.6

A schematic of the experimental setup is shown in figure 5.2. The whole set-up is placed inside a sealed box (Box A) to minimize the effect of airflow on the pressure readings. When the experiment is conducted at 50 °C, only Box B is heated to that temperature using a temperature controller with a strip heater. The reason for only

heating the small box (Box B) is because the pressure sensors, contained in the big box (Box A) have a temperature compensation of 15 to 45 °C. This means that when operating at higher temperatures, the reading from the sensors will not be accurate. The nanoporous membrane is glued on an aluminum plate (Figure 5.3). A hole is drilled on the plate to fit a tube which connects to an airtight glass syringe (I.D.=14.57 mm, 10 ml, Hamilton Company) and a digital pressure sensor (Mensor, Inc) (Accuracy: 0.02% Full scale, precision: 0.06% Full scale), for pressure measurement, using a T-connector. The syringe is attached to a NE-400 double syringe pump set to the desired flow rate. Pressure is recorded using a custom LabVIEW program.

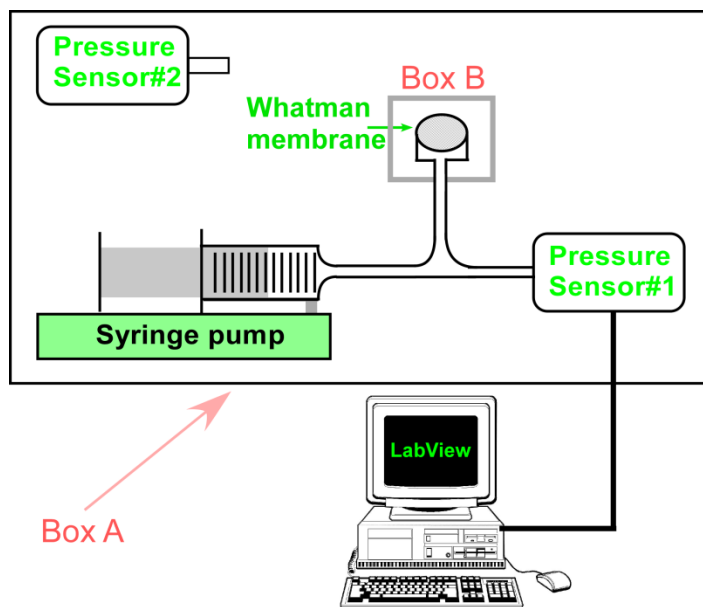


Figure 5.2: Schematic of the setup used to measure the pressure versus the flow rate for the track-etched Whatman membranes. Box A is kept at room temperature all the time. Box B is either left at room temperature or heated to 50 °C depending on the experiment.

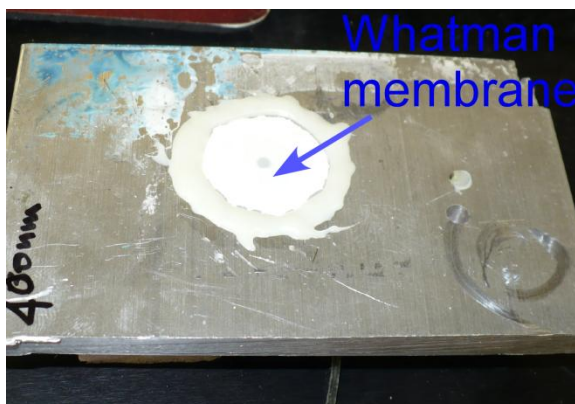


Figure 5.3: Image of the nanoporous Whatman membrane glued on an Aluminum substrate. A hole for gas flow is drilled on the plate underneath the membrane.

Two pressure sensors are used, #1 is connected to the membrane setup, and the 2<sup>nd</sup> one (Pressure sensor#2) is used to measure the pressure inside the box (room pressure). Pressure reading is started with the syringe pump turned off. The initial collected pressure data are used to account for the offset reading between the two pressure sensors. Once enough data points are collected, the syringe pump is started. Seven flow rate values have been used in these experiments (10, 30, 50, 100, 200, 300, 350  $\mu\text{l}/\text{min}$ ).

#### 5.4 Materials:

SEM images of the Whatman membranes were analyzed using ImageJ software to determine the average pore density and size. About 80 measurements were taken for each pore size on each face using different SEM images. To determine the pore density, about ten images for different regions of the membrane surface were used, the number of pores are counted and divided by the total area calculated using the SEM image scale bar and ImageJ. The average membrane pore sizes on the front side are different than the one on the back side. It was hard to obtain clear images for the 15 nm membranes because the pore size was too small (Table 5.2).

Table 5.2: Comparison of the manufacturer and measured membrane pore size and pore density. Pore size is measured through analysis of SEM images of the membranes using ImageJ software. About 80 measurements were taken and averaged. Pore density is calculated by counting the number of pores on the image and dividing it by the image area (about 10 images used for pore density calculation).

Manufacturer reported pore size (nm)	Measured pore size back side (nm)	Measured pore size front side (nm)	Calculated pore density $\times 10^8$
400	345.1	451.8	-----
80	71.9	82.9	4
30	35.4	29.6	-----
15	-----	-----	-----

### 5.5 Experimental results

An example of the pressure difference versus time plot for the 15 nm pore size membrane is shown in figure 5.4. Pressure is given enough time to stabilize before moving to the next flow rate value. Flow rate data versus the pressure were also collected when no membranes were connected to the experimental set up. These pressure values are subtracted from the overall pressure to exactly determine the pressure difference across the membrane. Pressure versus flow rate due to the tubing and different fittings are shown in figure 5.5. As expected, flow rate is increasing linearly with pressure, and a change of the experimental box temperature did not affect the tubing/fittings flow resistance.

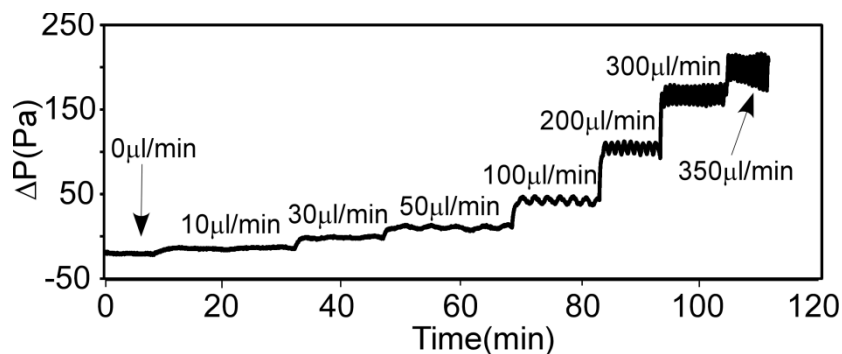


Figure 5.4: Pressure difference across the 15 nm Whatman membrane versus time for different flow rate values set on the syringe pump.

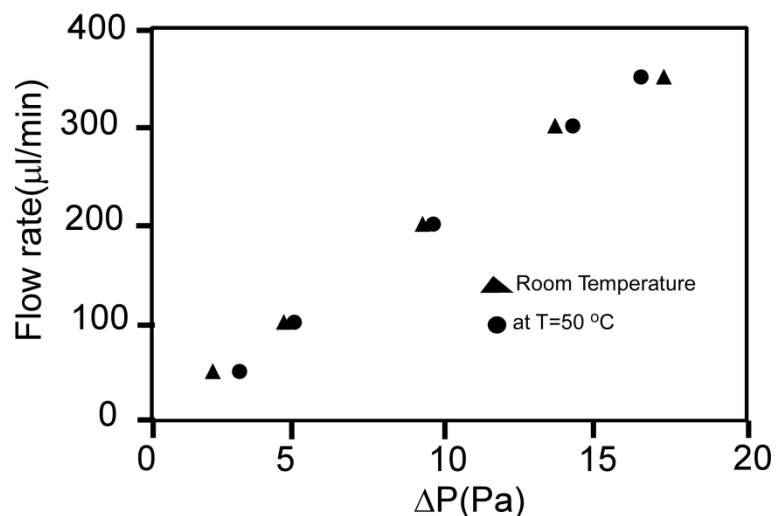


Figure 5.5: Flow rate versus the pressure difference when no membrane is connected to the set up. The circular data corresponds to the situation when the experimental box was heated to 50 °C.

The following tables represent the experimental data obtained for the different membranes after subtracting the pressure due to the tubing/fittings.

**Data obtained when experimental box (Box A and B) at room temperature**

Table 5.3: Experimental data for the different nanoporous membranes when both boxes (A and B) are kept at room temperature.

15 nm pore size				
Experimental flow rate(µl/min)	P <sub>L</sub> (kPa)	P <sub>H</sub> (kPa)	ΔP (Pa)	P <sub>av</sub> (kPa)
50	98.5	98.52	22.82	98.51
100	98.45	98.51	52.4	98.48
200	98.44	98.55	110.1	98.49
300	98.45	98.62	168.63	98.54
350	98.47	98.67	196.1	98.57



30 nm pore size				
Experimental flow rate( $\mu\text{l}/\text{min}$ )	$P_L$ (kPa)	$P_H$ (kPa)	$\Delta P$ (Pa)	$P_{av}$ (kPa)
50	98.74	98.75	11.86	98.74
100	98.87	98.89	23.3	98.88
200	98.89	98.94	46.37	98.92
300	98.5	98.57	66.4	98.53
350	98.48	98.56	76.26	98.52

50 nm pore size				
Experimental flow rate( $\mu\text{l}/\text{min}$ )	$P_L$ (kPa)	$P_H$ (kPa)	$\Delta P$ (Pa)	$P_{av}$ (kPa)
50	100.42	100.42	3.43	100.42
100	100.40	100.42	6.91	100.41
200	100.4	100.41	13.64	100.4
300	100.38	100.4	20.11	100.39
350	100.37	100.39	22.14	100.38

80 nm pore size				
Experimental flow rate( $\mu\text{l}/\text{min}$ )	$P_L$ (kPa)	$P_H$ (kPa)	$\Delta P$ (Pa)	$P_{av}$ (kPa)
50	99.27	99.27	1.66	99.27
100	99.22	99.22	4.03	99.22
200	99.19	99.2	8.74	99.19
300	99.09	99.1	14.11	99.1
350	99.07	99.08	15.04	99.07

400 nm pore size				
Experimental flow rate( $\mu\text{l}/\text{min}$ )	$P_L$ (kPa)	$P_H$ (kPa)	$\Delta P$ (Pa)	$P_{av}$ (kPa)
50	99.42	99.43	1.78	99.43
100	99.44	99.44	3.36	99.44
200	99.48	99.48	6.52	99.48
300	99.51	99.52	9.98	99.51
350	99.52	99.53	10.39	99.53

**Data obtained when experimental box (Box B) at 50°C**

Table 5.4: Experimental data for the different nanoporous membranes when box A at room temperature and box B at 50 °C.

15 nm pore size				
Experimental flow rate( $\mu\text{l}/\text{min}$ )	$P_L$ (kPa)	$P_H$ (kPa)	$\Delta P$ (Pa)	$P_{av}$ (kPa)
50	99.30	99.36	57.42	99.33
100	99.37	99.48	114.61	99.42
200	99.32	99.55	226.15	99.44
300	99.32	99.66	336.67	99.49
350	99.71	99.31	391.69	99.51

50 nm pore size				
Experimental flow rate( $\mu\text{l}/\text{min}$ )	$P_L$ (kPa)	$P_H$ (kPa)	$\Delta P$ (Pa)	$P_{av}$ (kPa)
50	99.50	99.51	2.97	99.51
100	99.47	99.48	7.13	99.48
200	99.49	99.51	14.18	99.5
300	99.50	99.52	20.98	99.51
350	99.51	99.54	24.28	99.52

80 nm pore size				
Experimental flow rate( $\mu\text{l}/\text{min}$ )	$P_L$ (kPa)	$P_H$ (kPa)	$\Delta P$ (Pa)	$P_{av}$ (kPa)
50	100.14	100.141	3.12	100.14
100	100.14	100.15	5.396	100.143
200	100.14	100.15	10.71	100.15
300	100.14	100.16	15.80	100.15
350	100.13	100.15	18.25	100.144

400 nm pore size				
Experimental flow rate( $\mu\text{l}/\text{min}$ )	$P_L$ (kPa)	$P_H$ (kPa)	$\Delta P$ (Pa)	$P_{av}$ (kPa)
50	99.68	99.68	1.454	99.682
100	99.715	99.72	4.251	99.717
200	99.711	99.72	8.424	99.715
300	99.714	99.727	12.344	99.721
350	99.707	99.7215	14.727	99.714

## 5.6 Discussion

### 5.6.1 End effect

In many cases, the channels are assumed to be infinitely long and the end effects are neglected [92, 205, 206]. Titarev [207] used numerical solution of the linearized model collision integral to determine the mass flow of rarefied gas in a circular pipe as a function of length to radius ratio and degree of gas rarefaction. For the investigated membranes, the smallest length to radius ratio is 50, which corresponds to the 400 nm membrane. Based on the same work performed by Titarev [207], the end effects for this membrane size are less than 4% compared to a similar membrane with an infinite thickness. For the rest of membrane sizes, the length to radius ratios are 150, 240, 400, 800 for 80 nm, 50 nm, 30 nm, and 15 nm membrane pore sizes, respectively.  $L \gg a$ , the end effects or membrane entrance have no effects on the overall flow rate.

### 5.6.2 Tangential Momentum Accommodation Coefficient measurement

Initially, the objective of the flow analysis through the nanoporous membranes was to determine the TMAC value. As it has been shown in section 2.20, this coefficient has a value between 0 and 1, depends on many parameters such as channel wall temperature, material, and roughness and can affect the flow rate value. The technique that was followed to calculate the TMAC is similar to the one described in the following

references [183, 184], especially in the transitional and free molecular regimes. It consists of visually comparing the measured modified flow rates  $G$  with the available theoretical ones for various TMAC values.

The method starts by measuring a dimensionless mass flow rate  $G$  (Eq. (2.69)) through a cross section of the channel for different values of the rarefaction parameter

$$\delta = \sqrt{\pi} / 2Kn.$$

Large values of  $\delta$  correspond to the continuum regime, and small values to the free molecular regime. The variation of  $\delta$  was done by changing the channel pore size, large channel radius corresponds to larger values of  $\delta$ . Fitting equations of the  $G$  reported data in the literature versus  $\delta$  for different  $\alpha$  values were generated and used to calculate the new  $\alpha$  values using the measured  $G$  (Equations (2.73) and (2.74)). Table 5.5 shows the calculated  $\alpha$  values using the measured  $G$  and fitting equations.

Table 5.5:  $\alpha$  values calculated using the experimental  $G$  values and fitting equations from the literature.

Pore size (nm)	Both boxes (A and B) at room temperature		Box A at room temperature and box B at 50°C	
	$\alpha$ from fit eq.(2.73)	$\alpha$ from fit eq.(2.74)	$\alpha$ from fit eq.(2.73)	$\alpha$ from fit eq.(2.74)
400	1.63	1.590	1.64	1.603
80	0.84	0.846	0.984	0.988
50	-0.33	-0.316	-0.261	-0.251
30	-1.009	-0.996	-----	-----
15	-7.196	-7.21	-2.424	-2.44

The obtained TMAC values were larger than one for the 400 nm membrane, and negative for 15, 30, and 50 nm membranes. In both cases, these are not practical. Only 80 nm membrane yielded reasonable value. Another conclusion from the table is that the

TMAC values are in the same range for a given pore size, however they are different when the pore size is changed. One question that we raised during data analysis is: are the flow rates we are measuring accurate? To answer this question, the experiments were repeated and compared to different theoretical model reported in the literature.

### 5.6.3 Comparison of the experimental results with theoretical models

The experimental pressure data are used in the equations, stated in the theoretical equations section, in order to calculate the flow rate through the membranes. Tables 5.6 and 5.7 give the ratio of the calculated flow rate to the corresponding experimental one. For the 400 nm membrane, the calculated flow rates are larger than the experimental. On the other hand, for the smaller membranes, 50, 30, and 15 nm, experimental data are larger. A very slight increase in the data collected inside the heated box can be inferred from the tables. We believe that the discrepancy in the flow rate data for small pores is due to the absence of a surface diffusion term in the models used. The next section will show the results obtained with a model in which gas flow and surface diffusion flow were combined.

Table 5.6: Comparison between experimental and theoretical flow rate through the Whatman membranes. Numbers in the table correspond to the ratio of theoretical to experimental flow rate. Experimental box set up is kept at room temperature (25 °C).

	Sharipov equation Eq (2.69)	Arkilic equation Eq (2.66)	Poiseuilles flow Eq (2.67)	Knudsen flow Eq (2.30)	Knudsen and Poiseuilles flows combined Eq (2.68)
400	×9	×2.2	×3.8	×7.63	×11
80	×0.75	×0.05	×0.08	×0.8	×0.88
50	×0.28		×0.19	×0.3	×0.32
30	×0.2		×0.008	×0.22	×0.23
15	×0.06		×0.0012	×0.065	×0.066

Table 5.7: Comparison between experimental and theoretical flow rate through the Whatman membranes. Numbers in the table correspond to the ratio of theoretical to experimental flow rate. Box A is at 25 °C and box B is at 50 °C.

	Sharipov equation Eq (2.69)	Arkilic equation Eq (2.66)	Poiseuilles flow Eq (2.67)	Knudsen flow Eq (2.30)	Knudsen and Poiseuilles flows combined Eq (2.68)
400	×12	×2.8	×4.4	×10	×13.25
80	×1	×0.06	×0.09	×1	×1.09
50	×0.333		×0.018	×0.33	×0.33
15	×0.25		×0.0023	×0.14	×0.14

#### 5.6.4 Surface flow through the nanoporous membranes

The equation derived by Sears [187] and described in the background chapter is used.  $K$  value for the smallest pore (15 nm) is calculated using experimental data (pressure, flow rate, and working gas properties) based on equation (2.83). The reason for using the 15 nm membrane is because surface diffusion is more likely to occur when the pore size is smaller. The calculated  $K$  is then used to calculate the molecular diameter,  $d$  (Equation (2.78)) which is then used to calculate the  $K$  values for the other membrane sizes using equation (2.78) (Table 5.8). The molecular diameter,  $d$ , is calculated for the different flow rates (50, 100, 200, 300, 350  $\mu\text{l}/\text{min}$ ) and an average value is used.

Table 5.8:  $K$  for the 15 nm membrane was calculated using the experimental data and equation (2.83). Equation (2.78) was then used to determine  $d$  and calculate  $K$  for the other membrane sizes.

Membrane size (nm)	15	30	50	80	400
calculated $K$ room temperature	14.43	3.6	1.27	0.5	0.02
Calculated $K$ box B at 50°C	6.05	-----	0.54	0.21	0.01

The calculated  $K$  values were then used in equation (2.82) to calculate the flow rate. The next set of tables shows the calculated flow rate values. Using a diffusion term in the equation improved the flow rate data. For the 30 nm, and 50 nm, the calculated flow rates are close to the experimental ones (Table 5.9). Also, the magnitude of the flow rate for the biggest pore size (400 nm) decreased. The calculated molecular diameter  $d$  is  $3.02 \times 10^{-11}$  m when boxes A and B are at room temperature (25 °C) and  $7.29 \times 10^{-11}$  m when box A at 25 °C and box B at 50 °C These values are about one order of magnitude less than reported value [208]. This last analysis indicates that further focus needs to be directed to the surface diffusion flow effect.

Table 5.9: Calculated flow rate using the using the calculated  $K$  values (Table 5.8) and equation (2.82).

Experimental flow rate (µl/min)	Calculated flow rate (µl/min) using $K$ values (400nm pore size membrane)	
	Both boxes at room temperature (25 °C)	Box A at room temperature and box B at 50 °C
50	420.79	349.29
100	793.60	1018.19
200	1539.51	2017.64
300	2358.79	2956.66
350	2453.88	3527.30

Experimental flow rate (µl/min)	Calculated flow rate (µl/min) using $K$ values (80nm pore size membrane)	
	Both boxes at room temperature (25 °C)	Box A at room temperature and box B at 50 °C
50	46.13	71.71
100	112.23	124.16
200	243.43	246.43
300	393.17	363.59
350	419.21	419.90

Experimental flow rate ( $\mu\text{l}/\text{min}$ )	Calculated flow rate ( $\mu\text{l}/\text{min}$ ) using $K$ values (50nm pore size membrane)	
	Both boxes at room temperature (25 °C)	Box A at room temperature and box B at 50 °C
50	35.26	21.28
100	71.05	51.03
200	140.33	101.56
300	206.88	150.20
350	227.70	173.88

Experimental flow rate ( $\mu\text{l}/\text{min}$ )	Calculated flow rate ( $\mu\text{l}/\text{min}$ ) using $K$ values (30nm pore size membrane)	
	Both boxes at room temperature (25 °C)	Box A at room temperature and box B at 50 °C
50	53.29	-----
100	104.72	-----
200	208.37	-----
300	298.35	-----
350	342.62	-----

Experimental flow rate ( $\mu\text{l}/\text{min}$ )	Calculated flow rate ( $\mu\text{l}/\text{min}$ ) using $K$ values (15nm pore size membrane)	
	Both boxes at room temperature (25 °C)	Box A at room temperature and box B at 50 °C
50	43.01	50.70
100	98.74	101.18
200	207.37	199.54
300	317.58	296.92
350	369.28	345.36

## 5.7 Conclusion

Accurate determination of the flow rate across a membrane for a given pressure difference is crucial in predicting its performance in many devices and applications. In this chapter, experimental data, pressure and flow rate, are collected for track-etch Whatman membranes of different pore sizes, 15, 30, 50, 80, and 400nm. A simple set up was used for this purpose, the membrane is glued on an aluminum plate which has a drilled hole with glued plastic tubing connecting to the pressure sensor and a



programmable syringe pump using a T-connector. The flow rate is set on the pump, and the corresponding pressure increase is recorded versus time with the pressure sensor. For the largest pore size membrane, the calculated flow rate is larger than the experimental, while for the smaller pore sizes, 50, 30, and 15 nm, the opposite trend is observed. A better data correlation is observed for the for the 80 nm pore size, the ratio of the calculated/experimental flow rate is around one when the transitional flow or Sharipov equation is used. The use of a theoretical equation, which has a surface diffusion term, showed a better correlation. Further work will be directed toward the use of a better diffusion term.

## CHAPTER 6: CONCLUSIONS AND FUTURE WORK

This last chapter will review and summarize the dissertation research, identify the main methods used, discuss their implications in the study and finally explore future work to improve the device performance.

### 6.1 Conclusions

The Knudsen pump operates based on the thermal transpiration principal, which is defined as the drifting of gas molecules from one side to the other of a narrow channel when a thermal gradient is established. In most previously reported work on the Knudsen pump, a resistive heater heats one side while the other side is passively cooled using a heat sink. A more developed version of the same pump used a Peltier device to actively cool and heat the cold and hot side, respectively. In both designs, a lot of heat is lost because of the metallic heat spreaders used to transfer heat to the sides of the nanoporous membrane and due to the unavoidable air gaps existing between the nanoporous membrane and heat sink/heater/metallic heat spreaders. An efficient solution to these drawbacks is described and implemented in this research dissertation. It consists of making the nanoporous membrane out of a thermoelectric material such that the air gaps are eliminated and the heating and cooling take place where it is needed.

Powder metallurgy is used to fabricate a nanoporous thermoelectric element. The main steps of powder metallurgy are powder preparation using high energy ball milling, pressing in a die, and finally the thermal treatment or sintering. P-type  $\text{Bi}_2\text{Te}_3$

thermoelectric material is used in this work because of its high figure merit  $Z$  at room temperature. Porosity, thermal, and electrical testing as described in chapter 3 showed the feasibility of using the fabricated thermoelectric sample in a thermal transpiration based pump. A nanoporous thermoelectric material is obtained with a 6 MPa pressure and a 200 °C sintering temperature under running argon. After soldering electrical contacts to the thermoelectric nanoporous sample, the latter is placed and sealed in a machined plastic channel with plastic tubes glued on the top cover for connection to the pressure sensors. The channel depth is exactly equal to the thermoelectric element thickness. For an input power of 3.3 W, a flow rate of about 1.8  $\mu\text{l}/\text{min}$  and a 300 Pa pressure difference are obtained. A great portion of the power consumed is due to the poor quality electrical contacts. The obtained flow rate is sufficient for many biomedical applications such as microdialysis and drug delivery devices.

The 4<sup>th</sup> chapter describes the mathematical model of the thermoelectric based Knudsen pump. Thermoelectric equations which relate the heat flux terms with the physical properties of the thermoelectric element are combined with Sharipov's equation. The latter is valid in all flow regimes and relates the flow rate, temperature, pressure differences, and channel dimensions for a Knudsen pump. Two expressions are derived. The largest pressure that can be obtained is found by setting the mass flow rate to zero, and the largest mass flow rate is found by setting the pressure difference to zero. One of the key findings from this derivation is that the maximum pressure difference is independent of the thermoelectric dimensions. This special characteristic of the pump makes it a potential candidate in many microsystems and MEMS devices.

The analysis also shows that the quality of the thermoelectric material as reflected by its figure of merit  $Z$  value has a great effect on the pressure difference and flow rate generated by the pump. The higher the figure of merit  $Z$ , the higher the flow rate and pressure generated by the Knudsen pump.

The tangential momentum accommodation coefficient (TMAC), which is defined as the amount of gas molecules reflected diffusively by the channel wall, was investigated with the generated model. This coefficient depends on many parameters such as surface type and roughness, pressure, and temperature, and is widely assumed to be equal to unity in many applications. Three TMAC values have been investigated: 0.6, 0.8, and 1. It was found that as the TMAC value increases, the generated pressure increases while the flow rate decreases. These results indicate that a careful determination of the TMAC value is necessary for better prediction of the pressure difference and flow rate.

Using the same mathematical model, it was found that a decrease in the pore size results in an increase in the maximum pressure difference and a decrease in the maximum flow rate. For heavier gases such as xenon (Xe) and argon (Ar), the opposite trend is observed. The heavier the working gas, the smaller the maximum pressure difference and higher the maximum flow rate.

The gas flow through nanoporous track-etch Whatman membranes showed that the TMAC is not the right parameter to solve the discrepancy between theoretical and experimental flow rate. Also it was found that the inclusion of surface diffusion flow term in the modeling equation improves the correlation between the experimental and theoretical flow rate and pressure.

## 6.2 Future work

As demonstrated on the mathematical model analysis (chapter 4), as the thermoelectric pore size becomes smaller, the generated pressure becomes larger. The milling and sintering conditions, described in chapter 4, which have led to an operational Knudsen pump using an average pore radius of 434 nm. The corresponding Knudsen number,  $Kn$ , assuming air as the working gas, is about 0.16. This value coincides with the early stage of the transitional flow regime. A further improvement of the thermoelectric fabrication conditions such that the pore size results in a free molecular regime flow should substantially increase the generated pressure and therefore improvement in the pump efficiency. These improvements may be obtained using the following: increasing the milling time to obtain a smaller grain size, solving the powder agglomeration through use of different powder characterization techniques, and choosing the right combination of pressure, sintering temperature and pressing and sintering time.

A great portion of the power consumed by the fabricated thermoelectric based pump is due to the low quality electrical contacts. Regular tin-lead solders were used with the fabricated devices. Electroplating and solution based material deposition are by far the best way to deposit different layers for electrical contacts. In this work, these techniques were avoided because of the concern of clogging the thermoelectric element pores.

If the porous thermoelectric element can be filled with some polymeric solvent-dissolvable material, aqueous electroplating can then be performed without any worries of clogging the pores. This should lead to improved, low resistance electrical contacts. Another technique to improve the electrical contacts is through the use of intermediate

thin layers. They can be deposited using sputtering or an evaporation technique. Cobalt and nickel are examples of materials that permit tin-lead materials to adhere well to  $\text{Bi}_2\text{Te}_3$ .

Analysis of data on the gas flow through nanoporous membranes showed promising results when a surface diffusion flow term is added to the modeling equation. The gas molecular diameters that were obtained, in both room temperature and 50 °C experiments, were about one order of magnitude less than the reported values in the literature. One way to improve the calculated flow rate is through introduction of a rough Van der Waals type of correction for the molecular size as suggested by Hill [186]. The free area per molecule is  $(1/\sigma)-b$  instead of  $1/\sigma$  ( $b=\pi d^2/2$ ). A different expression can then be used to calculate the mass flow rate as described in the paper by Hill [186], section B: mobile adsorption at higher surface concentrations, constant temperature.

## REFERENCES

1. Jing Liu , N.K.G., Kensall D. Wise , Yogesh B. Gianchandani and Xudong Fan *Demonstration of motionless Knudsen pump based micro-gas chromatography featuring micro-fabricated columns and on-column detectors* Lab on a Chip 2011. **11**(20): p. 6.
2. Zareian-Jahromi, M.A., et al., *Design, Modeling, and Fabrication of MEMS-Based Multicapillary Gas Chromatographic Columns*. Microelectromechanical Systems, Journal of, 2009. **18**(1): p. 28-37.
3. Astle, A.A., et al., *Theoretical and experimental performance of a high frequency gas micropump*. Sensors and Actuators A: Physical, 2007. **134**(1): p. 245-256.
4. Lu, C.-J., Steinecker, William H., Tian, Wei-Cheng, Oborny, Michael C., Nichols, Jamie M., Agah, Masoud, Potkay, Joseph A., Chan, Helena K. L., Driscoll, Jeffrey, Sacks, Richard D., Wise, Kensall D., Pang, Stella W., and Zellers, Edward T., *First-generation hybrid MEMS gas chromatograph*. Lab on a Chip, 2005. **5**(10): p. 1123-1131.
5. Das, A.N., et al. *Design and Manufacturing of a Fourier Transform Microspectrometer*. in *Nanotechnology, 2008. NANO '08. 8th IEEE Conference on*. 2008.
6. Miller, R.A., et al., *A MEMS radio-frequency ion mobility spectrometer for chemical vapor detection*. Sensors and Actuators A: Physical, 2001. **91**(3): p. 301-312.

7. Young, R.M., *Analysis of a micromachine based vacuum pump on a chip actuated by the thermal transpiration effect*. Journal of Vacuum Science & Technology B: Microelectronics and Nanometer Structures, 1999. **17**(2): p. 280-287.
8. Xue, J. and J.A. Hopwood, *Microwave-Frequency Effects on Microplasma*. IEEE Transactions on Plasma Science, 2009. **37**(6): p. 816-822.
9. Wilson, C.G. and Y.B. Gianchandani, *Silicon micromachining using in situ DC microplasmas*. Microelectromechanical Systems, Journal of, 2001. **10**(1): p. 50-54.
10. Iza, F. and J. Hopwood, *Influence of operating frequency and coupling coefficient on the efficiency of microfabricated inductively coupled plasma sources* Plasma Sources Science and Technology, 2002. **11**: p. 7.
11. Wilson, C.G. and Y.B. Gianchandani, *Spectral detection of metal contaminants in water using an on-chip microglow discharge*. Electron Devices, IEEE Transactions on, 2002. **49**(12): p. 2317-2322.
12. Hayamizu, S., et al., *Development of a bi-directional valve-less silicon micro pump controlled by driving waveform*. Sensors and Actuators A: Physical, 2003. **103**(1-2): p. 83-87.
13. McNamara, S. and Y.B. Gianchandani. *A micromachined Knudsen pump for on-chip vacuum*. in *TRANSDUCERS, Solid-State Sensors, Actuators and Microsystems, 12th International Conference on, 2003*. 2003.
14. McNamara, S. and Y.B. Gianchandani, *On-Chip Vacuum Generated by a Micromachined Knudsen Pump*. Microelectromechanical Systems, Journal of, 2005. **14**(4): p. 741-746.



15. Kim, J., et al., *Photopolymerized check valve and its integration into a pneumatic pumping system for biocompatible sample delivery*. Lab Chip, 2006. **6**(8): p. 1091-1094.
16. Tai, C.-H., et al., *Automatic microfluidic platform for cell separation and nucleus collection*. Biomedical Microdevices, 2007. **9**(4): p. 533-543.
17. Reynolds, O., *On Certain Dimensional Properties of Matter in the Gaseous State*. Philosophical Transactions of the Royal Society of London, 1879. **170**: p. 727-845.
18. Maxwell, J.C., *On Stresses in Rarified Gases Arising from Inequalities of Temperature*. Philosophical Transactions of the Royal Society of London, 1879. **170**: p. 231-256.
19. Gupta, N.K.a.G., Yogesh B., *Thermal transpiration in zeolites: A mechanism for motionless gas pumps*. Applied Physics Letters, 2008. **93**(19): p. 193511-3.
20. Gupta, N.K. and Y.B. Gianchandani, *Porous ceramics for multistage Knudsen micropumps—modeling approach and experimental evaluation*. Journal of Micromechanics and Microengineering, 2011. **21**(9): p. 095029.
21. Pharas, K., S. Miles, and S. McNamara, *Thermal transpirational flow in the transitional flow regime*. Journal of Vacuum Science & Technology A: Vacuum, Surfaces, and Films, 2012. **30**(5): p. 050603-050603-4.
22. Kunal Pharas, S.M., *Knudsen pump driven by a thermoelectric material*. J. Micromech. Microeng, 2010. **20**: p. 7.

23. van Lintel, H.T.G., van De Pol, F. C. M., and Bouwstra, S., *A piezoelectric micropump based on micromachining of silicon*. Sensors and Actuators, 1988. **15**(2): p. 153-167.
24. Smits, J.G., *Piezoelectric micropump with three valves working peristaltically*. Sensors and Actuators A: Physical, 1990. **21**(1–3): p. 203-206.
25. Smits, J.G., *Piezoelectric micropump with microvalves*. 1990, Google Patents.
26. Smits, J.G. *Piezoelectric micropump with microvalves*. in *University/Government/Industry Microelectronics Symposium, 1989. Proceedings., Eighth*. 1989.
27. Koch, M., Harris, N., Evans, A. G. R., White, N. M., and Brunnschweiler, A. *A novel micromachined pump based on thick-film piezoelectric actuation*. in *Solid State Sensors and Actuators, 1997. TRANSDUCERS '97 Chicago., 1997 International Conference on*. 1997.
28. C G J Schabmueller, M.K., M E Mokhtari, A G R Evans, A Brunnschweiler, and H Sehr, *Self-aligning gas/liquid micropump*. Journal of Micromechanics and Microengineering, 2002. **12**(4): p. 420.
29. Junwu, K., Zhigang, Yang, Taijiang, Peng, Guangming, Cheng, and Boda, Wu, *Design and test of a high-performance piezoelectric micropump for drug delivery*. Sensors and Actuators A: Physical, 2005. **121**(1): p. 156-161.
30. Lee, S.W., Sim, Woo Young, and Yang, Sang Sik, *Fabrication and in vitro test of a microsyringe*. Sensors and Actuators A: Physical, 2000. **83**(1–3): p. 17-23.

31. Guo-Hua, F.a.E.-S., Kim, *Piezoelectrically actuated dome-shaped diaphragm micropump*. *Microelectromechanical Systems, Journal of*, 2005. **14**(2): p. 192-199.
32. Geipel, A., Doll, A., Goldschmidt, F., Jantscheff, P., Esser, N., Massing, U., and Woias, P. *Pressure-Independent Micropump with Piezoelectric Valves for Low Flow Drug Delivery Systems*. in *Micro Electro Mechanical Systems, 2006. MEMS 2006 Istanbul. 19th IEEE International Conference on*. 2006.
33. Bin, M., Sheng, Liu, Zhiyin, Gan, Guojun, Liu, Xinxia, Cai, Honghai, Zhang, and Zhigang, Yang. *A PZT insulin pump integrated with a silicon micro needle array for transdermal drug delivery*. in *Electronic Components and Technology Conference, 2006. Proceedings. 56th*. 2006.
34. Zengerle, R., Ulrich, J., Kluge, S., Richter, M., and Richter, A., *A bidirectional silicon micropump*. *Sensors and Actuators A: Physical*, 1995. **50**(1-2): p. 81-86.
35. Cabuz, C., Herb, W. R., Cabuz, E. I., and Son Thai, Lu. *The dual diaphragm pump*. in *Micro Electro Mechanical Systems, 2001. MEMS 2001. The 14th IEEE International Conference on*. 2001.
36. Zengerle, R., Richter, A., and Sandmaier, H. *A micro membrane pump with electrostatic actuation*. in *Micro Electro Mechanical Systems, 1992, MEMS '92, Proceedings. An Investigation of Micro Structures, Sensors, Actuators, Machines and Robot. IEEE*. 1992.
37. Besharatian, A., Kumar, K., Peterson, R. L., Bernal, L. P., and Najafi, K. *A scalable, modular, multi-stage, peristaltic, electrostatic gas micro-pump*. in *Micro*

*Electro Mechanical Systems (MEMS), 2012 IEEE 25th International Conference on.* 2012.

38. Popescu, D.S., Lerch, P., Dunare, C., and Dascalu, D. *Modelling and optimisation for an electrostatic actuation of a valveless micropump using a silicon buckled membrane.* in *Semiconductor Conference, 1997. CAS '97 Proceedings., 1997 International.* 1997.
39. Böhm, S., Olthuis, Wouter, and Bergveld, Piet, *A plastic micropump constructed with conventional techniques and materials.* *Sensors and Actuators A: Physical*, 1999. **77**(3): p. 223-228.
40. Gong, Q., Zhou, Zhaoying, Yang, Yihua, and Wang, Xiaohao, *Design, optimization and simulation on microelectromagnetic pump.* *Sensors and Actuators A: Physical*, 2000. **83**(1–3): p. 200-207.
41. Yamahata, C., Lotto, C., Al-Assaf, E., and Gijs, M. A. M., *A PMMA valveless micropump using electromagnetic actuation.* *Microfluidics and Nanofluidics*, 2005. **1**(3): p. 197-207.
42. Yamahata, C., Chastellain, M., Parashar, V. K., Petri, A., Hofmann, H., and Gijs, M. A. M., *Plastic micropump with ferrofluidic actuation.* *Microelectromechanical Systems, Journal of*, 2005. **14**(1): p. 96-102.
43. Tingrui Pan, S.J.M., Eleanor M Kai, and Babak Ziaie, *A magnetically driven PDMS micropump with ball check-valves.* *Journal of Micromechanics and Microengineering*, 2005. **15**(5): p. 1021.

44. Nisar, A., Afzulpurkar, Nitin, Mahaisavariya, Banchong, and Tuantranont, Adisorn, *MEMS-based micropumps in drug delivery and biomedical applications*. Sensors and Actuators B: Chemical, 2008. **130**(2): p. 917-942.
45. Zdeblick, M., *Integrated, microminiature electric to fluidic valve*. 1989, Google Patents.
46. Jeong, O.C.a.Y., Sang Sik, *Fabrication and test of a thermopneumatic micropump with a corrugated p+ diaphragm*. Sensors and Actuators A: Physical, 2000. **83**(1–3): p. 249-255.
47. Cooney, C.G.a.T., Bruce C., *A thermopneumatic dispensing micropump*. Sensors and Actuators A: Physical, 2004. **116**(3): p. 519-524.
48. Jun, D.H., Sim, Woo Young, and Yang, Sang Sik, *A novel constant delivery thermopneumatic micropump using surface tensions*. Sensors and Actuators A: Physical, 2007. **139**(1–2): p. 210-215.
49. Kim, J.-H., Na, Kwang-Ho, Kang, C. J., and Kim, Yong-Sang, *A disposable thermopneumatic-actuated micropump stacked with PDMS layers and ITO-coated glass*. Sensors and Actuators A: Physical, 2005. **120**(2): p. 365-369.
50. Lagoudas, D.C., *Shape Memory Alloys: Modeling and Engineering Applications*. 2008: Springer.
51. Shin, D.D., Mohanchandra, Kotekar P., and Carman, Gregory P., *Development of hydraulic linear actuator using thin film SMA*. Sensors and Actuators A: Physical, 2005. **119**(1): p. 151-156.

52. Zhang, H.J.a.Q., C. J., *Characterization and MEMS application of low temperature TiNi(Cu) shape memory thin films*. Materials Science and Engineering: A, 2006. **438–440**(0): p. 1106-1109.
53. Makino, E., Mitsuya, Takashi, and Shibata, Takayuki, *Fabrication of TiNi shape memory micropump*. Sensors and Actuators A: Physical, 2001. **88**(3): p. 256-262.
54. Benard, W.L., Kahn, Harold, Heuer, A. H., and Huff, M. A., *Thin-film shape-memory alloy actuated micropumps*. Microelectromechanical Systems, Journal of, 1998. **7**(2): p. 245-251.
55. Xu, D., Wang, Li, Ding, Guifu, Zhou, Yong, Yu, Aibing, and Cai, Bingchu, *Characteristics and fabrication of NiTi/Si diaphragm micropump*. Sensors and Actuators A: Physical, 2001. **93**(1): p. 87-92.
56. Shuxiang, G.a.F., T. *SMA actuator-based novel type of micropump for biomedical application*. in *Robotics and Automation, 2004. Proceedings. ICRA '04. 2004 IEEE International Conference on*. 2004.
57. Iverson, B. and S. Garimella, *Recent advances in microscale pumping technologies: a review and evaluation*. Microfluidics and Nanofluidics, 2008. **5**(2): p. 145-174.
58. Baruah, A.K.R.a.M., B. *Thermally actuated MEMS based silicon micropump*. in *Communications, Devices and Intelligent Systems (CODIS), 2012 International Conference on*. 2012.
59. Jiangtao, P., Quanbo, Zou, Zhimin, Tan, Xin, Qian, Litian, Liu, and Zhijian, Li. *The study of single-chip integrated microfluidic system*. in *Solid-State and*

- Integrated Circuit Technology, 1998. Proceedings. 1998 5th International Conference on.* 1998.
60. Zou, J., Ye, X. Y., Zhou, Z. Y., and Yang, Y. *A novel thermally-actuated silicon micropump.* in *Micromechatronics and Human Science, 1997. Proceedings of the 1997 International Symposium on.* 1997.
  61. Kwang-Seok, Y., Il-Joo, Cho, Bu, Jong-Uk, Chang-Jin, Kim, and Euisik, Yoon, *A surface-tension driven micropump for low-voltage and low-power operations.* *Microelectromechanical Systems, Journal of,* 2002. **11**(5): p. 454-461.
  62. Hoshino, K., Tritayaprasert, Soroj, Matsumoto, Kiyoshi, and Shimoyama, Isao, *Electrowetting-based pico-liter liquid actuation in a glass-tube microinjector.* *Sensors and Actuators A: Physical,* 2004. **114**(2-3): p. 473-477.
  63. Colgate, E.a.M., Hirofumi, *An investigation of electrowetting-based microactuation.* *Journal of Vacuum Science & Technology A: Vacuum, Surfaces, and Films,* 1990. **8**(4): p. 3625-3633.
  64. Yoshimi, Y., Shinoda, Kenichi, Mishima, Masatomo, Nakao, Kenta, and Munekane, Kohta, *Development of an artificial synapse using an electrochemical micropump.* *Journal of Artificial Organs,* 2004. **7**(4): p. 210-215.
  65. Jang, J.a.L., Seung S., *Theoretical and experimental study of MHD (magnetohydrodynamic) micropump.* *Sensors and Actuators A: Physical,* 2000. **80**(1): p. 84-89.
  66. Richter, A.a.S., H. *An electrohydrodynamic micropump.* in *Micro Electro Mechanical Systems, 1990. Proceedings, An Investigation of Micro Structures, Sensors, Actuators, Machines and Robots. IEEE.* 1990.

67. Woodson, H.H.a.M., J.R., *Electromechanical Dynamics: Fields, forces, and motion*. 1968: Wiley.
68. Abhari, F.J., Haslina; Yunus, and Nurul Amziah Md, *A Comprehensive Study of Micropumps Technologies*. International Journal of Electrochemical Science, 2012. **7**(10): p. 16.
69. Hobson, J.P., *Accommodation Pumping- A New Principle for Low Pressures*. Journal of Vacuum Science and Technology, 1970. **7**(2): p. 351-357.
70. Hobson, J.P., and Salzman, D. B., *Review of pumping by thermal molecular pressure*. Journal of Vacuum Science & Technology A, 2000. **18**(4): p. 1758-1765.
71. S. E. Vargo, E.P.M., G. R. Shiflett, W. C. Tang, *Knudsen compressor as a micro- and macroscale vacuum pump without moving parts or fluids*. Journal of Vacuum Science & Technology A 1999. **17**(4): p. 6.
72. Muntz, E.P., Sone, Y., Aoki, K., Vargo, S. and Young, M., *Performance analysis and optimization considerations for a Knudsen compressor in transitional flow*. Journal of Vacuum Science & Technology A: Vacuum, Surfaces, and Films, 2002. **20**(1): p. 214-224.
73. Hemmerich, J.L., *Primary vacuum pumps for the fusion reactor fuel cycle*. Journal of Vacuum Science & Technology A, 1988. **6**(1): p. 144-153.
74. Hobson, J.P., *Accommodation Pumping—A New Principle for Low Pressures*. Journal of Vacuum Science & Technology, 1970. **7**(2): p. 351-357.
75. Logan, R.M.a.S., R. E., *Simple Classical Model for the Scattering of Gas Atoms from a Solid Surface*. The Journal of Chemical Physics, 1966. **44**(1): p. 195-201.



76. Tracy, D.H., *Thermomolecular pumping effect*. Journal of Physics E: Scientific Instruments, 1974. **7**(7): p. 533.
77. Knudsen, M., *Eine Revision der Gleichgewichtsbedingung der Gase. Thermische Molekularströmung*. Annalen der Physik, 1909. **336**(1): p. 205-229.
78. Knudsen, M., *Thermischer Molekulardruck der Gase in Röhren und porösen Körpern*. Annalen der Physik, 1910. **336**(3): p. 633-640.
79. G. Pham-Van-Diep, P.K., E. P. Muntz, D. P. Weaver. *A micromechanical Knudsen Compressor*. in *International Symposium on Rarefied Gas Dynamics*. 1995.
80. Vargo, S.E.M., E. P. *Initial results from the first MEMS fabricated thermal transpiration-driven vacuum pump*. in *RAREFIED GAS DYNAMICS 22nd International Symposium .AIP Conference*. 2001.
81. Vargo, S.E.M., E. P.; Shiflett, G. R.; Tang, W. C., *Knudsen compressor as a micro- and macroscale vacuum pump without moving parts or fluids*. Journal of Vacuum Science & Technology A: Vacuum, Surfaces, and Films, 1999. **17**(4): p. 6.
82. Vargo, S.E., *The development of the MEMS Knudsen compressor as a low power vacuum pump for portable and in situ instruments*. 2000, University of Southern California: United States -- California. p. 147 p.
83. M. Young, Y.L.H., E.P. Muntz, G. Shiflett. *CHARACTERIZATION OF A RADIANTLY DRIVEN MULTISTAGE KNUDSEN COMPRESSOR*. in *ASME International Mechanical Engineering Congress and Exposition*. 2003. Washington, D.C.

84. Young, M., Shiflett, G, Muntz, E. P., Vargo, S. *Thermal transpiration as a co-located micro-scale source of high pressure gas for MEMS devices.* in *ASME International Mechanical Engineering Congress and Exposition.* 2001. New York.
85. Gupta, N.K., *A motionless gas micropump using thermal transpiration in bulk nanoporous materials.* 2010, University of Michigan: United States - Michigan.
86. Gupta, N.K. and Y.B. Gianchandani. *A planar cascading architecture for a ceramic Knudsen micropump.* in *Solid-State Sensors, Actuators and Microsystems Conference, 2009. TRANSDUCERS 2009. International.* 2009.
87. Gupta, N.K., S. An, and Y.B. Gianchandani. *A monolithic 48-stage Si-micromachined Knudsen pump for high compression ratios.* in *Micro Electro Mechanical Systems (MEMS), 2012 IEEE 25th International Conference on.* 2012.
88. Naveen K Gupta, S.A., and Yogesh B Gianchandani, *A Si-micromachined 48-stage Knudsen pump for on-chip vacuum.* *Journal of Micromechanics and Microengineering*, 2012. **22**(10): p. 105026.
89. S. An, N.K.G., and Y.B. Gianchandani, *A MONOLITHIC 162-STAGE TWO-PART KNUDSEN PUMP FOR HIGH COMPRESSION RATIO,* in *Solid-State Sensors, Actuators, and Microsystems Workshop.* 2012: Hilton Head Island, South Carolina. p. 14-17.
90. An, S., Gupta, N. K., and Gianchandani, Y. B., *A Si-Micromachined 162-Stage Two-Part Knudsen Pump for On-Chip Vacuum.* *Journal of Microelectromechanical Systems*, 2013. **PP**(99): p. 1-1.

91. Sone, Y., *Kinetic Theory and Fluid Dynamics*. Modeling and Simulation in Science, Engineering and Technology. 2002, Boston: Birkhäuser
92. Seleznev, F.S.a.V., *Data on Internal Rarefied Gas Flows* Journal of Physical and Chemical Reference Data, 1998. **27**(3): p. 50.
93. Todreas, N.E.a.K., M.S., *Nuclear Systems*. 2010: Taylor & Francis.
94. Loeb, L.B., *The Kinetic Theory of Gases*. 2004: Dover Publications.
95. Siu, M.C.I., *Equations for Thermal Transpiration*. Journal of Vacuum Science & Technology, 1973. **10**(2): p. 368-372.
96. Loeb, L.B., *The kinetic theory of gases*. 3rd ed. 1961: Dover
97. J-G. Choi, D.D.D., and H. D. Do, *Surface Diffusion of Adsorbed Molecules in Porous Media: Monolayer, Multilayer, and Capillary Condensation Regimes*. Industrial & Engineering Chemistry Research, 2001. **40**(19): p. 4005-4031.
98. Kennard, E.H., *Kinetic theory of gases: with an introduction to statistical mechanics*. 1938: McGraw-Hill Book Company, inc.
99. Williams, J.C., *Thermal Transpiration—A Continuum Gasdynamics View*. Journal of Vacuum Science & Technology, 1971. **8**(2): p. 446-450.
100. Sharipov, F., *Rarefied gas flow through a long tube at arbitrary pressure and temperature drops*. Journal of Vacuum Science & Technology A: Vacuum, Surfaces, and Films, 1997. **15**(4): p. 2434-2436.
101. Sharipov, F., *Non-isothermal gas flow through rectangular microchannels*. Journal of Micromech. & Microeng, 1999. **9**(4): p. 394.
102. Shakhov, E.M., *Generalization of the Krook kinetic relaxation equation*. Fluid Dynamics, 1968. **3**(5): p. 95-96.

103. Sharipov, F., *Rarefied gas flow through a long tube at any temperature ratio*. Journal of Vacuum Science & Technology A, 1996. **14**: p. 9.
104. Seebeck, T.J., *Ueber den Magnetismus der galvanischen Kette*. 1822: Deutsche Akademie der Wissenschaften zu Berlin.
105. Goldsmid, H.J., *Electronic refrigeration*. 1986: Pion.
106. Tilley, R.J.D., *Understanding Solids: The Science of Materials*. 2013: Wiley.
107. Li, S.S., *Semiconductor Physical Electronics*. 2007: Springer.
108. Rowe, D.M., *Handbook of Thermoelectrics*, ed. B. Raton. 1995, FL: CRC Press.
109. Goldsmid, H.J., *Thermoelectric refrigeration*. 1964: Plenum Press.
110. DiSalvo, F.J., *Thermoelectric Cooling and Power Generation*. Science, 1999. **285**(5428): p. 703-706.
111. Snyder, G.J. and E.S. Toberer, *Complex thermoelectric materials*. Nat Mater, 2008. **7**(2): p. 105-114.
112. Rosi, F.D., *Thermoelectricity and thermoelectric power generation*. Solid-State Electronics, 1968. **11**(9): p. 833-868.
113. Goldsmid, H.J. and R.W. Douglas, *The use of semiconductors in thermoelectric refrigeration*. British Journal of Applied Physics, 1954. **5**(11): p. 386.
114. Gelbstein, Y., Z. Dashevsky, and M.P. Dariel, *High performance n-type PbTe-based materials for thermoelectric applications*. Physica B: Condensed Matter, 2005. **363**(1-4): p. 196-205.
115. Dresselhaus, M.S., Chen, G., Tang, M. Y, Yang, R. G, Lee, H., Wang, D. Z, Ren, Z. F, Fleurial, J. P. and Gogna, P., *New Directions for Low-Dimensional Thermoelectric Materials*. Advanced Materials, 2007. **19**(8): p. 1043-1053.

116. Caillat, T., A. Borshchevsky, and J.P. Fleurial, *Properties of single crystalline semiconducting CoSb<sub>3</sub>*. Journal of Applied Physics, 1996. **80**(8): p. 4442-4449.
117. Nolas, G.S., Morelli, D. T. and Tritt, Terry M., *SKUTTERUDITES: A Phonon-Glass-Electron Crystal Approach to Advanced Thermoelectric Energy Conversion Applications*. Annual Review of Materials Science, 1999. **29**(1): p. 89-116.
118. Slack, G., in *Handbook of Thermoelectrics*, D.M. Rowe, Editor. 1995, CRC Press: FL.
119. Sales, B.C., Mandrus, D. and Williams, R. K., *Filled Skutterudite Antimonides: A New Class of Thermoelectric Materials*. Science, 1996. **272**(5266): p. 1325-1328.
120. Nolas, G.S., Cohn, J. L., Slack, G. A. and Schujman, S. B., *Semiconducting Ge clathrates: Promising candidates for thermoelectric applications*. Applied Physics Letters, 1998. **73**(2): p. 178-180.
121. Wood, C., *Materials for thermoelectric energy conversion*. Reports on Progress in Physics, 1988. **51**(4): p. 459.
122. M. S. Dresselhaus, M.S., and L.D. Hicks, *Thermoelectric figure of merit of a one-dimensional conductor*. Phys. Rev. B., 1993. **47**.
123. M. S. Dresselhaus, M.S., and L.D. Hicks, *Effect of quantum-well structures on the thermoelectric figure of merit*. Phys. Rev. B., 1993. **47**.
124. Nolas, G.S., J. Sharp, and J. Goldsmid, *Thermoelectrics: Basic Principles and New Materials Developments*. 2001: Springer.
125. Drabble, J.R. and C.H.L. Goodman, *Chemical bonding in bismuth telluride*. Journal of Physics and Chemistry of Solids, 1958. **5**(1-2): p. 142-144.

126. Yamashita, O., S. Tomiyoshi, and K. Makita, *Bismuth telluride compounds with high thermoelectric figures of merit*. Journal of Applied Physics, 2003. **93**(1): p. 368-374.
127. Yamashita, O. and S. Tomiyoshi, *High performance n-type bismuth telluride with highly stable thermoelectric figure of merit*. Journal of Applied Physics, 2004. **95**(11): p. 6277-6283.
128. Pfann, W.G., *Zone melting*. 1966: Wiley.
129. Champness, C.H., Chiang, P. T., Grabowski, K. and Muir, W. B., *Influence of Growth Conditions and Tellurium Phase on the Thermoelectric Properties of Bismuth Telluride-Type Materials*. Journal of Applied Physics, 1968. **39**(9): p. 4177-4183.
130. Jiang, J., Chen, Lidong, Bai, Shengqiang, Yao, Qin and Wang, Qun, *Thermoelectric properties of p-type  $(Bi_2Te_3)_x(Sb_2Te_3)_{1-x}$  crystals prepared via zone melting*. Journal of Crystal Growth, 2005. **277**(1-4): p. 258-263.
131. Jariwala, B. and D.V. Shah, *Stacking fault in  $Bi_2Te_3$  and  $Sb_2Te_3$  single crystals*. Journal of Crystal Growth, 2011. **318**(1): p. 1179-1183.
132. Pan, S., Okano, Y., Tsunekawa, S. and Fukuda, T., *Kyropoulos method for growth of nonlinear optical organic crystal ABP (4-aminobenzophenone) from the melt*. Journal of Crystal Growth, 1993. **129**(1-2): p. 365-366.
133. Fukuda, T., Y. Uematsu, and T. Ito, *Kyropoulos growth and perfection of  $KNbO_3$  single crystal*. Journal of Crystal Growth, 1974. **24-25**(0): p. 450-453.
134. Pastor, R.C. and A.C. Pastor, *Crystal growth above 2200°C by the Verneuil method*. Materials Research Bulletin, 1966. **1**(4): p. 275-282.

135. Laudise, R.A., Sunder, W. A., Barns, R. L., Cava, R. J. and Kometani, T. Y., *Czochralski growth of doped single crystals of  $\text{Bi}_2\text{Te}_3$* . Journal of Crystal Growth, 1989. **94**(1): p. 53-61.
136. Hyun, D.-B., Hwang, Jong-Seung, Shim, Jae-Dong and Oh, TaeSung, *Thermoelectric properties of  $(\text{Bi}_{0.25}\text{Sb}_{0.75})_2\text{Te}_3$  alloys fabricated by hot-pressing method*. Journal of Materials Science, 2001. **36**(5): p. 1285-1291.
137. Kim, H.C., Oh, T. S. and Hyun, D. B., *Thermoelectric properties of the p-type  $\text{Bi}_2\text{Te}_3\text{-Sb}_2\text{Te}_3\text{-Sb}_2\text{Se}_3$  alloys fabricated by mechanical alloying and hot pressing*. Journal of Physics and Chemistry of Solids, 2000. **61**(5): p. 743-749.
138. Yang, J., Aizawa, T., Yamamoto, A. and Ohta, T., *Thermoelectric properties of p-type  $(\text{Bi}_2\text{Te}_3)_x(\text{Sb}_2\text{Te}_3)_{1-x}$  prepared via bulk mechanical alloying and hot pressing*. Journal of Alloys and Compounds, 2000. **309**(1-2): p. 225-228.
139. Goldsmid, H.J., *The Electrical Conductivity and Thermoelectric Power of Bismuth Telluride*. Proceedings of the Physical Society, 1958. **71**(4): p. 633.
140. Goldsmid, H.J., *Introduction to Thermoelectricity*. 2009: Springer-Verlag Berlin Heidelberg.
141. Pope, A.L., Zawilski, B. and Tritt, T. M., *Description of removable sample mount apparatus for rapid thermal conductivity measurements*. Cryogenics, 2001. **41**(10): p. 725-731.
142. Dames, C.a.C., Gang,  *$1\omega$ ,  $2\omega$ , and  $3\omega$  methods for measurements of thermal properties*. Review of Scientific Instruments, 2005. **76**(12): p. 124902-124902-14.
143. Kosky, P.G., D.H. Maylotte, and J.P. Gallo, *Ångström methods applied to simultaneous measurements of thermal diffusivity and heat transfer coefficients:*

- Part 1, theory*. International Communications in Heat and Mass Transfer, 1999. **26**(8): p. 1051-1059.
144. Creese, R., *Introduction to Manufacturing Processes and Materials*. 2013: Taylor & Francis.
145. Reddy, L.K., *Principles of Engineering Metallurgy*. 2007: New Age International (P) Limited.
146. Madsen, D., *Print Reading for Engineering and Manufacturing Technology*. 2012: Cengage Learning.
147. Pietsch, W., *Agglomeration in Industry: Occurrence and Applications*. 2004: Wiley.
148. Kaushish, *Manufacturing Processes*. 2008: Prentice-Hall Of India Pvt. Limited.
149. ANGELO, P.C.a.S., R., *POWDER METALLURGY: SCIENCE, TECHNOLOGY AND APPLICATIONS*. 2008: PHI Learning.
150. Rahaman, M.N., *Ceramic Processing and Sintering*. 2003: Taylor & Francis.
151. Carter, C.B.a.N., G., *Ceramic Materials: Science and Engineering*. 2007: Springer.
152. Kang, S.-J.L., *Sintering - Densification, Grain Growth, and Microstructure*. Elsevier.
153. German, R.M., *Coarsening in Sintering: Grain Shape Distribution, Grain Size Distribution, and Grain Growth Kinetics in Solid-Pore Systems*. Critical Reviews in Solid State and Materials Sciences, 2010. **35**(4): p. 263-305.
154. Coble, R.L., *Sintering Crystalline Solids. I. Intermediate and Final State Diffusion Models*. Journal of Applied Physics, 1961. **32**(5): p. 787-792.



155. Elizarova, J.-C.L.a.T.T., *Gaseous Microflows*, in *Microfluidics*, S. Colin, Editor. 2010, Wiley. p. 448.
156. Hurlbut, F.C., *Two Contrasting Modes for the Description of Wall-Gas Interactions*, in *Rarefied Gas Dynamics: Experimental Techniques and Physical Systems*, B.D.a.W. Shizgal, D.P., Editor. 1994, American Institute of Aeronautics and Astronautics. p. 633.
157. Hayes, W., *Hypersonic Flow Theory*. 2012: Elsevier Science.
158. Millikan, R.A., *Coefficients of Slip in Gases and the Law of Reflection of Molecules from the Surfaces of Solids and Liquids*. *Physical Review*, 1923. **21**(3).
159. Stacy, L.J., *A Determination by the Constant Deflection Method of the Value of the Coefficient of Slip for Rough and for Smooth Surfaces in Air* *Phys. Rev.*, 1923. **21**: p. 11.
160. Dyke, K.S.V., *The Coefficients of Viscosity and of Slip of Air and of Carbon Dioxide by the Rotating Cylinder Method*. *Phys. Rev.*, 1923. **21**: p. 16.
161. Tekasakul, P., Bentz, J. A., Tompson, R. V., and Loyalka, S. K., *The spinning rotor gauge: Measurements of viscosity, velocity slip coefficients, and tangential momentum accommodation coefficients*. *Journal of Vacuum Science & Technology A*, 1996. **14**(5): p. 2946-2952.
162. Fremerey, J.K., *The spinning rotor gauge*. *Journal of Vacuum Science & Technology A*, 1985. **3**(3): p. 1715-1720.
163. Agrawal, A.a.P., S. V., *Survey on measurement of tangential momentum accommodation coefficient*. *Journal of Vacuum Science & Technology A*, 2008. **26**(4): p. 634-645.

164. Bentz, J.A., Tompson, R. V., and Loyalka, S. K., *Measurements of viscosity, velocity slip coefficients, and tangential momentum accommodation coefficients using a modified spinning rotor gauge*. Journal of Vacuum Science & Technology A, 2001. **19**(1): p. 317-324.
165. Bentz J. A., T.R.V., and Loyalka S. K., *The spinning rotor gauge-measurements of viscosity, velocity slip coefficients, and tangential momentum accommodation coefficients for N-2 and CH4* Vacuum, 1997. **48**(10): p. 8.
166. Comsa, G., Fremerey, J. K., Lindenau, B., Messer, G., and Röhl, P., *Calibration of a spinning rotor gas friction gauge against a fundamental vacuum pressure standard*. Journal of Vacuum Science & Technology, 1980. **17**(2): p. 642-644.
167. Omelik, A.I., *Experimental determination of the speed ratio in free-molecular flow of nitrogen*. Fluid Dynamics, 1973. **8**(4): p. 668-670.
168. Rettner, C.T., *Thermal and tangential-momentum accommodation coefficients for N2 colliding with surfaces of relevance to disk-drive air bearings derived from molecular beam scattering*. Magnetics, IEEE Transactions on, 1998. **34**(4): p. 2387-2395.
169. S. M. Liu, P.K.S., E. L. Knuth *Satellite drag coefficients calculated from measured distributions of reflected helium atoms*. The American Institute of Aeronautics and Astronautics, 1979. **17**: p. 6.
170. C. Bing-Yang, J.S., M. Chen, and Z-Y. Guo, *Molecular Momentum Transport at Fluid-Solid Interfaces in MEMS/NEMS: A Review*. Int. J. Mol. Sci., 2009. **10**: p. 69.

171. Steinheil, M.S.a.E. *Measurement of Momentum Accommodation Coefficients on Surfaces characterized by Auger Spectroscopy, SIMS and LEED*. in *Rarefied Gas Dynamics*. 1974. Porz-Wahn, Germany.
172. Maxwell, J.C., *The Scientific Papers of James Clerk Maxwell*. 1965, New York: Dover publications.
173. E. B. Arkilic, M.A.S., and K. S. Breuer, *Gaseous slip flow in long microchannels*. *Journal of Microelectromechanical Systems*, 1997. **6**(2): p. 167-178.
174. Karniadakis, G., Beskok, A., and Aluru, N., *Microflows and Nanoflows: Fundamentals and Simulation*. 2005: Springer.
175. Errol B. Arkilic, K.S.B., and Martin A. Schmidt, *Mass flow and tangential momentum accommodation in silicon micromachined channels*. *J. Fluid Mech.*, 2001. **437**: p. 15.
176. Cercignani, C., *The Boltzmann Equation and its applications*. Vol. 67. 1988: Springer New York.
177. Loyalka, S.K., *Approximate Method in the Kinetic Theory*. *Phys. Fluids*, 1971. **14**(11): p. 2291-2294.
178. S. K. Loyalka, N.P., and T. S. Storvick, *Some numerical results for the BGK model: Thermal creep and viscous slip problems with arbitrary accommodation at the surface*. *Phys. Fluids*, 1975. **18**(9): p. 1094-1099.
179. S. Colin, P.L., and R. Caen, *Validation of a Second-Order Slip Flow Model in Rectangular Microchannels*. *Heat Transfer Engineering*, 2004. **25**(3): p. 23-30.
180. S-S. Hsieh, H.-H.T., C-Y. Lin, C-F. Huang, and C-M. Chien, *Gas flow in a long microchannel*. *Int. J. Heat and Mass Transfer*, 2004. **47**(17-18): p. 3877-3887.

181. N-T. Nguyen, a.S.T.W., *Fundamentals and applications of microfluidics*. 2002, Boston: Artech House.
182. S. M. Cooper, B.A.C., M. Meyyappan, R. Raju, and S. Roy, *Gas Transport Characteristics through a Carbon Nanotubule*. Nano Letters, 2003. **4**(2): p. 377-381.
183. Graur, I.A., Perrier, P.,Ghozlani, W. and Méolans, J. G., *Measurements of tangential momentum accommodation coefficient for various gases in plane microchannel*. Physics of Fluids, 2009. **21**(10): p. 9.
184. P. Perrier, I.A.G., T. Ewart, and J. G. Méolans, *Mass flow rate measurements in microtubes: From hydrodynamic to near free molecular regime*. Phys. Fluids, 2011. **23**(4): p. 11.
185. Sharipov, F.M., and Seleznev, V. D., *Rarefied gas flow through a long tube at any pressure ratio*. Journal of Vacuum Science & Technology A, 1994. **12**(5): p. 2933-2935.
186. Hill, T.L., *Surface Diffusion and Thermal Transpiration in Fine Tubes and Pores*. The Journal of Chemical Physics, 1956. **25**(4): p. 730-735.
187. Sears, G.W., *A Note on the Flow of Gases through Very Fine Tubes*. The Journal of Chemical Physics, 1954. **22**(7): p. 1252-1253.
188. O. V. Sazhin, S.F.B., and F. Sharipov, *Accommodation coefficient of tangential momentum on atomically clean and contaminated surfaces*. Journal of Vacuum Science & Technology A, 2001. **19**(5): p. 2499-2503.
189. Eklund, P.C. and A.K. Mabatah, *Thermoelectric power measurements using analog subtraction*. Review of Scientific Instruments, 1977. **48**(7): p. 775-777.

190. Sumanasekera, G.U., L. Grigorian, and P.C. Eklund, *Low-temperature thermoelectrical power measurements using analogue subtraction*. Measurement Science and Technology, 2000. **11**(3): p. 273.
191. O'Neill, M.J., *Measurement of Specific Heat Functions by Differential Scanning Calorimetry*. Analytical Chemistry, 1966. **38**(10): p. 1331-1336.
192. Archer, D.G., *Thermodynamic Properties of Synthetic Sapphire ( $\alpha$ -Al<sub>2</sub>O<sub>3</sub>), Standard Reference Material 720 and the Effect of Temperature-Scale Differences on Thermodynamic Properties*. Journal of Physical and Chemical Reference Data, 1993. **22**(6): p. 1441-1453.
193. Patterson, A.L., *The Scherrer Formula for X-Ray Particle Size Determination*. Physical Review, 1939. **56**(10): p. 978-982.
194. Abderrazzak Faiz, S.M., Alexander D Bell and Gamini Sumanasekera, *Nanoporous Bi<sub>2</sub>Te<sub>3</sub> thermoelectric based Knudsen gas pump*. J. Micromech. Microeng, 2014. **24**.
195. Xiong, K., et al., *First Principles Study of Metal/Bi<sub>2</sub>Te<sub>3</sub> Interfaces: Implications to Improve Contact Resistance*. MRS Online Proceedings Library, 2009. **1166**: p. null-null.
196. Kacsich, T., et al., *Films of Ni-7 at% V, Pd, Pt and Ta-Si-N as diffusion barriers for copper on Bi<sub>2</sub>Te<sub>3</sub>*. Journal of Physics D: Applied Physics, 1998. **31**(19): p. 2406.
197. Liang, M.-W., H.-T. Yen, and T.-E. Hsieh, *Investigation of electroless cobalt-phosphorous layer and its diffusion barrier properties of Pb-Sn solder*. Journal of Electronic Materials, 2006. **35**(7): p. 1593-1599.

198. Kohn, A., et al., *Evaluation of electroless deposited Co(W,P) thin films as diffusion barriers for copper metallization*. *Microelectronic Engineering*, 2001. **55**(1-4): p. 297-303.
199. Khattab, N.M. and E.T. El Shenawy, *Optimal operation of thermoelectric cooler driven by solar thermoelectric generator*. *Energy Conversion and Management*, 2006. **47**(4): p. 407-426.
200. Fraisse, G., Ramousse, J., Sgorlon, D. and Goupil, C., *Comparison of different modeling approaches for thermoelectric elements*. *Energy Conversion and Management*, 2013. **65**(0): p. 351-356.
201. Rowe, D.M., *General Principles and Basic Considerations*, in *Thermoelectrics Handbook*. 2005, CRC Press. p. 1-1-1-14.
202. P. Gonçalves, A., Lopes, E. B., Alves, E., Barradas, N. P., Franco, N., Rouleau, O. and Godart, C., *New Approaches to Thermoelectric Materials*, in *Properties and Applications of Thermoelectric Materials*, V. Zlatić and A. Hewson, Editors. 2009, Springer Netherlands. p. 51-67.
203. Anderson, J., *Fundamentals of Aerodynamics*. 2010: McGraw-Hill Education.
204. Bell, A., W.D. Ehringer, and S. McNamara, *Scavenged body heat powered infusion pump*. *Journal of Micromechanics and Microengineering*, 2013. **23**(11): p. 114019.
205. Seleznev, F.M.S.a.V.D., *Flows of rarefied gases in channels and microchannels*. 2008: Russian Academy of Science, Ural Branch, Institute of Thermal Physics.

206. Sharipov, I.G.a.F., *Gas flow through an elliptical tube over the whole range of the gas rarefaction*. European Journal of Mechanics - B/Fluids, 2008. **27**(3): p. 335-345.
207. Titarev, V.A., *Rarefied gas flow in a circular pipe of finite length*. Vacuum, 2013. **94**(0): p. 92-103.
208. Zhang, Y., *Indoor Air Quality Engineering*. 2004: Taylor & Francis.

APPENDIX A: DETERMINATION OF THE PORE SIZE AND SURFACE AREA  
USING IMAGE J

Measuring the powder particle size and pore area using imageJ software

Open imageJ software.



Open the SEM image to be analyzed; this can be done by dragging the SEM image onto the imageJ window, Cntrl-O, or via File → Open → select SEM image (Figure A-1).



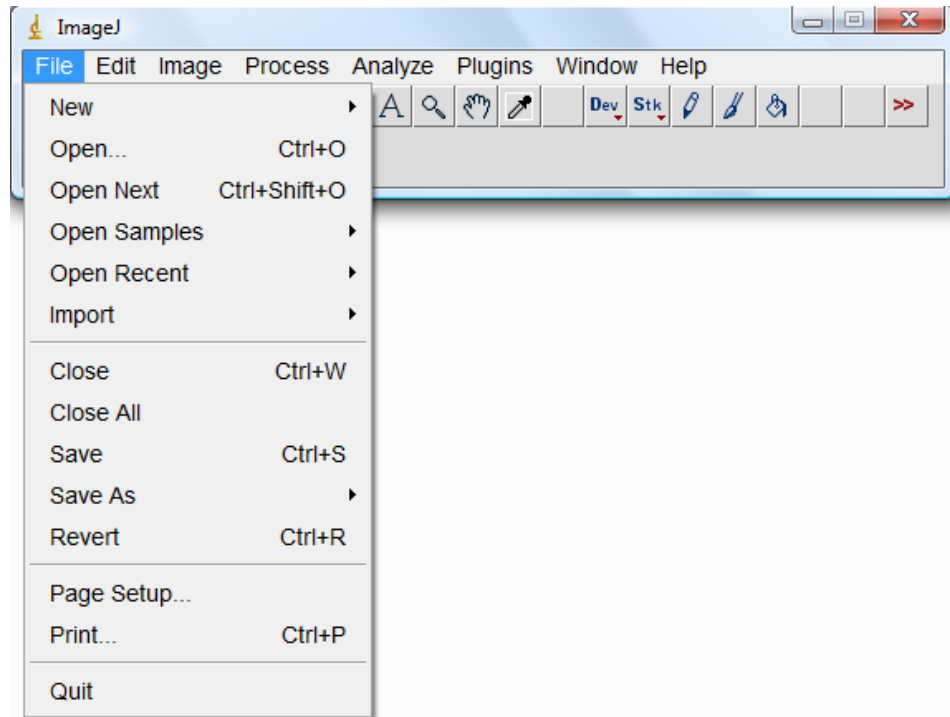


Figure A-1: ImageJ main window containing the menu bar and the different tools for image analysis.

### Set measurement scale

On the SEM image, draw a line over 100 nm scale (Figure A-2), line is shown in yellow.

Next go to Analyze → set scale. In set scale enter 100 in the 'known distance' box and change 'unit of length' box to nm, check global (Figure A-3). The scale bar value and unit can change depending on the image.

Draw the new line and confirm that the measurement scale is correct.

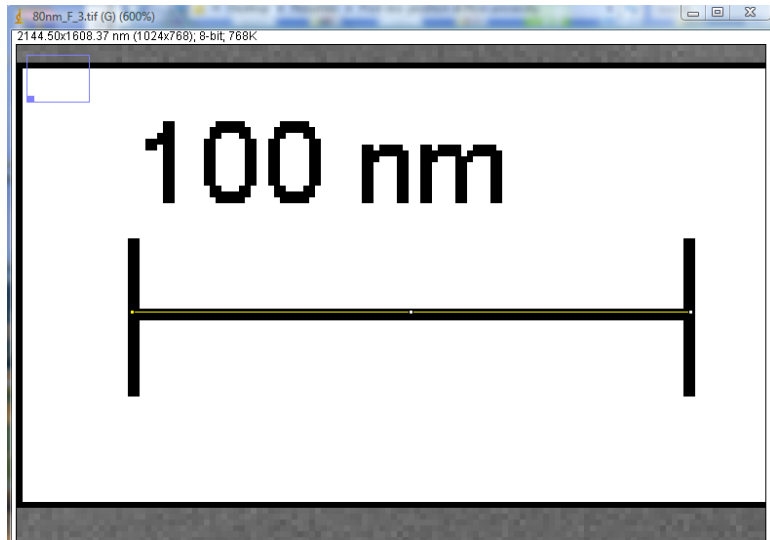


Figure A-2: A line (Yellow color) is drawn on top of the SEM scale bar line to define the

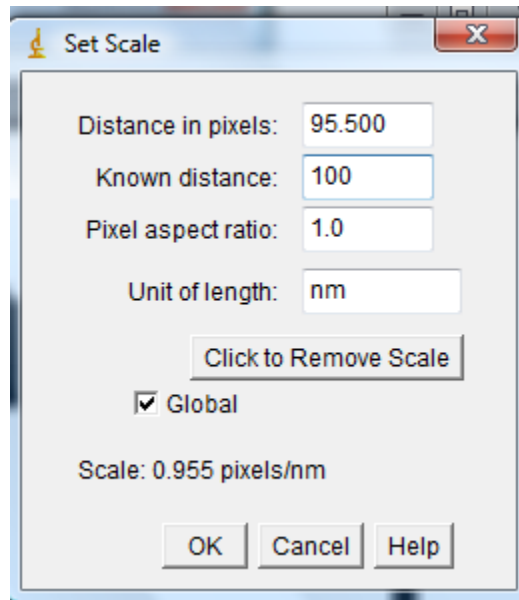


Figure A-3: set scale window allows the definition of the true spatial scale of the image. A line with a known distance is used to perform the calibration.

Go to the image and draw a line equal to the powder particle. Multiple lines can be drawn, once a line is drawn, click on 't' to add the line to the ROI manager list (Figure A-4). Once finished, click on 'm' or 'measure' on the ROI manager window and measurements will be displayed on a new window. Figure A-6 shows measurements on the pore size of a nanoporous membrane (Figure A-5). In order to measure the area of a

pore, one needs to use oval, elliptical selection tool for circular areas, and the freehand tool for random areas instead of the line tool. The other steps are the same.

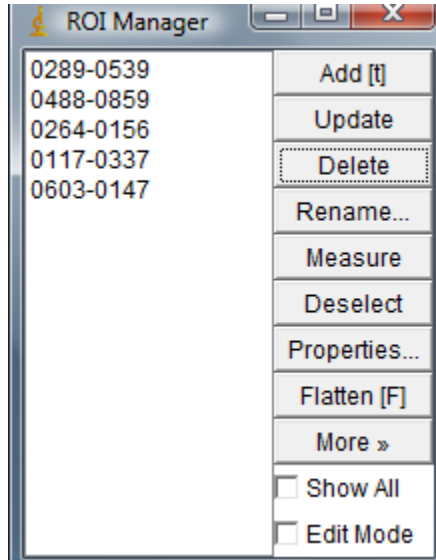


Figure A-4: ROI manager showing all the drawn lines. Once Measure button is selected, measurements are displayed in a result window. Checking 'Show All' shows all drawn geometries in the image being analyzed.

List of parameters to be recorded in the results table can be defined through Analyze → set measurements.

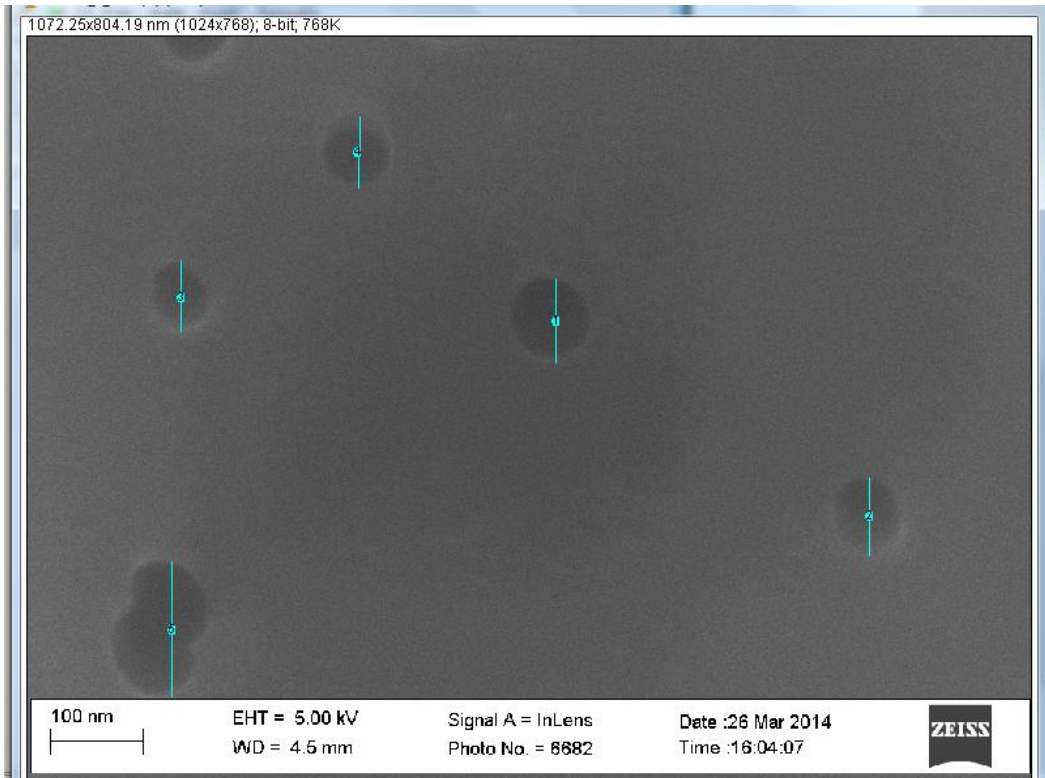


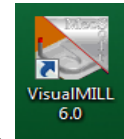
Figure A-5: SEM image of a nanoporous membranes, the blue lines are used to measure the pore size. The 100 nm scale bar is used to define the measurement scale.

	Area	Mean	Min	Max	Angle	Length
1	94.295	70.132	62.118	89.303	-90	89.354
2	87.717	86.639	75.890	106	-90	82.373
3	78.945	85.694	73	111	-90	75.393
4	80.041	80.647	71.765	93.111	-90.796	75.405
5	151.311	82.196	72.014	110.333	-90	143.804

Figure A-6: Results window is open once 'm' or 'measure' is selected. Parameters shown on the table are defined through analyze → set measurements.

## APPENDIX B: Machining the channel for the thermoelectric sintered sample using the CNC machine

After drawing the part in SolidWorks and saving as .igs format. It is then transferred to the computer connected to the CNC machine.



Open Visual Mill 6.0 by clicking on the following icon, then select File/Open or the open icon and select the .igs file (Figure B-1).



Figure B-1: Opening the part to be machined in Visual Mill 6.0.

The imported part, in this case is a 13 mm wide channel, is shown in figure B-2.

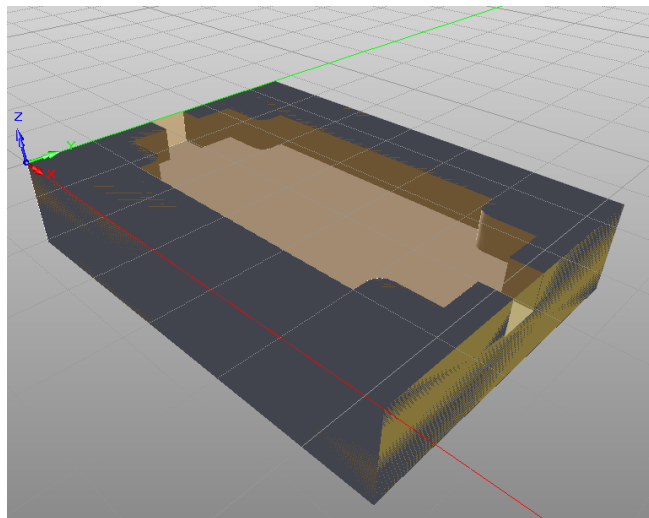


Figure B-2: igs file imported to Visual Mill 6.0 showing the channel to be machined.

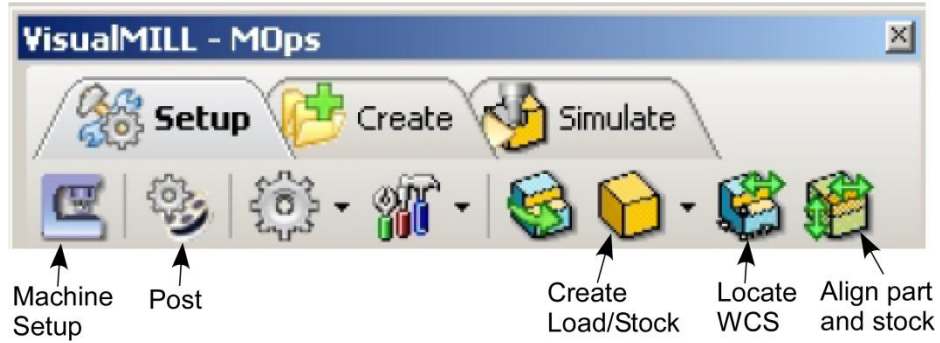


Figure B-3: Setup tab.

Go to the visual mill MOPs browser and select the setup tab (Figure B-3).

- Select machine setup and make sure the machine is set up for 3 axis milling (Figure B-4).

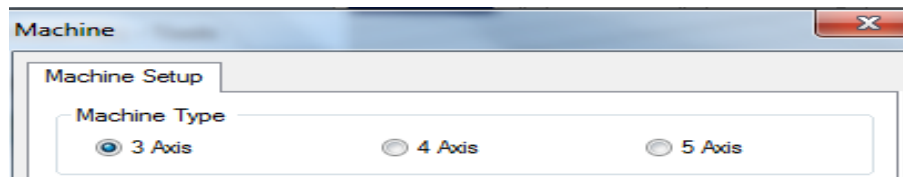


Figure B-4: Machine tab in which the machining type is specified. The channels for the thermoelectric samples were machined using 3-axis machine type.

- Select post from the setup tab and make sure that Mach3-MM is selected as the post processor setting (Figure B-5).

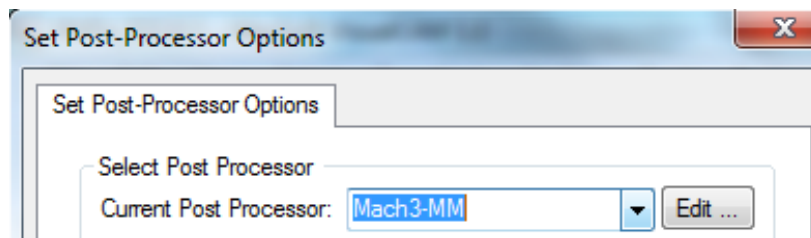


Figure B-5: Post-Processor tab in which Mach 3-MM is used in this case.

- Select **Create load/stock** and create a box stock. Then press copy model bounding box. This button will give you the exact dimensions of the stock in order to machine the part (Figure B-6).

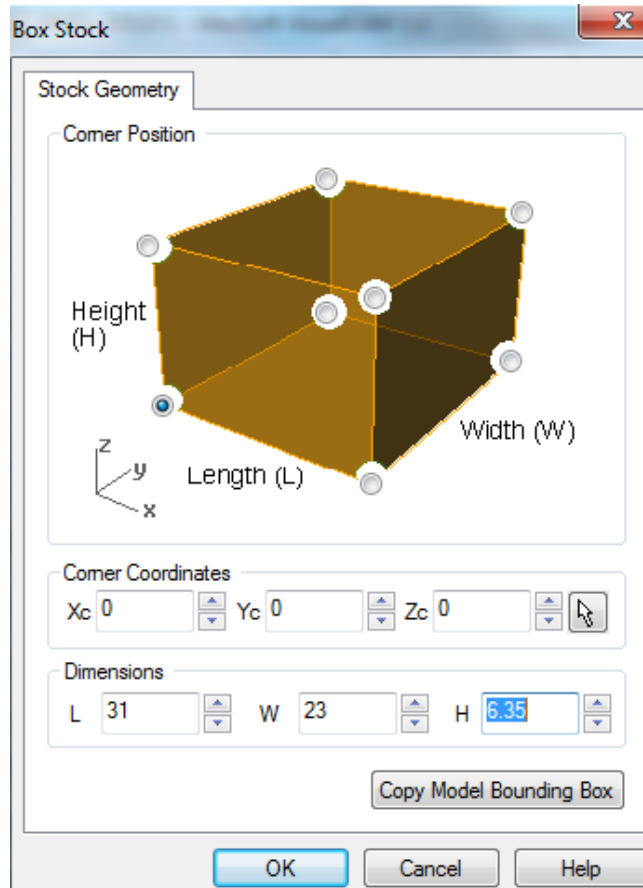


Figure B-6: Box Stock window, clicking “Copy Model Bounding Box” transfers the channel dimensions. The overall size of the plastic channel is 31 mm long and 23 mm wide. The machined plastic is 6.35 mm thick.

- Click on **Locate WCS** from the **setup tab**. Select set to stock box under the set WCS origin, select highest z for the zero face, and select the southwest corner for the zero position. Then click ok (Figure B-7).

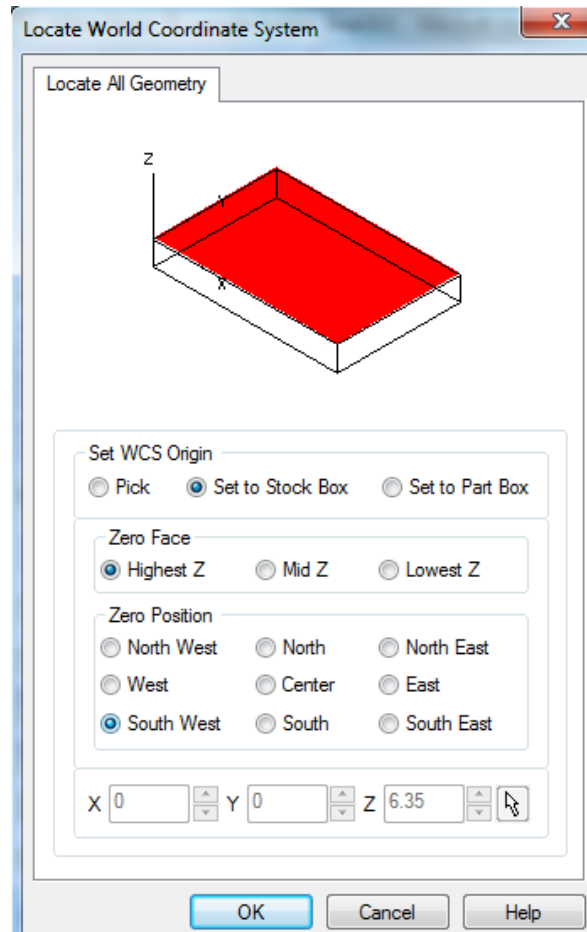


Figure B-7: Setting the Stock Box coordinates.

- Click on **Align part and stock** from the setup tab to align the part with the stock. Select move part from the object to move list, select bottom for z alignment, and select center for XY alignment. Then click ok (Figure B-8).



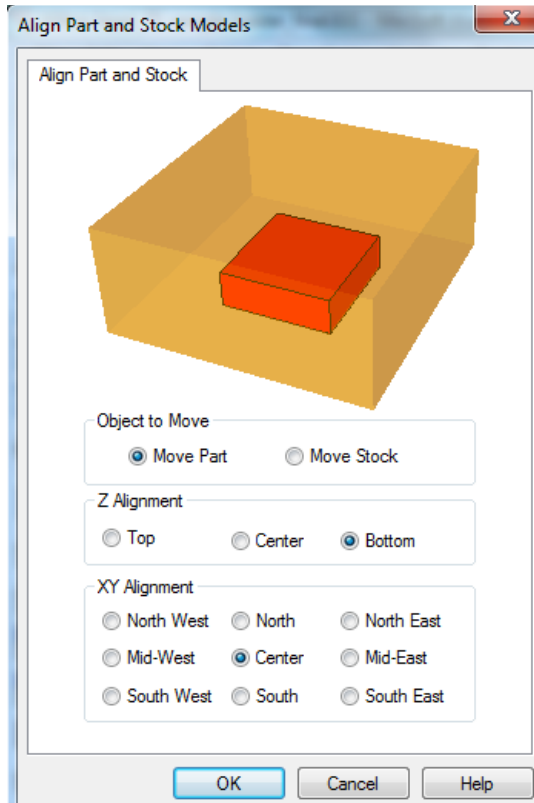


Figure B-8: Align Part and Stock tab.

- To create tools, go to the visual mill tools browser and select **Create/Edit tools**.
- Create a tool name. Add all the dimensions needed for that tool in the window. Make sure each dimension is exact or else the machining will be off quite a bit.
- Go to the **Properties tab** and for the material select carbide unless the tool is HSS. For the first tool created, make its tool number 1. Find out how many flutes the tool has and add that number to the number of flutes box. Keep adjust register 0, Cutcom register 0, Zoffset 0, and coolant none (Figure B-9).
- Next click on the **Feeds and Speeds tab**. Enter the Spindle Speed, Plunge Feed, Approach Feed, Engage Feed, Cut Feed, Retract Feed, and Departure Feed (Figure B-9).Table B-1 gives some suggested values.

- Then press ok, your tool with its set feeds and speeds and dimensions will be listed in the tools browser.

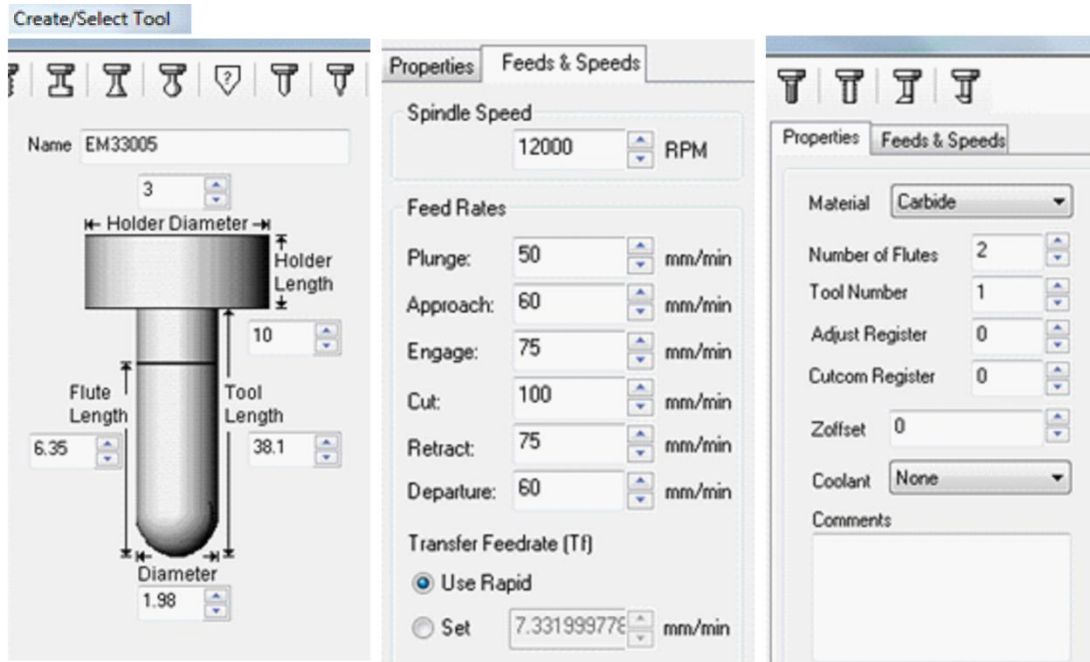


Figure B-9: Create/select tool tab.

Table B-1: Some Feeds and speeds values which can be used to machine plastic.

Spindle Speed (RPM)	Plunge Feed mm/min	Approach Feed mm/min	Engage Feed mm/min	Cut Feed mm/min	Retract Feed mm/min	Departure Feed mm/min
12000 - 15000 for plastic.	50% of the cut feed rate	60% of the cut feed rate	75% of the cut feed rate	100-300	75-225	60-180

- To create rough machining operations click the **Create tab** on the MOPs browser, select **3 Axis Milling** and choose **Horizontal Roughing** (Figure B-10).

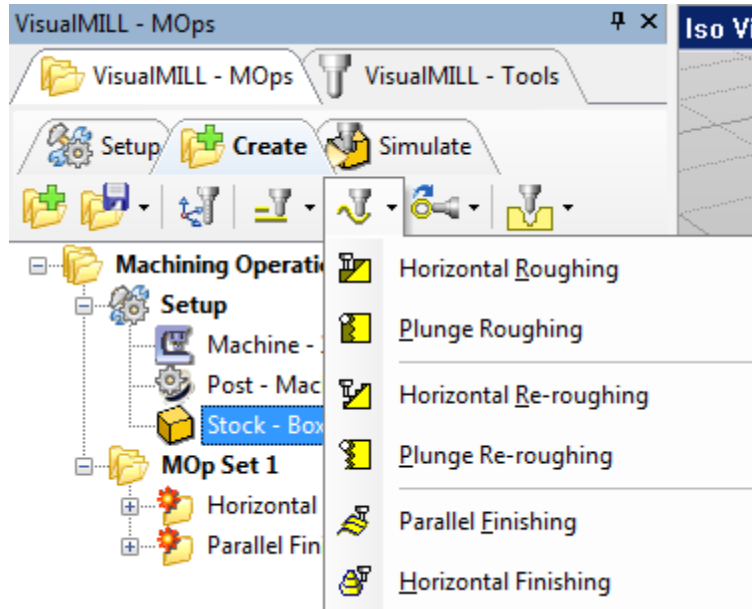


Figure B-10: Visual Mill Create tab.

- On the **Machining Features/Regions** tab, click on **Select Curves as Regions** and then select the channel (Region) to be machined (Figure B-11).

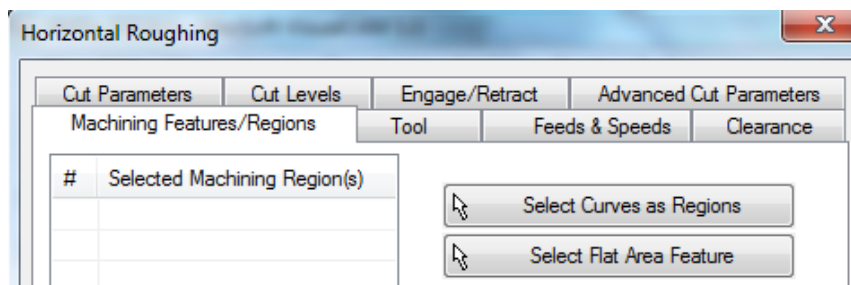


Figure B-11: Machining Features/Regions tab.

- On the **Tools** tab select the tool that will be used from the list given then click on **Create/select tool**. Double check all information given about the tool dimensions properties and **Feeds & Speeds** before going further, then click OK.
- Then click on the **Clearance** tab, set the clearance plane definition to automatic and cut transfer method to clearance plane (Figure B-12).

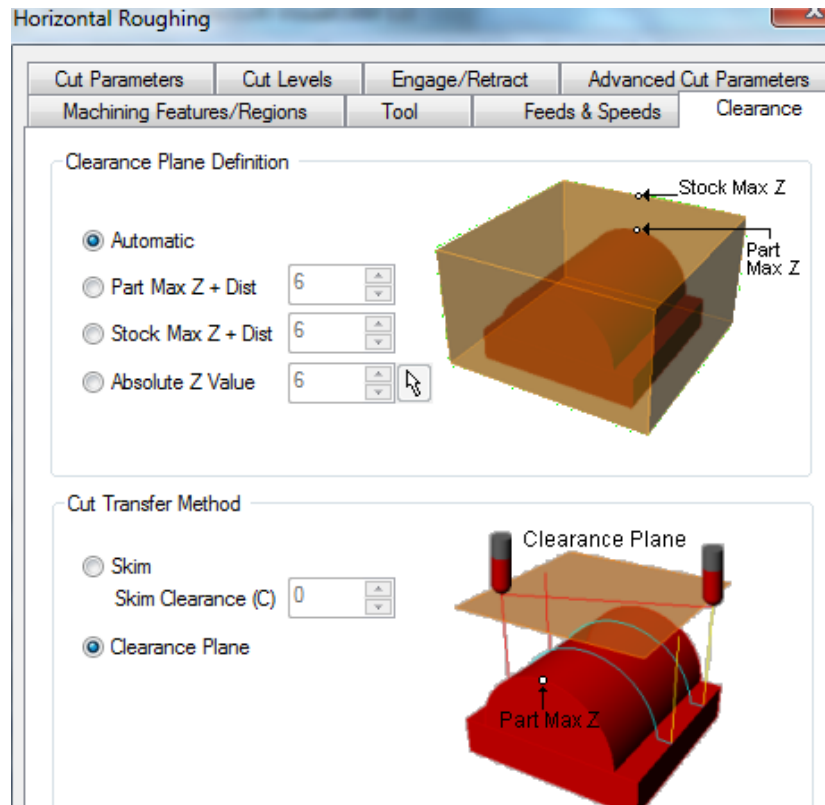


Figure B-12: Clearance tab.

- Then click on the **Cut Parameters tab**, set intol to 0.001 outol to 0.001 and stock to 0.025. Cut pattern should be set to stock offset, cut direction should be mixed, offset is inside, nothing set for linear, and step over control should be set at 40% for % tool diameter (Figure B-13).

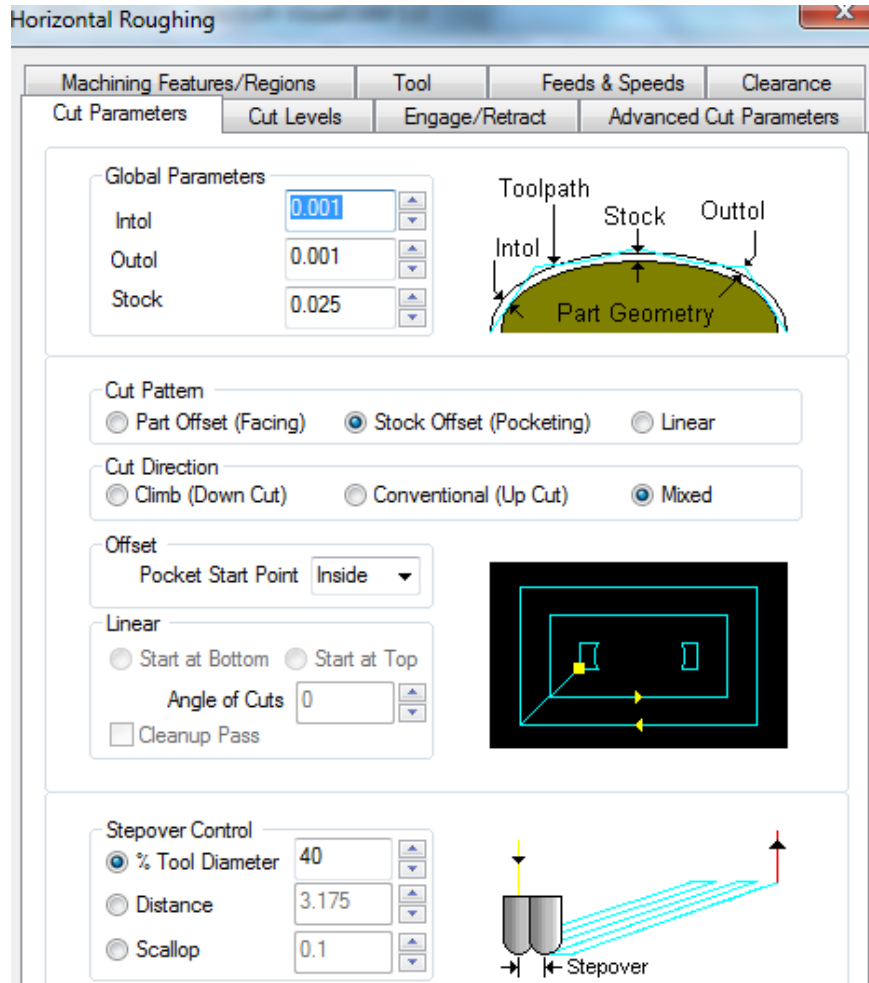


Figure B-13: Cut Parameters tab.

- Then click the **Cut Levels** tab and for step down control enter 25% tool diameter, for cut levels select depth first and for cut levels select clear flats (Figure B-14).

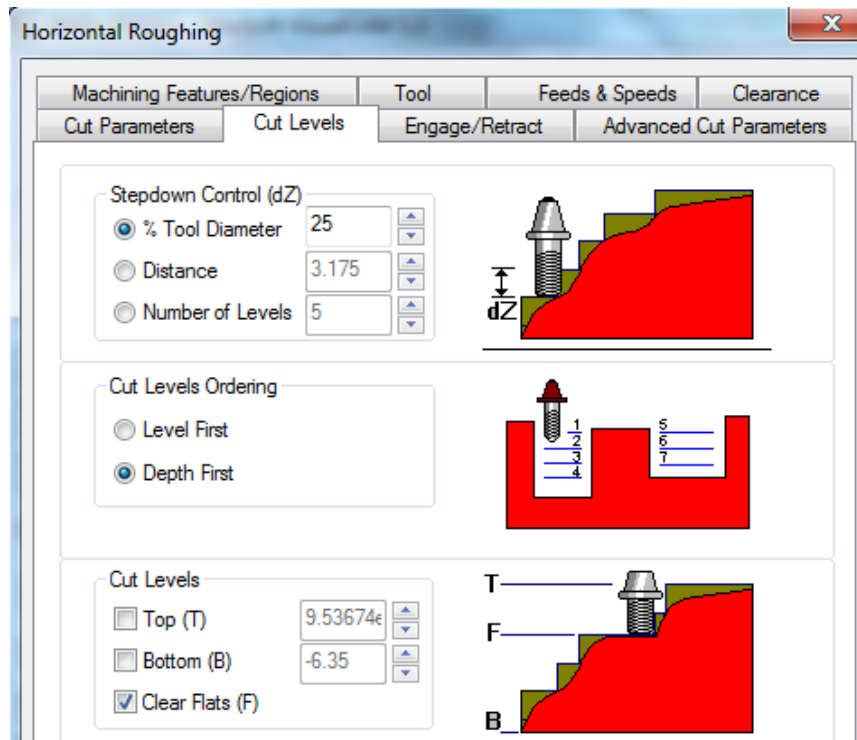


Figure B-14: Cut Levels tab.

- Leave the **Engage/Retract** and **Advanced Cut Parameters** tab as they are and click **generate**. It should take a few minutes to generate a tool path.



- After the **Horizontal Machining**, **Finishing Machining** was also performed. Most of the steps are similar to the Horizontal Machining except minor changes:
  - Click on the **cut parameters** tab, set stock to 0. Start side should be bottom, angle of cuts 0, and step over control should be set at 15% for % tool diameter.

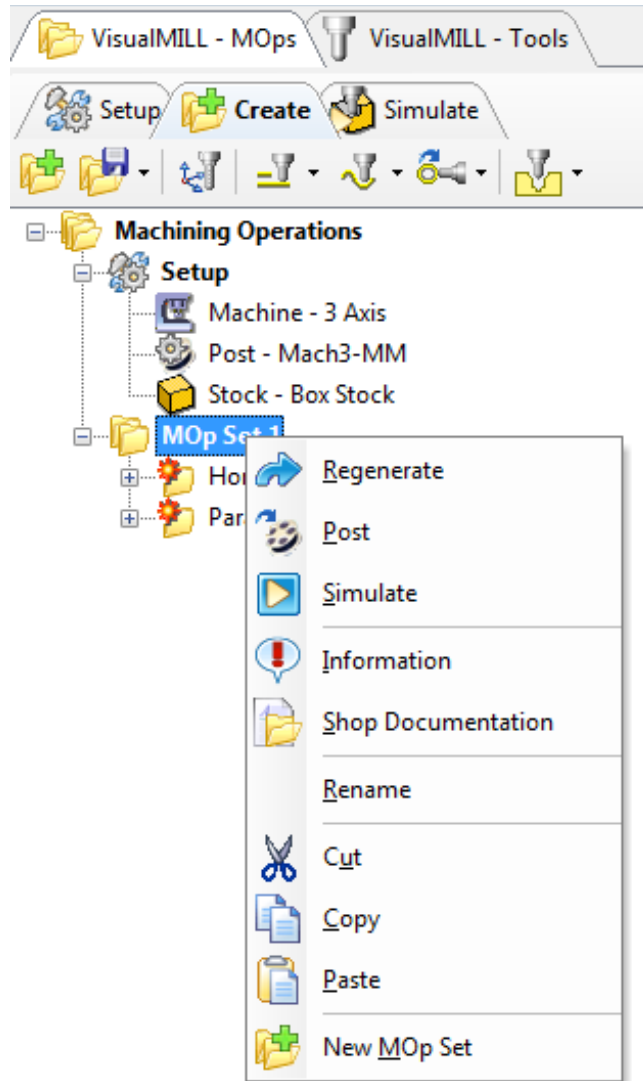


Figure B-15: Posting the G-code after setting the Horizontal and Finishing Machining.

- The last step with Visual Mill 6.0 analysis is to post the G-code. Right click machining operations from the setup tab and select post all (Figure B-15). Save the nc file.
- Next, on the MINITECH CNC computer, start the program **MACH 3 CNC** given



by the MINITECH Corporation, the desktop icon looks like this

- Next go to file, select upload g-code, then find the nc file saved to the computer made from visual mill, click on it and press ok (Figure B-16).

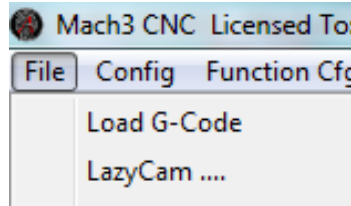


Figure B-16: Opening the G-code in the Mach3 CNC.

- Place double sided tape to the bottom face of the stock material about to be machined. Place the bottom face of the stock to the top face of the mill bed, and make sure it is aligned with the bed both in x and y axis.
- For the machine operation just uploaded, the tool that will be used in those machining operations is attached to the spindle.
- Next, the zero on the stock material is located and marked. On the **Mach 3** program, we go to the **jog tab** and use the x, y, and z buttons to move the tool to the marked position (Figure B-17).

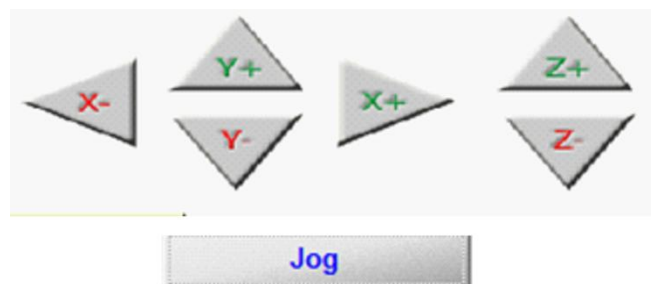


Figure B-17: Jog tab in the Mach 3. X, Y, and Z are used to change the stock holder position.

- Next, in the **jog tab** click z+ so that the tool is 1-2mm above the material, go to the **tools/fixtures tab** and for the **tool probe position** category press set and for the **probing start position** press set (Figure B-18).



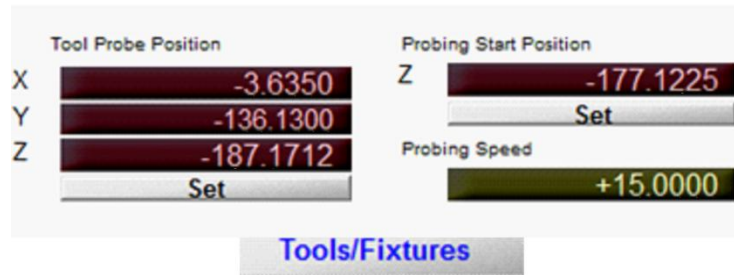


Figure B-18: Tools/Fixtures tab where the zero position is set.

- Next, to the right of the CNC computer there is a computer for the spindle motor. Turn on the computer using the switch at the bottom and use the up and down arrows to select the speed you want. For milling plastic 12000-15000RPM should be selected. Then press the start button and the spindle should start to rotate at the speed you selected.
- Next go to the cnc computer and click on the **control tab** and press **cycle start**. The uploaded program from visual mill should start running.
- If a tool breaks or an emergency occurs you can press Esc on the keyboard or press the stop button in the controls tab to stop the program, to stop the spindle press the off switch at the bottom of the spindle computer.
- If you want to stop the program in the middle of a machining operation and continue later, press the stop button on the control tab and turn spindle off. When you come back to finish the machining operation, turn the spindle on first at the speed you need, and then hit cycle start.
- An example of the machining path followed to make the channel along with the corresponding G-code is shown in figure B-19.

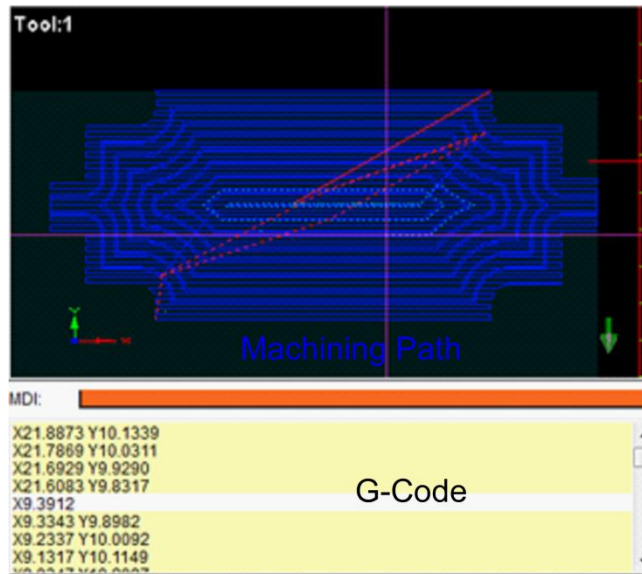


Figure B-19: Running G-code in the Mach 3. The line being executed is highlighted. The machining path is shown in blue color.

## CURRICULUM VITAE

### **Abderrazzak Faiz**

#### SUMMARY OF QUALIFICATIONS

- ◆ 4+ years hands-on experience in the area of semiconductor microfabrication and MEMS devices.
- ◆ Extensive experience with carbon nanotubes growth using Chemical Vapor Deposition (CVD).
- ◆ Developed a process for the fabrication of nanoporous thermoelectrics using powder metallurgy.
- ◆ Excellent communication skills, both in oral and written.

#### EDUCATION

Ph.D. Mechanical Engineering  
08/2014

University of Louisville, Louisville, KY, USA

Dissertation: “Nanoporous Bi<sub>2</sub>Te<sub>3</sub> Thermoelectric Based Knudsen Gas Pump”

Advisor: Dr. Shamus McNamara

*GPA 3.83/4.0*

M.Sc Physics and Astronomy

08/2008

University of Louisville, Louisville, KY, USA

*GPA 3.975/4.0*

B.S. Electrical Engineering (IEEA)

06/2005

Associate Degree Physics & Chemistry/Physics

06/2003

Cadi Ayyad University Beni-Mellal, Morocco

#### TECHNICAL SKILLS AND INSTRUMENTATIONS EXPERTISE

##### Material characterization

- SEM , EDAX, XRD, Ellipsometry
- Particle Size Analyzer to measure powder size distribution
- 4-probe measurement of resistivity and sheet resistance
- Differential Scanning Calorimeter to measure specific heat using Sapphire as reference
- Dektak surface profilermeter for measuring micromachined channel height
- InfraScope temperature measurement for capturing thermal images and video of thermoelectrics

##### Micro-fabrication

- Wet and dry oxidation, Wet etching, March RIE
- E-beam/thermal evaporator, RF/DC Sputtering, Optical Photolithography

## EXPERIENCE

University of Louisville

Research Assistant, *Mechanical Engineering Dept.*

08/08- 08/14

- Successfully fabricated and tested multiple operational carbon nanotube based devices for key biological application of proteins separation.
- Growth of aligned carbon nanotube inside microfabricated glass channels, and on silicon wafer using different catalysts (Fe, Co, Ni, and AlO<sub>2</sub>).
- Complete fabrication, characterization, and testing of nanoporous thermoelectrics using ball milling and pressure/pressureless sintering techniques.
- Fabricated and tested the first bi-directional thermoelectric based Knudsen pump.
- Mathematical modeling of heat transfer through the thermoelectric based Knudsen pump leading to a better understanding of the pump performance.
- Built a temperature controller to eliminate temperature fluctuations during PDMS based pumps testing.

Teaching Assistant, *Physics and Astronomy Dept.*

08/06 – 05/08

Final-year project, National Office for Electricity, *Morocco.*

04/05 -06/05

- Assisted mechanical/electrical technicians with routine activities and ensured operations proficiency leading to successful reduction of downtime in maintenance.

## PEER REVIEWED JOURNAL PUBLICATIONS

A. Faiz, S. McNamara, A. Bell, G. Sumanasekera: “*Nanoporous Bi<sub>2</sub>Te<sub>3</sub> thermoelectric based Knudsen gas pump*” *J. of Micromech. and Microeng.* 24, 035002, 2014.

A. Faiz, and S. McNamara: “*Mathematical model of a nanoporous thermoelectric based Knudsen pump*” *JVST A: Vacuum, surfaces, and Films*, 32, 041601, 2014.

## CONFERENCE PROCEEDINGS/PRESENTATIONS

A. Faiz, S. McNamara: “*Nanoporous Thermoelectric Knudsen Pump Integrated with a Microfluidic Channel*” 12th International Workshop on Micro and Nanotechnology for Power Generation and Energy Conversion Applications, Atlanta Georgia, USA, December 2 -5 2012

A. Faiz, S. McNamara: “*Nano-Porous Bi<sub>2</sub>Te<sub>3</sub> Thermoelectric Based Knudsen Gas Pump*” 2013 KY NanoSymposium, Louisville KY, USA, August 16-17 2013.

A. Faiz, A. Bell, S. Miles, K. Pharas, and S. McNamara: “*Recent Progress of the Knudsen pump*” 17<sup>th</sup> Annual KY EPSCoR Conference, Lexington KY, May 17, 2012.

A. Faiz, and S. McNamara: “*Peltier effect based Knudsen pump*” 2013 KY EPSCoR Annual Conference, Louisville KY, October 17, 2013.